

Intensified yellow fever and Zika virus production in animal cell culture

Dissertation

zur Erlangung des akademischen Grades

**Doktoringenieur
(Dr.-Ing.)**

von Alexander Nikolay (M.Sc.)
geb. am 27. Juli 1988 in Detmold

genehmigt durch die Fakultät für Verfahrens- und Systemtechnik
der Otto-von-Guericke-Universität Magdeburg

Promotionskommission: Prof. Dr.-Ing. Kai Sundmacher
Prof. Dr.-Ing. Udo Reichl
Prof. Dr. Francesc Gòdia
Prof. Dr. Michael Butler

eingereicht am: 3. August 2019
Promotionskolloquium am: 20. Februar 2020

Abstract

Flaviviruses are transmitted to humans primarily by the bite of an infected mosquito. After infection, the virus can cause severe disease patterns ranging from congenital malfunction to lethal hemorrhagic fever. The lack of specific treatments for flavivirus-related diseases turns vaccination to the only preventive countermeasure. An effective vaccine was already developed against yellow fever virus (YFV) being considered as the prototypic flavivirus. Until now, the vaccine is still manufactured in embryonated chicken eggs using traditional production methods. However, production capacities are difficult to expand at low profit margins, leading to a chronic undersupply of the vaccine. New production processes are required that can be ideally transferred to newly emerging and re-emerging flaviviruses such as Zika virus (ZIKV).

This work aimed to develop a next-generation, cell culture-based YFV vaccine production process. Of particular interest was the fast and efficient virus production with perfusion bioreactor systems as well as transferability to manufacturing of other flaviviruses such as wild-type ZIKV which replicates only at low cell-specific titers.

In the first two parts of this work, YFV propagation in different cell substrates was investigated. Initial infection experiments with adherent Vero cells, which are regarded as a typical reference for flavivirus replication, revealed cell-specific virus yields of about 10 infectious virions per cell (PFU/cell). To overcome anchorage-dependent scale-up limitations for large-scale production, various suspension cells were infected. Thereby, BHK-21_{SUS} and EB66[®] cells demonstrated highest viral permissiveness. Sequential virus adaptation to EB66[®] cells resulted in maximum cell-specific virus titers similar to Vero cells. However, due to slow virus spreading in the cell population, either multiplicity of infection (MOI) had to be increased or infection periods had to be extended beyond typical batch infection conditions. This enabled the infection of the entire cell population leading to increased viral titers. Finally, semi-continuous two-stage cultivations were performed. They indicated the absence of replication-interfering non-infectious virus particles, which could have otherwise disturbed the production process in perfusion mode.

In the third and fourth part, YFV production in batch cultivation was transferred to a perfusion process. First infection experiments with BHK-21_{SUS} cells in pseudo-perfusion mode enabled high cell concentrations of 5.9×10^7 cells/mL and similar cell-specific virus yields compared to batch infections (7–11 PFU/cell). The production process was then transferred to 1 L bioreactors coupled to scalable membrane-based perfusion units such as the tangential flow filtration (TFF) and the alternating tangential flow filtration (ATF) system. The fast growing EB66[®] cell line reached 9.5×10^7 cells/mL in perfusion mode applying the ATF system. Virus titers of 7.3×10^8 PFU/mL were achieved in less than two weeks. The total amount of virus in a 700 mL bioreactor would have been sufficient to deliver raw material for almost 10^7 doses of live-attenuated YFV vaccine. Subsequently, the process was transferred to ZIKV production. For this

purpose, various Brazilian ZIKV isolates were tested and the high-yield ZIKV^{RJ} isolate was identified. Cell-specific virus yields could be further increased from 0.5 to 5.5 PFU/cell by sequential virus adaptation to the EB66[®] cells. For the subsequent ATF perfusion process, an online biomass probe for perfusion rate control was used. This minimized manual intervention and increased the batch-to-batch reproducibility. A large-volume cryo-bag was utilized for direct bioreactor inoculation, providing additional production flexibility. This process enabled very high cell concentrations (1.6×10^8 cells/mL) and ZIKV titers (1.0×10^{10} PFU/mL). To this end, volumetric productivities of the intensified perfusion process (8.1×10^{10} PFU/L/day) even exceeded the batch culture (1.7×10^{10} PFU/L/day) previously considered the most efficient production mode.

The fifth part of this thesis covered the use of online multi-frequency capacitance probes to estimate cell growth during perfusion operation and virus infection. Three mathematical models were used to describe viable cell concentration and viable cell volume. The first-order linear regression model correlated permittivity signals with offline cell count data and allowed an accurate estimation of cell concentrations. However, the correlation parameter had to be slightly adjusted for each cultivation. The same accuracy was observed for partial least squares regression models with multivariate data analysis of spectroscopic frequency data. The best approximation was obtained by using the Cole-Cole equation to calculate the cell volume. Subsequently, additional raw data from the online probe were evaluated to detect virus-induced changes in the cell and to deduce virus dynamics. No dielectric signal or parameter could be assigned to virus replication. Instead, the capacitance probe could be reliably used for cell growth monitoring throughout the infection phase. Only during the cell decline phase, discrepancies between offline determined and online estimated cell concentrations occurred.

In the last part of this work, different hollow fiber membranes were systematically evaluated with regard to filter fouling and membrane permeability in order to allow for direct virus harvesting. Eight membranes of five different materials (cut-offs between 0.08 μm and 1.68 μm) were characterized. Measurements of the zeta potential suggested a principle repulsion between colloids (e.g. cells, particles) of the culture broth and the membranes. Subsequently, membrane roughness, surface structure and porosity were characterized using scanning electron microscopy. Polysulfone (PS) membranes were identified with best fouling properties (smooth surface structures and high porosity) for highest permeate volumes. This was confirmed in filtration experiments with YFV-infected BHK-21_{SUS} cells in cross-flow filtration mode. A large-pored 0.34 μm PS membrane was particularly suitable for direct virus harvest over an extended time period. A small-pored 0.08 μm PS membrane, on the other hand, retained virions almost completely in the bioreactor system, but also accumulated DNA and protein impurities.

Overall, important aspects of process intensification were elaborated. The presented perfusion process yielded in very high YFV titers and was successfully transferred to the production of ZIKV. In general, it is a well-suited platform for process development and intensification in vaccine manufacturing, particularly for viruses that replicate only at low cell-specific virus yields.

Kurzfassung

Flaviviren werden primär durch den Biss einer infizierten Mücke auf den Menschen übertragen. Nach Infektion kann das Virus schwere Krankheitsbilder verursachen, die von angeborenen Fehlfunktionen bis hin zu tödlichem hämorrhagischem Fieber reichen. Da es keine gezielten Behandlungen für flavivirusbedingte Krankheiten gibt, ist die Impfung die einzige präventive Gegenmaßnahme. Ein wirksamer Impfstoff gegen das Gelbfiebertvirus (YFV), das als prototypisches Flavivirus gilt, wurde bereits entwickelt. Bislang wird dieser Impfstoff noch in bebrüteten Hühnereiern nach traditionellen Produktionsmethoden hergestellt. Jedoch lassen sich die Produktionskapazitäten nur schwer erweitern und durch die geringe Gewinnmarge kommt es immer wieder zu Lieferengpässen des Impfstoffs. Neue Produktionsverfahren werden benötigt, die sich idealerweise auf neue und wieder aufkommende Flaviviren übertragen lassen. Ein Beispiel dafür ist das Zika-Virus (ZIKV), welches sich nur bei niedrigen zellspezifischen Ausbeuten vermehren lässt.

Ziel dieser Arbeit war die Entwicklung eines zellkulturbasierten YFV-Impfstoffproduktionsprozesses. Der Schwerpunkt lag dabei auf einer schnellen und effizienten Virusproduktion mit Perfusionsbioreaktorsystemen, die sich auch auf andere Flaviviren, wie beispielweise dem Wildtyp-ZIKV, anwenden ließ.

In den ersten beiden Teilen dieser Arbeit wurde die YFV-Vermehrung in verschiedenen Zellsubstraten untersucht. Erste Infektionsexperimente mit adhärennten Vero-Zellen, die als typische Referenz für Flavivirusvermehrung gelten, zeigten zellspezifische Virusausbeuten von etwa 10 infektiösen Viruspartikeln pro Zelle (PFU/Zelle). Um den Transfer in den Produktionsmaßstab zu erleichtern, wurden nun Suspensionzellen infiziert. Dabei zeichneten sich BHK-21_{SUS} and EB66[®]-Zellen durch eine hohe virale Permissivität aus. Die sequentielle Virusadaption an EB66[®]-Zellen führte zu maximalen zellspezifischen Virustitern ähnlich den der Vero-Zellen. Bedingt durch die langsame Ausbreitung des Virus in der Zellpopulation, musste jedoch entweder die Multiplizität der Infektion (MOI) erhöht oder Infektionsperioden über typische Batch-Infektionsprozesse hinaus verlängert werden. Beide Maßnahmen ermöglichten die Infektion der gesamten Zellpopulation, die zur Steigerung der Virusausbeute führte. Schließlich wurden semi-kontinuierliche, zweistufige Kultivierungen durchgeführt. Dabei wurden keine replikationsinterferierende, nicht-infektiöse Viruspartikel nachgewiesen, da diese andernfalls den Produktionsprozess in Perfusion hätten stören könnten.

Im dritten und vierten Teil wurde die YFV-Herstellung von einem Batch-Prozess zu einem Perfusionsprozess weiterentwickelt. Erste Infektionsexperimente mit BHK-21_{SUS}-Zellen in Pseudo-Perfusion ermöglichten hohe Zellkonzentrationen von $5,9 \times 10^7$ Zellen/mL und ähnliche zellspezifische Virusausbeuten im Vergleich zu Batch-Infektionen (7–11 PFU/Zelle). Der Produktionsprozess wurde anschließend auf 1 L-Bioreaktoren übertragen, die an skalierbare, membranbasierte Perfusionseinheiten wie dem Tangentialflussfiltrations- (TFF) oder alternierenden Tangentialflussfiltrationssystem (ATF) gekoppelt wurden. Die schnell wachsende EB66[®]-Zelllinie

erreichte $9,5 \times 10^7$ Zellen/mL in dem ATF-System. Dabei wurden Viruskonzentrationen von $7,3 \times 10^8$ PFU/mL in weniger als zwei Wochen erreicht. Diese Virusmenge wäre ausreichend gewesen, um unaufgereinigtes Material für nahezu 10^7 YFV-Impfstoffdosen eines Lebendimpfstoffs bereitzustellen. Im Anschluss wurde der Prozess auf die ZIKV-Produktion übertragen. Dafür wurden zunächst verschiedene brasilianische ZIKV-Isolate getestet. Die höchsten Ausbeuten wurden mit dem ZIKV^{RJ} Virusisolat erreicht. Die zellspezifischen Ausbeuten konnten durch die sequentielle Virusadaption an EB66[®]-Zellen von 0,5 auf 5,5 PFU/Zelle weiter erhöht werden. Für den folgenden Perfusionprozess wurde eine Online-Biomassesonde zur Perfusionenratenkontrolle installiert. Dadurch wurden manuelle Eingriffe minimiert und die Reproduzierbarkeit der Kultivierungen erhöht. Zur direkten Beimpfung des Bioreaktors wurde ein großvolumiger Kryobeutel verwendet, wodurch zusätzliche Produktionsflexibilität erreicht wurde. Dieser Prozess ermöglichte extrem hohe Zell-Konzentrationen ($1,6 \times 10^8$ Zellen/mL) und ZIKV-Titer ($1,0 \times 10^{10}$ PFU/mL). Dabei übertrafen die volumetrischen Produktivitäten des intensivierten Perfusionprozesses ($8,1 \times 10^{10}$ PFU/L/Tag) sogar die bisher als effizientester Produktionsmodus geltende Batchkultur ($1,7 \times 10^{10}$ PFU/L/Tag).

Der fünfte Teil dieser Arbeit behandelte den Einsatz von Online-Multifrequenzkapazitätssonden zur Abschätzung der Biomassezunahme während des Perfusionbetriebs und der Virusinfektion. Dafür wurden drei mathematische Modelle zur Beschreibung der lebensfähigen Zellkonzentration und des lebensfähigen Zellvolumens untersucht. Das lineare Regressionsmodell erster Ordnung korrelierte Permittivität mit Offline-Daten und erlaubte eine genaue Abschätzung der Zellkonzentrationen. Jedoch mussten die Korrelationsparameter für jede Kultivierung geringfügig angepasst werden. Eine ähnliche Präzision wurde für das PLS-Regressionsmodell (partial least squares regression) und multivariater Datenanalyse der spektroskopischen Frequenzdaten beobachtet. Die beste Annäherung wurde durch die Verwendung der Cole-Cole-Gleichung zur Berechnung des Zellvolumens erzielt. Anschließend wurden zusätzliche Rohdaten der Online-Sonde ausgewertet, um virusbedingte Veränderungen in der Zelle zu erkennen und daraus auf die Virusdynamik zu schließen. Jedoch konnte kein dielektrisches Signal oder Parameter der Virusvermehrung zugeordnet werden. Stattdessen ließ sich die Kapazitätssonde aber zuverlässig über die gesamte Infektionsphase zur Biomasseaufzeichnung verwenden. Lediglich während der Absterbephase traten Diskrepanzen zwischen offline-bestimmten und online-geschätzten Zellkonzentrationen auf.

Im letzten Teil dieser Arbeit wurden verschiedene Hohlfasermembranen hinsichtlich Fouling und Membranpermeabilität zur direkten Virusernte systematisch bewertet. Acht Membranen aus fünf verschiedenen Materialien (Ausschlussgrößen zwischen $0,08 \mu\text{m}$ und $1,68 \mu\text{m}$) wurden charakterisiert. Messungen des Zeta-Potenzials deuteten auf eine prinzipielle Abstoßung zwischen den Zellen und Partikeln in der Kulturbrühe mit den Membranen hin. Im Anschluss wurden mit Hilfe eines Rasterelektronenmikroskops die Membranrauigkeit, Oberflächenstruktur und Porosität charakterisiert. Dabei fielen die Polysulfon-Membranen positiv auf, die aufgrund glatter Oberflächenstrukturen und hoher Porosität für hohe Permeatvolumen geeignet wären. In anschließenden Tangentialflussfiltrationsversuchen mit YFV-infizierten BHK-21_{SUS} Zellen wurde diese Vermutung bestätigt. Eine großporige $0,34 \mu\text{m}$ Polysulfon-Membran eignete sich besonders zur direkten Virusernte über einen längeren Zeitraum. Eine kleinporige $0,08 \mu\text{m}$ PS-Membran hingegen

konzentrierte Viruspartikel vollständig im Bioreaktorsystem, wobei sich jedoch auch DNA- und Proteinverunreinigungen ansammelten.

Zusammenfassend wurden in dieser Arbeit wichtige Aspekte der Prozessintensivierung erarbeitet. Der entwickelte Perfusionsprozess ermöglichte sehr hohe Titer von YFV und wurde erfolgreich auf die Produktion von ZIKV übertragen. Generell können die durchgeführten Studien als Basis für die Prozessentwicklung und -intensivierung in der Impfstoffherstellung dienen, insbesondere für Viren, die sich nur bei geringen zellspezifischen Virusausbeuten vermehren lassen.

Table of Contents

Abstract	III
Kurzfassung	V
List of Abbreviations	XII
List of Symbols	XIV
1 Introduction	1
2 Theoretical Background	3
2.1 Flaviviruses.....	3
2.1.1 Virion structure and replication cycle.....	4
2.1.2 Yellow fever virus.....	7
2.1.2.1 Disease pattern.....	7
2.1.2.2 Viral spreading.....	7
2.1.2.3 Historical vaccine development and today's manufacturing.....	8
2.1.2.4 Global demand and strategies for disease control.....	9
2.1.3 Zika virus.....	10
2.1.3.1 Disease pattern.....	10
2.1.3.2 Viral spreading.....	11
2.1.3.3 Current vaccine approaches and challenges.....	12
2.2 Cell substrates – Vero, BHK-21 and EB66® cells.....	13
2.2.1 Vero cells.....	13
2.2.2 BHK-21 cells.....	14
2.2.3 EB66® cells.....	15
2.3 Process intensification.....	16
2.3.1 High cell density perfusion processes.....	16
2.3.1.1 Increased surface areas for adherent cells.....	16
2.3.1.2 External membrane-based perfusion systems.....	17
2.3.2 Perfusion rate control.....	21
2.3.3 Capacitance as an online biomass signal.....	23
2.3.3.1 From a dielectric principle to a biomass probe.....	23
2.3.3.2 Capacitance measurement and dielectric parameter calculations.....	25
2.3.4 Hollow fiber membranes.....	27
2.3.4.1 Membrane fouling.....	28
2.3.4.2 Membrane properties.....	30
2.3.4.3 Membrane operations to reduce fouling.....	32
3 Materials and Methods	34
3.1 Cell line maintenance.....	34
3.1.1 Cell passaging.....	36

3.1.2	Cryo vial freezing	36
3.1.3	Cryo vial thawing	37
3.1.4	Cryo bag preservation and direct bioreactor inoculation	37
3.1.5	Vero cell adaptation to suspension growth.....	37
3.1.6	Characteristic cell growth parameters	38
3.2	Semi-continuous two-stage shake flask cultivations	39
3.3	Pseudo-perfusion in shake flasks	39
3.4	Bioreactor cultivations	40
3.4.1	General assembly	40
3.5	Microcarrier cultivations.....	41
3.6	Perfusion bioreactor cultivations	42
3.6.1	Tangential flow filtration cultivations	42
3.6.2	Alternating tangential flow filtrations	43
3.6.3	Perfusion rate strategies.....	44
3.7	Flavivirus propagation	45
3.7.1	Sequential virus adaptation	47
3.7.2	Virus enrichment by centrifugation.....	47
3.8	Offline cell concentration measurements.....	47
3.8.1	Automated whole cell counting.....	47
3.8.2	Manual whole cell counting	49
3.8.3	Manual nuclei counting	49
3.9	Metabolite measurements	49
3.10	Virus quantification	50
3.10.1	Plaque assay	50
3.10.2	One-step TaqMan-based RT-qPCR.....	50
3.11	Flow cytometric analysis of flavivirus-infected cells	52
3.11.1	Production and purification of the 4G2 antibody	52
3.12	Capacitance measurements	53
3.12.1	Correlation and estimation of biomass	53
3.12.2	Calculation of dielectric parameters for virus dynamics.....	55
3.13	Membrane testing.....	56
3.13.1	Pore size distributions	56
3.13.2	Membrane surface charge	56
3.13.3	Cell broth zeta potential	57
3.13.4	Scanning electron microscopy.....	57
3.13.5	Filtration experiment	57
3.13.6	DNA and protein quantification	58
4	Results and Discussion	60
4.1	Yellow fever virus production with adherent Vero cells	60
4.1.1	Virus replication and scale-up into bioreactors	60
4.1.2	Turbidity and capacitance measurements.....	64
4.1.3	Towards suspension-adapted Vero cells	66
4.1.4	Summary	69
4.2	Yellow fever virus propagation in suspension cells	69
4.2.1	Alternative cell substrates	69

4.2.2	Virus production dynamics	72
4.2.3	Virus evolution in semi-continuous cultivation	74
4.2.4	Summary	76
4.3	Process intensification for yellow fever virus production	77
4.3.1	Pseudo-perfusion cultivation.....	77
4.3.2	Perfusion cultivation	81
4.3.3	Summary	88
4.4	Transfer of a perfusion cultivation to Zika virus production.....	89
4.4.1	Scouting experiments with adherent cells.....	89
4.4.2	Automated perfusion cultivation.....	91
4.4.3	Summary	97
4.5	Potentials and limitations for the use of a capacitance probe in virus production processes.....	98
4.5.1	Biomass correlation.....	98
4.5.2	Dielectric properties of a cell population	107
4.5.3	Summary	112
4.6	Hollow fiber membranes for perfusion cultivations.....	113
4.6.1	Membrane characterization	113
4.6.2	Performance of membranes in cross-flow operation	119
4.6.3	Summary	125
5	Conclusion	127
6	Outlook	131
	List of Figures	133
	List of Tables	135
	List of Publications	137
	Bibliography	139
7	Appendix	158
A7.1	Materials and devices.....	158
A7.2	Standard operating procedures.....	161
A7.2.1	SOP – Flavivirus plaque assay.....	161
A7.2.2	SOP – One-step TaqMan RT–qPCR	161
A7.2.3	SOP – Synthesis of <i>in-vitro</i> RNA copy number standards.....	161
A7.2.4	SOP – Immunostaining for flow cytometric flavivirus detection.....	161
A7.4	Supplementary	162

List of Abbreviations

4G2-mAB	unconjugated monoclonal antibody against E protein
AER	avian endogenous retrovirus
AFM	atomic force microscopy
AGE1.CR	primary duck retina cell line
AGE1.CR.pIX	primary duck retina cell line modified with pIX capsid protein from adenovirus
ALV	avian leucosis virus
ADCC	antibody-dependent cell cytotoxicity
ADE	antibody-dependent enhancement
ATCC	American Type Culture Collection
ATF	alternating tangential flow filtration
ATF-M	ATF cultivation with manual perfusion rate adjustments to maintain metabolite levels
ATF-17pL	ATF cultivation with perfusion rate control at 17 pL/cell/day
ATF-34pL	ATF cultivation with perfusion rate control at 34 pL/cell/day
BHK-21	baby hamster kidney cell from subclone 13
BHK-21_{sus}	suspension-adapted BHK-21 cell
bp	base pairs
C6/36	ATCC CRL-1660 insect cell line
C	viral capsid protein
CA	cellulose acetate
CD	viable cell diameter in μm
CDM	chemically defined medium
CN	cellulose nitrate
C_t	threshold cycle
CSPR	cell-specific perfusion rate in pL/cell/day
CSVY	cell-specific virus yield in PFU/cell
CV	coefficient of variation
CZC	congenital Zika syndrome
D	vessel diameter in cm
D₉₀	estimated particle cut-off in μm
DENV	Dengue virus
dH₂O	deionized Milli-Q-grade water
DLS	dynamic light scattering
DMSO	dimethyl sulfoxide
DO	dissolved oxygen
E	viral envelope protein
EB66[®]	embryonic stem cell from Pecking duck
ER	endoplasmic reticulum
EYE	Eliminate Yellow Fever Epidemics strategy workgroup
FACS	fluorescence-activated cell sorting
FBS	fetal bovine serum
FCS	fetal calf serum
GBS	Guillain–Barré syndrome
glc	glucose
gln	glutamine
HB-4G2	hybridoma cell line expressing 4G2 mAB
HEK293SF	human embryonic kidney SF-3F6
hpi	hours post infection in h
ICG	International Coordination Group on Vaccine Provision
ID	inner diameter in mm
IAV	Influenza A virus
IDT	IDT Biologika Dessau-Roßlau
IEV	intracellular enveloped virion
IGF	insulin-like growth factor
IPTG	isopropyl- β -D-thiogalactopyranosid

JEV	Japanese encephalitis virus
MDCK.SUS2	susp. adapted madin darby canine kidney CL-34
ME	mixed cellulose ester
mock	uninfected control group treated as infected culture
MOI	multiplicity of infection in PFU/cell
mPES	modified polyethersulfone
MVA	Modified vaccinia Ankara virus
NIH	National Institutes of Health
NRC	National Research Council of Canada
nSEC	normalized standard error of calibration in %
NTC	no template control
NS	non-structural viral protein
PAT	process analytical technology
PBG	ProBioGen Berlin
PBS	phosphate buffered saline
PE	polyethylene
PS	stable porcine kidney cell line
pO₂	partial pressure of oxygen in %
pyr	pyruvate
BGM	protein expression medium
PES	polyethersulfone
PFA	paraformaldehyde
PFU	plaque forming unit in PFU
PLS	partial least squares
prM	viral precursor protein-membrane protein complex
PS	polysulfone
PTF	pulsating tangential flow
RI	refraction index dimensionless
RKI	Robert Koch-Institute Berlin
RMSC	root-mean-square standard error of calibration
PVP	poly(vinyl pyrrolidone)
RT	room temperature (average 21°C)
RT-qPCR	quantitative reverse transcription polymerase chain reaction
RV	bioreactor volume in L
RV/d	bioreactor volume exchange per day in L/day
SCM	serum-containing medium
SEC	standard error of calibration in %
SEM	scanning electron microscope
SEP	root-mean-square standard error of prediction in %
SET	standard error of transfer in %
SFM	serum-free medium
(+)ss-RNA	positive polarity single-stranded RNA
SPF	specific-pathogen-free
T	impeller diameter in mm
TBEV	tick-borne encephalitis virus
TGN	<i>trans</i> -Golgi network
TFF	tangential flow filtration
TMP	transmembrane pressure in mbar
UAB	Autonomous University of Barcelona
UFRJ	The Federal University of Rio de Janeiro
VCC	viable cell concentration in cells/mL
VCV	viable cell volume in pL
Vero	epithelial kidney cells from African green monkey
Verosus	suspension-adapted Vero cell
vRNA	viral RNA molecules
YFV	yellow fever virus
YFV-17D	European yellow fever vaccine virus
YFV-17DD	Brazilian yellow fever vaccine virus
WHO	World Health Organization
ZIKV	Zika virus

List of Symbols

Symbol	Unit	Description
α	–	Cole-Cole alpha
γ	s ⁻¹	shear rate at membrane wall
$\Delta\varepsilon_{max}$	–	maximum permittivity discrepancy from f_1 to f_∞
$\Delta\varepsilon$	–	relative permittivity discrepancy from f_c to f_∞
Δt	h	sampling time interval
ε	–	relative permittivity
ε_s	–	residual static low-frequency permittivity
ε_∞	–	background permittivity at 10 MHz
η_m	mPa s	hydrodynamic viscosity of medium at 37 °C
θ	°	contact angle between fluid and membrane
μ	h ⁻¹	specific cell growth rate
Φ_v	–	biovolume fraction
$\Phi_{v,p}$	–	predictive biovolume fraction
σ	mS/cm	static suspension conductivity
σ_0	mS/cm	static medium conductivity
σ_i	mS/cm	intracellular conductivity
σ_{reject}	–	rejection coefficient
A_{filter}	m ²	filtration surface
C_{cap}	μF/cm ²	capacitance
C_m	μF/cm ²	cell membrane capacitance
$C_{MC,BR}$	carriers/mL	concentration of microcarriers in bioreactor
$C_{MC,sp}$	carriers/mL	desired concentration of microcarriers
C_{vir}	virions/mL	concentration of infectious virus
$C_{vir,max}$	virions/mL	maximum concentration of infectious virus
$C_{vir,inf}$	virions/mL	concentration of infectious virus at time point of infection
$CSPR$	pL/cell/day	cell-specific perfusion rate per day
$CSYV$	virions/cell	cell-specific virus yield
d_c	μm	viable cell diameter
\hat{d}_c	μm	estimated viable cell diameter
f_∞	MHz	characteristic frequency at 10 MHz
f_1	MHz	characteristic frequency at 0.3 MHz
f_c	MHz	characteristic frequency
f_n	–	number of hollow fibers
f_x	MHz	frequency at X MHz
g	m/s ²	gravitational force
G	mS/cm ²	conductance
G_m	mS/cm ²	membrane conductance
J	L/h/m ²	surface-specific permeate flux
MOI	virions/cell	multiplicity of infection
$N_{C,FR}$	cells/chamber	cell count in Fuchs-Rosenthal hemocytometer
N_m	carriers/mg	amount of microcarriers per dry weight
N_{MC}	carriers/well	amount of microcarriers per well
N_{vc}	cells	number of total viable cells
NTU_{880}	–	turbidity at a wavelength of 880 nm
q_s	pmol/cell/h	substrate consumption rate
Q_{perf}	mL/min	perfusion rate
r	mm	inner fiber lumen radius
r_c	μm	average cell radius
\hat{r}_c	μm	estimated cell radius
r_c	h ⁻¹	cell growth rate
R	m ⁻¹	total membrane resistance

Symbol	Unit	Description
$\overline{RV/d}$	mL/day	reactor volume exchange rate per day
R_m	m^{-1}	hydraulic membrane resistance
R_{bl}	m^{-1}	boundary layer resistance
s_0	mM	substrate concentration in perfusion medium
t_D	h	population doubling time
TMP	mbar	transmembrane pressure
V_1	mL	fresh medium volume to cell growth shake flask
V_2	mL	cell broth volume to virus production shake flask
V_3	mL	fresh medium volume to virus production shake flask
V_4	mL	cell broth volume removed from virus production shake flask
V_c	$\mu\text{L}/\text{mL}$	viable cell volume per medium volume
\widehat{V}_c	$\mu\text{L}/\text{mL}$	estimated viable cell volume per medium volume
V_E	mL	perfusion volume
VCC	cells/mL	concentration of viable cells
VCV	$\mu\text{L}/\text{mL}$	viable cell volume/fraction
V_{vir}	mL	virus seed volume inoculum
V_W	mL	bioreactor working volume
V_{well}	μL	volume per well
\dot{V}	L/h	volumetric flow rate in perfusion mode
\dot{V}_{perm}	L/h	permeate flow rate
X_c	cells/mL	viable cell concentration
\widehat{X}_c	cells/mL	estimated viable cell concentration
$X_{c,well}$	cells/mL	viable cell concentration in a well
$X_{tot,max}$	cells/mL	maximum cell concentration

1 Introduction

The flavivirus genus encompasses more than 53 single-stranded RNA viruses such as yellow fever virus (YFV), Zika virus (ZIKV), Japanese Encephalitis virus, West Nile virus and Dengue virus. These arthropod-borne viruses circulate between non-human primates in rainforest and sylvatic regions primarily through flavivirus-competent mosquitos such as *Aedes aegypti* and *Aedes albopictus*. The viral transmission to humans is rather accidental, but is linked to severe diseases in the individual. When the virus is introduced to densely populated regions with infected *Aedes* mosquitos, virus-related disease spreading can lead to major endemic outbreaks, putting thousands of unvaccinated people at serious risk [1].

The lack of specific therapies for disease treatment turns vaccination into the only preventive countermeasure. Already in 1937, a very effective live-attenuated YFV vaccine was developed and manufactured in embryonated chicken eggs [2]. Essentially unchanged, this vaccine production process requires about 12 months from ordering those specific eggs to vaccine release. This renders fast response difficult and bears the risk of a vaccine shortage, which occurred during recent endemic YFV outbreaks in Africa and the South Americas. In case of vaccine shortage, only dose-sparing practices can be applied to stretch vaccine supplies, but the depletion of global emergency stockpiles could not be prevented [3]. In addition, it has to be taken into account that mosquito vectors are on the rise and infest highly populated territories such as China so far considered to be free of YFV. This underpins the inherent threat to public health and the urgent need to expand global vaccine production capacities [4]. Furthermore, the recent spread of ZIKV in the South Americas has reached hitherto unknown dimensions. The link to severe microcephaly in newborns and other congenital defects prompted the World Health Organization to declare a global health emergency [5, 6]. As the development of vaccines against emerging and re-emerging flaviviruses, such as ZIKV, may compete with production resources required for various egg-based vaccines, alternative manufacturing platforms need to be considered.

The key to a successful vaccine manufacturing platform against existing and upcoming viral diseases is the use of animal cell culture. With the identification of continuous cell lines being highly permissive for viruses, it enables cell growth and virus propagation in cell culture medium and closed bioreactor systems ensuring sterility. In the following step, virions are harvested and processed following the respective viral vaccine strategy for manufacturing of live-attenuated or inactivated vaccines [7]. At this stage, options for cell culture-based YFV production processes are investigated with adherent Vero cells growing on surfaces such as tissue culture flasks for cell seed expansion and microcarriers in quasi-suspension for virus production [8, 9]. However,

microcarrier-based processes have general drawbacks for large-scale manufacturing, e.g. challenging bead-to-bead transfer, low cell/surface saturation density, limited microcarrier concentration and scalability [7]. Furthermore, cultivations require animal component-free media to reduce the risk of bacterial or viral contaminations and of batch-to-batch variations, while enabling optimum cell growth and, in particular, cell adhesion to the surface [10]. Facing problems to appropriately address these challenges, the development of cell-culture based YFV vaccine processes was not pursued to manufacturing scale [8].

Today, various suspension cell lines are available for virus production and therefore, cell-culture based YFV production processes can be re-evaluated. Suspension cells can be easily expanded by volume increase to fully exploit the capacity of bioreactors. As a result, suspension cells are the current choice for most large-scale biomanufacturing processes [11]. In the scope of process intensification, the space requirement of culture vessels can be reduced by retaining suspension cells in the bioreactor to achieve very high cell concentrations, while used medium is continuously exchanged with fresh perfusion medium. The key to a successful process, however, is to avoid a drop in cell-specific virus yield during scale-up and automated perfusion rate control for high batch-to-batch reproducibility. Well-described cell retention devices rely on the use of hollow fiber membranes that enable to increase cell concentrations by a factor of 40 and higher [12]. However, membrane-based retention devices are also known to partially retain the product such as recombinant proteins and virions in the bioreactor [13]. Therefore, the establishment of strategies is essential to either keep all virus particle in the bioreactor or to allow for continuous harvesting via the membranes into the permeate.

The aim of this work was to develop an intensified cell culture-based flavivirus production process. Therefore, a live-attenuated YFV was chosen as model system to design and optimize production processes, which were later transferred to other flaviviruses, e.g., the wild-type ZIKV. In a first step, flavivirus-related assays such as plaque assay, RT-qPCR and flow cytometry were established. This allowed a thorough analysis of the typical virus replication and infection optimization. In a second step, alternative cell substrates were screened, preferably cells growing in suspension. The identified suspension cells were then directly cultivated in bioreactors allowing various process intensification options such as perfusion cultivation. Finally, a closer look was taken at perfusion rate control, and on the right choice of a hollow fiber membrane for continuous virus harvesting.

In the following, a theoretical background on flaviviruses, permissive cell substrates and process intensification strategies is provided. The subsequent chapter describes the methods and the materials used to perform all experiments of this project. In the next chapter, results are presented on YFV propagation in adherent and suspension cells moving towards process intensification in perfusion cultivations and virus retention studies. Finally, a conclusion and a brief outlook of this work are given.

2 Theoretical Background

The first section of this chapter introduces the flavivirus genus with a particular focus on YFV and ZIKV. Subsequently, cell substrates suitable for the production of viral vaccines against flaviviruses are discussed. In the last section, options for intensified vaccine production processes using membrane-based perfusion systems are outlined. This includes an overview on the use of capacitance probes, and an introduction in the use of hollow fiber membranes for virus harvesting/retention addressing problems related to membrane fouling.

2.1 Flaviviruses

The flavivirus genus belongs to the family of *Flaviviridae* (derived from the Latin word *flavus* meaning yellow referring to a typical disease symptom). It encompasses more than 53 virus members with 73 serotypes. Viruses such as YFV, ZIKV, Japanese Encephalitis (JEV), West Nile (WNV), Dengue (DENV), and tick-borne encephalitis virus (TBEV) can cause severe diseases in humans and were declared as global health threats [14]. Flaviviruses are mainly transmitted by the bite of an infected arthropod (mostly mosquito or tick, but not all vectors are known) and assigned to the arbovirus group B [15]. Viruses circulate between their natural hosts, in particular monkeys, which inhabit rainforest or sylvatic regions (Figure 2.1 A). The transmission from mosquitoes to humans entering such regions is rather incidental. Due to the fact that most flaviviruses replicate only to low titers in humans, the human as viral host is typically considered as dead-end. However, a high threat occurs when infected humans introduce the flavivirus into highly populated regions, where the mosquito transmission vector is present (Figure 2.1 B). Only a few virus particles in the mosquito are sufficient to replicate to infectious titers in the mosquito's saliva and to pass on the virus to progeny mosquitoes by transovarian transmission [16]. This can result in endemic virus outbreaks and global virus spreading due to increased travel activities. In addition, certain flaviviruses such as ZIKV are well-enough adapted to humans and replicate to high titers enabling sexual transmission. The close connection of the sylvatic and urban transmission cycle turns viral spreading barely controllable and eradication is therefore impossible [17]. In the following, the general flavivirus structure is described and further details on YFV- and ZIKV-related diseases and vaccines are elaborated.

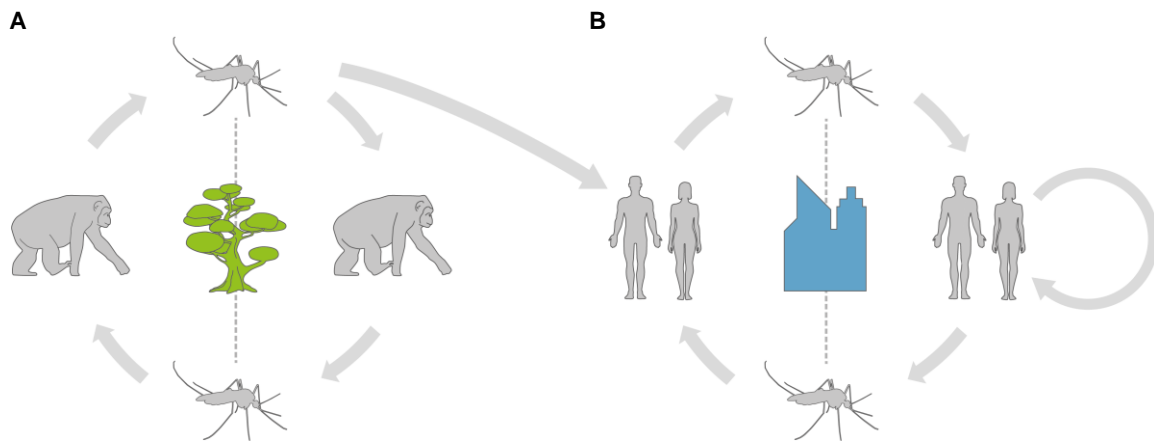


Figure 2.1 | Transmission cycles of flaviviruses. (A) Flaviviruses are mostly transmitted by infected mosquitoes between hosts in rainforest or sylvatic regions. Transovarial transmission is indicated as dotted vertical line. (B) When the virus is introduced to urban regions, it can be transmitted in endemic cycles between humans. Venereal transmission is known for certain flaviviruses such as ZIKV replicating to high virus titers in the human body.

2.1.1 Virion structure and replication cycle

The flavivirus genome consists of a single-stranded RNA molecule of positive polarity ((+)ss-RNA), which is surrounded by a spherical capsid (C) protein layer and a lipid bilayer presumably derived from the endoplasmic reticulum (ER) of the host cell [18]. The surface of intracellular virions consists of precursor membrane (prM) and envelope (E) proteins forming a heterodimer complex. The membrane (M) protein is a small proteolytic fragment anchored in the bilayer membrane by two transmembrane helices and links the pr fraction of prM. During virus maturation, the pr peptide is cleaved and the E protein rearranges to antiparallel dimers with the M protein. Three of the M-E protein heterodimers form one peplomer essential for receptor binding. The surface becomes smoother and the virion turns infectious before release (Figure 2.2). The size of a single virion is approximately 40-50 nm [19].

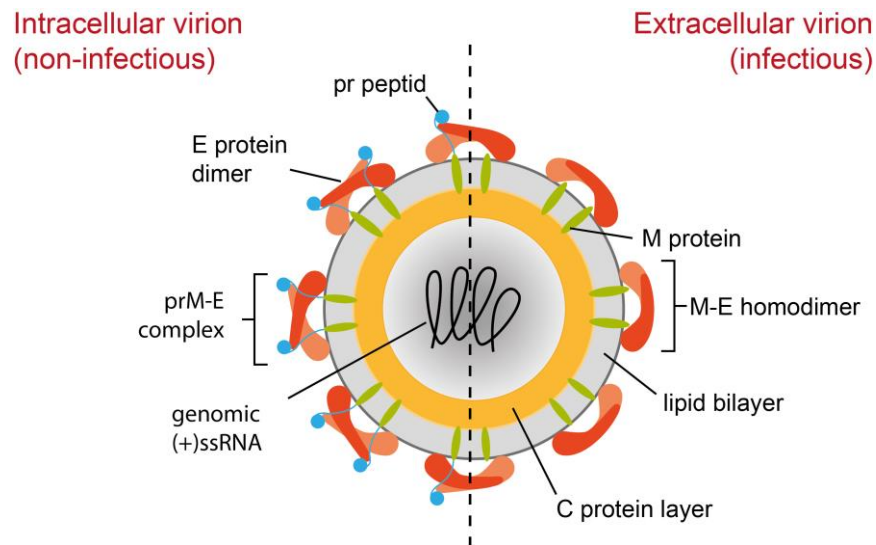


Figure 2.2 | Simplified structure of the flavivirus particle. The genomic (+)ssRNA is surrounded by viral capsid (C) proteins and a lipid bilayer from the endoplasmic reticulum of the host cell. **(Left side)** Intracellular virions with prM-E complex are non-infectious. **(Right side)** During virus maturation, pr peptide cleavage initiates conformational changes on the virion surface and particles become infectious.

During natural transmission, virions enter the mosquito in the course of its full blood meal. They spread through the midgut into other tissues, particularly the reproductive tract and salivary glands, and replicate [20]. If the infected mosquito bites a human, virions can be transmitted to the human body and infect cells such as monocytes, macrophages and dendritic cells [21]. Virions eventually spread to other tissues and organs via the bloodstream (viremia). The subsequent viral replication follows a specific cycle, which is illustrated in Figure 2.3. The virions attach to the cell membrane via the viral E protein to specific, but unidentified cell surface receptors [22]. After virus adsorption, clathrin-mediated endocytosis enables virus entry into the cell. Subsequent pH-dependent fusion with the endosomal membrane leads to the release of viral RNA (vRNA) into the cell cytoplasm [22-25]. The following translation of the genomic (+)ss-RNA takes place at the rough ER in specialized membrane complexes [20]. These partially isolated organelles may be fundamental to inhibit the host cell immune response by shielding double-stranded RNA or 5'-phosphorylated RNA from detection [26]. Starting from a single open reading frame, a polyprotein is formed by the host cell machinery, and co- and post-translated into three structural (C, E and M protein) and seven non-structural (NS) proteins [20]. While the structural proteins are present in the mature virion, NS proteins are formed immediately after infection to mediate various enzymatic activities essential for protein processing and genome replication [23, 27]. The self-organized C protein forms an icosahedral capsid that envelops the viral genome. The RNA is additionally surrounded by an ER-derived lipid bilayer, which facilitates anchoring of E and prM proteins via C-terminal transmembrane domains (Figure 2.2) [28]. During virus assembly, the prM protein serves as a chaperone and masks the fusion peptide segment located on the E protein [29, 30]. Simultaneously, the immature virus particle is *N*-glycosylated and finally released from the ER. Virions are further processed in a mildly acidic environment of the Golgi apparatus, where glycotransferases extend glycan antennae to form larger hybrid or complex glycosylation structures [31]. In the subsequent *trans*-Golgi

network (tGN), the prM protein is cleaved by the host cell enzyme furin into a pr peptide and an M protein. This results in a dissociation of E/prM heterodimers into E and M homodimers accompanied by a global conformational change of the virion. The matured virions become infectious and bud into the extracellular environment before virus-induced burst-like release. The cleavage of the pr peptide is a prerequisite for the infectivity of the virion [20, 22, 25, 29]. If errors occur during assembly (i.e. lack of viral RNA, lack of C protein) or maturation, non-infectious subviral particles and immature virions can be respectively formed [29].

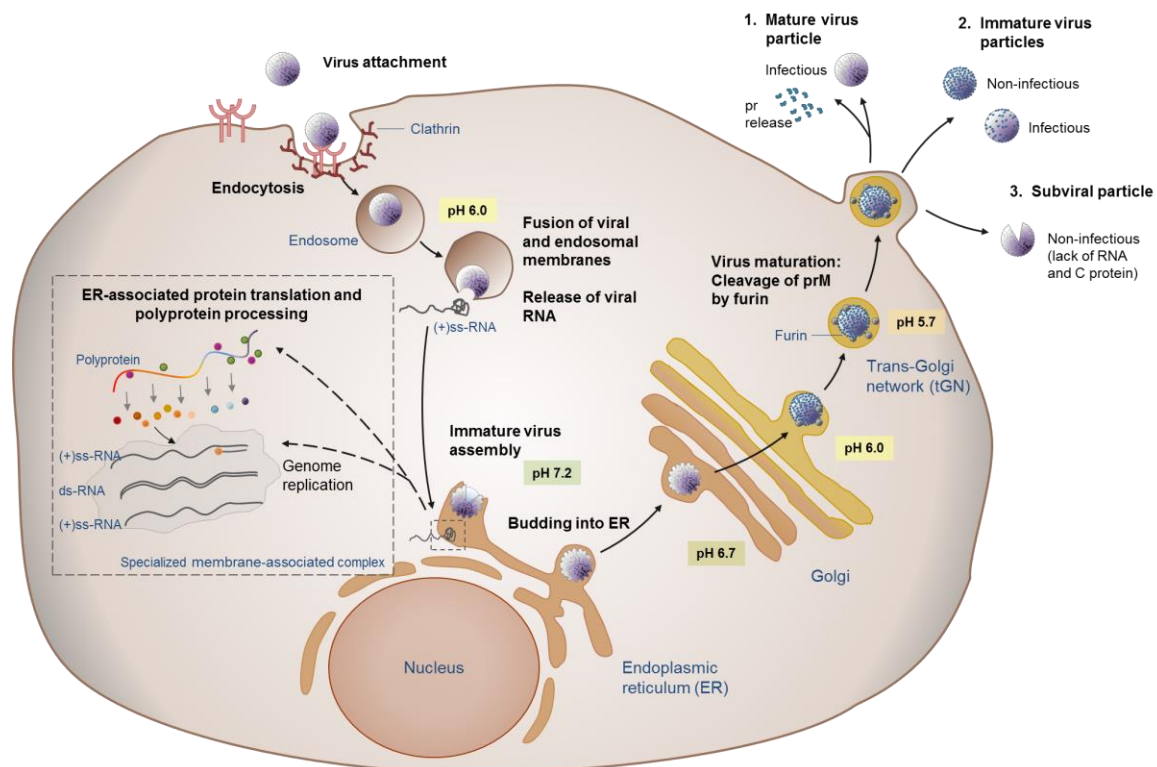


Figure 2.3 | Flaviviruses replication cycle. Virions bind to cellular surface receptors and become internalized by clathrin-dependent endocytosis. The acidic pH in the endosome fuses viral and endosomal membranes and (+)ssRNA is released into the cytoplasm. The immature virus assembly takes place at the rough endoplasmic reticulum (ER) in specific, but still unknown membrane complexes. The viral genome encodes for one polyprotein, which is processed co- and post-translationally to three structural and seven non-structural proteins. Capsid (C) proteins and progeny RNA are enveloped by an ER-derived bilayer, which contains viral precursor membrane (prM) and envelope (E) proteins. The immature virus particle is glycosylated and transported through the secretion pathway. In the last step of virus maturation, the pr of the M protein is cleaved by the cellular endoprotease furin, which exposes the fusion peptide segment of the E protein. This turns the virion infectious and is released into the extracellular space. If the virus maturation is disturbed, immature virus particles can be formed. If genomic and/or C protein packaging is disturbed, subviral particles can lack infectivity.

2.1.2 Yellow fever virus

The virus has its origin in West Africa and was introduced to new countries during the slave trade 400 years ago [32]. When YFV spread to urban regions without natural population immunity, disease outbreaks were usually fatal. The development of a highly effective live-attenuated vaccine enabled first disease control, but today's vaccine demand exceeds current global production capacities. This chapter provides information on virus pathogenesis and viral spreading. In addition, it gives a historical excursion on the vaccine development. Finally, vaccine production capacities and demand are briefly discussed.

2.1.2.1 Disease pattern

Once infected with YFV, the disease shows typical incubation periods of about three to six days before the patient will go through either one or two successive phases of the yellow fever disease. The first phase starts with a sudden increase in fever, which is accompanied by unspecific symptoms such as muscle pain, headache, chills and loss of appetite. Most patients regenerate after three to four days and show a lifelong protection without any long-term damage. However, 15-25 % of infected people undergo a second toxic phase with a high mortality rate. YFV is neuro-viscerotropic and can cause viremia, liver, kidney and myocardial damage, bleeding and encephalitis. The severe damage to the liver is manifested as icterus, also known as jaundice, which first discolors the eyes and then the skin. In later stages, virions infect and lyse cells in blood vessel walls, causing bleeding in mouth, nose, eyes and stomach. Half of the patients in the second phase die within ten to 14 days after the onset of symptoms [20, 33].

2.1.2.2 Viral spreading

Due to the transmission cycle of YFV, its spreading is only controllable with extensive vaccination campaigns. Currently, more than 48 endemic areas in Africa and Latin America with a total population of 900 million people are particularly at risk [34]. Other regions such as Asia, where the main urban transmission vector *Aedes aegypti* is inhibited, are still considered to be free of yellow fever. The fear of an endemic outbreak in this region, however, is high and due to its high population density comprehensively monitored by the World Health Organization (WHO) (Figure 2.4). Global warming and increased travelling activities lead the global expansion of the mosquito and enhance potential viral spreading. For a long time, the Sahara Desert was considered as the northern border of the mosquito vector. However, with increasing earth temperature, the mosquito could already reach the Mediterranean sea via Morocco and Turkey and may spread to the Alps via Spain and Greece in the next few years [35]. Every year, around three million people from Asia, Europe and North America travel to endemic yellow fever areas contributing to the risk of viral spreading [36]. Thus, predictive studies for geographical receptivity to yellow fever transmission are of high importance and can be used for specific vaccination recommendations preventing outbreaks.

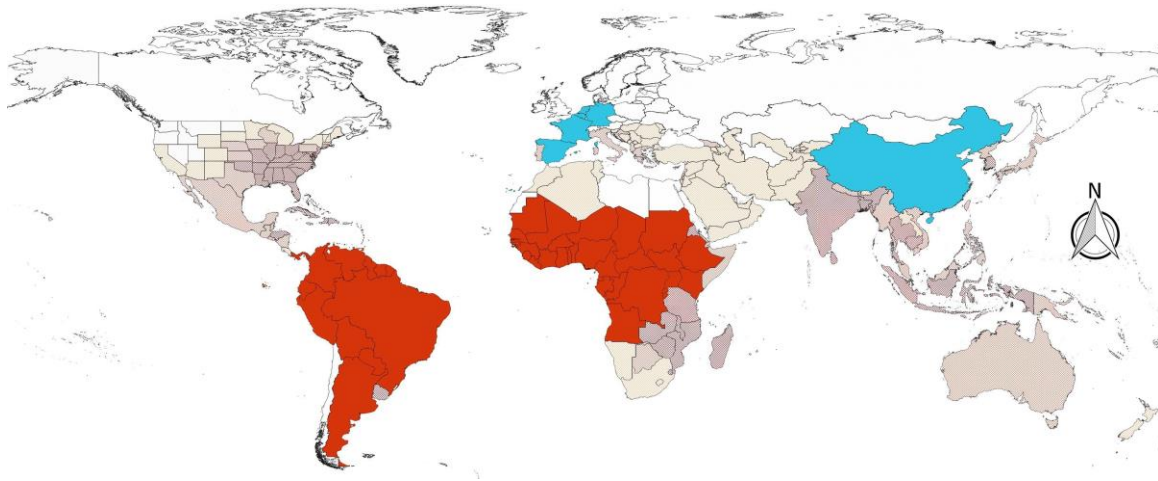


Figure 2.4 | Global yellow fever occurrence and risk map. Disease distribution corresponds with the global risk of viral infection. Status of infection occurrence: Not reported, autochthonous vector borne transmission, travel-related occurrence. Countries/territories at risk: No risk, mid risk, high risk. Adopted from Leta and colleagues, licensed under CC-BY-NC-ND [35].

2.1.2.3 Historical vaccine development and today's manufacturing

With the end of the First World War, research activities towards yellow fever disease and its transmission increased again. First speculations of bacterial spirochetes in brain tissue as causative agent were refuted [37], and theories moved towards a virus-related infection. In the late 1930s, two African patients were found suffering from mild yellow fever symptoms and a blood sample was injected into rhesus monkeys. The monkeys turned ill and proved to be a susceptible animal system for the pathogen. This allowed to maintain and study wild-type YFV for the first time. Important infection studies followed, where serum from immune humans was injected into monkeys, which were subsequently challenged with YFV. Interestingly, the monkeys survived and the first idea for a vaccine arose [38]. With Pasteur's pioneering works for attenuating rabies virus in non-host nervous tissue, Theiler and colleagues began to work with two different wild-type YFV isolates, namely the French strain [39] and the Asibi strain [40]. They inoculated the virus intracerebrally into mice and detected reasonable virus titers, but lower hepatic damage and systemic illness back in rhesus monkeys. After 128 passages in mouse brains, the French strain was attenuated and elicited an adequate protection. The resulting French neurotropic vaccine (FNV) was mostly used in French colonies in Africa beginning of 1934 [41]. However, 48 years later, the production of the French vaccine was discontinued due to laborious vaccine administration by scarification and high incidences of encephalitic reactions in children [42]. Back in the times, the Asibi strain was excessively passaged 18 times in mouse embryo tissue, 58 times in minced whole chicken embryo tissue and, finally, 128 times in minced whole chicken embryos without nervous tissue. The resulting strain seemed to be sufficiently attenuated as it lost its viscerotropism and neurotropism and failed to kill mice [43]. The selected virus isolate was named YFV-17D. Later, deep sequencing revealed mutations in the prM and E protein regions [44] and diminished quasi-species diversity in comparison to the Asibi strain [45], but the mechanism of attenuation still remains unclear. The 17D isolate was further passaged and two vaccine strains called 17DD at passage level 195 and 17D-204 at passage

level 204 were derived. Both vaccines are produced with new techniques, such as virus replication in embryonated eggs and freeze drying. YFV vaccines appeared to be safe until cases of encephalitis were noted due to unfavorable mutations during continuous subcultivations [46]. The regulation of passage numbers was introduced known as today's seed lot system. Additionally, human serum in the vaccine was substituted to reduce the risk for Hepatitis cross-infections [47]. In 1962, a contamination with avian leucosis virus (ALV) was detected in the YFV-17D lot and attempts of eliminating the oncolytic retrovirus by incubation with ALV antibodies and ultracentrifugation fortunately succeeded.

To the present day, 17DD and 17D-204 substrains are the only approved vaccine substrates used for vaccine manufacturing. Both low-cost vaccines are manufactured in specific-pathogen-free (SPF) embryonated chicken eggs [48]. Therefore, 7- to 9-day old embryonated eggs are infected with the virus. After three to four days, maximum virus titers are reached and infected embryos are isolated [46]. Pooled embryos are first conditioned with water for injection, homogenized and subsequently centrifuged to separate the virus in the supernatant from the pulp. Finally, stabilizers such as gelatin and sorbitol are added before the live-attenuated vaccine is lyophilized. The manufacturing process is very simple and does not require advanced downstream processing. However, the current manufacturing platform has certain limitations. The availability of fertilized eggs can be strongly hindered if other vaccine manufacturing processes, such as seasonal influenza vaccines, are prioritized. Furthermore, the overall supply is at risk if avian pathogen outbreaks threaten poultry farms. Typical lead times of SPF eggs are around 12 months, which strongly impair fast reaction in case of urgent vaccine demands [1, 49]. As the production capacity cannot be simply ramped up, it requires careful production planning. The egg-based manufacturing process still requires manual interventions in many countries (such as carbonizing, infection, sealing, harvesting), particularly complicating the maintenance of good manufacturing practices at high humidity and limited facility equipment. Additionally, the process gives inconsistent yields per embryo ranging between 100 and 300 vaccine doses which, in turn, impedes dose planning [50]. Finally, low profit margins of the vaccine, mostly directed to developing countries, diminishes the interest of large vaccine manufacturers for production.

Each vaccine dose has a minimum potency of approximately $4 \log_{10}$ plaque forming units [51]. It is injected subcutaneously into the upper arm. Vaccine-related side effects of 5 % are usually harmless and manifest themselves in rare cases in mild fever, headache and aching limbs. Nevertheless, severe visceral (0.4 cases per 100,000 doses) and neurotropic diseases (0.8 cases per 100,000 doses) with high lethality can occur. The pathogenesis is pathologically and clinically similar to naturally acquired yellow fever. The cause of such serious adverse events is not fully understood but is potentially related to individual host factors [52]. In addition, anaphylactic reactions (1.8 cases per 100,000 doses) can occur due to allergies to chicken egg protein residues or production-related use of gelatin [20].

2.1.2.4 Global demand and strategies for disease control

The global demand for YFV vaccines has increased significantly in recent years. While in the year 2000, about 5 million doses were needed, the demand increased in the year 2007 to 34 million doses. For the years 2016 and 2017, a demand of 54 million doses per year was forecasted,

exceeding the global supply of the manufacturers by about 10 %. Current estimations about 1.5 billion doses would be required to eliminate epidemics within the next decades and to protect 900 million people at risk. This would correspond to a global annual demand of up to 213 million vaccine doses following a seven year plan [53, 54].

In response to severe yellow fever outbreaks in Guinea with global vaccine shortages and many deaths, the International Coordination Group (ICG) on Vaccine Provision started to improve cooperation and coordination for routine vaccination programs, prevention campaigns and emergency stockpiling [55]. As of May 2016, 3 million of a total number of planned 6 million vaccine doses were stockpiled to control future outbreaks. However, with the devastating epidemic 2016 in Angola and its neighboring countries, the Democratic Republic of Congo and Uganda, with over 700,000 cases of YFV infection and almost 500 deaths, the global emergency stockpile was completely used that year despite intensified production efforts. In fact of this demand, a total of 18 million vaccine doses would have been needed to prevent the spread of the epidemic. This exceeded manufacturing capacities by 12 million doses or 200 %. As an emergency measure, the WHO approved a dose saving strategy in which one fifth of the normal dose required to protect the population was administered [3].

Currently, there are only four vaccine manufacturers world-wide (in Brazil, France, Russia, and Senegal) with WHO prequalification able to supply vaccines for immunization programs. As the production is considered to be complex and the market unattractive, concerns arose for effective vaccine coverage. In 2016, the Eliminate Yellow Fever Epidemics (EYE) strategy was launched with three main objectives: (i) protect at-risk population, (ii) prevent spreading, and (iii) contain outbreaks [56]. Funds and organizations such as UNICEF try to negotiate binding agreements with manufacturers to meet those objectives in the future.

2.1.3 Zika virus

A fatal ZIKV outbreak in the Americas caught global attention in May 2015, when an unprecedented increase in microcephaly cases was associated to the ZIKV infection. The virus was first characterized in the 1940s, when it was isolated from sentinel monkeys in the Zika Forest in Uganda. Sporadic infections of humans have been reported in Africa since 1952 [57], but as clinical symptoms were rather mild, lack of general interest led only to rudimentary virological knowledge. With the recent outbreak, however, the interest has changed and vaccine developments are progressing rapidly. This chapter covers the clinical disease pattern, viral spreading and summarizes current attempts in vaccine development.

2.1.3.1 Disease pattern

The incubation period for Zika fever ranges from three to 14 days. In only 20 % of all cases, the acute phase is entered by the onset of fever, maculopapular rash, joint pain, headache and conjunctivitis [58]. After three to five days, the virus releases into the bloodstream and remains detectable in blood serum during a viremia period of one week. This enables the virus to spread to other tissues.

When it enters the genitourinary tract, ZIKV remains persistent and infectious for periods of more than six months. It is also detectable in the conjunctival fluid of the eye, resulting in conjunctivitis in 15 % of all patients [59]. Symptoms typically decline after one to seven days. A serological protection for re-infection is currently assumed, but requires further confirmation [60, 61].

Although ZIKV causes only mild symptoms in healthy people, the virus can induce severe malformations in fetuses and increases the mortality rate (congenital Zika syndrome, CZC). Studies on Zika fever during pregnancy revealed the detection of virions in the brain and amniotic fluid of newborns or stillborns with microcephaly [6]. Such abnormalities were confirmed via ultrasound detection in almost 30 % of fetuses from ZIKV-infected pregnant women in Brazil [58]. The risk for encephalitis occurrence can be as high as 13 % when the infection takes place in the first trimester [62]. Subsequent *in-vitro* studies revealed that the virus lyses human neural progenitor cells [63] and decreases brain organoid growth rates [64] giving additional evidence to microcephaly and other congenital defects [65]. Thus, ZIKV-associated Guillain–Barré syndromes (GBS) were investigated and first reported in French Polynesia [66]. GBS was found to concurrently occur with acute infection but also aftermath [67, 68]. Both, the direct infection or autoimmune-mediated targeting of neurons and glial cells leads to the demyelination of peripheral nerves. This results in paralysis symptoms [66]. The occurrence of typical symptoms is reported for 1 in 4,000 cases [66]. Newer findings, however, scrutinize the causative mechanisms. The final association with ZIKV infection requires further controlled settings [69].

2.1.3.2 Viral spreading

ZIKV was presumably transferred from Africa to Micronesia and in 2013/14 to the Pacific region and the Americas. Due to the rapid spread and lack of preventive or therapeutic countermeasures, the WHO declared the outbreak to a global health emergency. Due to travel activities, the virus spread around the globe and confirmed ZIKV cases were reported in more than 60 countries within shortest time (Figure 2.5). Now in 2019, it appeared that the epidemic curve has fully abated in Brazil, indicating a native immunity of the local population to the ZIKV. This limited further ZIKV transmission and finally resulted to a certain self-extinction, but also reduced need for an immediate vaccine.

Aedes aegypti and *Aedes albopictus* are considered as main urban transmission vectors in urban and sub-urban regions. Both mosquitoes inhabit similar regions around the world, while *Aedes albopictus* has additionally invaded the east coast of the United States and European Mediterranean coast regions including Italy [70]. The vector competence was tested in different approaches, and ZIKV transmission rates varied around 3-75 % in dependence of environmental factors [71, 72]. In addition, certain ZIKV cases revealed also non-vector transmission routes between humans via sexual contact [73, 74] and also blood transfusion [75]. Due to the high adaptability of the virus to new host systems, ZIKV infections finally yielded in detectable, infectious titers with a long-term persistence of up to six months not only in sperm, urine [76], vaginal secretion [75], but also in breast milk [77].

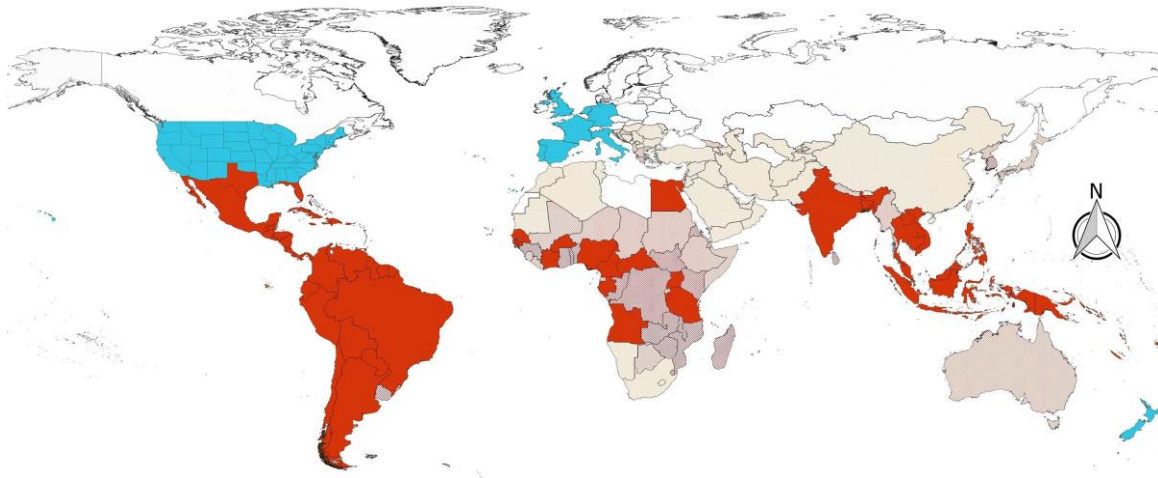


Figure 2.5 | Global Zika fever occurrence and risk map. Disease distribution corresponds with the global risk of viral infection. Status of infection occurrence: Not reported, autochthonous vector borne transmission, travel-related occurrence. Countries/territories at risk: No risk, mid risk, high risk. Adopted from Leta and colleagues, licensed under CC-BY-NC-ND [35].

2.1.3.3 Current vaccine approaches and challenges

There is no vaccine or therapeutic countermeasure to prevent or treat ZIKV infection. Although ZIKV infection is not fatal in itself, it correlates with devastating consequences such as congenital Zika syndrome and neurological complications (e.g. GBS). An effective vaccine is therefore of great importance. Regulatory authorities reacted promptly and established working frames. They identified women in child-bearing ages with high priority for vaccination and residents in endemic countries, but also travelers to those regions. Furthermore, the WHO outlined two strategies: (i) Broad universal vaccination campaigns followed by routine immunization, and (ii) spontaneous mass vaccination campaigns before or during endemic ZIKV outbreaks [78]. The support from official side and the potential target market size stimulated vaccine developments. With the successful track record of existing vaccines against flaviviruses (YFV, JEV, TBEV), vaccines against ZIKV are expected to become available within the next years. Currently, more than 45 vaccine candidates are being developed and several are tested in clinical trials [79] (WHO vaccine pipeline tracker: [80]).

Although ZIKV strains can be categorized into two genetic lineages, African and American/Asian, ZIKV consists of one serotype with minor variabilities so that a complete cross-protection is given within both lineages [81, 82]. Thus, a monovalent ZIKV vaccine based on one lineage may be sufficient. The objective of most common approaches are vaccines based on the E protein optionally together with the M or prM protein for conformational conservations of the epitope [83]. Those antigenic structures can be provided by an inactivated vaccine. However, its potential to mimic natural infection and virus replication for an effective CD8⁺ T-cell response is limited. Therefore, live-attenuated vaccines are also considered although they bear the risk of unintentional infection or persistence. In consequence, a variety of further strategies based on, i.e., chimeric constructs, DNA plasmids and virus-like particles are equally explored and further elaborated elsewhere [79, 84].

ZIKV vaccine development comes along with certain hurdles. Each vaccine candidate will require considerable safety testing to impose concerns about fetal abnormalities and GBS after vaccination. As even low levels of viremia resulted in congenital Zika syndrome [85], it is presumed to require sterilizing immunity (complete protection without detectable ZIKV at any time) and robust T-cell response to avert fetal transmission during pregnancy [86]. This is challenging as sterilizing immunity has not yet been achieved with available flavivirus vaccines (JEV and TBEV are inactivated vaccines). To achieve a fast viral clearance, all three major lymphocyte subsets (CD4⁺ T-cell, CD8⁺ T-cell, B cells) are most likely only achievable with a live-attenuated or a virus-like particle strategy [87-89]. Additionally, the high structural and high sequence homology to related diseases such as DENV can lead to cross-reactive antibodies. Thereby, antibody-dependent enhancement (ADE) potentially promoting re-infections can result in even more severe outcomes. This was recently demonstrated with anti-DENV and anti-ZIKV antibodies with respective reciprocal virus infection in cell culture or mice [90, 91]. Reassuringly, this was not yet observed in non-human primate or human studies [92, 93]. Careful monitoring will be indispensable for further vaccine development, also with respect to other flaviviruses co-circulating in countries with ZIKV occurrence. Finally, challenges for clinical evaluation of ZIKV vaccine candidates are given by limited pool sizes of pregnant women, while offering a favorable ratio of risk to potential benefits [94]. Thereby, the geographical selection of the clinical trial site is crucial as people in areas with previous ZIKV exposure show a seroprevalence as high as 70 %. This may turn mathematical modelling for ZIKV evaluation into an essential approach to identify future areas for efficacy studies [79].

2.2 Cell substrates – Vero, BHK-21 and EB66® cells

In the following sections, three potential producer cell lines for viral vaccine production are introduced. Their fast cell growth, viral susceptibility (possessing the receptor complement needed for viral entry) and high viral permissiveness (allowance for viral replication) for a large variety of viruses generally qualify them for the production of flaviviruses.

2.2.1 Vero cells

Vero cells were first isolated by Yasumura and Kawakita in 1962. They extracted epithelial cells of the kidney of a female African green monkey (*Chlorocebus sp*) and were immortalized by spontaneous transformation [95]. Besides the robust cell growth, adherent Vero cells demonstrated a high permissiveness for different viruses such as SV-40, measles virus, arboviruses, rubella virus, polioviruses, influenza viruses, simian syncytial viruses and many others [96]. The reason for this cellular property may be due to deletion sites on chromosome 12 encoding for a type 1 interferon gene cluster and cyclin-dependent kinase inhibitor genes [97]. Two years later, the cell was shared

at passage number 93 with the National Institutes of Health (NIH) in the US with fully filed documentation on history and cultivation conditions. Since then, Vero cells became one of the most used continuous cell lines and an exceptionally valuable substrate for the production of biological pharmaceuticals. The lineage was submitted to the American Type Culture Collection at passage 113 and seeds were stockpiled at passage 121 for general availability. Most vaccine manufacturers work with passage levels in the 140s and limit further passaging to about 20 cell culture passages, as higher cell passages were tested positive for tumorigenicity (injection of intact cells causing nodules, lung and lymph node metastases; above passage 191 [98-100]) and for oncogenicity (injection of cell lysate causing tumor formation in nude mice; above passage 162 [96]).

A variety of veterinary and human vaccines are manufactured with adherent Vero cells in different bioreactor systems (roller bottles, multi stacks, microcarrier bioreactors, fixed-bed bioreactors) [7, 101, 102]. The major limitation of this very potent cell line is its surface-dependent cell growth, typically in monolayer formation. First attempts to adapt Vero cells to suspension growth resulted in poor cell growth and strong aggregate formation [103]. When other publications reported on the successful Vero cell adaptation to single suspension cells, a HeLa cell contamination was suspected and potentially confirmed as the submitted cell bank sVero p66 (DSM ACC2791) was removed from the cell culture collection. Recent conference contributions, however, give hope for future availability as suspension cells were reported from different work groups to stably grow to 3×10^6 cells/mL in stirred-tank bioreactors [104, 105]. Further improvements are thus foreseeable and, probably, it is only a matter of time until a suitable medium will be developed that supports robust growth to high cell concentrations.

2.2.2 BHK-21 cells

The baby hamster kidney fibroblast cell (BHK-21) line was derived from kidneys of five one-day-old unsexed hamsters of the species *Mesocricetus auratus* by Macpherson and Stoker in 1961 [106]. The pseudodiploid subclone C13 was picked after continuous cultivation of 84 days with one interruption for cryo preservation. As this adherent BHK-21 cell line provided robust cell growth, appropriate protein folding and complex *N*-linked and authentic *O*-linked glycosylation patterns, it has been used for the production of recombinant proteins, e.g. coagulation factors VIIa (NovoSeven, Novo Nordisk) and VIII (Kogenate, Bayer Schering; Helixate, ZLB Behring). Additionally, BHK-21 cells showed a high permissiveness to a spectrum of virus families, such as rabies virus and foot-and-mouth disease virus. For veterinary rabies vaccine production in the 1970s, BHK-21 cells were adapted to grow in suspension and were cultivated in 5000 L bioreactor scale with Eagle's medium and 5 % bovine serum [107, 108]. The production process for the foot-and-mouth vaccine followed in a 1000 L scale with serum-supplemented medium [109]. Despite this long track-record, the use of BHK-21 cells for human vaccine production is seen highly controversial, as intact cells have been demonstrated to be tumorigenic in mice (without forming metastasis) [110, 111]. Despite those concerns, human vaccine testing was already conducted with inactivated BHK-21 cell-derived rabies vaccine. The study showed excellent efficacy and a high safety profile [112, 113] but due to ethical issues and remaining safety concerns, the approach was never continued. Nevertheless, a primary kidney-derived hamster (PHK) cell line was licensed for the production of

JEV SA 14-14-2 vaccines in China [114]. To bring the BHK-21 cell into a similar position, the substrate needs to meet WHO prequalification standards, which will require further purity, safety and consistency studies [110]. Significant improvements in downstream processing with respect to DNA and host cell protein depletion should facilitate future licensing. Other potential concerns derive from the BHK-21 cell-derived glycosylation profile. Typically, non-human terminal α -Gal and Neu5Gc structures are formed, so that the glycosylated vaccine may bear the general risk for spontaneous allergic responses and chronic inflammation after human administration. Thus, the use of BHK-21 cells may continue to be limited to human biotherapeutics [115, 116].

2.2.3 EB66® cells

The EB66® cell line is a duck embryonic stem cell-derived substrate and was isolated by Vivalis (today Valneva SE). It belongs to the EBx® series of multiple clones suitable for the production of viral vectors and viruses generated with the motivation to replace embryonated chicken eggs and primary chicken embryo fibroblasts. Due to their spontaneous (no genetic, chemical or viral) immortalization, EBx® cell lines are considered to be non-genetically modified organisms (GMOs) [117]. The first candidate, EB14® (derived from an unknown chicken strain), showed an avian endogenous retrovirus (AER) contamination so that subsequent work was discontinued. When the AER contamination was confirmed for all available chicken strains, the focus was shifted to duck strains. During the derivation process, 22,000 embryonated Peking duck eggs were sacrificed to isolate the yolk and to cultivate suspension cells in co-culture with adherent replication-suppressed mouse feeder cells. After multiple adaptation steps, isolated embryonic stem cells were obtained that allowed to derive stable EB66® cells free of extraneous agents and with cell concentrations of about 9×10^6 cells/mL in bioreactors and batch mode [118, 119]. Since 2017, a chemically defined medium became available supporting even higher cell concentrations and the production of different viruses in a monophasic cultivation (obsolete media exchange for virus production) [120]. The high permissiveness of EB66® cells was proven for a large panel of viruses such as influenza A virus (IAV), measles, herpes type 1 and 2, alphaviruses, Newcastle disease virus [118], influenza B virus [121], and modified vaccinia Ankara (MVA) [122]. The first veterinary vaccine (egg drop syndrome virus, EDSV) produced in EB66® obtained licensure in 2012, whereas the first human vaccine (H5N1 pandemic influenza vaccine) received marketing approval in 2014; both in Japan. Driven by the commercial interest of Valneva, the access to the EB66® cell line is highly restrictive and cells are mostly only available for veterinary, but also human vaccine manufacturers explaining the limited literature coverage.

An additional field of application for EB66® cells is the production of recombinant therapeutic proteins. EB66® cells stably expressed IgG1 mABs at concentrations around 1 g/L. The strongly reduced content of fucose was linked to significantly enhanced antibody-dependent cell cytotoxicity (ADCC) activity playing an important role in the efficacy of mAb therapy [123].

2.3 Process intensification

Over the last decades, the upstream processing community gained a better understanding for animal cell maintenance and developed robust basal growth media to cultivate suspension cells in serum-free or chemically defined media exceeding 5×10^6 cells/mL in typical batch operations. This improved handling of cells paved the way for advanced process development based on techniques established for prokaryotic and certain eukaryotic production processes. Today, biotherapeutics, i.e. recombinant proteins, were already approved and entered the market, for which process intensification was beneficial [124]. For viral vaccine production, initial objectives of process intensification encompassed increased cell concentrations, increased viral titers and increased volumetric virus productivities. The scope has since been expanded to media optimization, cell line generation, process automation and increased process robustness [125]. Additional strategies aiming at increased cell-specific virus yields address optimum cultivation parameters (e.g. temperature, pH), process changes for infection (e.g. volume-reduction or expansion, specific virus production media) and virus-related factors (e.g. multiplicity of infection (MOI), virus adaptation, trypsin addition). Further information is given in the review from Gallo & Nikolay *et al.* [7].

In the following, options for high cell density cultivation are introduced for adherent and suspension cells. The particular focus is on suspension cells and membrane-based perfusion systems employing a recirculation pump. In a next step, various perfusion rate control strategies are addressed and briefly discussed. For a better understanding of online biomass probes, a theoretical excursion into impedance measurement is given and the application linked to the field of animal cell culture. Finally, as most perfusion systems rely on membranes, a section is dedicated to hollow fiber membranes, general fouling principles, membrane properties and mechanical countermeasures to reduce fouling.

2.3.1 High cell density perfusion processes

Perfusion processes aim at cell concentrations often beyond typical upper limits of batch and fed-batch processes with $2\text{--}20 \times 10^6$ cells/mL. Therefore, cells are constantly supplied with fresh medium, while nutrient depletion is prevented and inhibitory metabolites/substrates are removed. Adherent cells are attached to a surface simplifying the medium exchange. Suspension cells, whereas, require perfusion bioreactors with shear-reduced recirculation of the cell broth and a cell retention device. The following section focuses on micro- and macrocarrier cultivations, i.e. on solutions for the recirculation of suspension cells, as latter are intensively used in this work. The hollow fiber membrane as part of the external pump loop is addressed in a later section.

2.3.1.1 Increased surface areas for adherent cells

The scale-up of adherent cells for vaccine production is achieved by enlarging the cell growth surface area. Instead of increasing the amount of roller bottles or multi stacks (static systems), many

cells can be grown on microcarriers in quasi-suspension in bioreactors or on macrocarriers in fixed-bed bioreactor systems.

Today, dextran-based microcarriers (e.g. Cytodex-1, GE) are widely used enabling fast cell attachment and cell growth. But also new microcarrier materials with improved cell adhesion properties and larger surfaces still enter the market [126]. In general, the microcarrier concentration cannot be arbitrarily increased as quasi-suspension conditions result in frequent collisions between carriers resulting in friction and cell abrasion [127]. Furthermore, increased microcarrier concentrations also require a higher power input to avoid sedimentation. In combination with technical challenges for an efficient bead-to-bead transfer, use of microcarrier cultivations is considered to be strongly limiting for process intensification. As an alternative, adherent cells can be cultivated on macrocarriers, e.g. highly porous polyester microfiber carriers or discs. Compact bioreactor solutions provide surfaces of up to 1000 m² in a 25 L fixed bed volume with extendable perfusion tanks aside (e.g. iCELLis[®] 1000, Pall). For such high surface/volume ratios, the continuous medium exchange is essential. Cultivations are typically initiated with relatively low cell inoculum (in dependence on plating efficiency) and cell spreading in fixed-beds takes place for a period of two weeks or longer. Difficulties arise if the cell growth is inhomogeneous and cells do not colonize the entire fixed-bed surface [128]. Limitations can arise at high cell concentrations when the volumetric oxygen transfer coefficient (k_{LA}) of the bioreactor is insufficient [129]. Furthermore, direct cell quantification is strongly impeded, especially for macroporous materials entrapping the cells. Thus, direct measurements based on impedance measurement or indirect measurements (e.g. metabolite uptake rate, oxygen consumption rate) can be necessary [130, 131]. Finally, product harvesting can be impaired, in particular, if the virus accumulates intracellularly and cell disruption is required [132]. Fixed-bed bioreactor solutions are currently in great demand for the upstream processing and scale-up of viral vector production. High costs for pre-validated and pre-characterized fixed-bed bioreactors, but also established backup supply chains reduce profit margins, in particular unpleasant for low-margin vaccine production.

2.3.1.2 External membrane-based perfusion systems

External membrane-based perfusion systems consist of a recirculation loop employing a pump and a membrane retaining cells within the bioreactor system. This section is dedicated to the pump system and respective flow profiles, while basic properties of membranes are further addressed in section 2.3.4.

To circulate cell culture broth in cross-flow mode along a membrane, positive displacement pumps with different operating principles can be chosen: peristaltic pumps [133], rotary positive displacement pumps [134], impeller pumps [135], piston pumps [136], or diaphragm pumps [137]. The flow profile varies in dependence of the chosen pump system. Peristaltic and impeller pumps are typically operated in unidirectional flow (tangential flow filtration – TFF, idealized to pulsation-free flow in Figure 2.6 A). When rotational speeds and directions are modified, it can result in unidirectional pulsating (pulsating tangential flow filtration – PTF, Figure 2.6 B) or bidirectional pulsating flows (alternating tangential flow filtration – ATF, Figure 2.6 C), respectively. Pump types such as piston pumps and diaphragm pumps operate typically in ATF operation (Figure 2.6 D) but can be also changed to PTF operation by valve switching (Figure 2.6 C).

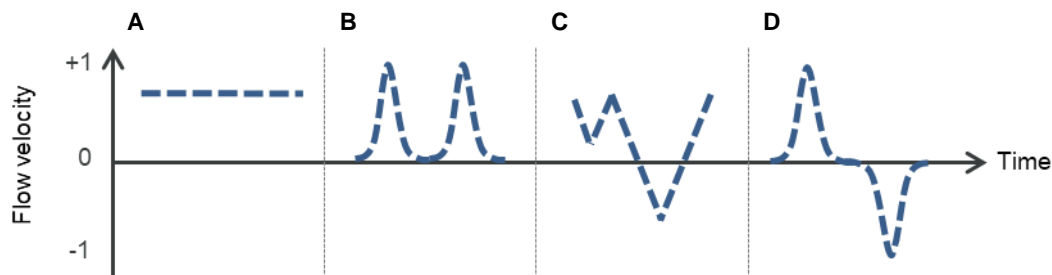


Figure 2.6 | Flow velocity profiles of different pump systems in an external perfusion pump loop. Peristaltic and impeller pumps enable (A) linear unidirectional flow (TFF) and (B) pulsating unidirectional flow directions (PTF). When flow directions switch, the flow velocity profile forms a pulsating, alternating flow (C). Pump types such as piston and diaphragm pumps enable (D) alternating flow directions (ATF) and can be also modified to (B) pulsating flows (PTF).

Peristaltic pumps mechanically deform a pump tubing from the outside as the rotor with a number of rollers turns. Thus, a mechanical and sterile barrier between the cell culture and pump remains lowering contamination risks significantly. However, this comes along with certain disadvantages, such as low maximum flow rates, high local shear stress accompanied by the risk of fatale tubing breakage. Nevertheless, such simple pump systems have proven to cultivate robust cell lines such as CHO cells, to 2.1×10^8 cells/mL [12].

Efforts towards shear-reduced pump systems resulted in centrifugal pumps originally developed for pulsation-free recirculation employed in dialysis machines. Based on the principle of magnetic levitation, an impeller operates contact-free in the magnetic field of a motor. Pump solutions from Levitronix meet cleanroom requirements and various pump sizes are available [135]. Before operation, the pump system needs to be primed with culture broth. Furthermore, the pressure head is sensitive to increasing viscosities and hydrodynamic pressure changes. Hence, the pump should be operated above minimum speeds to avoid circulation stops with increasing cell concentrations. Lastly, the hydrodynamic pressure limits the scalability of the system with respect to pumping height and impeller speed. Compared to horizontal operation, vertical dimensioning requires higher pump rates potentially exceeding the shear-sensitivity of animal cells. Thus, often claimed shear-friendliness needs further confirmation for larger scales. Although the pump is available and well-promoted throughout the community, feasibility studies in perfusion cultivations for larger scale are lacking. The general set-up for perfusion cultivation, as also used in this work, is illustrated in Figure 2.7 A.

Another pump system for perfusion application is the diaphragm pump. It shows low, punctual shear stress, but high pulsation rates, which results from two sequential phase cycles of suction and pumping. The controller can be delocalized with a single pneumatic pressure line to the pump housing. The first ready-to-use solution was an ATF system from Repligen with a single tubing connecting the vessel and the pump. This creates an alternating flow through an interconnected membrane. Its applicability to achieve high cell concentrations was demonstrated by perfusion cultivations exceeding 1.3×10^8 cells/mL for CHO cells and 3.6×10^8 cells/mL for PER.C6[®] cells [12, 138]. Single-use solutions of the scalable ATF system to 1000 L were patented and commercialized in 2016, also with the idea to extend expiring patents restricting its use in specific configurations. The pulsation flow profile can be important to counteract membrane fouling and to reduce product

retention (more details given in later parts of this chapter) [139]. The experimental set-up is visualized in Figure 2.7 B.

Similar to the ATF perfusion systems, new perfusion units are being established to circumvent patent issues related to existing ATF technologies. One solution is the Clio one-way single-use diaphragm pump (PerfuseCell), which uses a red laser sensor to set an exact position of a stretchable membrane in a translucent pump housing. This enables freely configurable pump cycles and extended process control. So-called duck valves in opposite flow directions at the entrance of the pump chamber enable re-circulation of cell culture in two steps. While the pump chamber is first filled through a duck valve positioned on one side, the cell culture is pushed through the opposing one. This results in a PTF flow across the interconnected membrane. Another small-scale solution was developed by Sartorius for the ambr 250 system. One perfusion pump (possibly as piston pump) is filled with cell broth by applying underpressure, while a second chamber is emptied by applying overpressure. This cycle is carried out sequentially, while a pinch valve directs the flows. Thus, a constant cross-flow filtration with reduced flow pulses can result.

In general, ready-to-use perfusion bioreactors are available enabling high cell concentrations for a large variety of suspension cells. This demands new operational variations in the form of hybrid processing. Thereby, a single perfusion bioreactor can be continuously operated as seed bioreactor to inoculate multiple batch cultivations in parallel or time-shifted [140]. Additionally, concentrated cells can be directly harvested from perfusion bioreactors for large-volume cell banking and to shorten seed train expansion by direct bioreactor inoculation. This can reduce process time and increase productivity [141].

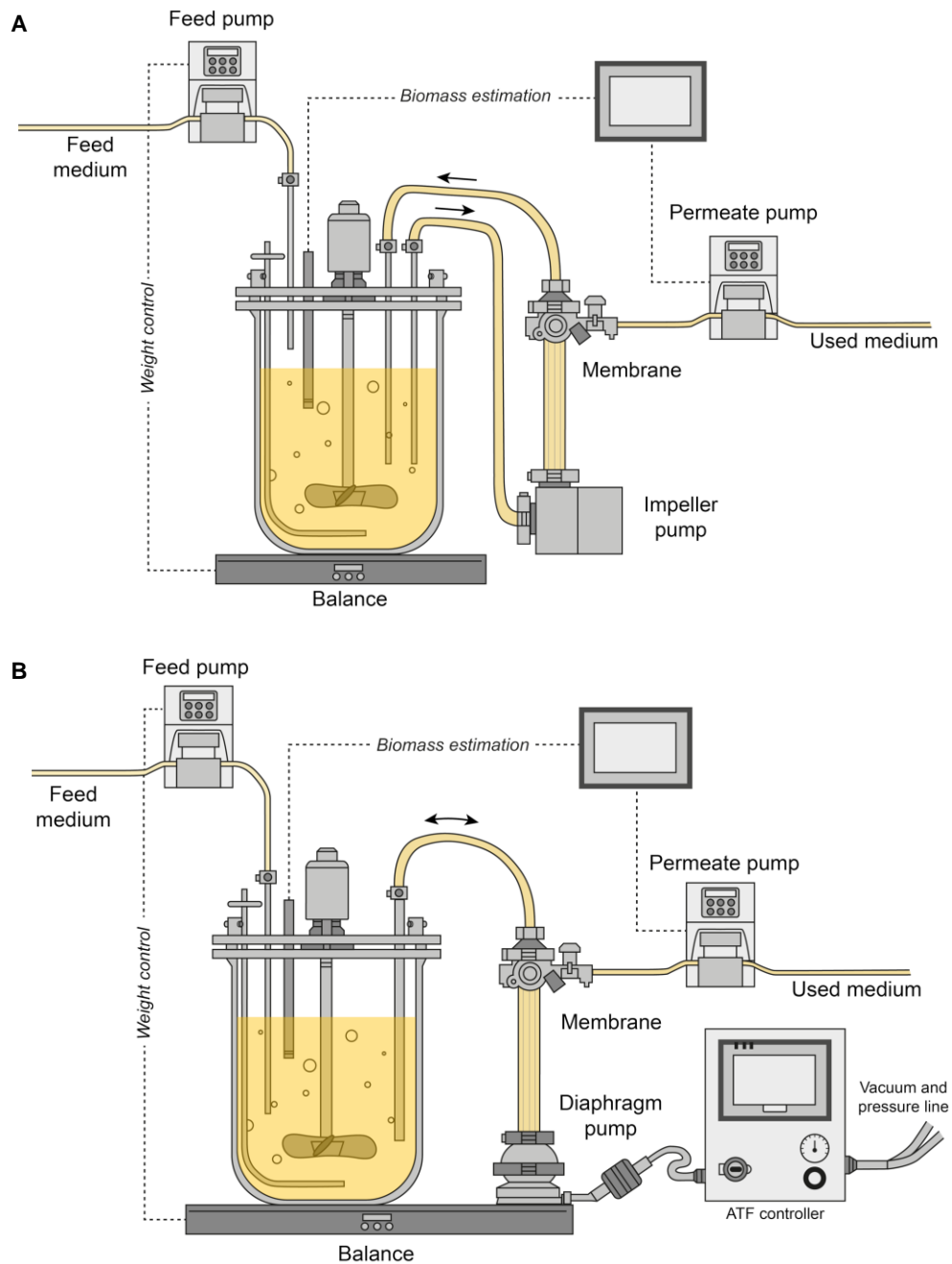


Figure 2.7 | Bioreactor set-up with perfusion units for cross-flow filtration operation. (A) Centrifugal impeller pumps are typically operated in constant or pulsed unidirectional flow, and **(B)** diaphragm pumps in bidirectional flow direction. The online biomass probe estimates the cell concentration and is used to control the permeate pump and to maintain a cell-specific perfusion rate.

2.3.2 Perfusion rate control

Versatile solutions to achieve high cell concentrations in perfusion bioreactor systems open the question regarding optimum perfusion rate control. Aside from media development, the right perfusion rate can be crucial for process intensification as it is often directly related to cell growth rates, maximum cell concentrations and overall perfusion medium usage. To compete with productivities in batch and fed-batch modes, it is essential to reduce perfusion rate to its minimum, while maintaining cell growth and virus replication performances (similar to the ‘push-to-low’ approach [142]). With time, different perfusion rate strategies arose, which are divided into three groups:

- (i) **Reactor volume exchange regime** The reactor volume (RV) exchange rate per day (RV/d) is a classic and simple strategy to describe the quantity of fresh medium to the bioreactor. Rates are either fixed or follow a rigid time regime to meet cellular demands of the increasing cell population. In combination with controlled cell-bleeding, steady cell concentrations can be reached. The strategy is often used for the efficient expression of recombinant proteins [143]. As the strategy is de-coupled from the biological system, it does not cover for biological variations. Hence, metabolite concentrations and cell-specific rates fluctuate during the cultivation (Figure 2.8 A). This strategy is commonly applied due to its simplicity and practicability, and the term RV/d became a fixed expression to characterize and compare perfusion processes, mostly for protein production. As the strategy does not rely on any measurements, it is often simply transferred especially to small-volume perfusion systems such as pseudo perfusion cultivations, where cells are temporarily over- or under-fed (Figure 2.8 B). However, the reproducibility is greatly limited, when the biological (e.g. growth rate) or technical system (e.g. inoculation concentration, timing) alter. Moreover, the perfusion rate does not necessarily reflect cellular demands and does not maintain a stable metabolic environment. The risk for over-feeding and wastage is given.
- (ii) **Cell-specific perfusion rate control** Here, the perfusion rate is permanently adjusted based on the viable cell concentration/volume in the bioreactor vessel (open-loop control). This results in a constant cell-specific perfusion rate (CSPR) throughout the cultivation, while the perfusion rate (RV/day) increases and metabolite concentrations vary to a certain degree due to changes in cell-specific substrate uptake and production rates (Figure 2.8 C). This strategy enables a constant supply of medium to each cell and creates an almost constant cellular environment primarily independent on the cell concentration [144]. Based on variations in cell growth, the reproducibility between different runs can be particularly given. However, media depletions may occur when too low CSPRs are chosen. Instead of manual perfusion rate re-adjustments at each sampling time point, online biomass probes can be used to control the perfusion rate pump automatically [145].
- (iii) **Metabolite-based perfusion rate control** The perfusion rate is adjusted constantly to maintain metabolite concentrations at a defined set point (closed-loop control). For practical application, one key metabolite is defined and a concentration chosen at which major depletions of other, in particular, limiting metabolites should become negligible. Typically,

perfusion rates increase with cell concentrations, whereas CSPRs vary due to changing uptake rates (Figure 2.8 D). This strategy is characterized by its robustness against biological variances (e.g. growth rates, uptake rates). However, due to costly online measurement devices with limited ranges of measurable analytes and extensive maintenance, this strategy is mostly performed with offline measurements.

An analogous approach is based on by-product concentrations, preferentially lactate. This non-intuitive approach aims at the nutritional supply, while reducing by-product levels. With the assumption of lactate being the major driver for decreasing pH values, the perfusion rate can be simply controlled by maintaining a certain pH set point. Lactate is either washed out (no cellular lactate uptake) or is consumed at low glucose levels [146]. Thereby, an online perfusion control is easily adaptable to every state-of-the-art bioreactor control system with pH control. However, a stable supply of sufficient medium is challenging and requires a good cell/medium understanding. Furthermore, the strategy is rather sensitive for cellular variations (e.g. unexpected stress).

The right choice of a perfusion rate strategy depends on certain criteria such as *(i)* ease of automation, *(ii)* robustness and *(iii)* costs. RV/d-based regimes without any control are the most rigid approach and only suitable for well-characterized processes. To increase the level of automation and process robustness, it requires online measurement tools and data processing for perfusion rate control. Online biomass probes monitor biovolumes in the culture broth. In consequence, it may be more practical to relate future process parameters to the measured variable, here cell volume (i.e. total cell volume, cell-volume specific productivity or yield) and not, as typically established, to cell concentration. Online metabolite measurement equipment is already affordable for glucose and lactate quantification. If the key metabolite can be defined by one of these measurable analytes, the metabolite-based strategy can be a practicable solution. The pH-based perfusion control is already in application, but requires comprehensive cell understanding to avoid problems with control. Despite above criteria, a control strategy should be ultimately chosen based on the main objective: *(iv)* minimizing medium usage for maximum productivity.

Beforementioned control strategies are particularly suitable for the cell growth phase, but may need to be adjusted for the virus infection phase due to changes in cellular physiology, e.g., growth rate, metabolic activity, and cell death. Process variations and options are discussed elsewhere by Nikolay & Bissinger [147].

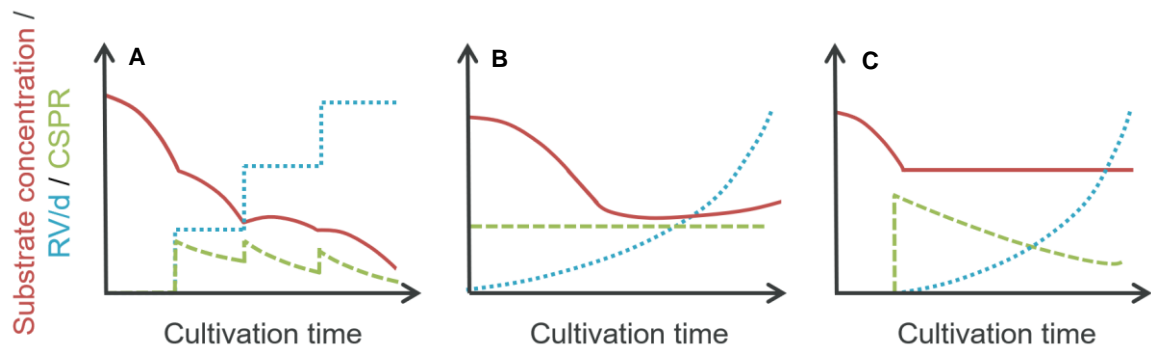


Figure 2.8 | Perfusion rate control strategies for high cell concentration cultivations. (A) Reactor volume exchange rates per day (RV/d; blue dotted line) increase stepwise following a scheme to meet assumed nutrient demands. This results in fluctuating substrate concentrations (red line) and cell-specific perfusion rates (CSPR; green dashed line). (B) The CSPR-based control strategy maintains defined CSPR levels from the beginning of the cultivation. The perfusion rate (RV/d) increases accordingly, whereas metabolite concentrations can vary. (C) The metabolite-based perfusion control strategy starts, when a certain set point is reached. Substrate levels are maintained, while the perfusion rate (RV/D) increases with cell growth and the CSPR sharply increases when set-point is reached, but typically, decreases subsequently to a lower consumption rate. Adopted from Nikolay and colleagues [147].

2.3.3 Capacitance as an online biomass signal

The principle of a capacitance biomass probe is based on the polarization of cells and particles with an intact membrane. Other materials such as gas bubbles, microcarriers and glass walls are not polarizable and generally do not interfere with the measurement. In 1988, first patents for online biomass probes using radio frequency and impedance measurement were registered. Shortly after, such probes were launched to the market and the hardware (e.g. interference factor elimination) and software (e.g. data processing and smoothening) were constantly improved. At the same time, the cell culture community started systematic approaches to interpret and evaluate data interpretation and improve biomass modeling. Its implementation to monitor adherent cell growth was demonstrated in various cultivation systems such as microcarrier and fixed-bed bioreactors to produce recombinantly expressed proteins [148-150]. The applicability was further demonstrated for suspension cells and the online biomass estimate was used for process automation such as CSPR-based feeding control or cell bleeding rate control [145, 151]. Current commercial products are recognized as a practicable solution for biomass measurement and are accepted as a PAT tool [152].

The following chapter introduces the principle of dielectric spectroscopy measurement. Finally, all dielectric parameters, which can be provided (either measured or calculated) by state-of-the-art biomass probes, are discussed.

2.3.3.1 From a dielectric principle to a biomass probe

Any matter can be described by its active (e.g. current, voltage) or passive electrical properties (e.g. dissipative or conservative elements). Materials with passive properties do not have electric sources, but function as resistors and capacitances [153]. This was confirmed for animal cells, when

cells with a poorly conducting cell membrane were positioned between two electrodes [154]. By inducing an electric field, free ions migrated through the cytoplasm within a cell membrane, which resulted in charge disturbances by polarization [155-157]. The change in the equilibrium potential and its extent can be measured as capacitance (C_{cap} ; usually in pF) or conductance (G ; usually in mS) in dependence of the geometry of the measuring device (here simplified as plane-parallel plates with area (A) and distance (d), typically also expressed as cell constant k in m^{-1} reflecting the electrode geometry). The resulting relative permittivity (ϵ ; dimensionless) and conductivity (σ ; usually in S/m) of the dielectric material can be derived from:

$$\epsilon = C_{cap} \cdot \frac{1}{\epsilon_0} \cdot \frac{d}{A} \quad (1)$$

$$\sigma = G \cdot \frac{d}{A} \quad (2)$$

where ϵ_0 , known as ‘permittivity of the free space’, is the capacitance of a unit cell containing vacuum (8.8×10^{-12} F/m) [158]. The relative permittivity ϵ is the capacitance normalized to the geometry of the electrodes and thus dimensionless. It describes the ease of polarization, while the conductivity σ describes the ease of electric charge migration [158]. The electric polarization was further studied by Frick and Cole. They applied a step function excitation signal and monitored a declining relaxation process in the order of seconds. The observed dispersion time from the excited state to the ground state was thereby a function of the frequency f [159]. This was explained by incomplete charge displacement of all ions before the direction was inverted (Figure 2.9). Schwan continued with similar studies and applied higher frequency fields in the range of 10 kHz to 2 GHz. He observed different polarization mechanisms and introduced three dielectric dispersion types [160], which were later extended by a fourth dispersion:

- (i) α -dispersion occurs below 10 kHz: lateral ion movement along membranes
- (ii) β -dispersion occurs at 0.1 to 10 MHz: cell membrane polarization
- (iii) γ -dispersion occurs above 10 MHz: dipolar molecule polarization
- (iv) δ -dispersion occurs above 2 GHz: water polarization, not distinguishable to γ [161]

The radio frequency β -dispersion was first recognized as Maxwell-Wagner relaxation caused by intact cell membranes. Schwan was convinced from the concept to use dispersions for biomaterial characterization. Soon, mathematical models such as the Cole-Cole equation or Pauly-Schwan equation arose in the field of dielectric spectroscopy. Both describe properties of smallest round-shaped cells with the β -dispersion at different frequencies and time domains [162, 163]. Finally, this enabled the correlation of relative permittivity to viable cell volume [164, 165].

With this, the basis was set and with the use of existing models and boundary conditions (comprehensively reviewed in [161]), biomass probes were commercialized. Pioneering works were made by Aber Instruments and Fogale Nanotech. While the Aber product is currently integrated into the single-use portfolio as a Sartorius-branded product (i.e. single-use bioreactor and wave bioreactor bags), Fogale transferred the biotech business to Hamilton Bonaduz.

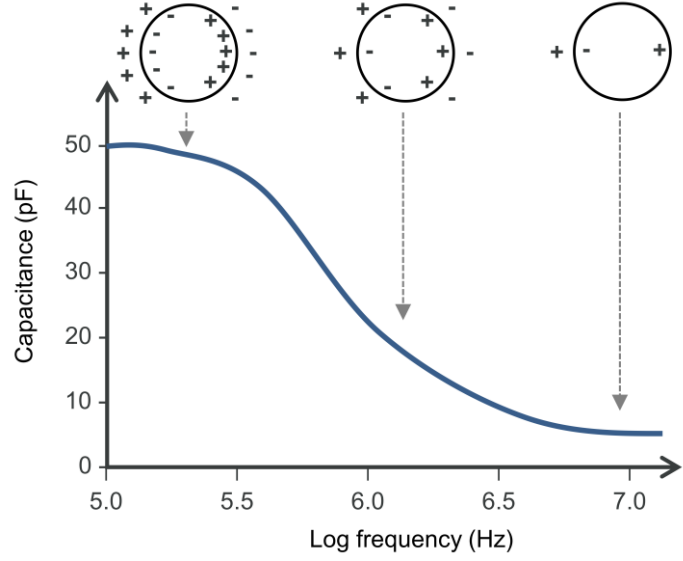


Figure 2.9 | Idealized β -dispersion of an animal cell culture. The decline in capacitance is measured in a frequency range between 0.1 and 10 MHz and plotted in log-scale. With increasing frequency, the polarization time decreases resulting in an incomplete cell polarization and lower capacitance plateau.

2.3.3.2 Capacitance measurement and dielectric parameter calculations

Typical four-terminal capacitance measurement probes work with two pairs of platinum electrodes. While one pair applies a dual-frequency field scanning from 0.3 to 10 MHz (as used in this work), the other measures the impedance, which is the vector sum of conductance (G , real part) and capacitance (C , imaginary part). From there, conductivity (σ) and relative permittivity (ϵ), respectively, are calculated and the characteristic β -dispersion is derived [161]. Based on the Maxwell-Fricke equation, Pauly and Schwan proposed a model to correlate the permittivity increment $\Delta\epsilon$ of the β -dispersion to the cell radius and by that the cell volume assuming a spherical shape Figure 2.10) [160, 163]:

$$\Delta\epsilon = \epsilon_s - \epsilon_\infty = \frac{9 \cdot r \cdot \varphi_c \cdot C_m}{4 \cdot [1 + r \cdot G_m \cdot (1/\sigma_i + 1/2\sigma_0)]^2} \quad (3)$$

where ϵ_s is the residual static low-frequency permittivity, ϵ_∞ the background permittivity signal at high frequencies (dimensionless), r (m) is the average cell radius, C_m (F/m²) is the membrane capacitance, G_m (S/m²) the membrane conductance, σ_i (S/m) is the intracellular conductivity, σ_0 (S/m) is the static conductivity of the medium derived from the following Bruggeman formula [166]:

$$\sigma_0 = \frac{\sigma}{(1 - \varphi_c)^{1.5}} \quad (4)$$

with σ as the static suspension conductivity, and φ_c as the biomass volume fraction assuming spherical cell shapes as:

$$\varphi_c = V_c \cdot X_c = \frac{4}{3} \cdot \pi \cdot r^3 \cdot X_c \quad (5)$$

with X_c (cells/mL) as viable cell concentration. With the fair assumption of very small G_m (equal zero), a large fraction of Equation (3) is eliminated and simplified to:

$$\Delta\varepsilon \approx \frac{9 \cdot r \cdot \varphi_c \cdot C_m}{4} \quad (6)$$

The model is valid for spherical cells with high viabilities (low membrane conductance $G_m \approx 0$) and a moderate cell volume fraction ($\varphi_c > 0.2$) [160, 165]. Subsequently, this enables to estimate the biovolume fraction based on the permittivity output signal $\Delta\varepsilon$ of the biomass probe. Additionally, the characteristic frequency (f_c , also called critical frequency) can be derived from the inflection point of the dispersion curve simplified as:

$$f_c = \varepsilon_\infty + \frac{\Delta\varepsilon}{2} \quad (7)$$

Experimental data suggest that f_c describes cell size changes (Figure 2.10). The angle of the β -dispersion at f_c describes the dielectric parameter α (also called Cole-Cole α) [167]. It can indicate the population heterogeneity of electrical properties. Simplified, the larger the slope, the more homogeneous the cell suspension in volume [168] (Figure 2.10). Finally, the Cole-Cole brothers described the Cole-Cole equation [165]:

$$f_c \approx \frac{1}{2\pi \cdot r \cdot C_m \cdot (1/\sigma_i + 1/\sigma_0)} \quad (8)$$

This equation enables the calculation of further dielectric parameters such as membrane capacitance (C_m) and intracellular conductivity (σ_i). Both parameters provide more in-depth analysis on the cellular status and are further elaborated in the Results section 4.5.2.

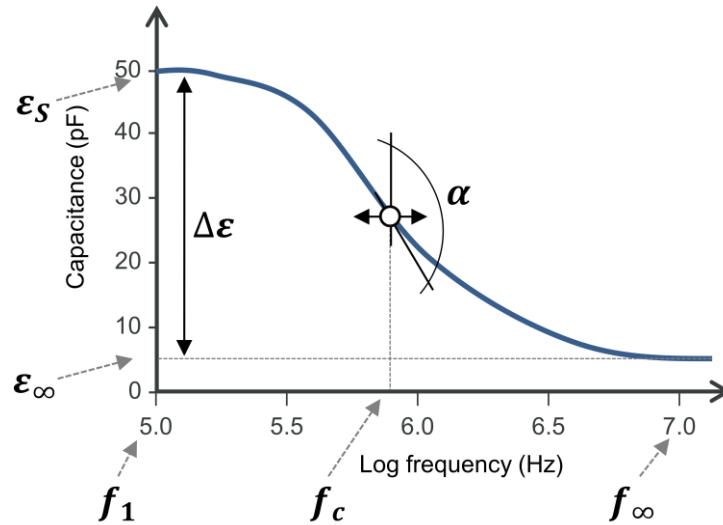


Figure 2.10 | Dielectric parameters derived from β -dispersion. The permittivity increment $\Delta\epsilon$ is measured between the high-frequency (f_∞) and low-frequency plateaus (f_1). The characteristic frequency (f_c) is at the inflection point of the β -dispersion and theoretically correlates with the average cell size. The phase angle α at f_c is derived from the Cole-Cole equation and is theoretically a measure for the cell size heterogeneity of the population.

2.3.4 Hollow fiber membranes

Cell retention devices can be typically classified by their physical separation principle such as filtration, sedimentation, ultrasonic fixation and dielectrophoretic exclusion [169]. Today, hollow fiber-based systems are mainly applied that are based on filtration employing microfiltration membranes. This enables a high cell retention, but membrane fouling can result in undesired and uncontrollable product retention [13, 170-172]. To improve filtration capacities and determine the localization of the product, a deeper understanding of, i.e., material, structure and pore size is essential.

The majority of industrial hollow fiber microfiltration membranes (0.1-10 μm) used for pharmaceutical application are membranes consisting of natural or synthetic polymers. They are made of one or more polymers, which can be mixed homogeneously or heterogeneously, depending on the compound mixture and manufacturing conditions. Based on the structural appearance, membranes can be either symmetric or asymmetric along the length and width. Symmetric membranes commonly achieve their separation efficiency from the pore size and accumulated cake on the membrane surface. In contrast, asymmetric membranes are characterized by their, e.g., thin membrane or strong supportive structure, which can be advantageous for high fluxes and mechanical stability, respectively. The structural appearance of the membrane on a macroscopic and microscopic level is determined from the selected material, but is also most certainly tuned by the production conditions [173-175].

A microfiltration separation process is selected based on particle size and shape, but also on physicochemical properties of the membrane such as surface charge and electrical potentials. These properties become more relevant with increasing material surface. Most properties typically interact

with each other and are strongly related to the exposed environment (e.g. pH, osmolality, temperature) [174].

Single hollow fibers are typically bundled and inserted into tube modules by embedding the ends in epoxide resins. Resulting hollow fiber modules are GMP compliant and interchangeably referred to as capillary modules. Such modules are usually operated in ‘inside-out’ mode (radial filtration from inner lumen to outside) to reduce the tendency for blockages in tightly packed systems. The scalability is obtained by increasing the total surface area by increasing the cross-sectional diameter relative to the length. This minimizes fiber blockage and reduces pressure loss along a module [176]. Current main manufacturers for hollow fiber modules as perfusion membrane are now Repligen (acquired Spectrum Labs in 2017) and GE Healthcare. Other producers with vast expertise in downstream processing are currently entering the market (e.g. Merck, Pall, AsahiKasei, Sartorius) and expand their areas of application to the upstream processing.

The following section provides further information on general membrane fouling mechanisms and bridges the gap from general membrane properties to filter fouling. Eventually, operating modes are discussed, which can be used to counter hollow fiber filter fouling in intensified perfusion bioreactor processes.

2.3.4.1 Membrane fouling

In general, three main mechanisms for filter fouling occur during filtration operation leading to a reduced transmembrane flux and increased membrane resistance (R). Typically, large size variations of foulants are present being smaller, equal and larger than the pore size (Figure 2.11 simplified to particles smaller than pores):

- (i) Internal fouling: Adsorption of membrane-compatible particles (particle size < pore size) to filter material leads to pore narrowing;
- (ii) Partial or complete pore blocking: Steric pore clogging with particles or agglomerates (particle size ~ pore size);
- (iii) Gel/cake layer formation: Additional solute layer formation of larger particles (particle size > pore sizes) on top of the membrane by adsorption and subsequent compression by smaller particles.

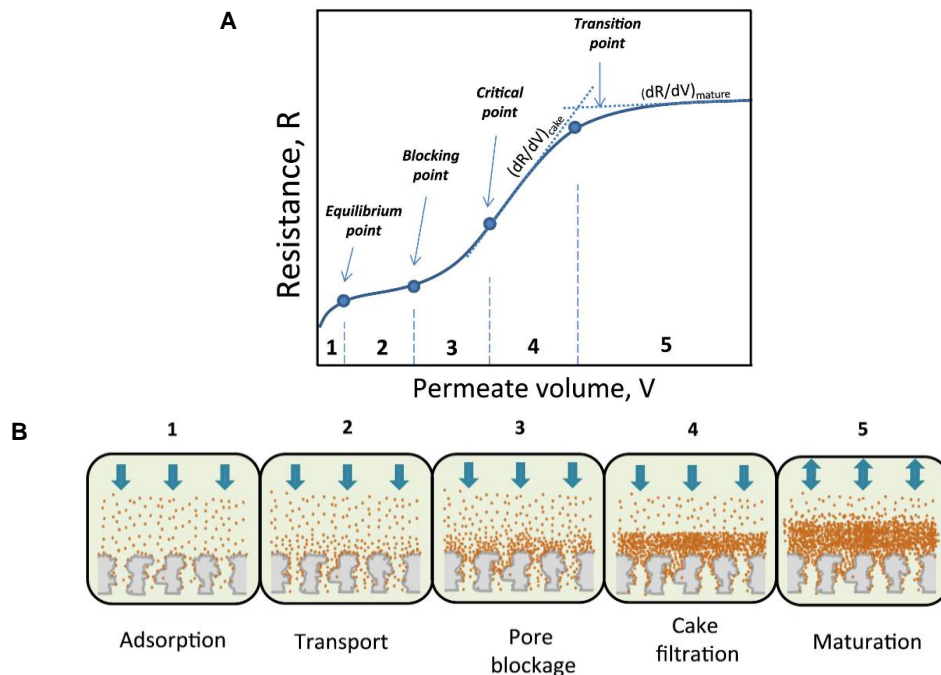


Figure 2.11 | Five phases of filter blocking for an idealized microfiltration process with constant pressure and particles smaller than the pore size. (A) The membrane resistance increases stepwise with progressing filter fouling. **(B)** The fouling of the membrane is caused by adsorption (1), pore blockage (3) and finally cake layer formation and compression (4 and 5) (reprinted from Trzaskus *et al.* [177], with permission from Elsevier).

In detail, internal fouling can be caused by small colloidal materials such as particles, exosomes, virions, proteins, DNA and salts with a binding affinity to the membrane material. Adsorption results in a closely bond deposition to the inner surface. This narrows membrane pores and the initial flux rapidly declines [178]. The effective exclusion limit shifts towards smaller particles. During the second fouling phase, macromolecules or agglomerates of similar sizes than the pores deposit on the surface and block pore openings, whereas largest pores are affected first [179, 180]. This leads to a steep flux decline. Bridge-like deposits above pores are typically dynamic and thus reversible [181]. In the third fouling phase, the solute concentration at the membrane surface exceeds its solubility or gel concentration, and precipitation starts forming a solid gel layer. The membrane becomes more impermeable and the original membrane property (e.g. binding affinity to contaminants) is now determined by the adsorbed macromolecules [182]. If the cake layer can be removed partially by, e.g., higher cross flow velocity, it is referred to as reversible gel layer, which can reach a stationary state. Typically, the solute deposition and layer thickening progresses over time resulting in the formation of an irreversible gel layer. Thereby, the cake layer is subject to two compressibility mechanisms: non-elastic (particle movement into open space of cake layer) and elastic mechanisms (particle deformation compresses the cake layer).

Membrane fouling leads to decreasing permeability. If the permeate flux is set to a defined value, it is correlated to an increasing transmembrane pressure (TMP) to overcome the increasing membrane resistance R . The resistance is typically described by in-series models with (semi-)empirical data as fundamental fouling models and are, in particular, for cell culture processes (including various particles sizes, different surface charges, concentrations and diverse transport

properties) very complex. The total resistance can be expressed as the sum of individual resistances, such as hydraulic membrane resistance (R_m) and boundary layer resistance (R_{bl}). In practice, R_m can be influenced during the membrane production by modifying parameters such as the hydrophilicity, surface porosity or pore size distribution; whereas R_{bl} can be controlled during the process by operational factors such as cross-flow velocities, backflushing or pulsating flow, but also by the addition of filter aids (i.e. inert plastic beads, coagulants) [183].

2.3.4.2 Membrane properties

Membrane properties are closely associated with the fouling behavior of a hollow fiber module and are therefore of major importance. The membrane material, but also specific fabrication procedures and post-modifications can thereby determine membrane properties such as pore size distribution, porosity, surface roughness and inner membrane surface charge.

Membrane material Common organic hollow fibers are made of polymers with certain properties. The following membranes are made of materials, which are typically steam autoclavable (exceptions may occur at pore sizes in the range of ultrafiltration membranes) and commercially available as fibers in hollow fiber modules:

- *Polyethersulfone* (PES) membranes are hydrophilic with a low, non-specific protein adsorption capacity. Typically, the membrane has an asymmetric pore structure with largest openings on one side and smaller pores on the opposite side.
- *Modified polyethersulfone* (mPES) membranes are based on PES materials and additionally functionalized to increase the surface hydrophilicity. The most common membrane modification methods involve material blending (e.g. with hydrophilic poly(vinyl pyrrolidone); PVP [184]), surface coating, chemical treatment with strong oxidizing agents, annealing with heat treatment, and solvent treatment [185]. Chemical modification by sulfonating agents (e.g. H_2SO_4) leads to an open pore structure containing negatively charged sulfonated grafted polymer chains. Post-treatments of readily made membranes can narrow membrane pores and can reduce the exclusion limit, which can become neglectable for larger pore sizes. Simultaneously, the modification shows higher rejection rate for negatively charged proteins by charge repulsion [186]. This allows higher protein retention. At pore sizes below typical microfiltration cut-offs, this modification requires additional preservatives such as glycerin to sustain pore structures.
- *Polysulfone* (PS) membranes are known for their low protein binding properties and high chemical stability to acids, bases and surfactants. The material possesses excellent thermal and mechanical resistance. The material is known for a high biocompatibility and is used extensively in, e.g., high-flux hemodialysis devices [176]. Certain PS modules are pre-wetted with alcohol and must be flushed before usage.
- *Mixed cellulose ester* (ME) membrane filters are derived from cellulose nitrate (CN) and contain a small content of cellulose acetate (CA). This membrane type is designed for high flux rates, low protein binding and possesses a high thermal stability. Pore

structures are typically more uniform and symmetric. ME modules are stored in glycerin as humectant to preserve the membrane durability.

- *Polyethylene* (PE) membranes are fabricated from the simplest class of vinyl polymers and are typically hydrophobic. The membrane structure ranges from macro granulate to undulated fiber bundles, which increase the transverse permeability and decrease concentration gradients. Due to its high mechanical stability, it can be used as support in other membrane composite modules [173].

Hydrophilicity It is usually assumed that fouling decreases with an increasing hydrophilicity of the polymeric material. Hydrophobic organic molecules otherwise tend to attach onto the surface. Material hydrophilicity can be measured by the water contact angle θ between the fluid and the membrane. An imbalance of molecular forces results in an interface or boundary that describes the surface tension. When the contact angle is less than 90° , the polarity difference is small and the liquid wets the surface. When θ equals zero, the liquid spreads over the surface. With small θ , the initial breakthrough pressure decrease as mass transfer requires less energy [173].

Pore size Selection of an appropriate pore size is critical for exclusion of certain particle sizes but also strongly determines the initial permeate flux or membrane resistance. The cut-off is defined as the minimum molecular weight of a globular molecule that is retained to 90 % (D_{90}). During filtration, the membrane resistance increases with fouling progression. Thereby, larger pores can be even more prone for complete pore blockage than smaller ones. After reaching steady-state conditions (cake formation vs. removal), membrane retention is similar regardless of the initial pore size as the effective cut-off is dominated by the filter cake layer [187].

Porosity and pore size distribution The porosity (surface and overall bulk porosity) is an important parameter and correlates to flux and wettability. Typical microfiltration membranes show a high bulk porosity (typically 70-80 %; ultrafiltration membranes around 10 %) [188], whereas surface porosities are often not equally important addressed. Pore sizes are generally distributed over a certain size range, which strongly depends on used materials and manufacturing conditions. Larger pores allow higher local permeate fluxes than smaller ones (pore selectivity). Hence, large pores are prone for stronger concentration polarization and therefore susceptible to deposition. The fastest fouling is typically observed for membranes with small porosity and a broad heterogeneous pore size distribution [188].

Roughness The surface roughness of a membrane is defined by the ‘hills’ and ‘valleys’ on the surface. Membrane roughness can be qualitatively evaluated and estimated by scanning electron microscope (SEM) imaging. More sophisticated tools are 3D imaging using atomic force microscopy (AFM) [189]. The impact of roughness on the membrane flux is not fully understood. On the one hand, it is reported that increased roughness results in higher fluxes based on larger surfaces available for membrane transport, e.g. in reverse osmosis filters [190], and increased wetting property of hydrophilic surfaces [191]. Furthermore, strong irregularities on the surface also hinder formation of fouling layers and formation of bridges near pore openings [192]. On the other hand, various reports reveal a clear correlation of increasing roughness with severe fouling, especially for reverse osmosis and nanofiltration membranes. Thereby, jagged surfaces with enlarged areas

enhance particle interactions to the membrane with particles preferably accumulating in valleys at reduced overflow velocity [193]. The resulting cake layer forms an additional diffusion barrier which cannot be further influenced by fluidic measures from the feed side. Membrane fouling progresses rapidly by particle inclusion to cavities between larger particles. This results in an irreversible formation of a filter cake layer sensitive to negative pressure on the permeate side. It is therefore apparent, that geometric structures of a valley are crucial for fouling followed by the intuition that smoother surfaces are less susceptible for solute deposition [194].

Zeta potential Electrostatic repulsion forces between evenly charged surfaces of the membrane and small colloidal materials prevent the accumulation of solute and diminish filter fouling. Most membranes have a negative zeta potential at a physiological pH value and behave as a barrier to similarly charged colloids underlying the exclusion mechanism [195]. Repulsion increases with high absolute values beyond a critical zeta potential of about -10 mV. The physiochemical property of the membrane depends strongly on pH value and ionic strength as well as certain charged proteins, such as albumin, which may block the membrane and shield surface-related repulsion mechanisms [194].

2.3.4.3 Membrane operations to reduce fouling

Long-term perfusion cultivations of animal cell culture enable high cell concentrations. With increasing concentrations, large quantities of particles are typically secreted and accumulated resulting in non-specific layer deposition. Pore narrowing and blockage decrease the effective cut-off and virus particles begin to retain in the bioreactor system. This can eventually prevent continuous product harvesting through the perfusion membrane. Additionally, as the membrane ages, the transmembrane pressure rises until the complete membrane is blocked, which finally terminates the perfusion run. Thus, operational strategies need to be established to minimize filter fouling, while being shear-friendly for sensitive cell cultures [196].

Firstly, concentration polarization and boundary layer resistances should be reduced to increase mass transfer coefficients. This can be achieved by a faster flow velocity (higher Reynolds numbers) in the filter lumen (e.g. higher flow rate, smaller hollow fiber diameter) or lower transmembrane flux (e.g. lower permeate flow rate, increased membrane area). The latter can be realized when a constant unidirectional flow (TFF) is modified to a pulsating unidirectional flow (PTF, Figure 2.12 A, B) by varying pump speeds. Cross-flow velocities increase periodically, which disturb the formation of the gel layer. Alternatively, certain pump systems such as piston or diaphragm pumps (see section 2.3.1.2) with two alternating suction and exhaust cycles can form a similar flow pattern by valve switching. Another option is the inversion of the flow direction at a given frequency resulting in an alternating bidirectional flow (ATF). This increases vortex formation and turbulence so that foulants are removed more effectively.

Secondly, hydraulic backflushing can be considered by reversing the permeate flow direction across the membrane. This can lift loose deposits on the membrane surface [139, 197]. Likewise, it can be achieved by quick inversions of the feed flow direction as described for ATF systems.

Thereby, membrane sections along the fiber change periodically the flow direction across the membrane facilitating continuous backflushing with each pump cycle (Figure 2.12 C) [198].

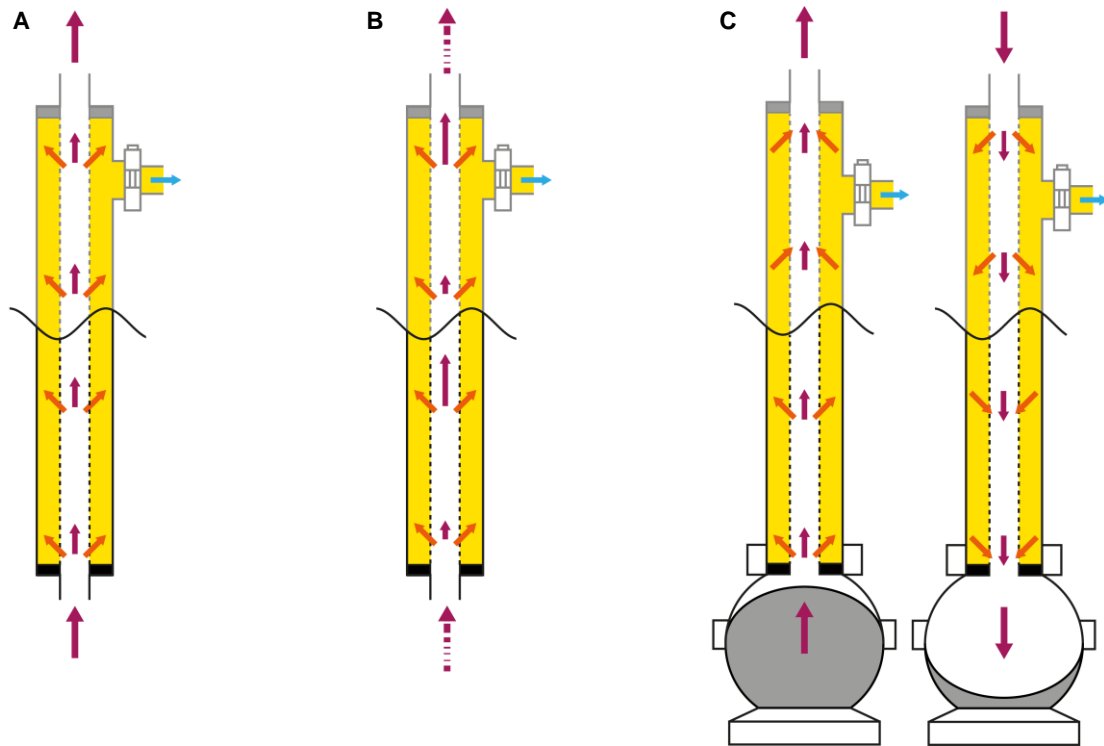


Figure 2.12 | Minimizing filter fouling during perfusion cultivations. (A) A typical unidirectional flow (TFF) can counter fouling by increased inlet flow velocity (single red arrow). (B) Pulsating flow velocities (PTF) support the removal of foulants even better (dotted red arrow). (C) In an alternating bidirectional cross-flow filtration (ATF) using a diaphragm pump, reverse flow velocities have maximum impact on foulants removal. For typical process operations (0.8 L/min), this causes reverse transmembrane flow (orange arrow) along the membrane with each pump cycle (backflushing). Additionally, the permeate flow (blue arrow) can be inverted by a permeate pump to counteract filter fouling (not shown here).

3 Materials and Methods

This chapter provides information on materials and methods used to generate the results for the experiments performed. The first sections describe general aspects of cell line maintenance, cell growth in different cultivation systems and flavivirus infection including perfusion cultivations. In the second part, assays used for cell counting, metabolite quantification, measurement of infectious and total flavivirus titers and virus dynamics are addressed. Finally, measurements and calculations are described to estimate the biomass and to determine cellular dielectric properties with an online capacitance probe. In addition, methods are addressed to characterize membrane fouling in different hollow fiber modules. Throughout this work, flavivirus-related standard operating procedures (SOPs) were established and are attached to this work (appendix A7.2). A list of consumables and equipment can be found in Tables A-1 and A-2 of the appendix.

3.1 Cell line maintenance

A variety of different cell lines (Table 3.1) was cultivated and screened to identify a suitable cell substrate for flavivirus production. Required basal cell growth media are listed in Table 3.2.

Table 3.1 | Overview of adherent (upper part) and suspension cell lines (lower part).

Abbreviation	Full name	Tissue	Species	Supplier
BHK-21	Baby hamster kidney C13	Kidney	Syrian golden hamster	IDT
C6/36	ATCC CRL-1660	Whole larvae	<i>A. albopictus</i> mosquito	RKI
PS	Stable porcine	Kidney epithelial	Wild boar	RKI
Vero	Vero WHO ECACC	Kidney	African green monkey	IDT
Vero E6	Vero ATCC C1008	Kidney	African green monkey	ATCC
AGE1.CR.plX	–	Primary retina cell	Muscovy duck	PBG ^[199]
AGE1.CR	–	Primary retina cell	Muscovy duck	PBG ^[199]
BHK-21 _{sus}	Susp. adapted BHK-21	Kidney	Syrian golden hamster	In house ^[200]
EB66 [®]	–	Stem cells, egg yolk	Peking duck	Valneva ^[118]
HB-4G2	Hybridoma cell D1-4G2-4-15	Spleen, B lymphocyte	Mus musculus	UFRJ
HEK293SF	Human embryonic kidney SF-3F6	Embryonic kidney	Homo sapiens	UAB/NRC
MDCK.SUS2	Susp. adapted madin darby canine kidney CL-34	Kidney epithelial	Female cocker spaniel	In house ^[201]

IDT = IDT Biologika Dessau-Roßlau, RKI = Robert Koch-Institute Berlin, ATCC = American Type Culture Collection, PBG = ProBioGen Berlin, UFRJ = The Federal University of Rio de Janeiro, UAB = Autonomous University of Barcelona, NRC = National Research Council of Canada.

Table 3.2 | Overview of basal cell growth media.

Category	Abbreviation	Name	Supplements	Supplier	Cell line
SCM	Z-Medium	Z-Medium based on GMEM	10 % FCS, 30 mM Glc, 2 g/L peptone	Gibco	BHK-21, PS, Vero
SCM	RPMI	RPMI-1640	10 % FCS	Gibco	HB-4G2
SCM	DMEM	Dulbecco's Modified Eagle's	5 % FCS	Gibco	Vero E6
SCM	L-15	Leibovitz's L-15 Medium	10 % FCS	Gibco	C6/36
CDM	CD_U3	CD_U3	2 mM Gln, 2 mM Ala, 10 µL IGF	PAA	AGE1.CR, AGE1.CR.plX
SFM	BGM	BHK cell growth medium	4 mM Gln, 4 mM Pyr	ud	BHK-21 _{sus} , Vero _{sus}
SFM	BGM8	BHK cell growth medium	8 mM Gln, 4 mM Pyr	ud	BHK-21 _{sus}
CDM	TC-X6D	Teutocell X6D	8 mM Gln	Xell	BHK-21 _{sus}
SFM	GRO-I	EX-CELL EBx GRO-I	2.5 mM Gln	SAFC	EB66 [®]
SFM	PRO-I	EX-CELL EBx PRO-I	2.5 mM Gln	Sigma	EB66 [®]
SFM	PRO-II	EX-CELL EBx PRO-II	2.5 mM Gln	Sigma	EB66 [®]
CDM	CDM4	HyClone CDM4Avian	2.5 mM Gln	Gibco	EB66 [®]
CDM	Smif8	Smif8 2xPGd	4 mM Gln	UEL	MDCK.SUS2
CDM	Xeno	Xeno-CDM	8 mM Gln	SBE	MDCK.SUS2, Vero _{sus}

SCM = serum-containing medium, SFM = serum-free medium, CDM = chemically defined medium; FCS = fetal calf serum, Glc = glucose, Gln = glutamine, Pyr = pyruvate, Ala = alanine, IGF = insulin-like growth factor; ud = undisclosed; UEL = University of Applied Sciences Emden/Leer, SBE = Shanghai BioEngine Sci-Tech, China.

3.1.1 Cell passaging

Adherent cells were passaged in tissue culture flasks (75 cm² or 175 cm², Greiner Bio One) when approximately 90 % confluency was reached. Therefore, the monolayer was washed twice with sterile phosphate buffered saline (PBS) and trypsinized (3 mL or 5 mL trypsin) for 5 min at 37 °C. For serum-containing medium (SCM), porcine trypsin at 500 U/mL (Gibco) was used and the reaction stopped by the addition of SCM. Cells in serum-free medium (SFM) and chemically defined medium (CDM) were trypsinized with fungus-derived TrypLE Selected (activity unknown, Thermo Fisher Scientific) and the reaction was stopped by dilution. A passage split ratio between 1:5 and 1:10 was chosen and tissue culture flasks were placed into humidified incubators at 37 °C and 5 % CO₂ (Heracell T6060, Heraeus). Adherent C6/36 insect cells were passaged at 80 % confluency by manual cell scraping (Falcon, Corning) with a split ratio of 1:5. Cells were incubated without CO₂ at 28 °C.

Suspension cells were passaged in the late exponential growth phase and inoculated at cell concentrations summarized in Table 3.3. Disposable Erlenmeyer shaker flasks (Corning) were placed in an orbital shaking incubator with 50 mm throw diameter (Multitron Pro, Infors HT). Mouse hybridoma suspension cells (HB-4G2) were cultivated in an upright standing tissue culture flask bottle (25 cm², treated polystyrene) with a working volume of 15 mL RPMI medium. The culture was placed in static incubators at standard conditions and passaged twice a week with a split ratio of 1:3.

Table 3.3 | Standard conditions to cultivate suspension cell lines.

Cell line	Baffles	Shaking speed	CO ₂ level	Inoculation conc.	Passages per week
AGE1.CR	Yes	185 rpm	5.0 %	8×10 ⁵ cells/mL	2
AGE1.CR.pIX	Yes	185 rpm	5.0 %	8×10 ⁵ cells/mL	2
BHK-21 _{sus}	Yes	185 rpm	5.0 %	5×10 ⁵ cells/mL	2
EB66 [®]	No	150 rpm	7.5 %	3×10 ⁵ cells/mL	2-3
HB-4G2	T25 flask *	static	5.0 %	~2×10 ⁵ cells/mL	2
HEK-293.SUS	No	185 rpm	5.0 %	3×10 ⁵ cells/mL	2-3
MDCK.SUS2	Yes	185 rpm	5.0 %	5×10 ⁵ cells/mL	2

* Tissue culture flask placed in upright position, inoculation concentration unknown.

3.1.2 Cryo vial freezing

Adherent cells and suspension cells were harvested during the exponential phase at about 90 % confluence or 70 % of the maximum cell concentration, respectively. Adherent cells were first detached. Both cell types then followed the same protocol. The cell concentration was determined (details in Chapter 3.8.1) and cells were centrifuged at 150g for 5 min at room temperature (RT). A final concentration of approximately 1×10⁷ cells/mL was adjusted with fresh growth medium and 10 % (v/v) DMSO was added. Cells were gently inverted in the freezing medium and quickly dispersed into 1.5 mL cryo vials (Cryo.S, Greiner). Cryo vials were either cooled stepwise (4 h at -20 °C, then 12 h at -80 °C) or gradually by using a freezing container (Mr. Frosty, Nalgene) filled with isopropyl alcohol at 4 °C (directly placed for 12 h at -80 °C). Subsequently, cryo vials were transferred into liquid nitrogen for long-term storage.

3.1.3 Cryo vial thawing

A frozen cryo vial was thawed in a preheated water bath at 37 °C until a small ice pellet remained. Cells were then gently aspirated and transferred into either coated tissue culture flasks for adherent cells (25 cm² surface area) or shake flasks for suspension cells (125 mL nominal volume, Greiner). Cold fresh basal growth medium (5 mL) was added dropwise over a time period of about 2 min to avoid sudden osmotic stress. Remaining cells in the cryo vial were resuspended in 1 mL cold medium and subsequently added to the culture. Cells were diluted to a working volume of 6 mL or 30 mL, respectively. Cells were then incubated at standard conditions, whereas suspension cells were first maintained at lower shaking frequency of 120 rpm for 4 h before being incubated at standard cultivation conditions.

3.1.4 Cryo bag preservation and direct bioreactor inoculation

EB66[®] cells were directly harvested at high cell concentration from ATF perfusion cultivations and used for large-volume cell banking. Cells were collected at concentrations above 2×10^7 cells/mL and viabilities greater than 95 %. Cells were centrifuged at 30 mL volumes at 300g for 5 min and 4 °C. The supernatant was replaced with conditioned freezing medium at 4 °C (CDM4Avian medium supplemented with 2.5 mM glutamine, 0.2 M sucrose and 20 % (v/v) DMSO). The cell pellet was gently resuspended and 15 mL were filled through a septum into a cryo bag (CryoMACS freezer bags 50, Miltenyi Biotec). The cryo bag was kept on ice and filling lines were subsequently sealed with a heat sealer. The bag was first placed into an overwrap protection bag and then frozen to -20 °C for 12 h. The cryo bag was finally transferred to -80 °C for long-term storage until use.

For direct bioreactor inoculation, a frozen cryo bag was removed from -80 °C and thawed in a water bath at 37 °C until a small ice pellet remained. The bag was carefully inverted to resuspend sedimented cells and then connected via the injection port to an empty bioreactor system (0.7 L working volume). The bioreactor was cooled to 10 °C by cold process water. While the inoculum was added dropwise into the vessel rinsing down the glass wall, cold basal growth medium was simultaneously added at 2.5 mL/min for 15 min. The pump speed was increased to 10 mL/min and when the liquid level covered half the impeller blades. Temperature control and stirring were initiated and stepwise increased over 30 min to final process values (37°C, 100 rpm).

3.1.5 Vero cell adaptation to suspension growth

The adaptation of the adherent Vero WHO parental ECACC 134th cell line to VeroSUS was conducted by two sequential adaptation approaches. For the first approach, anchorage-dependent Vero cells growing in Z-medium were passaged stepwise to adapt them to grow in serum-free or chemically defined medium, i.e., AEM (SFM), BGM (SFM), SFM4BHK21 (SFM; HyClone, Waltham), VeroExpress8 (SFM; Gibco), 42-Max-UB (CDM; Teutocell), CD-U3 (CDM), FreeStyle 293 (CDM; Gibco), Xeno (CDM) or SMIF8 PGd2x (CDM). Adherent cells were trypsinized with TrypLE Select after washing twice with PBS at a cell confluency of 95 % and transferred to a new tissue culture flask (75 cm²) with a split ratio of 1:5. The Z-Medium was stepwise diluted by the

new medium conditioned with 10 % old medium (fixed) from the previous passage and 20 % of the respective SFM or CDM (increased by 20 % with every passage). Within five passages, the serum content decreased to 0.1 g/L and the medium was changed to the desired growth medium. For the second approach, Vero cells were adapted to grow suspension by super-confluency state cultivation enabling cell budding [202]. In brief, adherent Vero cells were maintained in tissue culture flasks (175 cm²) and medium was stepwise exchanged with conditioned medium (desired medium increased by 20 % with each passage) when glucose concentrations dropped below 1.5 g/L. Throughout the adaptation period, cells formed multilayers and started to round up when dividing and remained in the supernatant. Suspension cells were collected and cultivated in pendulum spinners (in-house made) at 80 rpm and 30 mL working volume. YFV infection was performed at MOI 10⁻². Alternatively, suspension-adapted VeroSUS in Smif8 medium (thankfully provided by Prof. Dr. Klaus Scharfenberg, HS Emden/Leer) were stepwise adapted to grow in baffled shake flasks at 185 rpm and Xeno medium. Infection experiments with YFV were conducted at MOI 10⁻³.

3.1.6 Characteristic cell growth parameters

Specific growth rate The correlation between cell growth rate (r_c) and viable cell concentration (X_c) is described by the proportionality factor, also called specific growth rate μ expressed in (1/h). If endogenous (e.g. cell line) and exogenous factors (e.g. substrate concentration, temperature) were at optimum conditions, a maximum specific growth rate μ_{max} was obtained. The maximum specific growth rate was determined in the exponential growth phase with $X(t) = X_0 \cdot e^{\mu t}$ as

$$\mu_{max} \cdot X_c = \frac{dX_c}{dt} = r_c \quad (9)$$

Population doubling The population doubling time t_D (h) describes the minimum time a culture requires to double its concentration and was calculated with the maximum specific growth rate obtained in a cultivation.

$$t_D = \frac{\ln 2}{\mu_{max}} \quad (10)$$

Cell-specific metabolite uptake rate The differential value of substrate S_i consumed by the averaged cell concentration over the time is the cell-specific substrate uptake rate q_i per hour as (pmol/cell/h). An evaporation effect of 2 % of the total working volume per day was taken into account to correct X_c for long-term cultivations in for shake flask experiments.

$$q_i \cdot X_c = \frac{-dS_i}{dt} \quad (11)$$

3.2 Semi-continuous two-stage shake flask cultivations

Semi-continuous two-stage cultivation in shake flask scale were previously described in detail elsewhere [203, 204]. In brief, an one baffled shake flask with a working volume of 240 mL (1 L shake flask) and two baffled shake flasks with 168 mL (0.5 L shake flask) were inoculated with BHK-21_{SUS} cells and incubated at 150 rpm using standard conditions. After 16 h, the two smaller virus production shake flasks were infected with YFV at MOI 1. One day post infection, the continuous process was initiated: Every 12 h, a volume V_1 of 67 mL was extracted from the infected shake flasks (corresponding to residence time of 30 h while t_D was about 20 h). A volume V_2 was added, respectively, from the non-infected cell growth shake flask in dependence on the growth performance. V_2 was determined based at an initial dilution rate of 0.032 h^{-1} (90 % of $\mu_{\max} = 0.035 \text{ h}^{-1}$, which corresponds to residence times of about 32 h or higher; maximum 63 mL to be added) and constantly adjusted based on the actual cell growth rate to the previous sampling point. As V_1 was larger than V_2 of the virus production shake flask, the difference in volume was compensated with fresh medium. The shake flasks were constantly sampled and virus titers were quantified.

3.3 Pseudo-perfusion in shake flasks

Pseudo-perfusion cultivations were performed in 125 mL baffled shake flasks at a working volume of 30 mL to 50 mL. After 72 h batch operation, cells were centrifuged at 150g for 5 min at RT, the supernatant was replaced by 80 % with new pre-incubated medium (37 °C and 5 % CO₂ in incubator headspace) and the resuspended cell pellet transferred into the old shake flask. Centrifugation tubes and pipettes were subsequently rinsed with remaining 20 % fresh medium. Collected cells were also added to the shake flask. This perfusion rate strategy aimed at supplying cells with sufficient substrates. Based on cell-specific substrate uptake rates q_S , either time intervals for complete medium exchange (Δt , Equation 12) or the partial volume exchange (V_E , Equation 13) until a specific time point (before Δt) were calculated:

$$\Delta t = \frac{\ln\left(\frac{V_E \cdot \mu}{X_c \cdot V_w \cdot q_S}\right) + 1}{\mu} \quad (12)$$

$$V_E = (X_c) \cdot \frac{1}{\mu} \cdot (e^{\mu \cdot \Delta t} - 1) \cdot V_w \cdot q_S \quad (13)$$

where V_w is the working volume and q_S the cell-specific substrate consumption rate of the previous sampling interval. Experiments were performed with a set point of 2.5 mM glucose or 0.5 mM glutamine, respectively.

3.4 Bioreactor cultivations

3.4.1 General assembly

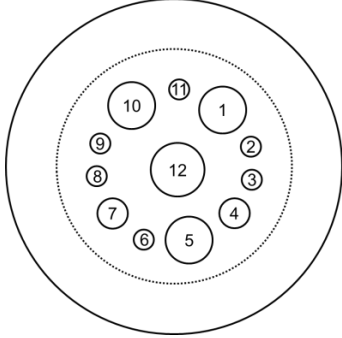
Cultivations at the MPI were conducted in a 1 L stirred tank double-jacket glass bioreactor (Univessel, Sartorius) with a digital control unit (DCU; BioStat B Plus) from Sartorius. Working volumes were in the range of 700 mL to 800 mL. The vessel was equipped with different impellers for specific applications and cell lines:

- (i) Microcarrier cultivations: Two 32 mm segment impellers (three blades, -45° angle in lower position of shaft, and $+45^\circ$ angle in upper position) configured in a bidirectional axial flow, impeller diameter (T) to vessel diameter (D) ratio (T/D) of 0.30, stirrer speed 60 rpm;
- (ii) BHK-21_{SUS} cultivations: One segment impeller (three blades, $+45^\circ$ angle, 32 mm diameter) in axial flow upstream position, T/D of 0.30, stirrer speed 120 rpm;
- (iii) EB66[®] cultivations: One segment impeller (three blades, $+30^\circ$ angle, 72 mm diameter) in axial flow upstream position, T/D of 0.65, stirrer speed 100 rpm.

Standard process parameters were monitored with a resistance thermometer (pT10, UMO MK), dissolved oxygen (DO) probe (InPro 6800, Mettler Toledo) and pH probe (405 DPas sc k8s, Mettler Toledo). Further probes such as capacitance probe (Incyte, Hamilton) and turbidity probe (Dencyte, Hamilton) were optionally used. The bioreactor was equipped with a micro-sparger unit ($\sim 20 \mu\text{m}$ pore size, Sartorius), a silicon septum for inoculation, and a 6 mm dip tube for dead-volume free sampling by a T-piece connecting a one-way sampling valve (Eppendorf) and an air filter ($0.2 \mu\text{m}$, 25 mm, Whatman) to push cells remaining in the dip tube after sampling back into the main vessel. The top-plate port assembly is shown in Table 3.4. Sterile quick connectors (STT, Sartorius) with a slot membrane were used to connect in- and outlets of the bioreactor. Basal growth medium was filled in the vessel and the temperature was set to 37°C . An oxygen level of 80 % ($p\text{O}_2$) was maintained by pulsed-aeration with pure oxygen. The pH value of the culture was optionally adjusted with CO_2 or 0.5 M NaOH and 0.5 M HCl. When process conditions (T, $p\text{O}_2$) stabilized, cells were inoculated through a needle.

Bioreactor cultivations at the UFRJ in Brazil were performed with a disposable Mobius 3 L stirred tank vessel (#CR0003L200, Merck Millipore), the ez-control unit (Applikon) and the BioXpert SCADA software bundle (v2, Applikon). A motor drive adapter was used to operate a P100 motor and the pre-configured marine impeller (T/D of 0.57) at 80 rpm. The bioreactor was heated with a 3 L thermal blanket (101087, Applikon). DO (Z010023525) and pH probes (Z001023551, both Applikon) with 235 mm length were used. A $p\text{O}_2$ set point of 80 % was maintained by pulsed sparging with pure oxygen through a sintered PE microsparger unit (15-30 μm nominal size) and a maximum flow rate of 0.1 L/min. In- and outlets were connected via sterile quick connectors (MPX series, Colder Products Company).

Table 3.4 | Assignment of vessel equipment to top-plate ports of the 1 L UniVessel for standard operation.

	Port No.	Inner port diameter	Assignment
	1	19 mm	ATF dip tube/outlet for TFF loop
	2	6 mm	Sample port
	3	6 mm	Septum
	4	13 mm	DO probe
	5	19 mm	Incyte probe/triport for pH control
	6	6 mm	Inlet for TFF loop
	7	13 mm	pH probe
	8	6 mm	Inoculation/feed
	9	6 mm	Temperature probe
	10	19 mm	Outlet with gas condenser
	11	6 mm	Gas inlet
	12	unknown	Drive/motor

Note: 19 mm ID ports have a Pg 29 screw thread, 13 mm ID ports a Pg 13.5, and 9 mm ID ports are without threads.

3.5 Microcarrier cultivations

Cytodex 1 microcarriers (GE Healthcare) were first added in a stock solution of 40 g/L in PBS for swelling according to manufacturer's instructions and then transferred to the respective medium for conditioning.

At the MPI, microcarrier cultivations with Vero cells were performed either in 250 mL spinner flasks (magnetic vertical two-blade impeller, Wheaton) or a 1 L UniVessel glass bioreactor. Spinner cultivations were performed at a working volume of 200 mL at 60 rpm, while pH and pO_2 levels remained uncontrolled. Cells were inoculated at a ratio of 30 cells/MC and infected with YFV at $MOI 4 \times 10^{-2}$ (based on measured titer at time point of infection). For preliminary studies in bioreactor-scale, microcarriers were added stepwise from 1.4 g/L to 2.2 g/L and finally 3.1 g/L to Z-medium while the turbidity at 880 nm (NTU_{880}) was recorded (Dencytee, Hamilton). The Vero pre-culture was prepared in tissue culture flasks (175 cm²) and the bioreactor was inoculated with 3.7×10^5 cells/mL (ratio of 29 cells/MC). Osmolality, pH value and metabolite concentrations were determined from the filtered supernatant (0.2 μ m, CellTrics, Sysmex). Cell growth on the microcarriers was estimated by capacitance measurements and hemocytometer counting (see Chapter 3.8.2). The cultivation was maintained at pH 7.2 using 0.5 M NaOH and cells were infected with YFV at $MOI 3 \times 10^{-2}$.

At the UFRJ in Brazil, Vero E6 cells were cultivated on 5 g/L Cytodex 1 microcarriers and a single-use Mobius system with 1.1 L DMEM. The bioreactor was inoculated at 1.5×10^5 cells/mL (ratio of 7 cells/MC) and Vero E6 cell concentrations were determined by manual nuclei counting (see Chapter 3.8.3). When the glucose concentration dropped below 0.7 g/L during the growth phase, the medium was partially exchanged. Therefore, the agitation was stopped, microcarriers sedimented and 950 mL of the used medium was replaced with fresh medium. Vero E6 cells were infected one day later with ZIKV^{ES.U} at $MOI 10^{-3}$.

3.6 Perfusion bioreactor cultivations

To perform membrane-based perfusion cultivations, an external flow loop containing a positive replacement pump and a hollow fiber module were added to the batch bioreactor. The permeate was extracted through the hollow fiber module by employing a peristaltic pump and a specific pump tubing (PharMed BPT NSF-51, ID 0.76 mm, wall thickness 0.86 mm, Saint-Gobain Biopharma). The pump was either set manually or controlled automatically by an online biomass probe. The feed pump was connected to the DCU and controlled to maintain a pre-set working volume of the bioreactor system. The following section describes the set-up and cultivation conditions for TFF (centrifugal pump) and ATF (diaphragm pump) perfusion cultivations. In addition, details on the perfusion rate control are provided.

3.6.1 Tangential flow filtration cultivations

Two 6 mm dip tubes were mounted onto the top-plate at opposite sides and used as inlet and outlet of the perfusion recirculation loop (see Table 3.4). The loop consisted of a short silicon tubing (ID 5 mm), which was connected to a magnetic impeller pump (PuraLev[®] 200MU, Levitronix). A 0.2 μm PES hollow fiber (1300 cm^2 , ID 1 mm, Refine) was directly mounted on the outlet flange of the pump in vertical position. On the membrane retentate side, a Pro-Connex flange (3/4" TC to 1/4" barb, Spectrum Labs) was used to connect a permeate line with an integrated sampling valve. The set-up was steam autoclaved, and placed on a balance after cooling (illustrated in Figure 2.7 A).

BHK-21_{SUS} cells were inoculated at 7×10^5 cells/mL in BGM medium for growth in batch mode. The pH value was controlled at 7.2 using 0.5 M NaOH. After 30 h, the impeller pump head and recirculation loop were primed with the cell broth by temporarily using an additional peristaltic pump. While opening the peristaltic pump head, the impeller pump was simultaneously started and operated at 1200-1300 rpm. After 70 h, the perfusion process was initiated and perfusion rates were adjusted manually to maintain glucose concentrations around 8 mM. To minimize overall medium usage, perfusion media were supplemented with key metabolites such as glutamine, glucose and pyruvate (Table 3.5). Cells were infected at 2×10^7 cells/mL with YFV at $\text{MOI } 10^{-2}$.

Table 3.5 | BHK-21_{SUS} perfusion media supplementation on the basis of BGM growth medium.

	Glutamine (mM)	Glucose (mM)	Pyruvate (mM)
Perfusion medium A _{BHK}	4	30	8
Perfusion medium B _{BHK}	12	40	8
Perfusion medium C _{BHK}	8	60	4
Perfusion medium D _{BHK}	12	40	8

EB66[®] cells were cultivated using the same set-up. The inoculation concentration was at 3×10^5 cells/mL and cells grew in serum-free GRO-I medium. A one-sided pH control was set for pH below 7, but as values remained between 7.3 and 7.1, the pH remained uncontrolled. After a

batch cultivation phase of 72 h, the recirculation pump was started at 1200 rpm and 8 h later the perfusion process was initiated. Perfusion rates were adjusted manually to maintain glucose levels above 5 mM. The perfusion medium was based on GRO-I medium and additionally supplemented with glutamine and glucose (Table 3.6). Cells were infected at 2.2×10^7 cells/mL with YFV (Vero cell-derived seed) at measured MOI 10^{-4} .

Table 3.6 | EB66[®] perfusion media supplementation on the basis of GRO-I growth medium.

	Glutamine (mM)	Glucose (mM)
Perfusion medium A _{EB}	4	–
Perfusion medium B _{EB}	4	16

3.6.2 Alternating tangential flow filtrations

A dip-tube (ID 10 mm) was mounted onto the top-plate (see Table 3.4) and connected with a C-Flex tubing to the vertically positioned membrane directly connected to the ATF 2 diaphragm pump (Refine). Both, the ATF2 system and the bioreactor were placed on one balance (set-up illustrated in Figure 2.7 B). The diaphragm pump cycles were controlled by a C24U-v2.0 control unit at a flow rate of 0.5 L/min for filling and 0.8 L/min for perfusion operation (advanced set points: max. P-flow 10 L/min; min. P-flow 0.2 L/min; max. E-flow 10 L/min; min. E-flow 0.2 L/min; pressure range -12 psi to 25 psi).

In Brazil, perfusion cultivations with BHK-21_{SUS} cells were performed under BSL-3 conditions with limited options for metabolite quantification, control of perfusion rate and gasses. A 3 L single-use Mobius bioreactor system was used and equal volumes of TCX6D/TC-LECC medium (both Xell) supplemented with 100 IU/mL Pen-Strep (Gibco). The ATF2 pump connected to a 0.2 µm PES hollow fiber membrane (1300 cm², ID 1 mm, Refine) and C-Flex tubing with dip-tube were steam autoclaved separately and afterwards inserted into the sterile Mobius bioreactor inside a biological safety cabinet. The bioreactor was inoculated at 7×10^5 cells/mL and operated in batch mode for 5 days. The glucose level dropped below 5 mM and 70 % of the working volume (1.5 L) was exchanged with fresh medium. Three days later, the perfusion process was started with a fixed perfusion rate of 0.4 RV/day with a perfusion medium based on basal growth medium supplemented with 16 mM glutamine and 1 % (v/v) MEM non-essential amino acids solution (Gibco). Cells were infected at 1.2×10^7 cells/mL. Therefore, the feeding with fresh medium was stopped, 30 % of the working volume were removed through the perfusion membrane and concentrated cells were infected with ZIKV^{PE} at MOI 10^{-3} . The stirring was then stopped periodically (3 min on, 15 min off) for a total of 1 h before the initial speed was set to 120 rpm. The bioreactor was filled with fresh growth medium to the initial volume. A pH value of 7.1 was maintained using 0.5 M NaOH.

At the MPI, EB66[®] cell cultivations were conducted in a BioStat bioreactor system with a working volume of 0.7 L and a 0.2 µm PES hollow fiber membrane (470 cm², ID 1 mm, Spectrum Labs). The vessel was filled with CDM4Avian medium and the pH was adjusted to 7.2 by CO₂

sparging. The bioreactor was inoculated at a starting cell concentration of 3×10^5 cells/mL. For the first ATF run (ATF-M), a manual metabolite-based perfusion strategy was followed. When the glutamine concentration reached 1 mM, perfusion was initiated and rates were constantly adjusted to avoid glutamine depletion and glucose concentrations below 5.5 mM (see following section for further details). Cells were infected with EB66[®] cell-adapted YFV at MOI 10^{-3} . The osmotic pressure of 265 mmol/kg or lower was re-adjusted by the addition of sodium chloride (stock solution of 5.13 M). The second ATF run (ATF-17pL) was operated with an automated perfusion rate control and a cell-specific perfusion rate (CSPR) of 17 pL/cell/day (see next section for further details). This CSPR was estimated from the ATF-M cultivation, where this value was reached while key metabolites were at sufficient quantities. To avoid osmotic pressure drops below 265 mmol/kg, the osmolality was adjusted manually using sodium chloride (stock solution of 5.13 M). Furthermore, 0.75 mM L-methionine (stock solution of 130 mM) was supplemented to the bioreactor at day four. Shortly after, 100 mL of the cell broth with 2.1×10^7 cells/mL was harvested to prepare cell seed cryo bags and the volume in the vessel was refilled with fresh medium. When cells reached 8.9×10^7 cells/mL, cells were infected with EB66[®] cell-adapted ZIKV at a measured MOI 10^{-3} . The third ATF run (ATF-34pL) was directly inoculated from the prepared cryo bag resulting in an inoculation concentration of 7.9×10^5 cells/mL. The CSPR was doubled to 34 pL/cell/day and cells were infected at 7.3×10^7 cells/mL with EB66[®] cell-adapted ZIKV at measured MOI 10^{-3} .

3.6.3 Perfusion rate strategies

Perfusion rates (Q_{perf} , mL/min) were either set manually (to a fixed RV/d perfusion rate or adjusted to prevent metabolite depletions) or controlled using an online biomass probe for CSPR-based control).

RV/d-based perfusion rate Fixed perfusion rates were chosen for first scouting experiments or when options for metabolite measurements were limited. The perfusion rate was expressed as:

$$RV/d = \frac{Q_{perf}}{V_W} \quad (14)$$

where V_W is the overall working volume (bioreactor and external recirculation loop). Initial values of about 0.5 h^{-1} were chosen and gradually increased with growing cells.

Metabolite-based perfusion rate control The manual control of metabolites was based on offline measured metabolites with a particular focus on glucose and glutamine levels. Specific minimum levels were defined (as provided in sections above) and perfusion rates were adjusted to maintain those concentrations. First, viable cell concentrations (X_C) were measured and substrate consumption rates of the last sampling interval (q_S , pM/cell/h) were determined. Then, the perfusion rate Q_{perf} was calculated assuming q_S is valid for the next time interval as:

$$Q_{perf} = \frac{X_c \cdot V_W \cdot q_S}{s_0} \quad (15)$$

where s_0 (mM) is the substrate concentration of the perfusion medium. To meet the expected metabolite demand until the next sampling point (Δt , in h), the last specific cell growth rate (μ) was determined and a prospective perfusion rate (Q_{prosp}) was calculated according to:

$$Q_{prosp} = \frac{X_c \cdot e^{\mu \Delta t} \cdot V_W \cdot q_S}{s_0} \quad (16)$$

Initial parameters of $\mu = 0.035 \text{ h}^{-1}$ and $q_{glc} = 28 \text{ pM/cell/h}$ were chosen for the BHK-21_{SUS} ATF perfusion cultivation. Q_{prosp} was calculated after each sampling point and a linear permeate profile from Q_{perf} to Q_{prosp} over time was set in the DCU until the next sampling. This strategy enabled constantly increasing media supply with increasing cell concentrations.

Automated CSPR-based perfusion rate control An online biomass probe (Incyte, Hamilton) was used to monitor cell growth and to control the perfusion rate maintaining fixed CSPR values. First, the online permittivity value was correlated linearly to offline measured viable cell concentrations. The correlation factor (also called cell density factor) was determined throughout the cultivation and re-adjusted in the controller (ArcView 265, Hamilton) when changes occurred. In dependence on the measured cell concentration, an analog output signal was forwarded from the controller to a 4–20 mA output box (243820, Hamilton) with a self-assembled cable (open-end AUX M12 cable) and a DIN rail bus connector (ME 22,5 TBUS 1,5/4P1S KMGY, 2201732, PhoenixContact). From there, open cable ends to port 1 and 2 in Channel 1 were connected with a 15-pin D-SUB male connector to the peristaltic permeate pump (Watson-Marlow). To obtain desired pump rates, the controller output signal needed to be configured. During a manual 2-point calibration at 4 and 20 mA current output, parameters were identified empirically. Configuration values of -12.5 for 4 mA and 1740 for 20 mA were chosen to obtain a CSPR of 17 pL/cell/day for the EB66[®] ATF-17pL cultivation. To obtain a CSPR of 34 pL/cell/day for the EB66[®] ATF-34pL cultivation, the cell factor was doubled and calibration parameters were kept constant (further details elsewhere [147]).

3.7 Flavivirus propagation

Adherent cells in tissue culture flasks were infected with flavivirus when a confluency of approximately 90 % was reached. First, the spent medium was discarded and the flavivirus seed was added to a desired MOI (based on plaque assay titer) using a reduced infection volume of 10 % of the initial working volume:

$$V_{virus} = \frac{X_c \cdot V_w}{C_{vir}} \cdot MOI \quad (17)$$

where C_{vir} (PFU/mL) is the virus titer of the seed virus material. It should be noted that desired MOI differed from measured MOI due to unspecific virus inactivation or direct adsorption after addition. To improve virus attachment and uptake into cells, the tissue culture flask was rocked every 15 min for 1 h and the medium was finally filled up to the original volume. Suspension cells were infected during the mid/late exponential growth phase and the virus was added directly to the cells. Virus samples harvested were collected, centrifuged at 2000g for 3 min to remove cell debris, and the supernatant was stored at -80°C until use. A list of all used flaviviruses in this study is given in Table 3.7.

Table 3.7 | Overview of flaviviruses used in this study.

Abbrev.	Long name	Source	Seed virus origin
YFV	Yellow fever virus WHO 17D-213/77	RKI, Matthias Niedrig	Vero
ZIKV ^{RJ}	Brazilian Zika virus isolate (Rio de Janeiro state)	Fiocruz, Thiago Souza	C6/36
ZIKV ^{ES,U}	Brazilian Zika virus isolate (Espírito Santo state)	UFRJ, Amilar Tanuri	Vero E6
ZIKV ^{ES}	Brazilian Zika virus isolate (Espírito Santo state)	Fiocruz, Ana Bispo de Filipis, Elena Caride	C6/36
ZIKV ^{PE}	Brazilian Zika virus isolate (Pernambuco state)	Fiocruz, Marli Tenório	C6/36
ZIKV ^{PB}	Brazilian Zika virus isolate (Paraíba state)	Fiocruz, Ana Bispo de Filipis, Elena Caride	C6/36
ZIKV MR766	African Zika virus isolate	UFRJ, Davis Ferreira	Vero E6

Note: Egg-derived YFV vaccine is a live-attenuated sub-strain of 17D-204 at passage 237. The lyophilized vaccine was reconstituted in PBS and the virus was expanded in Vero cells. Brazilian ZIKV strains were collected from different regions in Brazil during the ZIKV outbreak in 2015/2016. ZIKV was isolated from whole blood specimens of PCR-positive adult patients during the acute phase of symptoms, and the virus was expanded in cell culture.

The maximum cell-specific virus yield (CSVY) was calculated according to:

$$CSVY = \frac{C_{vir,max} - C_{vir,inf}}{X_{tot,max}} \quad (18)$$

where $C_{vir,max}$ is the maximum virus concentration, $C_{vir,inf}$ the virus concentration of the first sample after infection, and $X_{tot,max}$ the maximum cell concentration obtained until the time point of highest virus titer.

3.7.1 Sequential virus adaptation

YFV and ZIKV^{RJ} were both adapted sequentially to new cell substrates such as BHK-21_{SUS} and EB66[®] cells. Cells were growing in shake flasks under standard conditions and were infected at MOI 10⁻². Four days post infection, 70 µL of the cell broth was transferred to a subsequent shake flask with cells growing in the exponential growth phase. Further virus passaging was carried out with 50 µL every 72 h to select for fast-propagating viruses. Virus seeds were routinely collected and stored at -80 °C until quantification or further infection experiments.

3.7.2 Virus enrichment by centrifugation

ZIKV^{RJ} seed material was derived from a perfusion cultivation using EB66[®] cells (ATF-34pL) and 30 mL was harvested with a titer of 8.5×10⁹ PFU/mL. The sample was centrifuged at 5000g for 10 min at 4 °C and the supernatant removed. Then, 7.2 mL of a sucrose cushion (20 % (w/v) sucrose, 25 mM HEPES in PBS) was added to an ultra-clear tube with a nominal capacity of 38 mL (Beckman). Subsequently, 30.8 mL of virus supernatant was carefully overlaid. The sample was centrifuged at 103,745g for 289 min with a swing rotor SW28 and Optima TM LE-80K ultracentrifuge (Beckman Coulter). The pelleted ZIKV^{RJ} was re-conditioned in 200 µL TNE buffer (10 mM Tris, 0.2 M NaCl, 10 mM EDTA in PBS, pH adjusted to 7.4) and stored at -80 °C.

3.8 Offline cell concentration measurements

The cell concentration of adherent or suspension cell lines was determined offline either by trypan-blue dye exclusion or nucleus counting. While trypsinized cells and suspension cells were generally counted with an automated cell counter, adherent Vero cells from microcarrier cultivations were counted manually. Online biomass concentrations for perfusion cultivations are described in section 3.6.3 with further details in the following section 3.12.

3.8.1 Automated whole cell counting

The viable cell concentration (VCC, symbol: X_c) of adherent cells in tissue culture flasks was measured with the ViCell XR counter (Beckman Coulter). First the cell layer was washed twice with sterile PBS and subsequently detached by the addition of porcine pancreas-derived trypsin (Gibco) at 500 U/mL in PBS (0.5 mL trypsin for 25 cm² surface; 1.25 mL for 75 cm²; 3 mL for 175 cm²). The enzymatic digestion was stopped after approximately 5 min by the addition of an equal volume of fetal calf serum (FCS, Gibco). Cells were measured with ViCell acquisition settings for adherent cells (Table 3.8). The total cell count was considered as being viable since dead cells were considered to be removed during washing steps.

Single suspension cells were measured directly to obtain data on viable cell concentration, viability and cell size (d_{vc}). When cell clumps occurred, e.g. during bioreactor cultivations, agglomerates were primarily dispersed mechanically. If manual pipetting was not sufficient, cells were treated enzymatically: 1000 μL of the sample was centrifuged at 3000 rpm for 1 min (Multi-Spin PCV-3000, Grant-bio), and 950 μL of the supernatant was discarded. A volume of 450 μL porcine trypsin (500 U/mL) was added to the cell pellet, incubated for 10 min at 37 °C and stopped by the addition of 500 μL FCS before measurement. EB66[®] cell clumps were more robust. Thus, a bioreactor sample of 200 μL was added to 200 μL trypsin (5000 U/mL) and incubated for 10 min and 37 °C at 600 rpm in a thermomixer (Eppendorf). The reaction was stopped by the addition of 200 μL FCS and cells were counted in triplicates. Samples exceeding the linear measurement range (10^4 - 10^7 cells/mL as stated by manufacturer) were diluted with PBS. Data acquisition was performed with cell-specific settings determined empirically (Table 3.8).

Table 3.8 | ViCell settings for different cell lines.

	Adh. cells	AGE1.CR	BHK-21 _{SUS}	EB66 [®]	Hybridoma	MDCK
Min. diameter (μm)	5	8	10	8	7	8
Max. diameter (μm)	28	30	35	30	50	25
Number of images	50	100	100	100	50	100
Aspirate cycle	3	3	3	3	1	3
Trypan blue mixing cycle	3	3	3	2	3	3
Cell brightness (%)	85	90	85	90	85	85
Cell sharpness	80	100	80	100	100	80
Viable cell spot brightness (%)	90	85	90	85	75	90
Viable cell spot area (%)	4	3	4	3	5	4
Min. circularity	0	0.5	0	0.5	0	0
Decluster degree	Medium	High	Medium	High	Low	Medium

Note: Acquisition settings for adherent (adh.) cells were used for, e.g., Vero, BHK-21 and PS cells.

The viable cell volume (VCV, symbol: V_c , in μL) was calculated from ViCell measurements in triplicates. The cell concentration was measured as previously described and the average cell diameter was determined from the cell size distribution in individual classes as triplicates with a respective set of 100 images per single measurement. The V_c was calculation as:

$$V_c = \frac{\sum \left(d_{vc}^3 \cdot N_{vc} \cdot \frac{\pi}{6} \right)}{N_{vc}} \cdot X_c \quad (19)$$

where d_{vc} is the viable cell diameter and N_{vc} the total viable cell number.

3.8.2 Manual whole cell counting

Cell concentration measurements of adherent cells on microcarriers were performed based on the protocol by *Bock et al.* [205]. In brief, 1 mL of a homogeneous sample was washed by addition to a 15 mL falcon tube filled with 9 mL PBS. The supernatant was removed from sedimented microcarriers and the procedure was repeated twice. For optimum cell counting, the sample was diluted to a desired microcarrier concentration ($c_{MC,sp}$) of 1000 carriers/mL. Then, 100 μ L of the diluted sample was pipetted to wells of a flat-bottom 96 microtiter plate, filled with 100 μ L PBS and 200 μ L trypsin (500 U/mL) and incubated for 10 min at 37 °C. Adherent cells then detached from microcarriers by gentle resuspension. Microcarriers were counted and the supernatant removed for cell counting with a Fuchs-Rosenthal hemocytometer (Glaswarenfabrik Hecht). The cell concentration in the bioreactor was calculated as:

$$X_c = X_{c,well} \cdot 4 \cdot \frac{V_{well}}{N_{MC}} \cdot c_{MC,BR} \quad (20)$$

where $X_{c,well}$ is the cell concentration in one well, V_{well} the sample volume per well (here 100 μ L), N_{MC} the number of microcarriers per well, and $c_{MC,BR}$ the microcarrier concentration in the cultivation vessel.

3.8.3 Manual nuclei counting

At the UFRJ in Brazil, adherent Vero E6 cells on microcarriers were counted according to the total number of released nuclei. In brief, 150 μ L of the sample was transferred to 1350 μ L crystal violet solution (0.1 M citric acid, 0.1 % (w/v) crystal violet, 0.01 % Triton X-100), well mixed and incubated for 1 h at 37 °C. The sample was resuspended, microcarriers settled and the supernatant removed for counting. Stained nuclei were diluted in PBS and counted in a hemocytometer.

3.9 Metabolite measurements

Samples for metabolite measurements were centrifuged for 1 min at 3500 rpm (Fast Gene Mini Centrifuge, NIPPON Genetics). For virus-containing samples, the supernatant was additionally heat-inactivated for 3 min at 80 °C (QBT, Grant Instruments) and stored at –80 °C until use. Metabolite concentrations of glucose, glutamate, glutamine, lactate and ammonium were measured with a Bioprofile 100 Plus (Nova Biomedical). All measurements were performed in the validated working ranges by diluting with PBS (Table A7.3 in the appendix). Metabolite samples from bioreactor cultivations were collected and measured after the run with in-house prepared metabolite standards. The pyruvate concentration was determined with a Cedex Bio Analyzer (Roche). Amino acid concentrations were determined with an anion exchange chromatography (AccQ-TAG Ultra, Waters). Therefore, 10 μ L samples were derivatized, first, by adding 70 μ L borate buffer

(derivatization kit, Waters), well mixed and incubated for 1 min. Then, 20 μL derivatization reagent was added, again mixed and incubated for 10 min at 55 °C. Finally, amino acids were measured together with commercial amino acid standards (Waters).

3.10 Virus quantification

Quantitative flavivirus assays needed to be established within this work. The following section covers the plaque assay and RT–qPCR. Further details are found in the SOPs in the appendix (A7.2.1–A7.2.4).

3.10.1 Plaque assay

For flavivirus, plaque-forming units (PFU) were determined from the cell supernatant by an infectivity assay. First, 4×10^5 PS cells in 200 μL Z-Medium were added into each well of a 24-well plate. Then, 200 μL of a diluted virus sample in Z-Medium was added and incubated for 4 h at standard incubation conditions. The infected cell monolayer was overlaid with 1.6 % (w/v) carboxymethyl cellulose in Z-Medium and incubated for 60 h (ZIKV) or 84 h (YFV). Cells were then fixed with 3.7 % (v/v) formalin in PBS for 15 min and stained with naphthalin black (1 g naphthol blue black, 13.6 g sodium acetate, 60 mL glacial acetic acid, add to 1 L dH₂O) for 30 min. Plaques were counted and titers expressed as plaque-forming unit per volume (PFU/mL) in accordance to Spearman and Kärber [206]. An assay validation was performed and a coefficient of variation (CV) was determined to 14 %. Further information on the procedure and the validation is given in the SOP A7.2.1.

3.10.2 One-step TaqMan-based RT–qPCR

This section describes viral RNA (vRNA) molecule quantification by real-time reverse transcription quantitative PCR (RT–qPCR). To determine intracellular vRNA levels, cells were first centrifuged at 1000g and washed twice with PBS. Cells were lysed by ultra-sonication (150 Joule, 15 s, 90 % amplitude, 80 % pulse time) at 4 °C with a pre-cooled VialTweeter and UP200St controller (Hielscher Ultrasonics). It was confirmed that this step effectively lysed cells without affecting the infectious virus titer (Figure A7.2). The treated sample was centrifuged at 2000g for 3 min and the supernatant with released virus was further processed. To determine extracellular vRNA levels, the crude cell sample was centrifuged at 2000g for 3 min and the cleared supernatant was further processed. The following protocol is similar for intracellular and extracellular vRNA quantification.

Virus particles in the supernatant were purified with the NucleoSpin RNA Virus kit (Macherey & Nagel) according to the manufacturer's instructions. A set of primers and probes specific for YFV and ZIKV were applied as listed in Table 3.9.

Table 3.9 | Primers and probes used for real-time RT–qPCR.

Target	Name	Sequence (5' → 3')	Source
YFV 5' UTR	YFV_F	GCTAATTGAGGTGCATTGGTCTGC	Domingo 2012 [207]
	YFV_R	CTGCTAATCGCTCAACGAACG	
	YFV_P	6-FAM-ATCGAGTTGCTAGGCAATAAACAC-TAMRA	
ZIKV E protein	ZIKV_F	CCGCTGCCCAACACAAG	Modified according to Lanciotti 2008 [208]
	ZIKV_R	CCACTAACGTTCTTTTGCAGACAT	
	ZIKV_P	6-FAM-AGCCTACCTTGACAAGCAGTCAGACACTCAA-BHQ-1	

Primers were obtained from Thermo Scientific and TaqMan-based probes from TIB Molbiol.

To determine vRNA concentrations, reference standards were generated by *in-vitro* transcription. Therefore, seed YFV and ZIKV^{RJ} genomic RNA were reverse transcribed using the RevertAidH Minus RT kit (Invitrogen) following manufacturer's instruction, and subsequently amplified using Phusion DNA Polymerase with primers containing restrictions sites for XbaI in the forward primer and BamHI in the reverse primer, respectively. PCR products were purified from agarose gels using the QIAquick gel extraction kit (Qiagen) and cloned into a pUC19 plasmid using a T4-DNA ligase (NEB). After plasmid transformation into competent *E. coli* DH5 α cells, positive clones were selected in a blue–white screening using isopropyl- β -D-thiogalactopyranosid (IPTG) and β -X-Gal and stored in glycerol stocks at -80°C . Plasmids were isolated using the InnuPrep Plasmid mini kit (Analytik Jena) and sequence integrity was confirmed by its PCR product (agarose gel migration distance and Sanger-based sequencing). A T7 promotor sequence was introduced to the forward primers of the reference RNA standards, subsequently amplified *in-vitro*, and transcribed with a TranscriptAid T7 High Yield Transcription kit (Thermo Scientific). Target RNAs were purified using NucleoSpin RNA Clean-up (Macherey & Nagel) and the concentration was determined by spectrophotometry (NanoQuant Infinity 200Pro, Tecan). Further details on the synthesize of *in-vitro* RNA copy numbers can be found in the SOP A7.2.3.

For the development of a RT–qPCR method, various kits based on SYBR Green I or TaqMan were tested for sensitivity and reproducibility. The TaqMan-based QuantiNova Probe RT–PCR kit (Qiagen) performed best (Table 3.10) and was used in further parts of this work [209]. First, a standard dilution series until 10^{-7} (ZIKV) or 10^{-8} (YFV) was prepared in PCR Eppi strips and stored at -80°C until use. The Master Mix was prepared in a total reaction volume of 10 μL according to the manufacturer's recommendations. Using a pipetting robot, 2 μL RNA virus sample was added with an accuracy of 5 % to 8 μL of the Master Mix in the RotorDisc 100 (Qiagen). No template controls (NTCs) and samples were measured as duplicates in 45 PCR cycles in the Rotor-Gene Q (Qiagen) following the manufacturer's instructions. Further details on the RT–qPCR protocol can be found in the SOP A7.2.2. Based on the known amplicon fragment lengths of 89 bp for YFV and 77 bp for ZIKV, the average mass of 340 Da/bp and known RNA copy numbers in the standard dilution series, the total vRNA copy number in the samples was calculated in accordance to Frensing *et al.* [210].

The TaqMan-based one-step assay had a sensitivity threshold value (C_t) of 37 (for NTC control) and a minimum quantification limit of 1.99×10^2 RNA molecules per reaction. Considering a ratio of 10^5 vRNA molecules per 1 infectious virion (PFU), the RT–qPCR assay is a more sensitive quantification assay than the plaque assay (limit of detection ≥ 1 PFU). The amplification efficiency

of the RT-qPCR was determined to 96 %. For the assay validation, a coefficient of variations of 4 % CV for YFV and 3 % CV for ZIKV was obtained. Further details on the validation are provided in a in-house bachelor thesis [209].

Table 3.10 | RT-qPCR kits with different principles were tested for the quantification of flavivirus RNA copy numbers. The AgPath-ID one-step kit had the highest sensitivity and was chosen for further studies [209].

Name	Provider	Steps	Principle
Rotor-Gene SYBR Green PCR Kit	Qiagen (204074)	Two-step	SYBR Green I
QuantiNova Probe RT-PCR Kit	Qiagen (208354)	One-step	SYBR Green I
AgPath-ID One-Step RT-PCR	Life Technologies (AM1005)	One-step	TaqMan
QuantiNova Probe RT-PCR Kit	Qiagen (208352)	One-step	TaqMan

3.11 Flow cytometric analysis of flavivirus-infected cells

YFV infection dynamics in trypsinized adherent and suspension cell cultures were followed by imaging flow cytometry. A total of 2×10^6 cells were fixed in 2 % (*w/v*) paraformaldehyde (PFA) in PBS and placed for 30 min at 4 °C. Cells were centrifuged at 300g for 10 min. The pellet was resuspended in 1 mL PBS and added to 4.5 mL ethanol (70 %) for long-term storage at -20 °C until use. The subsequent staining steps were performed on ice and centrifugation was performed at 300g for 10 min at 4 °C. First, cells were centrifuged and washed once in 4.5 mL fluorescence-activated cell sorting (FACS) buffer (2 % (*w/v*) glycine, 0.1 % (*w/v*) bovine serum albumin in PBS). The sample was then resuspended in 1.5 mL FACS buffer and split into two tubes. The sample was centrifuged and 25 µL blocking buffer was added to the cell pellet and incubated for 30 min at 37 °C. Cells were washed once with 1.5 mL FACS buffer, before 25 µL of the primary 4G2-mAB (2.4 ng/µL, 1:250 dilution of in-house stock solution of 600 ng/µL LOT160901) was supplemented and incubated for 30 min at 37 °C in the dark. The sample was washed once with 1.5 mL FACS buffer before 25 µL of the secondary Alexa Fluor 488 antibody (AB; diluted 1:1000 in FACS buffer) was added. The suspension was incubated for 30 min at 37 °C in the dark, washed twice with 1.5 mL FACS buffer and 4 µL DAPI 10X solution was added. Stained cells were measured with the ImageStream X Mark II (Amnis, EMD Millipore). A set of 10,000 single cells per sample were acquired with the 60-fold lens. The laser power for each channel (375 nm and 488 nm) was adjusted based on a feature that relates to intensity of pixels called 'raw max pixel'. The data analysis was performed with IDEAS software in accordance to Frensing *et al.* [210]. Further details are provided in SOP A7.2.4.

3.11.1 Production and purification of the 4G2 antibody

HB-4G2 cells secrete the unconjugated monoclonal antibody (IgG2a and/or IgG1) pan-flavivirus (4G2-mAB). The mAB is directed against the loop region in the second domain of the E protein. With each passage (section 3.1.1), two third of the cell broth was harvested and centrifuged at 5000g

for 5 min at RT. The supernatant was stored at $-20\text{ }^{\circ}\text{C}$. After four weeks, harvest batches were pooled and centrifuged at $10,000g$ for 5 min at $4\text{ }^{\circ}\text{C}$. The 4G2-mAB was purified with an Äkta Explorer 100 (GE Healthcare) and a protein A ligand (HiScreen MabSelect SuRe LX, GE Healthcare) with PBS as binding buffer and 4 mL 100 mM sodium citrate (pH 3.0) as elution buffer. The protein concentration was measured using the Qubit Protein Assay Kit (Thermo Scientific) and Mithras LB 940 (Berthold Technologies) following the manufacturer's instructions, and adjusted to $600\text{ ng}/\mu\text{L}$. The purified 4G2-mAB was aliquoted and stored at $-80\text{ }^{\circ}\text{C}$ until use.

3.12 Capacitance measurements

The β -dispersion was recorded from 0.3 to 10 MHz using the Incyte probe and the ArcView Controller 265 (both Hamilton). Data acquisition was performed every 6 min, a high signal integration was chosen and the pulse filter deactivated. Before inoculation, the frequency scan was set to zero in cell culture medium at $37\text{ }^{\circ}\text{C}$ and 100 % DO. When the bioreactor was inoculated, relative permittivity ε , media conductivity σ_0 , characteristic frequency f_c and the Cole–Cole α value were recorded. The data set was processed in Microsoft Excel.

3.12.1 Correlation and estimation of biomass

Offline data on viable cell concentration (X_c) and viable cell volume concentration (V_c) were correlated to online relative permittivity data by linear regression, multivariate data regression or by applying the Cole-Cole equation. To assess the quality of correlations with certain cell growth phases, the cultivations were separated into (i) cell growth phase, (ii) cell growth and virus infection phase, and (iii) decline phase. A data set of three EB66[®] ATF perfusion runs was used to evaluate three different biomass correlation models.

Linear regression A linear regression model was built using the Excel 2010 spreadsheet. Offline measured X_c and V_c data (described in Section 3.8.1; X_c was derived from triplicates, V_c derived from mean cell diameters of cell size distribution measurements with a total set of three times 100 images) was correlated to online data on $\Delta\varepsilon$. Respective correlation factors such as cell factor c_x and c_v (slope) and y-intercept n_x and n_v were calculated as:

$$\hat{X}_c = \Delta\varepsilon \cdot c_x + n_x \quad (21)$$

$$\hat{V}_c = \Delta\varepsilon \cdot c_v + n_v \quad (22)$$

The quality of linear fittings was assessed by the F-test ($P \leq 0.05$). Therefore, the sum of squared residuals was calculated for the X_c and V_c regressions that were normalized to the maximum relative permittivity value. The descriptive model precision was tested for $\Delta\varepsilon_{max}$ (permittivity decrease from 0.3 to 10 MHz) and $\Delta\varepsilon$ (permittivity drop from adjustable working frequency f_1 in the region of f_c ; here ~ 1 MHz, to 10 MHz as provided by the controller).

Multivariate regression analysis A multivariate data regressions model was built in OriginPro 2018 (vb9.5, OriginLab) and was based on partial least square (PLS) analysis. In total, 17 distinct frequencies of the frequency band (0.3 to 10 MHz) were used as unscaled independent variables (k) to calculate regression factors for three dependent variables \hat{X}_c , \hat{V}_c and average cell diameter (\hat{d}_c). Dependent variables were derived from offline measurements. To evaluate standard errors for an increased data set, dependent variables (offline measurements) were interpolated between sampling points in 6 min intervals. A truncated singular value decomposition (SVD) algorithm was applied. To avoid noise by overfitting, k factors were cross-validated and ranked for elimination to obtain the lowest root mean square error [211].

Cole-Cole model The Cole-Cole model (Equation 8) was used to estimate \hat{X}_c and \hat{V}_c based on online impedance measurement. The estimated average cell radius (\hat{r}_c) was calculated as:

$$\hat{r}_c = \frac{1}{2\pi \cdot f_c \cdot C_m \cdot (1/\sigma_i + 1/\sigma_0)} \quad (23)$$

with the assumption of constant C_m and σ_i values. Both parameters were calculated as follows:

$$C_m = \frac{4 \cdot \Delta\varepsilon}{9 \cdot r_c \cdot \varphi_c} \quad (24)$$

$$\sigma_i = \frac{8\pi \cdot f_c \cdot \Delta\varepsilon \cdot \sigma_0}{9 \cdot \varphi_c \cdot \sigma_0 - 4\pi \cdot f_c \cdot \Delta\varepsilon} \quad (25)$$

The static conductivity of the medium σ_0 was derived from the Bruggeman formula in Equation 4. To obtain the first data point, φ_v was assumed to be zero. Subsequent calculations were performed with a predictive biovolume fraction $\varphi_{v,p}$ derived from the previous measurement. As scans were performed every 6 min, changes in $\varphi_{v,p}$ were expected to be negligible (in accordance to Opel *et al.* [212]). The predicted biovolume fraction was calculated with \hat{r}_c and $\Delta\varepsilon$:

$$\varphi_{v,p} = \frac{4 \cdot \Delta\varepsilon}{9 \cdot \hat{r}_c \cdot C_m} \quad (26)$$

The \hat{X}_c was estimated from:

$$\hat{X}_c = \frac{\varphi_{v,p}}{100} \quad (27)$$

and the \hat{V}_c was estimated based on:

$$\hat{V}_c = \frac{\varphi_{v,p}}{\frac{4}{3} \cdot \pi \cdot \hat{r}_c} \quad (28)$$

Linear regressions, PLS models or Cole-Cole models were evaluated for X_c and V_c correlation by calculating the coefficient of determination (R^2) and root-mean-square standard error of calibration (RMSC) of the training set with normalized measured values $y_{i,n}$ and regression values $\hat{y}_{i,n}$ as:

$$\text{RMSC} = \sqrt{\frac{\sum_{i=1}^{n_s} (\hat{y}_{i,n} - y_{i,n})^2}{n_s}} \quad (29)$$

where n_s is the number of data points. RMSC was further expressed as normalized standard error of calibration (nSEC) as:

$$\text{nSEC} = \frac{\text{RMSC}}{y_{i,n,\max} - y_{i,n,\min}} \quad (30)$$

The root-mean-square standard error of transfer (SET) followed with the mean of the measured data set and was expressed in percentage in accordance to Opel and Konakovsky [212, 213]:

$$\text{SET} = \frac{\sqrt{\frac{\sum_{i=1}^{n_s} (\hat{y}_i - y_i)^2}{n_s}}}{y_{i,\max} - y_{i,\min}} \quad (31)$$

3.12.2 Calculation of dielectric parameters for virus dynamics

The Cole-Cole α parameter was recorded and correlated to the cell size heterogeneity of the culture. Thus, single cell diameters, as obtained from ViCell measurements in triplicates, were clustered (from 8.1-29.9 μm in 0.2 μm steps) and the cell size distribution was plotted. To evaluate the width of the cell size distribution, the full width at half maximum (FWHM) was calculated.

Parameters $\Delta\varepsilon$, f_c , and σ were provided in the raw data set of the biomass software. To observe virus-related changes in C_m and σ_i during the cultivation run, parameters were calculated with offline data (r and φ_c) following the Equations (24) and (25).

To increase the precision, cell diameters estimated for time points between sampling were interpolated by fittings with polynomial functions. Required V_c data for φ_c were derived from PLS models of the online $\Delta\varepsilon$ signal (see Chapter 3.12.1). This increased the resolution between sampling points.

Orthogonal capacitance measurements were performed with MDCK.SUS2 cells and IAV infection in Xeno medium. Cells were cultivated in 400 mL bioreactor systems (DasGip, Eppendorf) at 80 rpm with 40 % pO_2 and a pH set point of 7.00. The first cultivation was performed in batch mode. The second was performed as mock (uninfected control group treated as infected culture) where the working volume was doubled and 30 U/mL trypsin was added. The third run was infected with IAV H1N1 at MOI 10^{-3} .

3.13 Membrane testing

Commercial hollow fiber membranes (Table 3.11) were tested for filter fouling in unidirectional cross-flow filtration operation. Thereby, a constant permeate flow was set and virus titers, DNA and protein concentrations measured in the permeate stream.

Table 3.11 | Tested hollow fiber filter modules for filter fouling and virus retention in cross-flow operation.

Number	Material	Surface area * (cm ²)	Inner diameter (mm)	Number of fibers per module
1	mPES	20	0.5	6
2	mPES	15	0.7	3
3	PES	28	0.5	9
4	PES	13	1.0	2
5	PS	28	0.5	9
6	PS	50	1.4	5
7	ME	20	0.6	5
8	PE	45	7.3	1

Note: Details on pore sizes and suppliers are undisclosed due to confidentiality agreements.

* Surface area as stated by suppliers; mPES = modified polyethersulfone, PES = polyethersulfone, PS = polysulfone, ME = mixed ester, PE = polyethylene.

3.13.1 Pore size distributions

To determine pore size distributions, a single hollow fiber (50 mm length) was potted with a hot glue gun into a PE tubing (5 mm inner diameter, ID). The end of the filter was closed with glue and subsequently wetted with the pore-filling liquid fluorinert FC-43 (3M). The pore size distribution was measured with a Porolux 500 (Porometer).

3.13.2 Membrane surface charge

To determine the zeta potential of the inner membrane surface, a single hollow fiber (90 mm length) was potted in a PE tubing (80 mm length, 5 mm ID) filled completely with two-component epoxy

resin and dried overnight. Glued ends were cut and the potted membrane was mounted between clamping cells of a SurPASS electrokinetic analyzer (Anton Paar). The streaming potential of membranes was measured in a 5 mM KCl electrolyte solution at a pH of 7.2 (± 0.1). The zeta potential was calculated from the streaming potential via the Fairbrother–Mastin equation [214].

3.13.3 Cell broth zeta potential

The zeta potential of the cell broth was measured in triplicates using 1.5 mL samples filled in a folded capillary zeta cell using a the Zetasizer Nano ZS (Malvern Instruments). The basal cell growth medium (BGM) was measured as dispersant with a refractive index (RI) of 1.33, based on refractometry measurements (RE40D Refractometer, Mettler Toledo). A Smoluchowski approximation was used to calculate the zeta potential based on the electrophoretic mobility and the sample was measured 30 times at 25 °C in triplicates following manufacturer’s recommendations.

3.13.4 Scanning electron microscopy

Native and fouling membranes were either cut manually or frozen in liquid nitrogen before being broken manually. Membrane fractions were fixed with carbon conductive tapes and carbon paint (DAG-T-502, Ted Pella) on specimen mounts, and vacuum-dried at 30 °C overnight. A 10 nm chromium layer was sputtered on the sample with a Quorum Q150T ES (Quorum). The cross section and surface morphology of the membranes was obtained using a scanning electron microscope (SEM) (JSM-6010LA, JOEL) at 5 kV.

3.13.5 Filtration experiment

BHK-21_{SUS} cells were cultivated in a 2.5 L DasGip bioreactor (DR03C) connected to a DasGip DCU (Eppendorf). Cells were infected with YFV at MOI 10⁻¹. All membranes were pre-wetted with dH₂O, subsequently gently drained and connected to an external recirculation loop with a peristaltic pump (Watson-Marlow). The membranes were tested in cross-flow filtration mode at a fixed shear rate (γ) of 2000 s⁻¹. Volumetric flow rates \dot{V} (mL/min) were adjusted based on the cross-sectional areas of each module:

$$\dot{V} = \frac{f_n \cdot \pi \cdot r^3 \cdot \gamma}{4} \quad (32)$$

where f_n is the number of hollow fibers and r the inner fiber lumen radius (mm). The permeate pump was set to a surface-specific filtration rate J of 33 L/h/m². Inlet, outlet and permeate pressure were measured with inline single-use polysulfone pressure transducers (either TC or luer lock, ACPM-799-01N, Spectrum Labs). Transducers were connected to a digital pressure monitor (KrosFlo Digital Pressure Monitor, Spectrum Labs) or to the peristaltic pump (KR2i, Spectrum

Labs) with 5 s sampling by PC software (Excel sheet KF Comm Complaint Workbook with interface software package from Ofni Systems). The total resistance (R , in m^{-1}) was calculated using the Darcy equation:

$$R = \frac{\text{TMP}}{\eta_m \cdot J} \quad (33)$$

where TMP (mbar) is the transmembrane pressure, η_m (0.69 mPa s at 37 °C) the dynamic viscosity of the medium and J ($\text{L}/\text{h}/\text{m}^2$) the permeate flux. With inlet equal outlet pressure, TMP corresponds to the pressure difference between the feed and permeate stream. J describes the ratio of the permeate flow rate $\dot{V}_{\text{permeate}}$ (L/h) to the filtration surface area A_{filter} (m^2) as:

$$J = \frac{\dot{V}_{\text{permeate}}}{A_{\text{filter}}} \quad (34)$$

The dimensionless Reynolds number was calculated as:

$$Re = \frac{u \cdot d_i}{\nu} \quad (35)$$

with

$$u = \frac{\dot{V}}{f_n \cdot r^2 \cdot \pi} \quad (36)$$

where u (mm/s) is the velocity of the fluid to the membrane, d_i (mm) the inner fiber diameter, and ν ($0.7 \text{ mm}^2/\text{s}$ at 37 °C) the kinematic viscosity. Samples of the bioreactor vessel and the permeate line were regularly taken, optionally processed and stored at -80 °C until use.

3.13.6 DNA and protein quantification

Protein and double-stranded (ds) DNA concentrations were measured with the Bradford assay (in triplicates, following in-house SOP 2.4) and the PicoGreen assay (in duplicates, following in-house SOP 2.5), respectively. In brief, bioreactor and permeate samples were centrifuged at 2000g for 2 min at 4 °C. The supernatant was inactivated at 80 °C for 2 min and by overnight incubation with 0.5 % (v/v) formaldehyde at 4 °C. Protein samples were diluted in dH_2O and well mixed with Coomassie brilliant blue (Quick Start Bradford Protein Assay, Bio Rad) in transparent flat bottom 96-well microtiter plates. The maximum of the absorption spectrum was measured at 595 nm (InfiniteM 200 PRO). For dsDNA quantification, PicoGreen dye (Quant-iT PicoGreen dsDNA Assay Kit, Thermo Scientific) was added to the sample and mixed well. Subsequently, samples were excited at 480 nm and the fluorescence emission intensity measured at 520 nm (InfiniteM 200 PRO). A standard solution was prepared from lambda DNA (D1501, Promega).

The rejection coefficient σ_{reject} was introduced to describe the fraction of retained product by the membrane and was calculated as:

$$\sigma_{reject} = 1 - \frac{C_p}{C_v} \quad (37)$$

where C_p ($\mu\text{g/mL}$) is the YFV, DNA or protein concentration in the permeate flow, respectively, and C_v ($\mu\text{g/mL}$) the concentration in the bioreactor.

4 Results and Discussion

The following chapter is divided into six parts following the progress made in flavivirus production and intensification. The first sections are devoted to YFV production and process intensification using adherent Vero cells, BHK-21_{SUS} and EB66[®] suspension cells. The knowledge gained is then applied for establishment of ZIKV production in suspension cells. The last two sections have a technical focus and are concerned about the use of an online biomass probe and different commercial hollow fiber membranes for perfusion operation.

4.1 Yellow fever virus production with adherent Vero cells

Adherent Vero cells are a well-known cell substrate suitable for the propagation of various viruses. In the following, their applicability for YFV production was examined and potential scale-up options were investigated.

4.1.1 Virus replication and scale-up into bioreactors

First, a working virus seed was generated from egg-derived YFV-17D virus material. The lyophilized virus was reconstituted in PBS and used to infect 90 % confluent Vero cells in four tissue culture flasks (each 175 cm² surface). The cell supernatant was collected 96 hpi and stored at -80 °C. Pooled virus harvests had a titer of 2.1×10⁸ PFU/mL. The virus seed was used for all infection studies of Vero cells in tissue culture flask and microcarrier-based bioreactor cultivations. Cells grew in serum-containing Z-Medium and experiments were performed as described in sections 3.5 and 3.7, respectively.

Tissue culture flask cultivations Vero cells were cultivated in tissue culture flasks (25 cm²) until 90 % confluency was reached (based on visual inspection of surface area). Cells were then infected with an MOI 2×10⁻²¹. Infected cells continued growing and maintained high viabilities for 5 days

¹ Note: Calculated MOI and measured MOI at time point of infection (toi) can vary by a factor of 5 to 10 due to virus inactivation after seed virus thawing. As a means for comparability, hereinafter MOIs are referred to as MOIs measured at toi if not stated otherwise.

(based on trypan blue exclusion). Then, cells started to detach, and viabilities strongly decreased. In parallel, the virus titer in the supernatant was measured. During the first 24 hpi, YFV titers dropped slightly and then increased to peaking titers of 1.9×10^7 PFU/mL after 96 hpi (Figure 4.1 A). In total, a maximum cell-specific virus yield of 11.9 PFU/cell was obtained (Table 4.1).

Microcarrier cultivations Static cultivations performed in tissue culture flasks and other cultivation systems have limited options for full process monitoring and control. Thus, a scalable production process was evaluated using Cytodex-1 microcarriers in quasi-suspension maintained in spinner flasks and in controlled bioreactor systems (Chapter 3.5). First, cells were inoculated to a spinner flask at a seeding concentration of 29 cells/MC in Z-Medium (ratio chosen based on fast adhesion kinetics described by Bock for Vero cells [215]). When cells reached a cell concentration of 1×10^6 cells/mL, cells were infected with YFV at $\text{MOI } 4 \times 10^{-2}$. Cells continued growing until full confluency. Finally, a virus titer of 8×10^6 PFU/mL was achieved resulting in a cell-specific virus yield of 3.6 PFU/cell (Figure 4.1 B, Table 4.1). During the cultivation, the pH value decreased constantly to 6.9 known to be suboptimal for YFV production (not shown here). To maintain pH values of 7.2, the process was transferred to a 1 L stirred-tank bioreactor vessel. With the typical impeller configuration for suspension cells, it required high stirrer speeds to maintain confluent microcarriers in quasi-suspension. However, the resulting, high shear stress on cells and carriers led to poor cell growth and microcarrier damage. Hence, the stirrer unit was adjusted by mounting two segment impellers in bidirectional axial flow direction. As a result, confluent microcarriers were kept in quasi-suspension and intact at stirrer speeds of only 60 rpm. Cells grew at controlled pH and $p\text{O}_2$ conditions to a final concentration of 1.7×10^6 cells/mL (Figure 4.1 C). YFV titers reached 2×10^7 PFU/mL resulting in a cell-specific titer of 10.8 PFU/cell. Based on the microcarrier surface area (as specified by the manufacturer), maximum surface-specific cell concentrations (cell saturation density) decreased from 7.2×10^5 cells/cm² in tissue culture flasks to 1.3×10^5 cells/cm² in stirred-tank bioreactors indicating lower cell growth on available surface, either due to morphological changes (i.e. reduced height and larger area to keep similar cell volume at higher shear conditions) or due to simple overestimation of available surface area as stated by the manufacturer (Table 4.1).

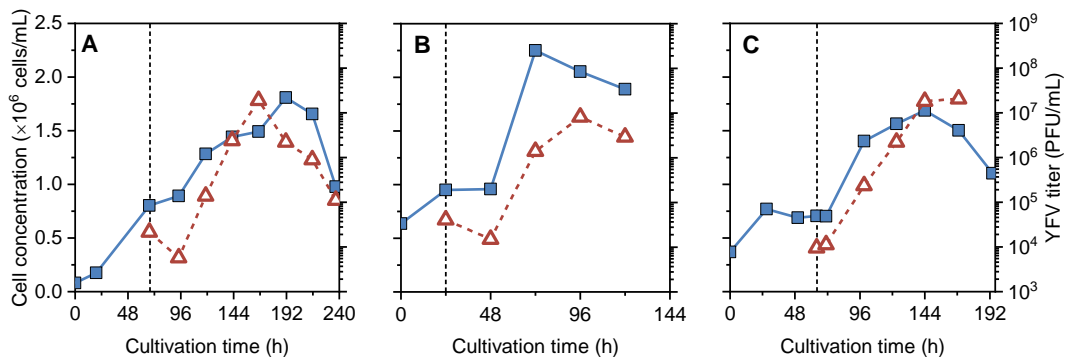


Figure 4.1 | Yellow fever virus production in adherent Vero cells at different scales. Viable Vero cell concentration (blue square) and infectious YFV titer (red triangle) in (A) tissue culture flasks with a surface of 25 cm², (B) in spinner flasks with 3 g/L Cytodex-1 microcarriers, and (C) in controlled bioreactors with 3 g/L Cytodex-1 microcarriers. Dotted vertical line indicates time point of infection.

Table 4.1 | Process results from yellow fever virus production in adherent Vero cells at different scales.

Scale	Viabl. Cell conc. ($\times 10^6$ cells/mL)	Surface-spec. VCC ($\times 10^5$ cells/cm ²)	Maximum YFV titer ($\times 10^7$ PFU/mL)	Cell-spec. virus yield (PFU/cell) *
T-flask ^a	1.8	7.2	1.9	11.9
Spinner with MC ^b	2.2	1.7	0.8	3.6
Bioreactor with MC ^b	1.7	1.3	1.8	10.8

VCC = viable cell concentration; surface-specific viable cell concentration is calculated with surface areas as provided by manufacturer: ^a 25 cm² surface area; ^b 3 g/L microcarrier concentration; * calculated according to maximum cell concentration until time point of highest virus titer (see Equation 18).

Bead-to-bead transfer Major constraints of microcarrier-based cultivations emerge when mechanical or enzymatic treatment is required to harvest confluent cells for the transfer into larger scales. Hence, a direct bead-to-bead transfer was investigated for Vero cells in Z-Medium. Previous inoculation experiments with 29 cells/MC revealed a ratio to colonize sufficient all microcarriers. After 72 h, empty microcarriers were added to the near confluent ones (103±38 cells/MC). To facilitate direct bead-to-bead contact, agitation was periodically stopped, i.e., 5 min agitation and 25 min static incubation. The cell spreading was monitored for the next 96 h (Figure 4.2). Within 2 h, first cells were already found on newly added microcarriers and 18 h later, microcarriers attached to each other by formation of cell bridging in quasi-suspension. After 96 h, all microcarriers became near to confluency and first cells started to detach.

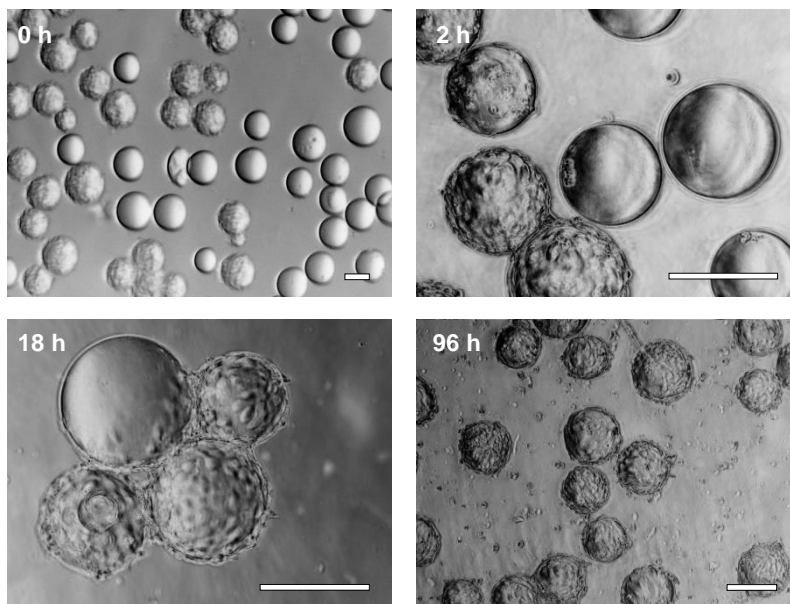


Figure 4.2 | Evaluation of bead-to-bead transfer for the scale-up of Vero cells on Cytodex-1 microcarriers. Vero cells grew on microcarriers (3 g/L) in Z-Medium and reached near confluency 72 h after inoculation. Empty microcarriers (1.5 g/L) were added and agitation was periodically stopped (time point 0 h). Cells started to spread to newly added microcarriers until all beads showed full confluency (96 h). Scale bar indicates 150 μ m.

Discussion First infection experiments confirmed that Vero cells are permissive for YFV. Shortly after infection, virus titers in the supernatant decreased, presumably due to virus adsorption to the cell and entry. After one day, extracellular titers increased indicating a slow virus replication of about 24 h. Finally, infectious titers peaked around 3-5 days post infection and decreased afterwards. Thereby, cell viabilities remained high over extended periods after infection and eventually decreased. This is consistent with general observations of YFV, which is considered to be a (slow) lytic virus. Flaviviruses are known to trigger cell survival as well as cell death via many signaling pathways leading to apoptosis, necrosis and autophagy. Unlike lytic viruses, flaviviruses can lose their ability to induce apoptosis in certain cells by inhibiting the type I interferon (IFN-I) signaling pathway [216, 217]. This may play only a minor role here, as Vero cells are known to be resistant to antiproliferative effects of IFN [218]. In the case of other cells, this strategy may be beneficial from the evolutionary perspective of the virus as infected cells are temporarily spared, which allows longer time periods of replication and enhanced viral yields. Overall, *in-vitro* experiments with Vero cells resulted in only low infectious virus titers of about 10 infectious virions per cell (PFU/cell) in agreement with reports from other workgroups (RKI Berlin, Prof. Niedrig; UFRJ, Prof. Tanuri) and industry (Valneva, Dr. Léon). The controlled bioreactor set-up enabled stable pH control at 7.2 known to be optimal for ZIKV replication [219]. In contrast, headspace aeration, as present for spinner flasks, was not sufficient to maintain preferred pH values in Z-Medium, potentially inactivating YFV titers at pH 6.8 and explaining the low infectious titers [220].

During the scale-up from tissue culture flasks to microcarrier cultivations, surface-specific cell concentrations decreased strongly by a factor of 5. This implies that nominal surface areas (as given by the manufacturer) may either not match to real surface available for cell growth or that morphological changes reduced cell saturation densities. In general, herein reached cell concentrations of approximately 6×10^5 cells/g_{MC} and cell concentrations are in good agreement with published data [221, 222]. Interestingly, cell concentrations on microcarrier beads reached a plateau at about 24 h after inoculation. This is typically observed during the so-called ‘cell adhesion phase’ between 0-24 h [205]. Attached cells quickly increase in cell diameter before cells start dividing into daughter cells with smaller diameters [223]. This finding can be confirmed by online cell volume data and is further elaborated in section 4.1.2. The bead-to-bead transfer is an attractive solution for the scale-up process [224]. Fortunately, Vero cells in Z-Medium successfully transferred to newly added beads after intermittent agitation. This enabled a direct cell expansion to the next process scale. However, it also results in very unsynchronized cell stages, where the parental cell is typically surface-limited and may undergo cell apoptosis, while daughter cells on empty microcarriers still divide. The function of formerly colonized microcarriers and resulting available surface area remains questionable. This may also explain that most manufacturers harvest the cell seed inoculum from static multilayer cultivations.

Previous attempts for inactivated YFV-17D and 17DD vaccine production with Vero cells on microcarrier beads were reported by Xcellerex (US) and Fiocruz (Brazil), respectively [8, 9]. In both studies, virus titers exceeded 10^8 PFU/mL. Certain details on process conditions revealed an increase in infectious titers by the use of serum-free virus production media and medium exchanges during YFV production phases. Therefore, similar strategies, i.e. biphasic process for optimum cell growth and virus production, serum-free media screening, medium exchange before infection, temperature decrease, optimized MOI and time point of infection (toi) optimization, can be considered equally. In addition, further process intensification strategies can be envisaged to increase cell

numbers by higher microcarrier concentrations (limited by bead collisions [7]) or the use of fixed-bed bioreactors in combination with perfusion modules [7]. However, adherent cells will always have limitations in scale-up eventually reducing the interest to change current egg-based production processes. Alternatively, suspension cells enable the establishment of various process intensification strategies with an easy transferability into manufacturing scale. Hence, the future focus should be on suspension cells in comparison to the Vero cell-based production process as reference standard.

4.1.2 Turbidity and capacitance measurements

Microcarrier-based cultivations remain difficult to characterize, e.g., as beads in bioreactors are not necessarily homogeneously distributed complicating manual sampling and cell quantification requires error prone pipetting and trypsinization steps. Hence, online turbidity and capacitance measurements were tested for the quantification of microcarriers and for the quantification of biomass. This section addresses briefly the specific use of online probes for quantifying adherent cells. Further in-depth experiments addressing the capacitance probe for suspension cells are described in section 4.5.

Turbidity During the consecutive addition of microcarriers, a Dencytee probe measured the turbidity at 880 nm. The signal increased abruptly with the addition of empty microcarriers and leveled off at elevated signal levels (Figure 4.3 A). Stable turbidity signals were correlated to the added microcarrier concentration and a linear regression was applied in the range of herein tested 3.1 g/L (Figure 4.3 B). In a second approach, the Vero cell inoculum was added to empty microcarriers in a bioreactor and the turbidity was recorded. After a sharp signal increase, the supernatant cleared while free cells in suspension decreased due to cell attachment to carriers. The lowest turbidity was obtained at around 10 h after inoculation and the value started to increase again (Figure A7.1).

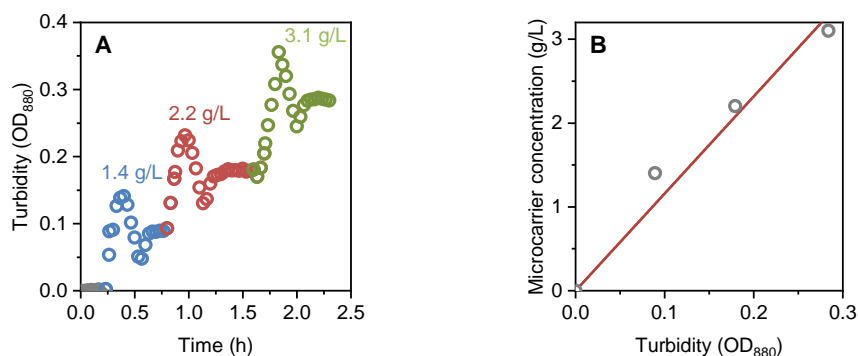


Figure 4.3 | Time course of turbidity measurement after Cytodex-1 microcarrier addition in stirred tank bioreactors. (A) Turbidity increase at OD₈₈₀ after consecutive addition of microcarriers to the bioreactor vessel (filled with Z-Medium and at standard cultivation conditions without cells). Colored symbols indicate microcarrier concentration (blue = 1.4 g/L, red = 2.2 g/L, green = 3.1 g/L) **(B)** Linear correlation of microcarrier concentration to the averaged plateau of the turbidity signal after each addition.

Capacitance To estimate the biomass, the capacitance signal was recorded and processed as described for various microcarrier cultivations. Exemplarily shown in Figure 4.4, Vero cells were grown on 3 g/L Cytodex-1 microcarriers and infected with YFV. The capacitance signal was correlated by linear regression to offline ViCell data on the overall viable cell concentration² (attached cells and cells in suspension excluding the plateau at 7×10^5 cells/mL, Figure 4.4). Interestingly, the online signal for biomass did not follow the plateau phase in cell concentrations. Eventually, differences occurred during the cell decline phase.

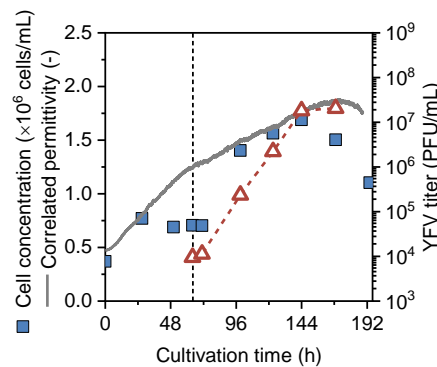


Figure 4.4 | Time course of capacitance measurement during Vero cell growth on Cytodex-1 microcarriers. Vero cell concentrations were determined with ViCell measurements (blue square). The online capacitance signal (grey line, processed by linear correlation to offline data) indicated a constant biomass increase. Dotted vertical line indicates time point of infection with YFV.

Discussion Previous cumbersome and error-prone methods for cell counting methods for microcarrier cultivations may be replaced by using online measurement probes. The turbidity and capacitance probe can provide useful information on microcarrier concentrations and cell growth of microcarrier-based cultivations. First, the turbidity probe was implemented in the bioreactor and the signal was related to offline measured microcarrier concentrations. However, the linear correlation requires further confirmation by smaller microcarrier additions. Furthermore, the probe required about 30 min to achieve a stable turbidity signal, which may be shortened by lowering smoothing settings. The principle remains promising for future microcarrier cultivations as the exact microcarrier concentration is required for cell seed inoculation preparation and adjustment of cell/MC ratios. In addition, the turbidity probe enabled to monitor cell attachment kinetics to microcarriers. This was confirmed in continuing studies using fixed-bed bioreactor systems at the MPI [128]. The turbidity signal decreased during the cell adhesion phase, which correlated well with offline measured cell concentrations in the supernatant. The online probe can be used to gain important information on cell attachment, but also indicates cell death-related turbidity increases, either by virus-related lysis or substrate limitations.

² Note: Cell volumes cannot be determined from ViCell measurements of microcarrier cultivations. Required incubation times for trypsinization of adherent cells affected cell sizes, as observed by comparing cell sizes of mechanical or enzymatically detached Vero cells from tissue culture flasks. Incubation times above 5 min resulted in cell volumes increases of up to 40 %, in particular for small cells derived from nearly confluent conditions (data not shown here).

The capacitance signal was used successfully to monitor cell growth on microcarriers. A discrepancy between online (biovolume with Incyte probe) and offline data (cell concentration with ViCell), especially after the cell adhesion phase, was noticed. Both data sets were not directly comparable as manual cell counting required trypsinization so that information on cell volumes typically altered. Thus, accurate cell volume measurements of attached cells proved to be difficult with existing offline methods. The discrepancy may be explained by the typical scheme of adherent cell growth: Inoculated cells attach randomly on beads, first expand in cell volume, and then in cell number (cell division) [205]. Finally, another discrepancy between both principles arose during the cell decline phase potentially derive from the cell viability determination. While ViCell measurements are based on trypan blue exclusion in binary mode (viable or dead), the capacitance probe determines viable cells through intact membranes for ion polarization in gradual mode. This impedes general comparability, whereas the decline phase plays in general a minor role for the process outcome.

Overall, the capacitance probe can be used for biomass estimation of microcarrier cultivations. Interestingly, it revealed a constant cell growth in biomass, while the cell concentration remained constant. In dependence of the variable, such online probe can be the preferred choice of quantification method for cell growth. The infection with YFV did not interfere with the online signal (see section 4.5.2) and can be more robust than alternative indirect strategies based on, e.g., metabolite or oxygen consumption rates [131, 225]. The applicability of biomass probes has been also demonstrated elsewhere and can be further used to standardize future cultivations [148, 149, 226]. Therefore, it might be useful to rethink current process standards such as MOI and to transfer it to biovolume-specific yields and rates. Furthermore, the technology can be transferred to fixed-bed bioreactor systems, which do not allow direct carrier sampling, as being currently under investigation at the MPI (data not shown) [128].

4.1.3 Towards suspension-adapted Vero cells

Process scale-up and intensification is significantly facilitated with suspension cells in large-scale manufacturing. Since adherent Vero cells are a good producer cell line for many viral vaccines, it would be desirable to adapt this cell line to growth in suspension cells for production. Therefore, attempts were made to sequentially adapt adherent Vero cells to suspension and serum-free or chemically defined medium by (i) continuous passaging and (ii) super-confluency state cultivation into sequentially “conditioned medium” (Chapter 3.1.5). Hereby, conditioned medium was derived from a stepwise conversion from Z-Medium to the desired medium and a fixed volume of 10 % of the medium the cells have been growing in for one full passage.

Regarding the first strategy, cells were split into the next level of adaptation and additionally kept as a fall-back at each prior condition. Despite multiple repetitive cultivations at certain levels, SMIF8 medium was the only suitable medium that facilitated VeroSUS cell growth in static conditions. The adaptation process required 20 days until cells grew in 100 % SMIF8 medium with a population doubling time (t_D) of about 80 h. When cells were subsequently transferred to shaken or stirred cultivation systems, they formed strong cell agglomerates that made stable cell maintenance difficult over an extended time period.

For the second adaptation approach, adherent Vero cells were maintained in the same tissue culture flask, while the medium was sequentially exchanged to the desired medium. After 60 days, cells in CD-U3, BGM or SMIF8 medium started to release into the supernatant (exemplarily shown for SMIF8 medium in Figure 4.5). Due to low cell viabilities in the supernatant (illustrated by cell release kinetics in Figure A7.3), viable cells were collected by centrifugation (Figure 4.5 C). This strategy resulted in growth of VeroSUS cells and enabled continuous cell harvesting from tissue culture flasks for about 12 months. Nevertheless the transfer to shaken or stirred cultivation systems remained challenging. Also here, the cell line showed strong clumping tendencies in all media and cells formed deposits rings on the glass wall at the interface to the headspace. Various additives (e.g. zinc, dextran, growth factors, dispersants, shear protectants) were tested to improve growth performance and ease of cell line handling. Finally, a medium mixture of BGM and SMIF8 (1:1) was identified suitable for pendulum stirrer cultivations achieving 2.9×10^6 cells/mL with a t_D of about 50 h. Infection studies with YFV resulted in marginal virus titers and cell-specific virus yields were below 0.1 PFU/cell (Figure 4.6 A).

Subsequent cell adaptation of VeroSUS cells from SMIF8 medium to Xeno medium [227] was performed by sequential adaptation. The obtained cell line had a similar growth performance, but reduced clumping behavior. This enabled more stable cell maintenance in shake flask cultivations reaching around 3.0×10^6 cells/mL with a t_D of about 48 h. Infected with YFV, titers of 1.1×10^7 PFU/mL and a cell-specific virus yield of 3.3 PFU/cell were obtained (Figure 4.6 B).

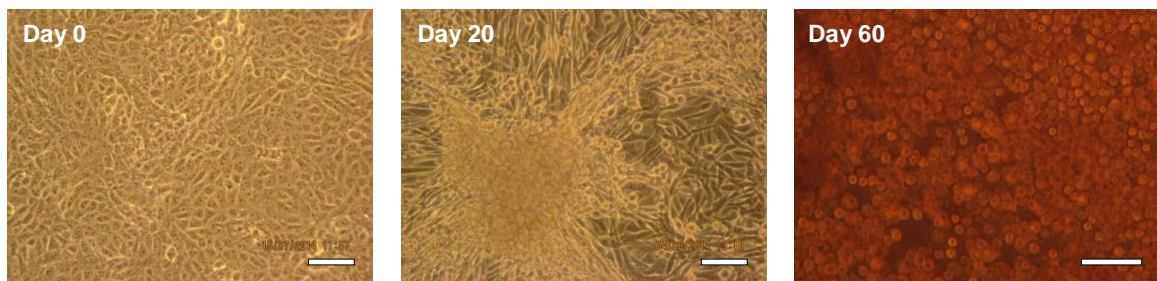


Figure 4.5 | Adherent Vero cell adaptation to suspension growth in SMIF8 medium. (Left) Confluent Vero cells were maintained in a tissue culture flask and the medium was stepwise exchanged to SMIF8 medium. (Middle) After 20 days, multilayers were formed. After two months, cells began to detach and bud into the supernatant. (Right) Suspension cells were regularly collected, concentrated and cultivated in pendulum spinners with BGM/SMIF8 medium (here at day 60).

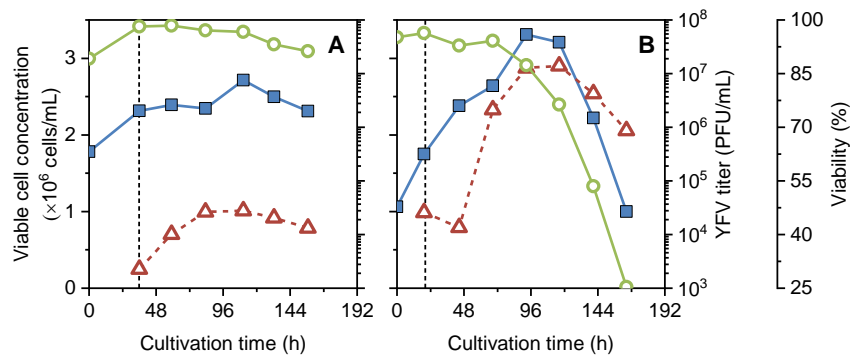


Figure 4.6 | Yellow fever virus production using Verosus cells in spinner and shake flasks. Verosus cells (blue square) were cultivated in (A) pendulum spinners and BGM/SMIF8 medium, and in (B) shake flasks and Xeno medium. Cells were infected with YFV (red triangle) and viabilities (green circle) were monitored. Dotted vertical line indicates time point of infection.

Discussion The adaptation of adherent Vero cells to suspension was a very cumbersome and labor-intensive process. Based on a super-confluency adaptation strategy [202], it was possible to adapt Vero cells to various media. While, CD-U3 medium and BGM did not promote suspension cell growth, BGM/SMIF8 and Xeno media were identified as suitable growth media. Overall, only a poor t_D of 48 h or higher were observed. This may be related to the super-confluency adaptation strategy minimizing evolutionary pressure for fast cell growth. While parental cells remained in confluent state for months, daughter cells released into the supernatant. This may have resulted in the generation of slow/non-growing suspension cells.

Adapted Verosus cells were found to be very sensitive to medium depletion and, in parts, showed a high tendency for cell clumping. Finally, the poor cell recovery rate of frozen cell stocks made the maintenance of this cell line in both media a challenge. Nevertheless, cell concentrations achieved are in agreement with data presented at recent conferences from the National Research Council of Canada and Institute Pasteur Tunis reporting similar Verosus cell concentrations of $2\text{--}3 \times 10^6$ cells/mL in stirred-tank bioreactors [104, 105]. Beyond cell concentrations, most critical is the permissiveness to allow high YFV titers. As the use of the newly generated Vero suspension cell line resulted in lower cell-specific virus yields than the parental adherent Vero cell, it may require further infection optimization only achievable with a more robust suspension cell line. Indications are given to aim for a producer cell line showing good growth rates and in the exponential cell growth phase during infection (further elaborated for suspension cells in Chapter 4.2).

Reasons for the weak adaptability to suspension growth of adapted cells remain unclear. Ideally, a cell population comprises a high genetic diversity to allow successful adaptation to new cultivation conditions. The genetic pool of available Vero cell lines may be restricted. Either cells may have never contained a suppressed anchorage-independent phenotype or may have lost it during intense cell passaging at adherent conditions. Nevertheless, the success of Verosus cell adaptation in various laboratories to date give hope that the generation of a fast growing cell line may be feasibly, in case future media optimization is possible.

4.1.4 Summary

The adherent Vero cell is a well-established cell substrate for human and veterinary viral vaccine production [228]. In this section, the general use of adherent Vero cells for YFV replication was tested. First infection experiments proved the permissiveness of Vero cells with a maximum cell-specific virus yields of about 10 PFU/cell. The low yield underpins the importance for process intensification and high cell concentration required for manufacturing of live-attenuated YFV vaccines. To investigate scale-up options, quasi-suspension microcarrier cultivations were performed. Thereby, larger surfaces of Cytodex-1 microcarriers were poorly exploited due to reduced cell saturation density (cell number per surface) in comparison to simple tissue culture flasks. Nevertheless, similar cell-specific virus yields could be maintained in bioreactor cultivations with pH control. Interestingly, Vero cells in Z-Medium enabled a direct bead-to-bead transfer, which can simplify the transfer to larger process scales. From an analytical perspective, enzymatic treatment for cell harvesting and accurate cell counting was challenging. Additionally, information on cell volumes was lost during typical trypsinization periods. In consequence, online probes were investigated for monitoring of microcarrier cultivations. Turbidity measurements enabled estimation of microcarrier concentrations in well-mixed bioreactors and monitoring of cellular attachment dynamics. Use of a capacitance probe allowed to estimate cell growth on microcarriers, whereas discrepancies between biomass and offline cell count measurements arose. To avoid scale-up challenges with adherent Vero cells and to implement intensification strategies, the Vero cell was adapted to suspension growth in BGM/SMIF8 and Xeno medium over two months. Unfortunately, on top of the demanding cell line maintenance, cell-specific virus yields decreased to 3.3 PFU/cell with the tested media.

4.2 Yellow fever virus propagation in suspension cells

Current approaches to use Vero cells for vaccine production pose major challenges for large-scale manufacturing, and Vero_{SUS} cells are difficult to maintain in culture. The following sections address the use of alternative suspension cell lines for YFV production. Finally, various assays and methods were applied to gain a better understanding on flavivirus replication and spreading in shake flask cultivations.

4.2.1 Alternative cell substrates

In the early phase of process development, alternative cells with anchorage-independent growth properties were screened for efficient YFV replication. The permissiveness was evaluated on the basis of infectious virus titers in the cell supernatant and cell-specific virus yields. While the Vero_{SUS} cell showed a reduced cell-specific virus yield in comparison to its parental cell line, a comparative study was performed with BHK-21 cells. The adaptation and generation of the BHK-21_{SUS} cell was performed in-house and is described in detail elsewhere [229]. Subsequent

infection experiments revealed a similar viral productivity of about 11.3 PFU/cell compared to the adherent BHK-21 cell in Z-Medium (Table 4.2). To investigate the repeatability of maximum virus titers in dependency of the cell passage, BHK-21_{SUS} cells were infected in triplicates and monitored over 40 cell passages following the same infection protocol. Interestingly, when infecting cells above passage 18, cell concentrations and viabilities were kept high for an extended period. Thereby, viral titers decreased slightly below the standard deviation, but returned to initial values at passage 40 (Figure A7.4). During infection experiments with other suspension cell lines, EB66[®], MDCK.SUS2, CR[®] and CR.pIX[®] cells were proven to be susceptible for YFV, but only low viral titers (<2PFU/cell) were obtained in the supernatant (Table 4.2).

Table 4.2 | Overview on screened cell substrates for yellow fever virus production.

Growth	Cell substrate	MOI *	VCC †	YFV titer (PFU/mL)	CSVY ‡ (PFU/cell)
Adherent	Vero	0.03	7.2×10 ⁵ cells/cm ²	1.9×10 ⁷	11.9
	BHK-21	0.03	8.3×10 ⁵ cells/cm ²	2.5×10 ⁷	11.5
Suspension	Verosus (Smif/BGM)	0.001	2.7×10 ⁶ cells/mL	2.8×10 ⁴	<0.1
	Verosus (Xeno)	0.01	3.3×10 ⁶ cells/mL	1.1×10 ⁷	3.3
	BHK-21 _{SUS}	0.02	4.2×10 ⁶ cells/mL	4.8×10 ⁷	11.3
	EB66 [®]	0.001	1.5×10 ⁶ cells/mL	1.8×10 ⁷	1.2
	MDCK.SUS2	0.05	4.3×10 ⁶ cells/mL	5.6×10 ⁶	1.3
	CR [®]	0.001	3.2×10 ⁶ cells/mL	3.2×10 ⁵	<0.1
	CR.pIX [®]	0.01	7.3×10 ⁷ cells/mL	5.1×10 ⁶	0.7

* MOI relates to measured MOI; † maximum viable cell concentration obtained until time point of highest virus titer; ‡ CSVY = cell-specific virus yield, calculated according to Equation 18.

Note: seed virus material derived from adherent Vero cells

From these first results, the adaptation of the virus to the cell line was evaluated by sequential virus passaging. The seed virus strain was sub-cultured and maintained for multiple passages in BHK-21_{SUS}, EB66[®] and MDCK.SUS2 cells (Figure 4.7). Unfortunately, the virus cleared out in CR[®] and CR.pIX[®] cells due to the low cell-specific virus yield and, most likely, non-optimized MOI conditions. YFV titers in BHK-21_{SUS} cells reached maximum titers of 1.4×10⁸ PFU/mL already in the first passage and cell-specific titers of 15 PFU/cell were achieved. In contrast, virus titers in EB66[®] cells increased over 4-5 passages by one log, exceeding 1.0×10⁸ PFU/mL, and the time to reach maximum titers decreased from 4 to 2 days (Figure 4.7 B). Thereby, an increased cell-specific virus titer of 10 PFU/cell was achieved (Figure A7.5 A). Closer investigation with RT-qPCR determined viral RNA (vRNA) copy numbers correlated with maximum virus titers in the supernatant. The ratio of PFU to vRNA expressed the infectivity, which slightly increased from 0.03 % to 0.05 % (Figure A7.5 B, C). In MDCK.SUS2 cells, titers increased over the time course of virus adaptation to maximum yields of about 2.9×10⁷ PFU/mL corresponding to 2 PFU/cell (Figure 4.7 C). The work with MDCK.SUS2 cells was then discontinued. A rapid decline of infectious virus titers was observed in all approaches. A subsequent experiment with YFV spiked into CDM4Avian medium (without cells) revealed fast inactivation kinetics at higher temperature with half-life times as short as 11 h at 37 °C, 20 h at 33 °C and 63 h at 4 °C (Figure A7.6).

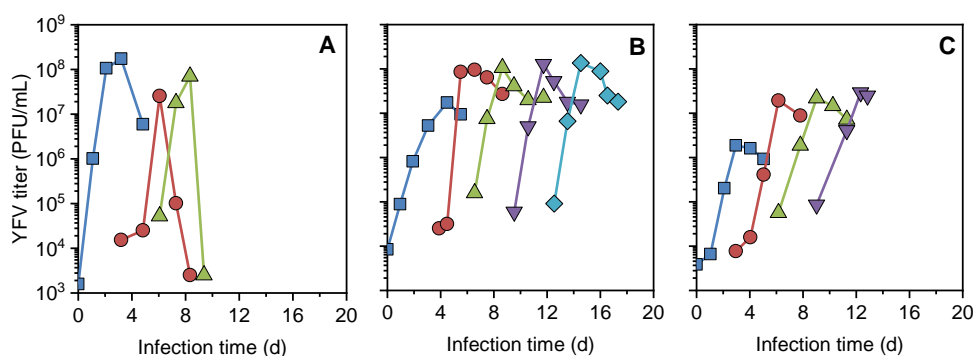


Figure 4.7 | Infectious virus titers during sequential passaging of yellow fever virus in different suspension cell lines. BHK-21_{SUS}, EB66[®] and MDCK.SUS2 cells were cultivated in shake flasks in BGM, CDM4Avian and Xeno medium, respectively. Cells were infected in the mid exponential growth phase at a targeted MOI of 0.01. Subsequent virus passaging was performed blindly 72 hpi and 48 hpi. Infectious virus titers achieved in (A) BHK-21_{SUS}, (B) EB66[®] and (C) MDCK.SUS2 cells. Time scale refers to continuous virus passaging. Each virus passage is indicated by a different color (blue = p1, red = p2, green = p3, purple = p4, turquoise = p5).

Discussion While the Vero cell-derived YFV seed material propagated well in BHK-21_{SUS} cells, YFV had to be first adapted over five passages to the EB66[®] cell substrate to obtain cell-specific titers similar to BHK-21_{SUS} cells. Especially with the excellent cell growth properties in batch mode (BHK-21_{SUS}: 7×10^6 cells/mL, t_D of 21 h; EB66[®]: 1.5×10^7 cells/mL, t_D of 14-19 h; Figure A7.7) both suspension cell lines were qualified for virus production. The virus production repeatability was further studied for BHK-21_{SUS} cells for 40 passages. Interestingly, cells above 18 passages showed a higher “resistance” with a higher viability against YFV infection. Further studies are required to investigate this cell age-dependent observation. Potentially, this may be associated to decreased virus titers at passage 18 until passage 30. If this observation holds true, certain passage restrictions may be considered for future process development.

The BHK cell is classified as tumorigenic [111] and therefore its use as substrate for live-attenuated human vaccines is controversial. Nevertheless, BHK-21_{SUS} cells can be used to scout flavivirus production in intensified production systems, i.e. high cell density perfusion cultivation. In addition, BHK cells may be used for the generation of virus material for virological studies. In contrast, EB66[®] cells have a good safety profile and were thoroughly characterized by the supplier [118]. Currently, EB66[®] cells are used for veterinary vaccine production but manufacturing of human vaccines is considered. As a result, taking these restrictions into account, both cell lines are well suited to large-scale manufacturing offering various options for process intensification, i.e. perfusion cultivations. Process intensification becomes even more important for viral vaccine production of low-yield viruses such as YFV. The high thermo-lability of YFV is a significant operational challenge regarding direct virus harvesting and post-processing.

The general adaptation mechanism for YFV to host cells is largely unknown and can occur on several levels affecting all steps in the virus replication cycle. RNA viruses have a generally high nucleotide mutation frequency. When the virions replicate, population variations arise around the consensus sequence of the population. Certain mutations are potentially beneficial and alter the

viral fitness (i.e. the relative ability to generate infectious progeny virions) [230]. To investigate adaptation-related changes at a genomic level, complementary *de-novo* virus sequencing is required [231]. Recent sequencing studies, however, revealed a highly conserved consensus sequence between different YFV-17D strains [232, 233]. Furthermore, not only host-cell specific post-translational modification such as phosphorylation [234], ubiquitination [235], and glycosylation [236], but also virus-derived changes in codon usage [237] are known. Those mechanisms can improve final virus titers at different replication stages, i.e. during virus replication, packaging and release. The specific role of the ER-derived lipid layer, which encapsulates the (+)ssRNA in the virions can also play an important role during the virus adaptation to a new host substrate. Overall, the ratio of infectious virions (PFU) to total YFV material (vRNA) (estimate the percentage of infectious virions) was increased by 40 % (from 0.03 % to 0.05 %) during adaptation. This indicates that virus maturation or stability may have been slightly improved. The high abundance of non-infectious flavivirus material has been also described elsewhere [238], but their *in-vitro* function is poorly studied. It is assumed that the highest fraction of non-infectious Dengue and West Nile virions was derived from inefficient prM protein cleavage during virus maturation [239, 240]. However, recent YFV maturation experiments with a 293T cell stably over-expressing furin (required to cleave prM for final virus maturation) did not lead to a higher proportion of infectious virions [241].

Overall, numerous adaptation mechanisms certainly contribute to the successful spreading of flaviviruses to various host systems such as mosquitoes, monkeys and humans. Thereby, the adapted virus has several functions to repeatedly balance the host cell stress response, while maintaining cell survival to ensure efficient viral protein production and virion assembly [26]. However, the increased fitness of the adapted virion to a cell substrate can be also associated to a loss of fitness as a live-attenuated viral vaccine in humans. In turn, it may require higher viral doses per vaccine administration to achieve the same immunogenicity level. Such safety and immunogenicity study are still missing. Instead, inactivated Vero cell-derived YFV vaccines were tested in hamsters and macaques, and two dose injections were necessary for effective immunization [8].

4.2.2 Virus production dynamics

The understanding of YFV replication dynamics in suspension culture is substantial for the design and optimization of efficient production processes. This section describes MOI studies performed in BHK-21_{SUS} cells to increase virus titers. Furthermore, viral spreading and infection ratios were monitored in an infected cell population by imaging flow cytometry.

MOI studies in BHK-21_{SUS} batch cultivations revealed maximum virus titers with an optimum MOI as low as 10^{-2} . A larger virus input did not result in higher titers, but maximum values were achieved faster. When the virus input was chosen below the optimum MOI, virus titers progressed slower to only reduced titers (Figure 4.8).

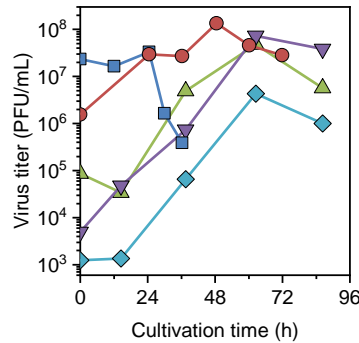


Figure 4.8 | Impact of multiplicity of infection on yellow fever virus titers in BHK-21_{sus} cells. Cells were cultivated in batch mode and shake flasks until 2.5×10^6 cells/mL. Subsequent infection was performed with Vero cell-derived YFV seed material at MOI 10 (blue), 1 (red), 10^{-1} (green), 10^{-2} (purple) and 10^{-3} (turquoise).

For imaging flow cytometry, infected cells from a batch cultivation were stained with in-house produced monoclonal antibodies directed against the loop region of the E protein (mAb 4G2; Chapter 3.11). A high MOI 10 infection was performed to synchronously infect the cell population and to study single-cycle infection dynamics (Figure 4.9 A). After 12 hpi, first infectious virions were determined in the supernatant, while only 6 % of all cells were detected as infected. The proportion increased to 70 % after 24 hpi and reached its maximum at 60 hpi. Interestingly, maximum YFV titers peaked already 30 hpi and subsequently decreased in parallel with cell concentration and viability (Figure 4.9 B, C). When lower MOI levels were chosen, infection dynamics were slowed down. At a threshold MOI of 10^{-3} , the cell population got only partially infected before entering the decline phase, and similar cell concentrations to the mock infection (9×10^6 cells/mL, without YFV infection) were obtained. Nevertheless, infected cells finally underwent cell lysis, while mock-infected cells remained vital above 90 % beyond the recorded time (data not shown).

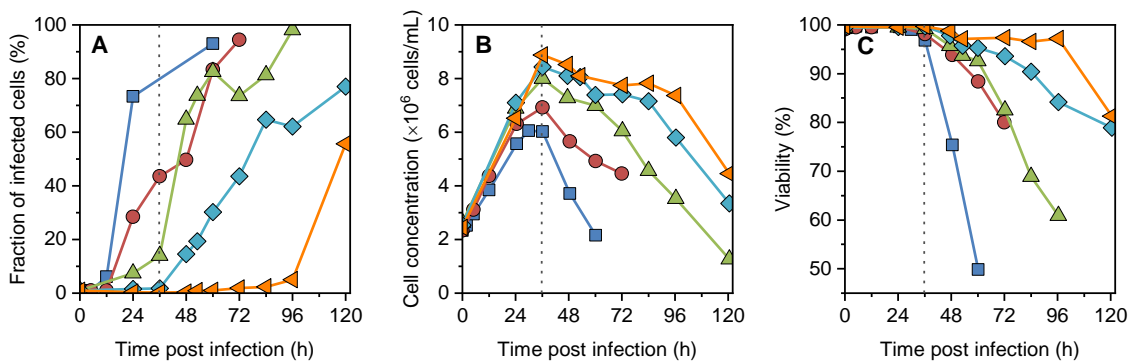


Figure 4.9 | Infection dynamics of yellow fever virus in BHK-21_{sus} cells at different multiplicities of infection. BHK-21_{sus} cells were maintained at standard shake flask conditions, infected with Vero cell-derived YFV seed virus and (A) the fraction of infected cells was determined with 4G2-mab and ImageStream X Mark II. (B) The viable cell concentration and (C) cell viability (based on trypan-blue exclusion) was monitored at MOI 10 (blue), 1 (red), 5×10^{-2} (green), 10^{-3} (turquoise), and 10^{-5} (orange). Dotted vertical line indicates cell decline phase.

Discussion For efficient YFV production in BHK-21_{SUS} cells in batch mode, the optimum MOI ranged between 0.01 and 10^{-3} , where minimum seed virus volume was required to obtain maximum virus titers. This is in general agreement as reported from collaboration partners (RKI, Vaneva). However, MOI conditions can be different for operation modes other than batch cultivation, i.e., perfusion cultivations with extended cell growth phases, which can require a lower initial virus input, to obtain similar final titers.

Moreover, virus infection dynamics were studied in a BHK-21_{SUS} cell population by flow cytometry. High MOI infections aimed at a complete and synchronous infection. However, only a low fraction of infected cells was detected at 12 hpi, which then steadily increased to 70 % at 24 hpi. For the detection of positive-infected cells, the assay required sufficient quantities of viral E protein as antigen. Hence, it may be possible that the applicability of the assay is limited by the sensitivity, in particular for early infection periods. The late infection onset is also observed with orthogonal methods such as single-cell vRNA tracking [242-244]. Latter method showed the highest sensitivity relying on the detection of intracellular vRNA levels. Nevertheless, earliest detection of infected cells was observed 3-6 hpi. Assuming synchronous infection at MOI 10, one would expect a distinct increase to 100 % infected cells by reaching the detection level of E proteins in each cell simultaneously (considering herein used flow cytometry method). Instead, a slow and heterogenic infection spreading in the cell population was observed. Considering this observation on single-cell-resolution, this may be explained by certain host-responses interfering with the viral life cycle in different phases. Further studies are needed to understand the cellular repertoire of viral intrusions to optimize infection conditions for virus production [26]. Therefore, the established imaging flow cytometry method could be extended to detect other viral proteins. This may allow to track virus assembly at different stages and to identify bottlenecks during replication.

Overall, YFV replication and population spreading were particularly pronounced for low MOI infections. First progeny virions were released at 12 hpi. This is in agreement with infection studies in Huh7.5, HeLa and 293T cells [242, 244, 245]. Subsequent infection waves were so slow that cells entered the decline phase due to media limitations before the population was completely infected. At such MOI conditions, the production system should be changed to facilitate a longer cultivation period with high viabilities to procure more time for the slow replicating YFV. From a process development prospective, this can be achieved by maintaining optimum process conditions, i.e., perfusion cultivation to constantly supply metabolites and to reduce inhibiting factors.

4.2.3 Virus evolution in semi-continuous cultivation

The amount of total vRNA copy numbers in the supernatant typically exceeded infectious virus particle concentrations by 2 to 4 log and remained stable, while infectious particles degraded quickly after peaking. The high ratio of non-infectious, defective particles (DP) raised the question of a possible interference with infectious YFV replication. Recently, a two-stage cultivation system was described that results in high MOI infection conditions and allows to study the presence of defective interfering particles (DIP) [210]. Here, the set-up was modified to investigate whether DIP formation plays a role in YFV infection with BHK-21_{SUS} cells.

For semi-continuous two-stage cultivations, BHK-21_{SUS} cells were cultured in three shake flasks. When cells reached 1×10^6 cells/mL, two shake flasks were infected with YFV. For the next

17 days, cells were transferred batch-wise from the uninfected cell growth shake flask to the two infected virus production shake flasks after medium removal (Chapter 3.2). This enabled a continuous virus production at increasing MOI infection conditions above MOI 40 (similar value to cell-specific virus yield in Figure 4.10 C). Over the course of operation, specific cell growth rates changed so that dilution rates needed to be adjusted. This resulted in a drop of cell concentration above 1.5×10^6 cells/mL. The cell retention time was then kept constant at about 30 h for the virus production shake flasks. Both infected virus shake flasks followed a similar pattern in cell growth and YFV titers (Figure 4.10 A, B). Due to the partial medium exchange, a virus fraction was always remained in the vessel and titers reached 5×10^7 PFU/mL and 1×10^8 PFU/mL, respectively. Thereby, the cell-specific virus yield increased throughout the cultivation (Figure 4.10 C). The fraction of infectious virions in relation to vRNA molecule levels remained around 0.02 % and slightly increased to 0.04 % (Figure 4.10 D).

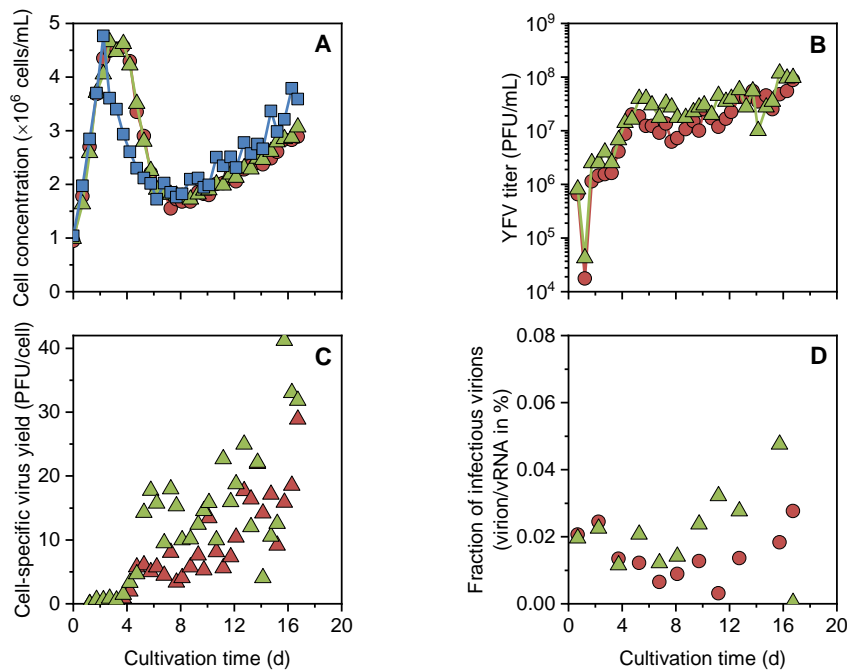


Figure 4.10 | Yellow fever virus production in a semi-continuous two-stage shake flask cultivation. (A) Viable cells were constantly transferred from the cell growth shake flask (blue) to two virus propagation shake flasks (#1 = green; #2 = red). (B) YFV titer increased in the virus production shake flasks at partial medium exchanges. (C) Cell-specific virus yield which can be directly translated to multiplicity of infection and (D) fraction of infectious virions.

Discussion Two-stage cultivation approaches have been recently used to study DPs in IAV production [210]. DIPs contain internal genomic deletions and studies suggest that such shorter genomes possess a replication advantage over full-length genomes [246]. Over the long run, DIPs accumulated and reduced infectious virus titers periodically [247]. A semi-continuous cultivation approach in shake flask scale was later applied to indicate the absence of DIPs for the MVA virus, and equally to confirm strong DIP formation for IAV in two different cell lines [203].

The role of non-infectious, immature YFV particles on virus spreading is still not clear. It is known that immature virus particles seem to stimulate the interferon (IFN) response in dendritic cells [241]. From a process point of view, this can only play a minor role in virus production since BHK-21 and EB66[®] cells are both described as defective in IFN production or insensitive to IFN (personal communication, A. León, Valneva SE and [248]). Here, a potential interference of DPs was investigated with the semi-continuous two-stage cultivation. Despite the accumulation of DPs in the cell broth, no obvious fluctuations in infectious titers occurred during the whole process time. This indicates the absence of a potential interference with mature virus replication meaning the absence of DIPs. The formation of DPs should be further verified by PCR and gel electrophoresis (following [247]). The assays can help to differentiate the origin of non-infectious particles, which may be either derived from poor virus maturation or internal genomic deletion.

In addition to the semi-continuous two-stage bioreactor system as investigative tool for replication interference, the cultivation system was a suitable solution for continuous YFV production. The system facilitated a self-stabilizing operational window and high virus titers were constantly produced during the 17 days cultivation time. Further optimization and automation could yield even higher virus titers but was beyond the given time frame of this work.

4.2.4 Summary

This chapter described the characterization of alternative suspension cell substrates for YFV production. Furthermore, reasons for the low cell-specific virus yields of around 10 PFU/cell were investigated using flow cytometric analysis and semi-continuous two-stage cultivation. First, a broad cell line screening of available suspension cells revealed a high viral permissiveness of BHK-21_{SUS} cells similar to adherent Vero cells. The importance of sequential virus adaptation to new cell substrates was underpinned by a 10-fold increase in cell-specific virus yields with EB66[®] cells. Thereby, the overall viral fitness, i.e. faster virus replication and higher virus titers, clearly increased and turned the EB66[®] cell line to be an attractive cell substrate. Screening experiments in batch mode identified a MOI in the range of 0.01 suitable to achieve maximum virus yields with minimum seed virus input. Further studies using imaging flow cytometry captured virus dynamics and spreading on the single-cell level. It revealed a slow, heterogenic virus spreading rising the question for potential host cell responses interfering with virus replication in the early stages. Finally, when infected at MOIs above 5×10^{-2} , all cells were infected and contributed to the overall virus titer. Lower MOI infection studies in batch mode showed that cells entered the decline phase due to media limitation before the entire population became infected. This underlines the importance of the right infection condition and well-designed growth/virus production media in alternative to other cultivation processes enabling longer cultivation times, i.e., by cultivating in fed-batch or perfusion mode. Finally, semi-continuous two-stage cultivations indicated the absence of replication-interfering, non-infectious virus particles (DIPs). Hence, the system can be a vital option to constantly produce YFV for extended time periods with an interesting option for continuous DSP of the labile virus. Due to the high mutation rates of the RNA virus, however, consideration should also be given to a limited virus passage number.

4.3 Process intensification for yellow fever virus production

Having identified BHK-21_{SUS} and EB66[®] cells as promising virus substrates, the YFV production process was subsequently intensified. With the idea of increased cell concentrations for higher virus titers (assuming constant cell-specific virus yields), the cells were grown to high cell concentrations and infected. First scouting experiments in shake flasks were performed in pseudo-perfusion mode with manual medium exchange to study potential “high cell density” effects. Subsequently, the process was transferred to stirred-tank bioreactors with membrane-based perfusion systems.

4.3.1 Pseudo-perfusion cultivation

Pseudo-perfusion cultivations in shake flasks at a working volume of 50 mL enabled high perfusion rates with relatively low media consumption. In a first step, the medium exchange protocol was optimized to minimize the cell losses during passaging (described in Chapter 3.3). Then, scouting experiments were performed to investigate maximum cell concentrations of BHK-21_{SUS} cells in BGM medium. Therefore, three different perfusion rate strategies were tested. While the rigid perfusion rate strategy was fixed at one reactor volume exchange per day (1 RV/day), perfusion rates were adjusted for the glucose- and glutamine-based strategies to supply respective metabolites at sufficient extracellular concentrations.

In the first cultivation with a fixed perfusion rate, BHK-21_{SUS} cells in BGM (supplemented with 4 mM glutamine) grew to maximum cell concentrations of 1.6×10^7 cells/mL with an average t_D of 38 h (exponential cell growth indicated by red dotted line in Figure 4.11 left). At 70 h cultivation time, chronic depletion of glutamine occurred before next scheduled medium exchanges with growing cell concentrations. This led to a constant decrease in cell-specific perfusion rates from 140 to 65 pL/cell/day (Figure 4.11 left). Due to the fast depletion of glutamine, further experiments were performed with basal BGM medium supplemented with 8 mM glutamine.

With the glucose-based strategy, BHK-21_{SUS} cells achieved 5.1×10^7 cells/mL with an average t_D of 28 h (illustrated in Figure 4.11 middle). Throughout the cultivation, glucose levels were successfully maintained above 1.5 mM by adjusting manual medium exchange intervals. Although the basal growth and perfusion medium was already supplemented with 8 mM glutamine, levels were always very low until next medium exchange. The observed cell-specific perfusion rate was relatively stable and reached an average value of 70 pL/cell/day. Hence, the perfusion rate increased to finally 4 RV/day (Figure 4.11 middle).

The glutamine-based strategy was successfully performed until 4.2×10^7 cells/mL (154 h) and concentrations were maintained above 0.3 mM (in BGM supplemented with 8 mM glutamine). However, due to the high cell concentration and glutamine uptake rates, medium exchange intervals decreased below 3.5 h (Table A7.4). Manually, this was barely maintainable for extended time periods due to handling issues and the necessity of prior perfusion medium incubation for the adjustment of pH, CO₂ and temperature. Hence, the perfusion rate control was changed to a glucose-based strategy. Time intervals increased to 5.5 h and media exchanges could be manually handled.

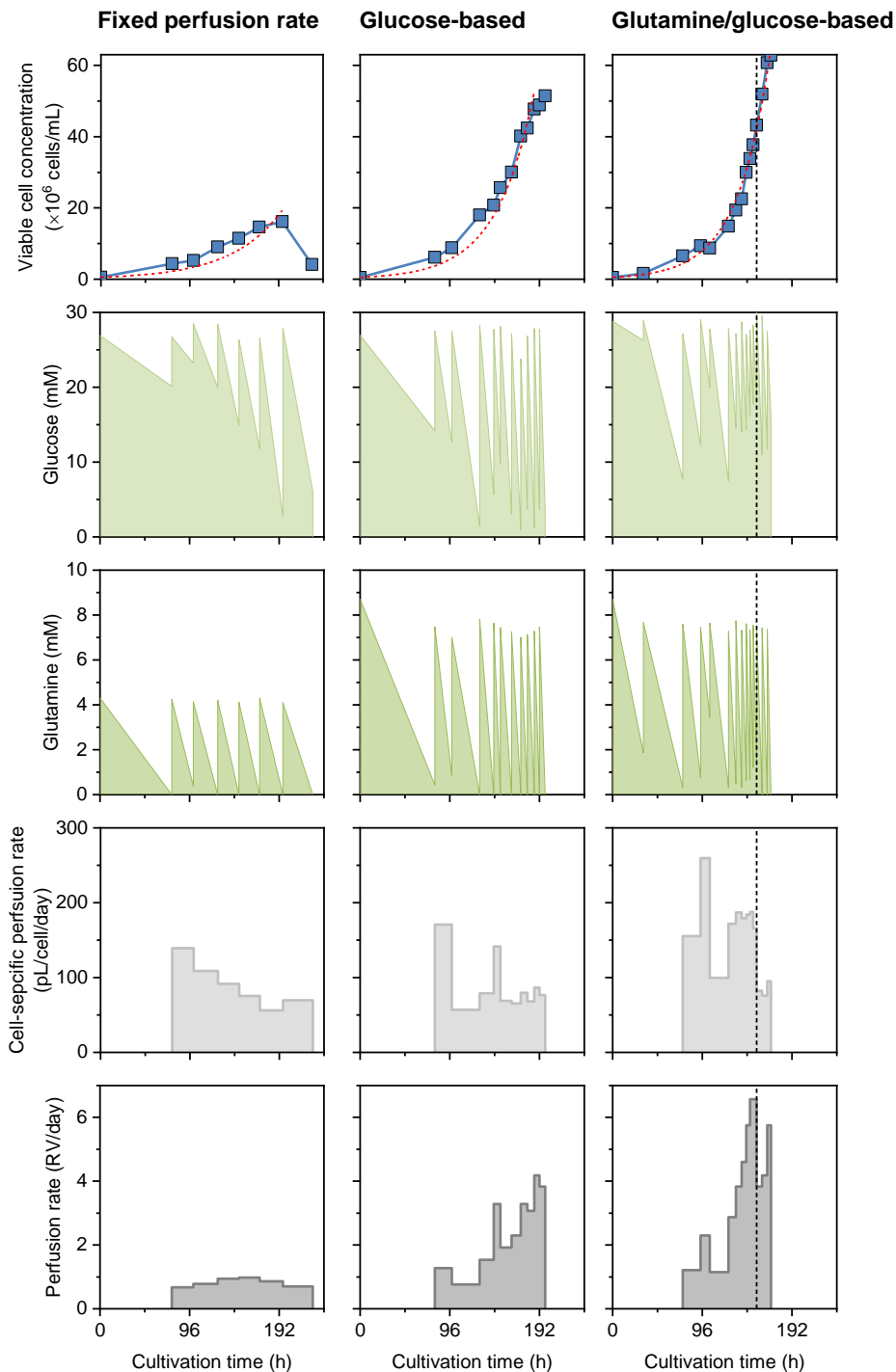


Figure 4.11 | Pseudo-perfusion cultivations of BHK-21_{sus} cells in shake flasks with different perfusion rate strategies. (Left) Fixed perfusion rate strategy at 1 RV/day (BGM medium with 4 mM glutamine). **(Middle)** Glucose-based perfusion rate control (BGM medium with 8 mM glutamine). **(Right)** Hybrid strategy; first glutamine-based perfusion rate control, and after 154 h (indicated by dotted vertical line) glucose-based control (BGM medium with 8 mM glutamine). Exponential cell growth indicated by red dotted lines with a population doubling time (t_D) of 38 h, 28 h and 24 h, respectively (from left to right).

However, reduced perfusion rates soon led to a depletion of glutamine after 160 h, while glucose levels were maintained above the set point. Finally, a hybrid (glutamine/glucose) strategy enabled highest BHK-21_{SUS} cell concentrations of 6.2×10^7 cells/mL with an average t_D of 24 h (Figure 4.11 right). Thereby, initial average perfusion rates of about 160 pL/cell/day were maintained during the glutamine-based perfusion phase, and sharply decreased to 80 pL/cell/day during the glucose-based phase. In parallel, perfusion rates increased stepwise to 6.6 RV/day and decreased with the change in strategy (Figure 4.11 right).

As a result of the scouting experiments, the hybrid perfusion rate strategy (primarily based on glutamine as key metabolite) was identified to ensure suitable metabolite supply enabling highest BHK-21_{SUS} cell concentrations. In a next step, the pseudo-perfusion cultivation was performed again and cells infected (Figure 4.12). When cells reached 2.1×10^7 cells/mL, they were infected with Vero cell-derived YFV at MOI 0.05. Infected cells continued growing with an average t_D of 25 h. When cells reached 4.2×10^7 cells/mL, the perfusion process was changed to the glucose-based strategy. Finally, cells reached maximum cell concentrations of 6.0×10^7 cells/mL before viabilities decreased abruptly. The extracellular virus in the used medium was constantly collected, and a total volume of 307 mL with an average infectious titer of 1×10^8 PFU/mL accumulated. Final YFV titers of the last harvest were at 4.3×10^8 PFU/mL corresponding to a cell-specific virus yield of 7.1 PFU/cell (summarized and compared with membrane-based perfusion systems in Table 4.3).

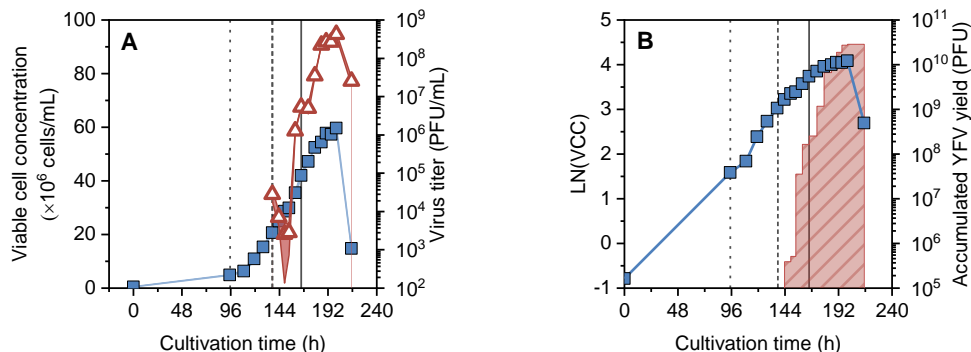


Figure 4.12 | Yellow fever virus production with BHK-21_{SUS} cells in pseudo-perfusion cultivation and shake flasks. Perfusion rates were first controlled based on extracellular glutamine concentrations and then changed to maintain glucose levels. **(A)** Cell concentration (blue square) and YFV titer (red triangle; area indicates standard deviation from two biological replicates with only minor differences). **(B)** Logarithmic cell growth (blue square) and total accumulated infectious YFV yield in the harvest (red striped area; upper values correspond to median of two biological replicates). Dotted vertical line indicates start of perfusion phase; dashed vertical line indicates time point of infection; solid vertical line indicates change from glutamine- to glucose-based perfusion rate strategy.

Discussion A pseudo-perfusion system was established in shake flask-scale to investigate the impact of process intensification on maximum BHK-21_{SUS} cell growth and cell-specific virus yields. The sufficient and adjusted supply with fresh medium based on glutamine and glucose concentrations enabled cell concentrations of 6.2×10^7 cells/mL. Such concentrations were never reported before for this cell line.

In the beginning of the study, a fixed perfusion rate of 1 RV/day was set, but glutamine was subject to frequent depletion. The maximum cell concentration was comparably low, and this result clearly underpinned a chronic undersupply with fresh medium. This was particularly evident in declining cell-specific perfusion rates, which were eventually associated to initial overfeeding and later underfeeding. An ideal perfusion rate profile will increase with the cell concentration. Hence, metabolite-based perfusion rates were tested. Thereby, glutamine and glucose proved to be important metabolites, potentially indicating the overall medium depletion (e.g. amino acid, vitamin and growth factor concentrations). Due to the fast glutamine uptake, the basal growth and perfusion medium was supplemented with 8 mM glutamine. This prolonged exchange intervals and enabled manual handling of the glutamine-based perfusion strategy until a certain cell concentration. Above 4×10^7 cells/mL, perfusion rates increased beyond practical applicability. To overcome this limitation, either the perfusion medium (especially the composition) needs to be optimized for BHK-21_{SUS} cells or controlled perfusion bioreactor systems should be used.

In a next step, cells in a pseudo-perfusion cultivation were infected with YFV to investigate the so-called “high cell density” effect. The effect was first introduced in 1982 and described cell-specific product losses due to increased cell concentrations [249]. In the following years, this term was frequently used to express general virus losses for a variety of different cell lines and viruses [250]. Over the time, the major cause was not *per-se* identified by increased cell concentrations as such, but by nutrient limitations or accumulation of inhibitory factors [125, 251-253]. Under this extended consideration, this effect can be a critical attribute strongly interfering with the idea of perfusion processes for intensified virus production. BHK-21_{SUS} cells were maintained at 6×10^7 cells/mL and YFV infection resulted in a cell-specific YFV titer of 7.1 PFU/cell for the last batch harvest (Figure 4.12). This is in the same range of typical batch infection experiments with 11.3 PFU/cell (Table 4.2). Considering error of infectivity assays and batch-to-batch variations, this finding suggests only a low effect or even the absence of density-related productivity losses. While high perfusion rates prevented nutrient limitations or the accumulation of inhibitors, findings could be related to non-ideal perfusion rates, uncontrolled process conditions in shake flasks at 6×10^7 cells/mL, but also to the technical nature of pseudo-perfusion cultivations (batch-wise medium and virus removal compared to accumulated titers in batch cultivations). A better comparison may be achieved by transferring the process to perfusion systems that retain the virus in the cultivation vessel (e.g. membrane-based perfusion systems).

Overall, pseudo-perfusion cultivations are a versatile tool to, e.g., identify maximum cell growth or key metabolites for process control. Due to the small volume and high throughput, it can be equally used for perfusion medium development with high cell density cultivations in parallel. Its application towards herein reported cell concentrations was never reported before. Besides BHK-21_{SUS} cells, a variety of other cell lines (e.g. CHO, CR.pIX[®], and MDCK.SUS cells) were successfully maintained in pseudo-perfusion cultivation achieving concentrations of up to 5×10^7 cells/mL [147, 254, 255]. The applicability was also tested for EB66[®] cells in CDM4Avian medium. However, cells coagulated and formed stirring rings at the shake flask wall (containing 10 % of total cell number in suspension with an average viability of about 60 %; more details provided in Nikolay *et al.* [256]), but required optimization was not further pursued. The transfer towards membrane-based perfusion systems was of higher relevance for large-scale vaccine production.

4.3.2 Perfusion cultivation

Having identified glutamine as an important metabolite for high cell concentrations in pseudo-perfusion cultivation, the YFV production process was then transferred to bioreactors with scalable membrane-based perfusion systems. First, BHK-21_{SUS} cells were cultivated in TFF mode and infected. The process was then transferred to EB66[®] cells in serum-free GRO-I medium (Chapter 3.6.1). Challenges arose when the EB66[®] perfusion cultivation was performed in chemically defined CDM4Avian medium. Hence, the applicability of an ATF set-up was investigated, to understand the shear-impact of both perfusion systems (Chapter 3.6.2). Due to the lack of online metabolite probes, all perfusion cultivations required manual sampling and offline metabolite measurements to adjust perfusion rates after each sampling point (Chapter 3.6.3).

First, BHK-21_{SUS} cells were cultivated in BGM supplemented with 4 mM glutamine. The 1 L stirred-tank bioreactor was equipped with an impeller pump (PuraLev) and a PES hollow fiber membrane (0.2 μm cut-off, 0.13 m^2 , Refine). The perfusion cultivation was performed in TFF operation and a pH value of 7.2 was set with 0.5 M NaOH. BHK-21_{SUS} cells were cultivated for 72 h in batch mode and after glutamine depletion the perfusion mode was started immediately. This coincided with a strong decrease of the t_D from 22 h to 48 h. Due to high glutamine uptake rates, metabolite levels could be only recovered after 1 day (Figure 4.13 C). The cell growth rate remained and cells grew until 1.9×10^7 cells/mL before YFV was added at MOI 10^{-4} . Cells continued growing and reached a maximum of 2.8×10^7 cells/mL with a peak YFV titer of 1.6×10^8 PFU/mL (Figure 4.13 A). To compensate for the high media demand and reduce overall perfusion rates, basal media were successively supplemented with different concentrations of glutamine, glucose and pyruvate (details provided in Table 3.5). This resulted in an average cell-specific perfusion rate of 22 pL/cell/day (Figure 4.13 B). Major limitations of essential amino acids were not detected (Figure 4.13 D). Overall, a cell-specific virus yield of 5.7 PFU/cell was obtained. With a total medium consumption of 3.0 L (included basal cell growth and perfusion medium), a media volume-specific cell yield (also called “media-depth” describing cell counts per total medium used [142]) of 7.4×10^6 cells/mL_{medium} was obtained. The performance of the perfusion cultivation was determined with a total volumetric YFV productivity of 2.7×10^8 PFU/L/day (summarized in Table 4.3). In parallel, YFV titers were measured in the permeate flow. Interestingly, despite the small virus particle size (~ 50 nm), only a minor fraction of virions migrated through the membrane (0.2 μm cut-off). Minimum rejection values of 70 % (titer reduction in permeate compared to bioreactor) quickly increased above 95 % with cultivation time (Figure A7.8).

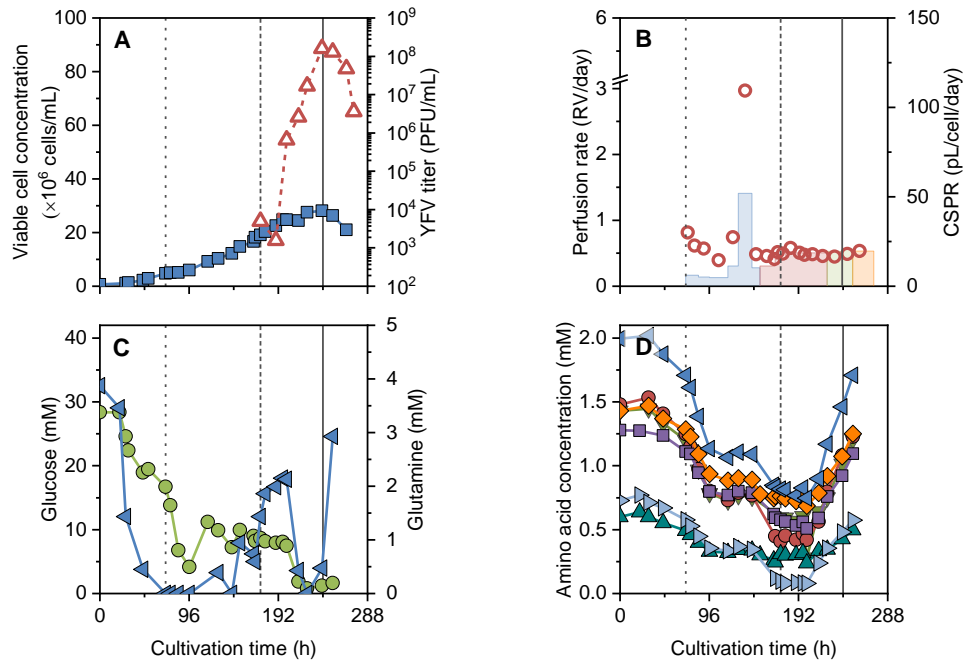


Figure 4.13 | Yellow fever virus production with BHK-21_{sus} cells in a 1 L bioreactor and tangential flow filtration (TFF) perfusion system. Cells grew in BGM supplemented with 4 mM glutamine. (A) Cell concentration (blue square) and YFV titer (red triangle). (B) Perfusion rates with different perfusion media (A_{BHK} = ■, B_{BHK} = ■, C_{BHK} = ■, D_{BHK} = ■; see Table 3.5) and cell-specific perfusion rate (red circle). (C) Glucose (green circle) and glutamine concentrations (blue triangle). (D) Essential amino acid concentrations of leucine (◄), lysine (●), valine (▼), isoleucine (◆), threonine (■), phenylalanine (►), methionine (▲). Dotted vertical line indicates start of perfusion operation; dashed vertical line indicates time point of infection; solid vertical line indicates cell decline phase.

The same bioreactor set-up with TFF perfusion system and a new PES membrane (0.2 μm cut-off, 0.13 m^2 , Refine) were subsequently used to cultivate EB66[®] cells in GRO-I medium (Figure 4.14). The pH remained uncontrolled as pH values did not decrease below pH 7.0 (one-sided pH control with 0.5 M NaOH). Cells grew for 72 h in batch mode with a t_D of 18 h. When the recirculation was started at 1200 rpm, the cell growth reduced to a t_D of 38 h, while high viabilities above 98 % remained (data not shown). After 8 h, the perfusion process was initiated and rates were adjusted manually to maintain sufficient glucose and glutamine concentrations. At a cell concentration of 3.0×10^7 cells/mL, cells were infected with the non-adapted Vero cell-derived YFV seed at $\text{MOI } 10^{-4}$. Cells continued growing for 72 h and reached 5.7×10^7 cells/mL. While the cells entered the decline phase, YFV titers increased to only 3.1×10^6 PFU/mL (Figure 4.14 A). Fluctuating cell growth and consumption rates required manual interventions, which amplified to strong variations in the perfusion rate profile. Due to the sudden increase in glucose uptake rates (potentially caused by offline measurement noise within the error range), the perfusion medium (B_{EB}) was additionally supplemented. Throughout the cultivation, the cell-specific perfusion rate decreased constantly from 125 to 12 pL/cell/day without obvious effects on the cell growth performance (Figure 4.14 B), while glucose and glutamine levels were maintained at sufficient levels (Figure 4.14 C). Overall, 6.1 L medium was used, resulting in a medium volume-specific cell yield of 6.7×10^6 cells/mL_{medium}. The total volumetric YFV productivity resulted in 3.3×10^7 PFU/L/day

(summarized in Table 4.3). Also here, virus titers were determined in the permeate flow, but again, more than 99 % of infectious virions remained within the bioreactor system and did not migrate across the hollow fiber membrane (Figure A7.8).

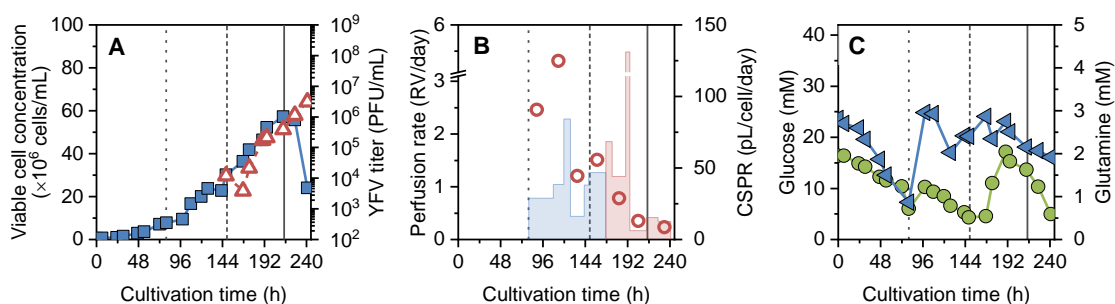


Figure 4.14 | Yellow fever virus production with EB66[®] cells in a 1 L bioreactor with tangential flow filtration perfusion system. Cells grew in GRO-I medium supplemented with 2.5 mM glutamine and were infected with Vero cell-derived (non-adapted) YFV seed. **(A)** Cell concentration (blue square) and YFV titer (red triangle). **(B)** Perfusion rates with different perfusion media (A_{EB} = GRO-I+4 mM glutamine, B_{EB} = A_{EB} +16 mM glucose, C_{EB}) and cell-specific perfusion rate (red circle). **(C)** Glucose (green circle) and glutamine (blue triangle) concentrations. Dotted vertical line indicates start of perfusion phase; dashed vertical line indicates time point of infection; solid vertical line indicates cell decline phase.

In a next approach, the EB66[®] cell cultivation was repeated to perform the infection with the EB66[®] cell-derived YFV seed virus. A new chemically defined CDM4Avian medium became also available facilitating excellent cell growth in shake flask cultivations (Figure A7.7). Thus, the process was transferred to the same bioreactor set-up with a TFF perfusion unit. However, with the start of the centrifugal pump at 1200 rpm, cell aggregates broke apart and cell concentrations, as well as viabilities, decreased abruptly (data not shown). Further trials with reduced pump rates and without membrane modules did not facilitate cell growth.

As consequence, the ATF system was tested. The bidirectional flow direction required only one dip tube and cells were pumped across the same PES membrane type (0.2 μm cut-off, 470 cm^2 , Spectrum Labs³). A minimum pump rate of 0.8 L/min was chosen for the diaphragm pump and perfusion rates were adjusted manually to maintain glucose levels above 5 mM and glutamine levels above 1 mM (hereafter referred to as ATF-M). Therefore, growth and consumption rates at last sampling period were used to predict required perfusion rates until the next sampling time. The perfusion pump rate was set via the DCU to follow a linear increase meeting the prospective perfusion rate (see Equations 15 and 16). Before inoculation, the pH was decreased to pH 7.2 with CO_2 gassing. In the following, pH values remained above pH 7.0. EB66[®] cells were inoculated and grew in batch mode with a constant t_D of 23 h (Figure 4.15). When the ATF pump was started after 48 h, cells continued growing without changes in the growth rate. However, when the perfusion process was started one day later (day 5), cells showed a reduced cell growth with a t_D of 43 h. Nevertheless, cells grew until 9.1×10^7 cells/mL and were subsequently infected with EB66[®] cell-adapted YFV

³ Spectrum Labs is the supplier of hollow fiber membranes for Repligen, where previous PES membranes were purchased. The PES material is considered identical with differences only in the module length and resulting membrane area. Hence, results are considered comparable.

virus (5th passage). Two days post infection, virus titers peaked with 7.3×10^8 PFU/mL, corresponding to a cell-specific virus yield of 7.7 PFU/cell (Figure 4.15 A). During the cultivation, glucose and glutamine levels were maintained mostly above the set point (Figure 4.15 C). Therefore, manual perfusion rates varied only slightly and increased to 1.5 RV/day. In parallel, the cell-specific perfusion rate initially decreased from 50 pL/cell/day and stabilized itself at 15 pL/cell/day (Figure 4.15 B). Subsequent amino acid quantification revealed a depletion of methionine with the decreased cell growth rate at day 5 (Figure 4.15 D). Based on a total media consumption of 6.2 L, a medium volume-specific cell yield of 1.1×10^7 cells/mL_{medium} was achieved. The total volumetric YFV productivity was calculated to 5.5×10^9 PFU/L/day (summarized in Table 4.3). As previously observed during other membrane-based perfusion cultivations, more than 99 % of the YFV particles were retained in the bioreactor vessel (Figure A7.8).

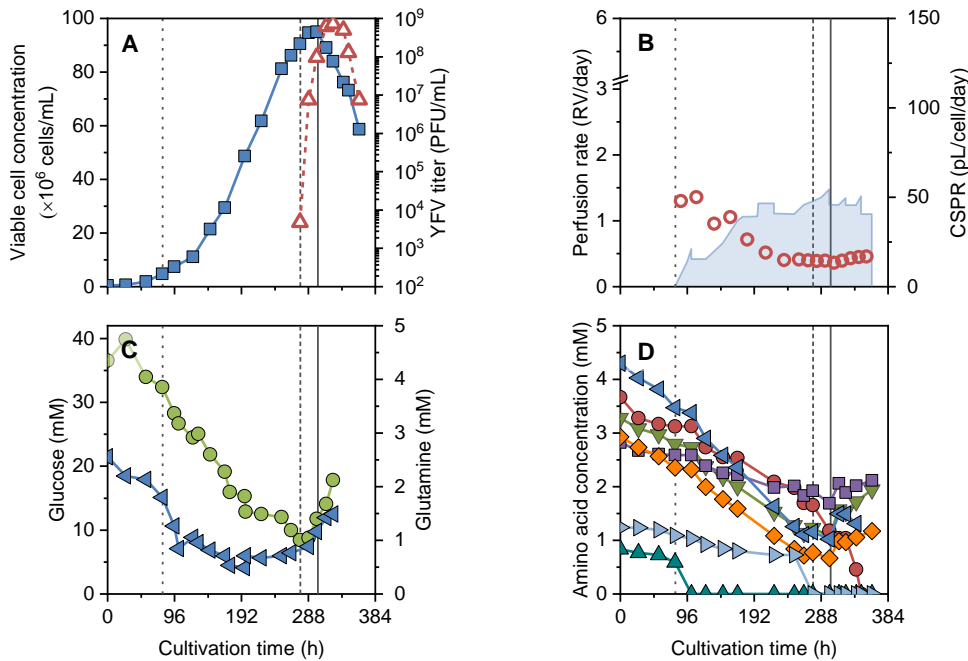


Figure 4.15 | Yellow fever virus production with EB66[®] cells in a 1 L bioreactor with alternating tangential flow filtration (ATF) perfusion system. Cells grew in CDM4Avian medium supplemented with 2.5 mM glutamine and were infected with EB66[®] cell-adapted YFV seed. **(A)** Cell concentration (blue square) and YFV titers (red triangle). **(B)** Perfusion rate with perfusion medium equal to basal growth medium (blue area) and cell-specific perfusion rate (red circle). **(C)** Glucose (green circle) and glutamine (blue triangle) concentrations. **(D)** Essential amino acid concentrations of leucine (◄), lysine (●), valine (►), isoleucine (◆), threonine (■), phenylalanine (▶), methionine (▲). Dotted vertical line indicates start of perfusion phase; dashed vertical line indicates time point of infection; solid vertical line indicates cell decline phase.

Table 4.3 | Process data for yellow fever virus production with BHK-21_{sus} and EB66[®] cells. Cultivations were performed in batch mode and shake flasks (upper part), and in pseudo-perfusion operation in shake flasks and perfusion operation in stirred-tank bioreactor systems with membrane-based perfusion units (lower part).

Cell line	Cultivation type *	Medium	Working volume	Max. cell concentration	Spent medium †	Cell-spec. perfusion rate	Media depth ‡	Virus titer	Cell-spec. virus yield	Volumetric virus productivity †
			L	cells/mL	L	pL/cell/day	cells/mL _{medium}	PFU/mL	PFU/cell	PFU/L/day
BHK-21 _{sus}	B	Shake flask	0.05	4.2x10 ⁶	0.03	-	4.2x10 ⁶	4.8x10 ⁷ ^a	11.3	1.3x10 ¹⁰
EB66 [®]	B	Shake flask	0.05	1.3x10 ⁷	0.03	-	1.3x10 ⁷	1.4x10 ⁸ ^b	10.0	2.7x10 ¹⁰
BHK-21 _{sus}	P	Ps.-perf.	0.05	6.0x10 ⁷	0.47	~ 160	4.3x10 ⁶	4.3x10 ⁸ ^a	7.1	7.3x10 ⁹
BHK-21 _{sus}	P	TFF-M	0.8	2.8x10 ⁷	3.0	30 – 16	7.4x10 ⁶	1.6x10 ⁸ ^a	5.7 ^a	2.7x10 ⁸
EB66 [®]	P	TFF-M	0.7	5.7x10 ⁷	6.1	125 – 12	6.7x10 ⁶	3.1x10 ⁷ ^a	<0.1 ^b	3.3x10 ⁷
EB66 [®]	P	ATF-M	0.7	9.5x10 ⁷	6.2	50 – 15	1.1x10 ⁷	7.3x10 ⁸ ^b	7.7 ^b	5.5x10 ⁹

Perfusion rates were adjusted manually to maintain glucose and glutamine concentrations. Ps.-perf. = pseudo-perfusion cultivation in shake flask; TFF-M = tangential flow filtration with manual perfusion rate control; ATF-M = alternating tangential flow filtration with manual perfusion rate control.

* B = batch cultivation; P = perfusion cultivation

† basal batch growth medium and perfusion medium until maximum virus titer was reached

‡ also called medium volume-specific cell yield, includes basal batch growth medium and perfusion medium (total medium)

^a non-adapted YFV seed from Vero cells

^b EB66[®] cell-adapted YFV seed (5th passage)

Discussion Scouting experiments in pseudo-perfusion cultivations indicated the absence of cell-density-related productivity losses. This turns perfusion cultivations with suitable perfusion rates into a potential solution for intensified YFV production. Hence, membrane-based perfusion (TFF and ATF) systems were used to achieve high BHK-21_{SUS} and EB66[®] cell concentrations for subsequent YFV infection.

BHK-21_{SUS} cells grew successfully in TFF mode to 2.8×10^7 cells/mL and exceeded reported cell concentrations of 6×10^6 cells/mL with perfusion spin filter units and 2×10^7 cells/mL with unknown perfusion units [257, 258]. The cell-specific YFV titers in BHK-21_{SUS} cells decreased from batch cultivation (11.3 PFU/cell) and pseudo-perfusion cultivation (7.1 PFU/cell) to the TFF cultivation (5.7 PFU/cell; summarized in Table 4.3). The slightly reduced virus titers during process intensification and scale-up should be further addressed. Presented experiments and observations indicate, that it requires a high cellular fitness (i.e. μ_{\max} of 0.03 h^{-1}) to yield maximum virus titers. As the cell growth rate strongly decreased to 0.014 h^{-1} (0.032 h^{-1} in batch cultivation), the cellular status potentially impaired virus replication. Furthermore, perfusion media were supplemented with key metabolites. This enabled low perfusion rates, but also posed the risk of an undersupply with other nutrients not being monitored. In addition, low dilution rates enhance the accumulation of potential inhibitory compounds. The increase in perfusion rates is expensive and should be considered, when process conditions (e.g. *toi*, MOI, pH) have otherwise been optimized for perfusion cultivations.

Alternatively, EB66[®] cells were tested being a more interesting cell substrate for the production of human viral vaccines (Chapter 2.2.3). First trials with EB66[®] cells in GRO-I medium and the TFF perfusion system clearly demonstrated its applicability for high cell concentrations (5.7×10^7 cells/mL). However, an infection at late cell growth phase with non-adapted YFV seed resulted in low virus titers. As already shown in previous batch cultivations, seed virus adaptation most likely played a major role and is apparently equally related to extended cell growth phases, as achieved during perfusion cultivation. With the release of the new CDM4Avian medium and promising cell growth in batch cultivations (Figure A7.7), further investigations focused in the use of this chemically defined medium. However, the TFF perfusion cultivation did not directly result in improved cell growth with the set-up and process parameters from previous cultivations in GRO-I medium. By starting the impeller pump, cell concentrations and viabilities decreased. In consequence, CDM4Avian medium did not seem to protect cells from mechanical shear impact to the same extent as the serum-free GRO-I medium. Even reduced impeller speeds and removal of the membrane could not overcome the negative impact of the pump to the cells.

Hence, a bioreactor system with ATF perfusion was tested to cultivate EB66[®] cells in CDM4Avian medium (ATF-M). Despite the manual perfusion rate control and fluctuating metabolite levels, cells grew to 9.5×10^7 cells/mL. The infection with the EB66[®] cell-adapted YFV resulted in cell-specific virus yields (7.7 PFU/cell) in the range of high-yield shake flask cultivations in batch mode (10 PFU/cell). Surprisingly, the CDM4Avian medium is originally a very nutrient-rich medium and only cell-specific perfusion rates of 15 pL/cell/day were required. This basal growth medium is furthermore well suited as a perfusion medium not demanding high metabolite supplementation. This is particularly advantageous for achieving high volumetric virus productivities, which take into account the total volume of used medium. This factor was previously stressed by Konstantinov and colleagues considering this in a “push-to-low” approach [142]. The basic idea is to minimize the use of medium in fed-batch and perfusion systems in order to become more

competitive compared to batch cultivations. On the medium-side, this can be ideally described by the media depth (cell counts per total medium used). Here, shake flask batch cultivations enabled 1.5×10^7 cells/mL_{medium}, while the perfusion cultivation was close to 1.1×10^7 cells/mL_{medium} (Table 4.3). Finally, all parameters (i.e. media depth, maximum cell concentration, cell growth rate, cell-specific virus yield) are important and essential to increase volumetric virus productivities and to compete against batch cultivations.

Presented perfusion cultivations were performed with manually adjusted perfusion rates. The strategy is well established [e.g. 12, 13, 254], although offline measurements and manual intervention are prone to errors and pose the risk of undetected over- or underfeeding. In addition, the reproducibility is often poor, e.g., due to offline measurement errors or time delays. Therefore, alternative control strategies are needed to ideally (i) replace manual handling and (ii) consider biological batch-to-batch variance. For the following perfusion cultivations, a cell-specific perfusion rate strategy was chosen due to simplicity and robustness (Chapter 2.3.2).

The perfusion processes were started step by step to unravel the influence of the pump before the subsequent addition of medium. With the start of the TFF impeller pump, both growth rates from BHK-21_{SUS} (in BGM medium) and EB66[®] (in GRO-I medium) cells decreased and never recovered. When EB66[®] cells were cultivated in CDM4Avian medium, the impeller pump did not support any cell growth. Comparing impeller and diaphragm pumps from the technical side, both pump systems were operated at different flow rates. While the impeller pump allowed minimum flow rates of 160 mL/min (determined at 1200 rpm), the diaphragm pump operated at a minimum flow rate of 800 mL/min (as given by pump controller). Despite smaller dip tube diameters for the TFF set-up, the theoretical shear stress in the tubing system (excluding impact of pump) was below the value of the ATF configuration (350 s^{-1} versus 1750 s^{-1} following Equation 32; rule of thumb: ideally below 2000 s^{-1}). Although the vortex effect by reversing flow directions of the ATF module was not considered yet, experimental data strongly suggest the use of a diaphragm pump results in lower shear stress of the cells. After all, it is known that the pump system and contact time to the cell are more important regarding the actual shear stress on cells than tubing diameters, membrane fibers and even tapering [170, 259, 260]. Although the impeller Puralev[®] pump is supposed to recirculate at low shear-stress, it did not seem to improve cell growth. Thus, its claim potential advantages for cultivation of shear-sensitive cells, obviously in combination with the medium, remains questionable. A good alternative is the ATF diaphragm pump.

Perfusion systems were operated with hollow fiber membranes with a nominal cut-off of 0.2 μm . Conversely, small YFV particles (40-50 nm in diameter) were expected to pass the membrane into the permeate flow. However, membrane rejection rates for YFV were above 70 % and increased rapidly above 99 % with filter fouling retaining thermolabile virus particles in the bioreactor (Figure A7.8). This is particularly counterproductive for the production of live-attenuated vaccines. Particle retention was not only observed for YFV but also for other viruses [13, 261, 262], but also for recombinant proteins at different membrane cut-offs (0.2-0.5 μm) using predominantly PES material [12, 172, 263]. Recent investigations on virus retention (in literature often referred to as “sieving”) have emphasized membrane pore narrowing that reduces effective cut-offs below virion or even protein sizes [264, 265] and is further investigated in Chapter 4.6. The ATF perfusion system is considered as suitable device to constantly remove the foulants by high cross flow velocity, bidirectional flow inversions and by alternating flow directions across the membrane (backflushing; Chapter 2.3.4.3). As this countermeasure was obviously not sufficient

enough to avoid pore narrowing, it requires a systematic study to test different hollow fiber membranes (material and cut-off) for reduced fouling. In case membranes that allow virions to pass into the permeate can be identified, continuous harvesting strategies can be implemented. This can add to the complexity as the perfusion rate is then not solely determined based on optimum cell growth and virus replication, but also on optimum product harvest and virus dilution rates (possibly changing MOI conditions of later infection waves). Alternatively, cell retention devices without a membrane (e.g. acoustic or inclined settlers [266, 267]) can be considered but scalability and retention efficiency at very high cell concentrations remain to be addressed in large-scale vaccine manufacturing.

4.3.3 Summary

Perfusion systems aim to intensify the production process through high cell concentrations. This applies if cell-specific virus yields can be maintained or ideally increased compared to batch infections. First scouting experiments were performed in pseudo-perfusion cultivations in shake flask. This enabled the screening of different perfusion control strategies. Finally, glutamine was identified as a promising control parameter to achieve very high BHK-21_{SUS} cell concentrations. When the same cultivation strategy was tested for EB66[®] cells, formation of strong cell clumps and attachment to the shake flask wall impaired efficient cell passaging. Therefore, this approach was not further optimized. The subsequent infection of BHK-21_{SUS} cells in pseudo-perfusion cultivations yielded very high YFV titers with similar cell-specific virus yields compared to batch infection. This suggested the absence (or only low impact) of cell density-dependent productivity losses (also called “high cell density effect”), but was rather associated to slightly decreased cell growth rates (indicator for cellular fitness and metabolic status). Encouraged by high YFV titers, the process was scaled into bioreactor systems with membrane-based perfusion devices. In TFF operation, the system enabled high BHK-21_{SUS} cell concentrations of 2.8×10^7 cells/mL and even higher concentrations of 5.7×10^7 cells/mL for EB66[®] cells in serum-free media. Limitations arose for EB66[®] cells in a chemically defined medium due to high shear stress from the impeller pump exceeded the shear-sensitivity of the cell in the medium. Hence, an ATF system with a diaphragm pump was tested. This enabled highest EB66[®] cell concentrations of 9.5×10^7 cells/mL to be achieved. Infection with the EB66[®] cell-adapted YFV seed resulted in very high titers of up to 7.3×10^8 PFU/mL in less than two weeks production time. Perfusion rates of the cultivations were controlled manually based on metabolite concentrations. For further improvements, an automated control strategy based on cell-specific perfusion rates would be desirable to minimize manual interventions. Finally, membrane-based perfusion processes resulted in a high accumulation of YFV particles in the bioreactor vessel. This enabled a batch-wise product harvest when maximum titers were reached.

4.4 Transfer of a perfusion cultivation to Zika virus production

With the sudden spread of ZIKV in the Americas 2016, there was an immediate need for Brazilian Zika virus material to study the disease at the virological and epidemiological level, and to investigate the consequences for humans. In Brazil, different ZIKV isolates have been collected from PCR-positive patients and were propagated in cell culture. However, efficient virus production, typically with adherent Vero or C6/36 cell lines, remained a challenge. This chapter describes first scouting experiments with adherent Vero, BHK-21 and BHK-21_{SUS} cells with certain restrictions on equipment available for cell culture under BSL-3 conditions in Rio de Janeiro. ZIKV isolates were then transferred to the MPI and a production process with EB66® cells was established. Investigations regarding high-yield production of wild-type virus can be of great value, concerning future viral vaccine production processes.

4.4.1 Scouting experiments with adherent cells

Available ZIKV propagation protocols were typically based on adherent Vero cells or C6/36 insect cells. Therefore, Vero cells were first cultivated in a bioreactor with a microcarrier concentration of 5 g/L (Chapter 3.5). After 72 h of cultivation, when the Vero cells reached 4.5×10^6 cells/mL (based on nuclei counting), cells were infected with ZIKV^{ES.U} at an MOI 10^{-3} . Three days later, at a cell concentration of 7.1×10^6 cells/mL, maximum ZIKV titers reached only 1.1×10^3 PFU/mL (summarized in Table 4.5).

Hence, a more promising BHK-21 cell substrate was additionally tested for ZIKV infection and replication. When different ZIKV isolates were available, their viral fitness (i.e. maximum titer and replication time) was tested in both Vero and adherent BHK-21 cells (Table 4.4). Both cell substrates showed a similar high viral permissiveness for the ZIKV isolates with maximum virus titers and cell-specific yields in the same order of magnitude. However, the titers among different isolates strongly varied from 4.1×10^5 PFU/mL to 1.6×10^7 PFU/mL. After this first screening, ZIKV^{PE} seemed to be the most promising virus isolate for further infection experiments.

Table 4.4 | Maximum virus titers and cell-specific yields of different Zika virus isolates achieved in adherent Vero and BHK-21 cells.

ZIKV isolate	Vero		BHK-21	
	Virus titer (PFU/mL)	Cell-spec. virus yield (PFU/cell)	Virus titer (PFU/mL)	Cell-spec. virus yield (PFU/cell)
ZIKV ^{PE}	1.6×10^7	48.1	1.3×10^7	40.8
ZIKV ^{ES.U}	2.8×10^6	8.9	3.1×10^6	9.9
ZIKV ^{ES}	1.2×10^6	4.0	4.1×10^5	0.9
ZIKV ^{PB}	n.p.	n.p.	2.9×10^6	9.3

n.p. = not performed due to limited virus availability. Note: Infection experiments were performed in tissue culture flasks (25 cm² surface) and Dulbecco's Modified Eagle medium. Virus isolates PE, ES, and PB derived from C6/36 insect cells, ES.U was additionally passaged in Vero cells. Vero cells were infected with MOI 10^{-3} and BHK-21 with MOI 0.01. Previous MOI infection studies showed that the maximum virus yields were independent from the chosen MOI at a threshold of 10^{-3} [268]. Thus, present infection is assumed to be comparable in its result.

To simplify the scale-up with BHK-21 cells, adherent cells were adapted stew-wise to suspension growth in TC-X6D medium. Although initial shake flask infection experiments with ZIKV^{PE} resulted in high concentrations of 7.1×10^6 cells/mL, cell-specific virus yields reached only 0.1 PFU/cell (Table 4.5). Subsequent RT-qPCR analysis revealed a decrease in extracellular vRNA levels during the first day post infection (successful virus adsorption/entry), but the expected increase in extracellular vRNA copy numbers at later time points was not observed (lacking virus release). The quantification of intracellular RNA levels revealed a 2000-fold increase compared to extracellular levels in the supernatant. This indicated a successful genomic replication, but hints of a bottleneck in the following virus replication steps (supplementary data provided in Nikolay *et al.*, 2017).

To extend the cultivation time for higher virus titers and increased cell concentrations, the process was transferred into a single-use 3 L bioreactor with an ATF perfusion system (Figure 4.16; Chapter 3.6.2). The pH value was controlled at pH 7.1, while glucose depletion was avoided by batch-wise medium exchange and subsequent perfusion operation. Perfusion rates were manually increased from 0.15 to 0.42 RV/day. Cells were infected with ZIKV^{PE} at an MOI 10^{-3} and reached a maximum cell concentrations of 1.1×10^7 cells/mL, a virus titer of 3.9×10^7 PFU/mL, and a cell-specific virus yield of 3.3 PFU/cell (Table 4.5).

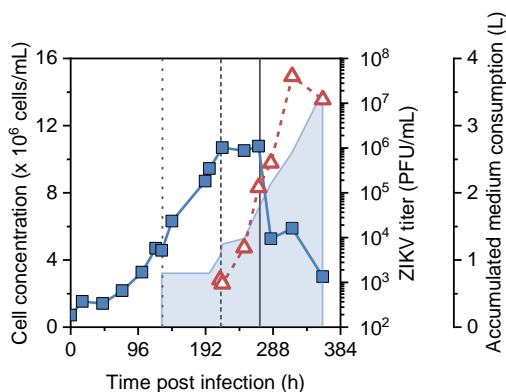


Figure 4.16 | ZIKV^{PE} production with BHK-21_{SUS} cells in a 3 L bioreactor and alternating tangential flow filtration (ATF) perfusion system. Cells grew in 1.2 L TC-X6D medium. Cell concentration (blue square), ZIKV titer (red triangle) and accumulated perfusion medium (blue area). Dotted vertical line indicates start of perfusion operation; dashed vertical line indicates time point of infection; solid vertical line indicates cell decline phase.

Discussion With the Zika outbreak in Brazil, a rapid solution was needed to generate high quantities of Brazilian ZIKV for virological studies. As ZIKV was typically propagated with adherent Vero cells in tissue culture flasks, the first approach aimed at microcarrier cultivations in a controlled bioreactor system. However, ZIKV titers were low and subsequent screening of different virus isolates revealed a low viral fitness of the ZIKV seed isolate from Espírito Santo state.

High YFV titers obtained previously in BHK-21_{SUS} cells suggested their use for ZIKV infection. Adherent BHK-21 cells demonstrated to be equally permissive for ZIKV isolates compared to Vero cells. However, the four Brazilian ZIKV isolates showed large differences in infectious virus titers. Since these Brazilian isolates showed a high genetic similarity sharing 97–100 % of

their genomic identity, even small differences in sequence can have a significant impact on propagation in host cells [269]. It clearly demonstrated that the viral fitness is not solely derived by the genomic sequence, but also by the virus history (e.g. source, cell substrate). Notably, the selection of the right isolate (here ZIKV^{PE}) can be decisive for the production of larger amounts of virus, notably, not necessarily resulting in a more potent vaccine.

The transfer to BHK-21_{SUS} cells did not yield in similar ZIKV^{PE} titers. Subsequent RT-qPCR analysis revealed a linear correlation of extracellular cycle threshold (c_T) values to infectious titers (PFU/mL) in the supernatant (data in Nikolay *et al.*, 2017). This enabled the interpretation of intracellular vRNA levels and suggested the relative retention of virus material. Again, successful virus entry and vRNA synthesis in BHK-21_{SUS} cells were observed, but vRNA molecular copy numbers increased to high levels. This may be related to poor virus maturation or release leading to low extracellular virus titers. The finding is in agreement with transmission electron microscopic observations, where ZIKV particles accumulated in cellular vesicles of adherent Vero cells [270]. In addition, similar to what was found for, i.e., MVA production [271], a direct cell-to-cell contact may have an additional benefit for optimum virus spreading. Hence, further virus adaptation to suspension cells can be important.

The subsequent bioreactor cultivation in perfusion mode was performed with limited possibilities regarding the monitoring of metabolite concentrations. This may have resulted in the depletion of various substrates and suboptimal cell growth, but infection with the original ZIKV^{PE} isolate achieved reasonable titers. The bioreactor cultivation with a working volume of 1.2 L clearly improved total virus production, and replaced more than 90 tissue culture flasks (175 cm² with 40 mL working volume). Notably, virus titers strongly increased beyond the stationary cell growth phase. In parallel, the pH value was kept at a favorable pH value of 7.1, potentially explaining better ZIKV titers than in uncontrolled tissue culture flasks [220]. However, cell-specific virus yields were about 10 times lower compared to ZIKV production in adherent BHK-21 cells. Based on the many advantages using suspension cells, further investigations should be performed to identify optimum process conditions (e.g. cell growth, perfusion rate, virus seed) and to improve the production process even further.

4.4.2 Automated perfusion cultivation

Based on the promising results obtained and the many open questions regarding a potential optimization of yields, the ZIKV production process was further developed at the MPI. First, an extended screening of Brazilian and African ZIKV isolates was performed. As a result, a ZIKV isolate from the state of Rio de Janeiro (referred to as ZIKV^{RJ}) yielded in 3-fold higher titers in adherent Vero cells than the previously selected ZIKV^{PE} by factor 3. In a second step, this virus isolate was sequentially adapted to replicate in the fast-growing EB66[®] cells and then used as virus seed to infect EB66[®] cells in automated perfusion bioreactors.

Virus adaptation The original ZIKV^{RJ} isolate was subcultured over five passages in EB66[®] cells growing in CDM4Avian medium. The first passage was infected at MOI 10⁻² and subsequent passages were performed blindly by transferring a small volume to the next shake flask (Chapter 3.7.1). Over the time course of virus adaptation, ZIKV replication became faster, and maximum

titers of 8.5×10^7 PFU/mL were achieved after 48 hpi. The 5th virus passage resulted in a maximum cell-specific virus yield of 5.5 PFU/cell (Figure 4.17 A, B; Table 4.5). However, infectious virus titers decreased fast and inactivation kinetics was further investigated in spiking experiments. ZIKV^{RJ} revealed a temperature-dependent half-life time of 8 h at 37 °C in the growth medium, which increased to 14 h at 33 °C and 41 h at 4 °C (Figure A7.6). Throughout virus passaging, vRNA copy numbers in the supernatant increased and accumulated to stable titers of 2.9×10^{11} molecules/mL (Figure 4.17 C). Thereby, the fraction of infectious particles increased from 0.03 % to 0.3 % until the 5th passage (Figure 4.17 D). This means that still one infectious ZIKV particle related to about 333 non-infectious vRNA copy numbers, which is not a usual finding. For IAV, for example, fractions of infectious virions between 0.3 % and above 25 % were reported for varying MOIs [272]. The 5th passage of EB66[®] cell-adapted ZIKV^{RJ} was stored and used for further infection experiments.

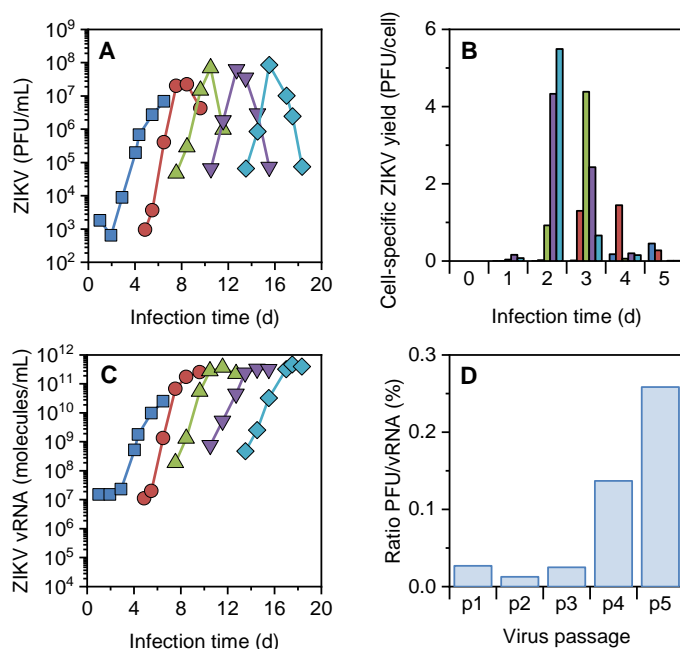


Figure 4.17 | Sequential passaging of Zika virus in EB66[®] cells. Cells were cultivated in shake flasks with CDM4Avian medium and infected with ZIKV^{RJ} at 4.3×10^6 ($\pm 0.8 \times 10^6$) cells/mL reaching final concentrations of 1.5×10^7 ($\pm 0.1 \times 10^7$) cells/mL 48 hpi. **(A)** Infectious virus titer during semi-continuous virus passaging. **(B)** Cell-specific virus yields at fixed time intervals for each virus passage. **(C)** Total viral RNA (vRNA) copy number in the supernatant during semi-continuous virus passaging. **(D)** Ratio of infectious particles (PFU) to vRNA copy numbers at time point of maximum, infectious virus titer for each virus passage (expressed in percentage). Each virus passage is indicated by a different color (blue = p1, red = p2, green = p3, purple = p4, turquoise = p5).

Perfusion cultivation To intensify ZIKV production, the process was transferred directly into bioreactors with a membrane-based perfusion system. Due to the reduced shear of the diaphragm pump on EB66[®] cells in CDM4Avian medium, the ATF perfusion unit was selected with PES membranes ($0.2 \mu\text{m}$, 470 cm^2 ; further details in Chapter 3.6.2). In order to increase the reproducibility of the cultivation, the perfusion rate was automatically adjusted by means of an online biomass probe (Chapter 3.6.3). Based on previous findings with metabolite-based perfusion rate

control, EB66[®] cells grew well at a minimum cell-specific perfusion rate of 15pL/cell/day. As a starting point, a low perfusion rate (here 17 pL/cell/day; ATF-17pL) and a high perfusion rate (here 34 pL/cell/day; ATF-34pL) were chosen. The Incyte online biomass probe signal was linearly correlated to offline measured viable cell concentrations. This enabled accurate cell concentration monitoring throughout the cultivation (further details are discussed in Chapter 4.5). The perfusion process was started shortly after cell inoculation. In the first run (ATF-17pL, Figure 4.18 left), cells grew with a t_D of 19 h. To avoid methionine depletion (as coincided with reduced growth rates observed in previous ATF-M run for YFV production), this essential amino acid was added prophylactically after 4 days. However, subsequent amino acid analysis revealed that methionine was depleted already shortly before supplementation (Figure 4.18 G). A decrease in cell-specific growth rate could not be overcome and the t_D increased to 80 h. EB66[®] cells were directly infected at 5.1×10^7 cells/mL with EB66[®] cell-adapted ZIKV^{RJ} (5th passage). Cells continued growing to 8.9×10^7 cells/mL and ZIKV titers peaked 96 hpi with 2.6×10^9 PFU/mL (Figure 4.18 A). As a result, a cell-specific virus yield of 30 PFU/cell was reached. With a total use of 6.5 L medium, this corresponded to a volumetric virus productivity of 1.8×10^{10} PFU/L/day (Table 4.5).

The second cultivation (Figure 4.18 right) was performed with a perfusion rate of 34 pL/cell/day. This time, the bioreactor was directly inoculated from a cryo-bag. Thawed cells were added to an empty, pre-chilled bioreactor vessel before cold growth medium was added (Chapter 3.1.4). As a result, the cultivation started with 7.9×10^5 cells/mL (theoretically 65 % of cryo-preserved cells) and a viability of 94 %. Cells recovered within one day and a t_D of 19 h was achieved. After 5 days, the growth slowed down to 40 h t_D (simultaneously with methionine depletion which was not additionally supplemented this time to minimize manual interventions; Figure 4.18 H). Cells were infected at 7.3×10^7 cells/mL with EB66[®] cell-adapted ZIKV^{RJ} (5th passage). Two days later, cell concentrations reached a maximum value of 1.6×10^8 cells/mL, and ZIKV titers peaked with 1.0×10^{10} PFU/mL (Figure 4.18 B) corresponding to a cell-specific virus yield of 65 PFU/cell. With a total consumption of 9.0 L medium, a volumetric virus productivity of 8.1×10^{10} PFU/L/day was achieved (Table 4.5).

In both perfusion cultivations, the set point of cell-specific perfusion rates was largely maintained as perfusion rates increased with cell growth (Figure 4.18 C, D). This resulted in sufficient glucose and glutamine concentrations, which increased with the onset of the cell decline phase (Figure 4.18 E, F).

Finally, ZIKV titers were quantified in the permeate stream. The finding underpinned previous observations of high virus retention by the 0.2 μ m PES hollow fiber membrane. Less than 1 % of the infectious virus particles in the bioreactor were detected in the permeate (data not shown).

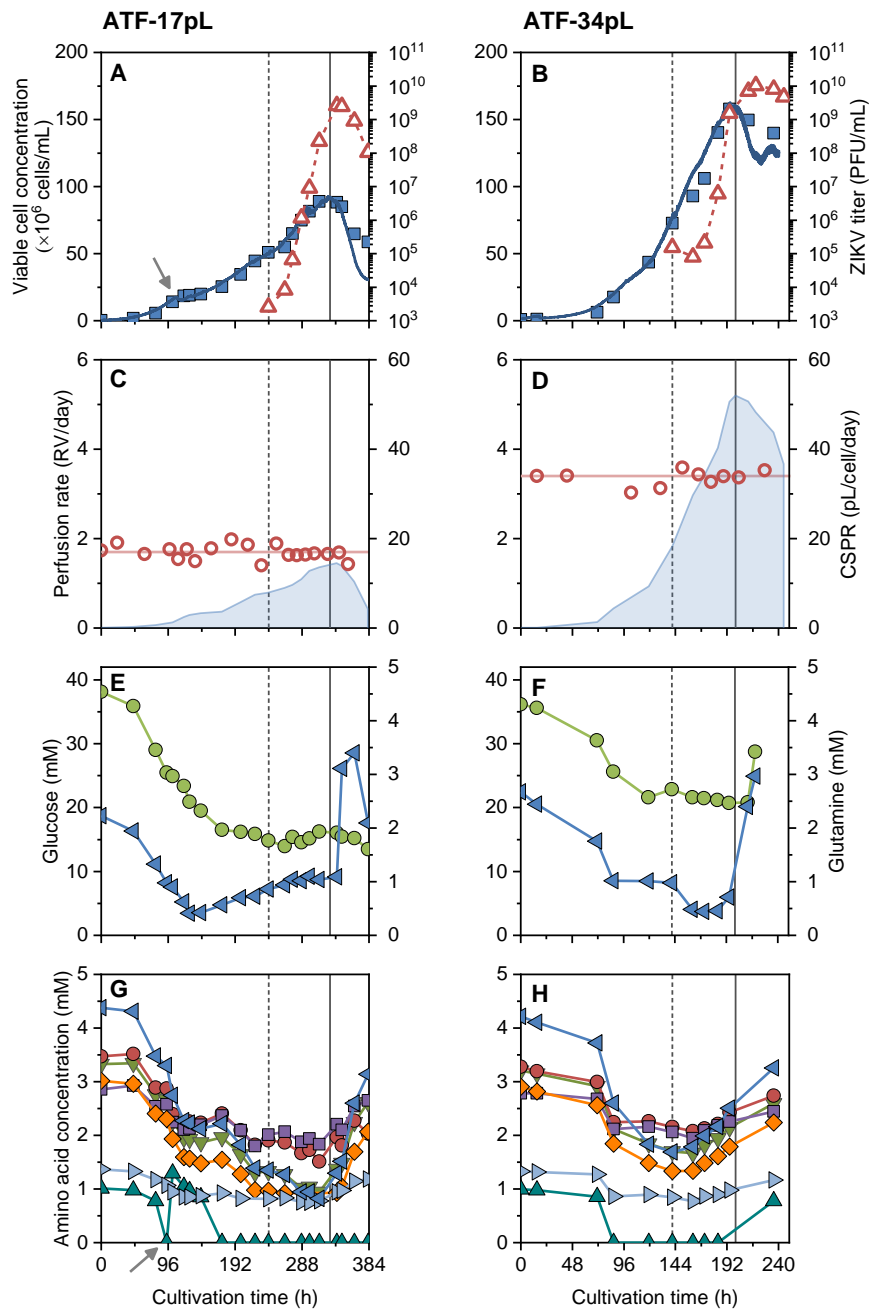


Figure 4.18 | Zika virus production with EB66[®] cells in a 1 L bioreactor with alternating tangential flow filtration (ATF) perfusion system and automated perfusion rate control. The perfusion rate was controlled automatically by the online biomass probe at a cell-specific perfusion rate of (left) 17 pL/cell/day (ATF-17pL) and (right) 34 pL/cell/day (ATF-34pL). Cells were infected with EB66[®] cell-adapted ZIKV^{RJ} seed. (A, B) Cell concentration (blue square), online biomass signal (solid line) and ZIKV titer (red triangle). Arrow indicates cell harvest for cell inoculum cryo bag preparation. (C, D) Perfusion rate (blue area) and cell-specific perfusion rate (red circle) with set points (indicated by red line). (E, F) Glucose (green circle) and glutamine concentrations (blue triangle). (G, H) Essential amino acid concentrations of leucine (◄), lysine (●), valine (▼), isoleucine (◆), threonine (■), phenylalanine (►), methionine (▲). Arrow indicates methionine addition. Perfusion operation was initiated with cell inoculation. Dashed vertical line indicates time point of infection; solid vertical line indicates cell decline phase.

Table 4.5 | Process data for Zika virus production in adherent Vero cells and suspension-adapted BHK-21^{sus} and EB66[®] cells. Cultivations were performed in batch operation (upper part) and in perfusion operation with stirred-tank bioreactor systems (lower part).

Cell line	Cultivation type *	Medium	Working volume	Max. cell concentration	Spent medium †	Cell-spec. perfusion rate	Media depth ‡	Virus titer	Cell-spec. virus yield	Volumetric virus productivity ‡
-	-	-	L	cells/mL	L	pL/cell/day	cells/mL _{medium}	PFU/mL	PFU/cell	PFU/L/day
Vero	B 5 g/L MC ^a	Z-Medium	1.2	7.1x10 ⁶ a,b	2.1	-	2.9x10 ⁶ c	1.1x10 ³	<0.1	7.2x10 ¹
EB66 [®]	B Shake flask	CDM4Avian	0.05	1.5x10 ⁷	0.05	-	1.5x10 ⁷ e	8.5x10 ⁷	5.5	1.7x10 ¹⁰
BHK-21 ^{sus}	P ATF-M	TC-X6D	1.2	1.1x10 ⁷	3.8	~60	4.4x10 ⁶ d	3.9x10 ⁷	4.6	9.3x10 ⁸
EB66 [®]	P ATF-17pL	CDM4Avian	0.7	8.9x10 ⁷	6.5	17	9.6x10 ⁶ e	2.6x10 ⁸	29.5	1.8x10 ¹⁰
EB66 [®]	P ATF-34pL	CDM4Avian	0.7	1.6x10 ⁸	9.0	34	1.2x10 ⁷ e	1.0x10 ¹⁰	64.9	8.1x10 ¹⁰

Perfusion rates were either manually adjusted to maintain glucose concentrations (ATF-M), or automatically adjusted to maintain cell-specific perfusion rates based on the online biomass estimation (ATF-XpL). MC = microcarrier cultivation. ATF = alternating tangential flow filtration.

* B = batch cultivation, P = perfusion cultivation

† basal batch growth medium and perfusion medium until maximum virus titer was reached

‡ also called medium volume-specific cell yield; includes basal batch growth medium and perfusion medium (total medium)

^a batch-wise cultivation with medium exchange at time point of infection.

^b based on nuclei counting

^c infected with ZIKV^{ESU} seed from Vero cells

^d infected with ZIKV^{PE} seed from C6/36 insect cells

^e infected with EB66[®] cell-adapted ZIKV^{RJ} seed (5th passage)

Discussion ZIKV production in EB66[®] cells enabled substantial process improvements by virus seed adaption and perfusion cultivation with automated perfusion rate control. The virus fitness increased on the basis of three observations: (i) increased infectious and total virus titers, (ii) faster replication and (iii) higher ratio of infectious virions to total vRNA molecules. The first two aspects were also found during YFV passaging and were elaborated in Chapter 4.2.1. Here, the infectious proportion of the overall ZIKV material increased by factor 10 at time points of maximum infectious titers (Figure 4.17 D). Interestingly, infectious virions did not appear to be more robust as the infectivity ratio rapidly decreased afterwards (Figure A7.9 A). Hence, it may be presumed that cell-adapted virions may be released in large quantities at once, while titers of slow non-adapted virions are longer affected by continuous temperature-dependent inactivation. The causality of cell lysis and release of host cell-derived proteolytic enzymes to virus inactivation is not yet fully investigated. In contrast, both perfusion cultivations enabled an extended cultivation period, which facilitated increased ZIKV infectivity ratios (Figure A7.9 B). The reason is unknown, but it seemed to allow a more favorable environment for virus maturation and/or stable conditions for ZIKV. This finally resulted in never reported ZIKV titers of 1.0×10^{10} PFU/mL and cell-specific virus yields of 65 PFU/cell. This clearly demonstrates that ATF perfusion processes not only enable high cell concentrations, but also improve ZIKV^{RJ} replication.

The ATF-34pL perfusion cultivation was initiated by direct bioreactor inoculation. Therefore, EB66[®] cell material (derived from ATF-17pL) was frozen in large-volume cryo bags at 6×10^7 cells/mL. The influence of DMSO (cryo protectant) was tested in subsequent thawing and inoculation experiments, but typical dilution factors reduced any negative impact on cell viability or growth (data not shown). The direct bioreactor inoculation was of great use to save preparation time for the cell seed inoculum and to gain flexibility for bioreactor cultivations. Higher cell concentrations for inoculation may even shorten process times until virus infection. In the future, well-characterized cell banks can reduce batch-to-batch variations and contribute to a more robust process performance with constant product quality and quantity [141].

To reduce manual interventions and avoid unprecise perfusion rate adjustments, the latter was controlled automatically by an online biomass probe (conceptually described by Dowd and colleagues [145]). This enabled a constant cell-specific perfusion rate, which was set based on previous metabolite-based high cell density cultivations (ATF-M). A lower (given by substrate consumption rates) and higher perfusion rate were chosen to test their impact on maximum cell concentrations. The higher perfusion rate enabled never reported EB66[®] cell concentrations of 1.6×10^8 cells/mL, both by the supply with metabolites and the removal of potential growth inhibitors. Thereby, the perfusion rate was not yet optimized. The infection did not impede the online biomass measurement and the strategy could be applied for the whole cultivation time. Here, a cell-specific perfusion rate of 34 pL/cell/day was chosen being significantly lower than typical perfusion rates (50-500 pL/cell/day) [142, 147, 254]. This enabled a very high medium use expressed as media depth of about 1.2×10^7 cells/mL_{medium}, while the batch cultivation achieved 1.5×10^7 cells/mL_{medium}. Particularly due to the increased cell-specific virus yield, the volumetric virus productivity of the perfusion cultivation increased by factor 4 compared to a batch infection (Table 4.5). In view of the fact that batch cultures are typically considered for optimum medium usage, this clearly underlines the potential of perfusion cultivations for high-yield ZIKV production.

As before (Chapters 4.2.3 and 4.4.2), most of the ZIKV material was retained by the membrane in the bioreactor vessel with a virus rejection rate above 99 % 24 h infection. Spiking experiments

with ZIKV revealed high virus inactivation rates with half-life times at 8 h in CDM4Avian growth medium at 37 °C. Therefore, the product should ideally be harvested directly from the bioreactor system and processed at lower temperature. A systematic study is required to investigate membrane fouling (e.g. non-specific accumulation of host cell DNA, proteins, and other compounds) with respect to membrane cut-off and materials.

4.4.3 Summary

The findings from previous YFV infection studies were successfully transferred to develop a high-yield ZIKV production process. Initial studies in Rio de Janeiro included the screening of different Brazilian ZIKV isolates in adherent Vero and BHK-21 cells. Both cell substrates showed a similar high viral permissiveness but virus titers strongly varied with different virus isolates. Having identified a high-yield virus isolate, such as ZIKV^{PE}, the process was transferred to BHK-21_{SUS} cells. However, viral titers were significantly lower for the suspension-adapted cell line. RT-qPCR revealed an intracellular accumulation of vRNA potentially associated to poor virus release. When the process was scaled into a bioreactor system with an ATF perfusion unit, larger quantities of ZIKV^{PE} were released during the cell decline phase. However, questions regarding optimum process conditions (e.g. cell substrate, virus seed, perfusion rate) remained open. In a next step, the high-yield ZIKV^{RJ} isolate was adapted to the EB66[®] cell substrate and cell-specific virus yields increased by factor 10. The 5th virus passage was used to infect subsequent ATF perfusion cultivations. The perfusion rate was controlled based on online estimated cell concentrations. This resulted in stable cell-specific perfusion rates and significantly reduced the number of manual interventions, which could increase reproducibility. Using a large-volumetric cryo bag, the production bioreactor was inoculated directly with EB66[®] cells. Without the need for seed train expansion, this allowed additional production flexibility and can contribute to higher batch-to-batch consistency. Finally, the perfusion cultivation enabled very high EB66[®] cell concentrations of 1.6×10^8 cells/mL and never reported ZIKV titers of 1.0×10^{10} PFU/mL. To this end, volumetric productivities even exceeded batch cultivations.

4.5 Potentials and limitations for the use of a capacitance probe in virus production processes

Capacitance probes are widely used to monitor cell growth in batch and fed-batch processes for recombinant protein production. However, little is known about the applicability for viral vaccine production and perfusion cultivations. This chapter examines the use of an Incyte biomass probe and different models for online biomass monitoring. At the end of this chapter, applications for in-depth analysis of cellular parameters and for virus production processes are explored.

4.5.1 Biomass correlation

Several approaches have evolved to determine biomass growth with capacitance probes. In the following section, three main models were applied to describe the relationship between capacitance data and VCC, VCV or cell diameter. A data set of three perfusion runs with EB66[®] cells (ATF-M, ATF-17pL and ATF-34pL) was evaluated. Due to the small number of perfusion runs, the data set could not be further separated into a training and validation set. Instead, each perfusion run was individually processed, calibration parameters averaged and the transferability among the three cultivations tested. This should determine the general robustness and transferability of each model. The qualitative measures were the normalized standard error of calibration (nSEC, Equation 30) and standard error of transfer (SET, Equation 31), respectively, in accordance to other studies [212, 213].

Bioreactor cultivation data set Cultivations were performed in the same bioreactor system (1 L Biostat) with the same set-up (ATF perfusion unit, probe positioning) and similar process conditions (medium, cell line, pO_2). Variations occurred in perfusion rate (manually adjusted based on metabolite levels, controlled CSPR of 17 and 34 pL/cell/h), cell inoculum (from shake flask or cryo bag), virus seed (YFV, ZIKV), optional supplementation (NaCl and methionine addition) and in pH value (one-sided pH control above pH 7.0). Main process variations are visualized in Figure A7.10, further details can be found in Chapter 3.6.2.

Incyte biomass measurement data The Incyte probe measured the capacitance at 17 different frequencies between 0.3-10 MHz and the ArcView controller calculated the permittivity ϵ . This formed the β -dispersion with each measurement point (exemplarily shown in Figure 4.19 A with linear scale). In parallel, the static suspension conductivity σ was measured and reported by the ArcView software (Figure 4.19 B). In a next step, the software calculated the Cole-Cole parameter α (divergence of measured to ideal dispersion), f_c (frequency at inflection point), $\Delta\epsilon_{max}$ (permittivity drop from f_{min} to f_{max}), and $\Delta\epsilon$ (permittivity drop from $f_1 \approx f_c$ to f_{max}) as visualized in Figure 2.10. The measurement data file was exported after each cultivation run and analyzed for further data processing.

The three models for biomass estimation required different input data (Figure 4.19 C-E). While the linear regression model relied on $\Delta\epsilon_{max}$ or $\Delta\epsilon$, the partial least squares (PLS) regression processed the relative permittivity data ϵ at each measured frequency. The Cole-Cole model relied on $\Delta\epsilon$, f_c and σ .

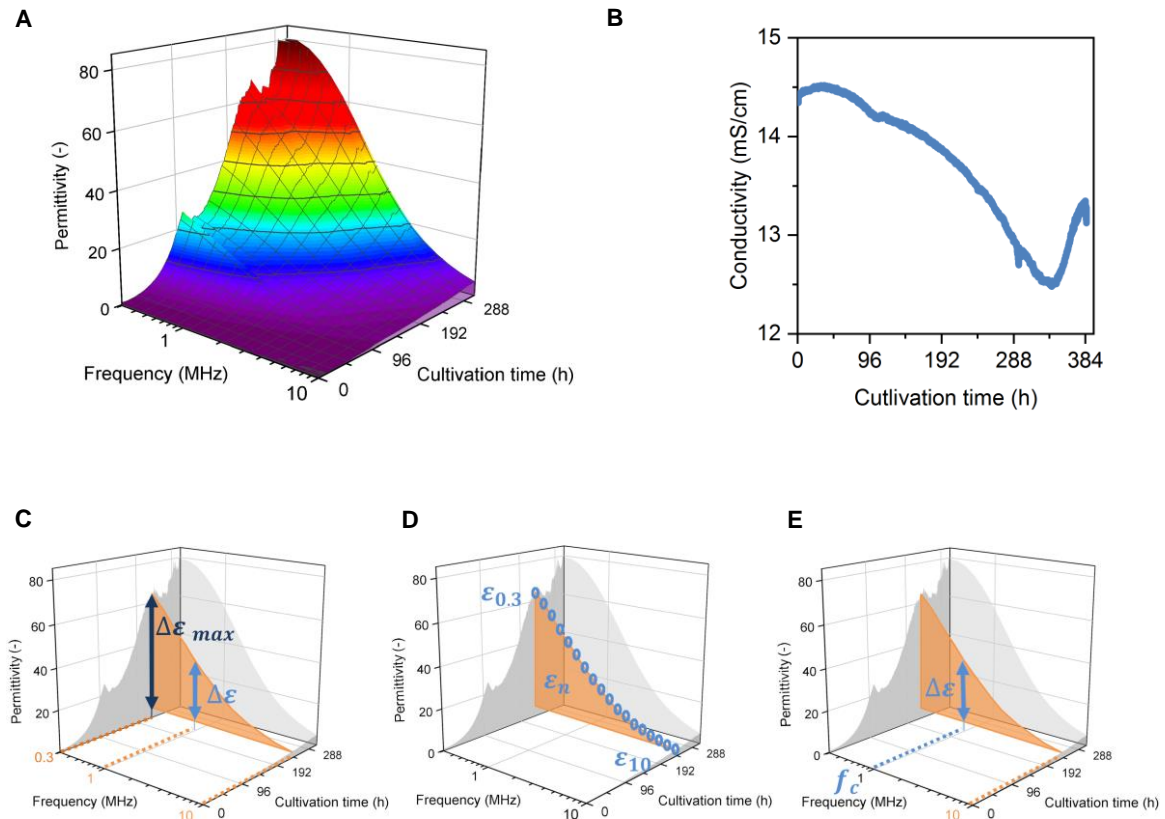


Figure 4.19 | Measurement data of the capacitance probe and input variables for biomass modeling. The Incyte biomass probe measured the capacitance and conductance of cell cultivations and was processed to (A) relative permittivity (ϵ ; dimensionless; color map illustrates permittivity levels) and (B) conductivity (σ). (C-E) To describe cell growth, the models required different input variables. (C) The first-order linear regression was tested with $\Delta\epsilon_{max}$ (f_1 and f_{max} ; here 0.3 MHz and 10 MHz) and $\Delta\epsilon$ ($f_1 \approx f_c$ and f_{max} ; here ~ 1 MHz and 10 MHz) of the β -dispersion. (D) The partial least squares (PLS) regression model required the spectroscopic data of ϵ at all distinct frequencies. (E) The Cole-Cole model processed data on $\Delta\epsilon$ and f_c . Furthermore, it required σ to calculate C_m and σ_i , two cell-specific dielectric parameters. Note: Figures are exemplary generated with the data set of the ATF-17pL perfusion cultivation.

Linear regression The first-order linear regression model was based on the correlation of online permittivity values to offline data on VCC or VCV. First, the signal linearity was tested with $\Delta\epsilon_{max}$ (typically used) and $\Delta\epsilon$ (proposed by Fogale). The regressions were compared by nSEC, and errors were averaged for all three perfusion cultivations (Table 4.6).

The permittivity difference $\Delta\epsilon_{max}$ described the VCC and VCV during the overall perfusion cultivation with an nSEC of 10 % and 8 %, respectively. When the cultivation was divided into (i)

“cell growth” phase, (ii) “cell growth and infection” phase and (iii) “cell decline” phase⁴, errors decreased partially. In particular, the cell growth and infection phase were described with a lower error of 5 % for both the VCC and VCV. When the permittivity difference $\Delta\epsilon$ was used, the errors decreased even further. The overall cultivation was described with an error of 8 % and 6 % for VCC and VCV, respectively. When the decline phase was excluded from the regression model, errors decreased to 3 % for the growth and infection phase. The regression model clearly indicated an overall higher signal linearity of $\Delta\epsilon$ compared to $\Delta\epsilon_{max}$ and described the VCV slightly better than the VCC. Hence, following biomass models and statistical analyses were based on the $\Delta\epsilon$ value during the cell growth and infection phase.

Table 4.6 | Signal linearity of $\Delta\epsilon_{max}$ and $\Delta\epsilon$ to offline data on viable cell concentration and viable cell volume in different phases of the cultivation.

Permittivity	Overall cultivation		Growth phase		Growth + infection phase		Decline phase	
	VCC	VCV	VCC	VCV	VCC	VCV	VCC	VCV
$\Delta\epsilon_{max}$	10 %	8 %	6 %	6 %	5 %	5 %	13 %	13 %
	± 4 %	± 1 %	± 3 %	± 2 %	± 1 %	± 2 %	± 9 %	± 8 %
$\Delta\epsilon$	8 %	6 %	4 %	3 %	4 %	3 %	6 %	12 %
	± 2 %	± 4 %	± 2 %	± 1 %	± 1 %	± 1 %	± 5 %	± 6 %

Normalized error of calibration (nSEC, Equation 30) was calculated for each ATF perfusion cultivation (ATF-M, ATF-17pL, ATF-34pL) and the value subsequently averaged. The overall cultivation was separated into a growth phase, growth and infection phase and decline phase. VCC = viable cell concentration; VCV = viable cell volume. $\Delta\epsilon_{max}$ is the permittivity drop from f_{min} to f_{max} ; $\Delta\epsilon$ from $\sim f_c$ to f_{max} . Indicates highest signal linearity for each evaluated phase.

The next step was to examine the regression quality of $\Delta\epsilon$ to VCC and VCV for each cultivation separately (Figure 4.20). In both cases, coefficients of determination (R^2) were equally high and further statistics revealed no significant difference between both linear regression estimations (F-test, $P \leq 0.05$). Accordingly, $\Delta\epsilon$ describes VCC and VCV equally well for individual perfusion cultivations.

⁴ Phases were consistently defined by the cell concentration (based on offline ViCell measurements) and time point of infection. Decreasing cell concentrations marked the onset of the decline phase and were not considered for the “cell growth and infection” phase.

4.5 Potentials and limitations for the use of a capacitance probe in virus production processes

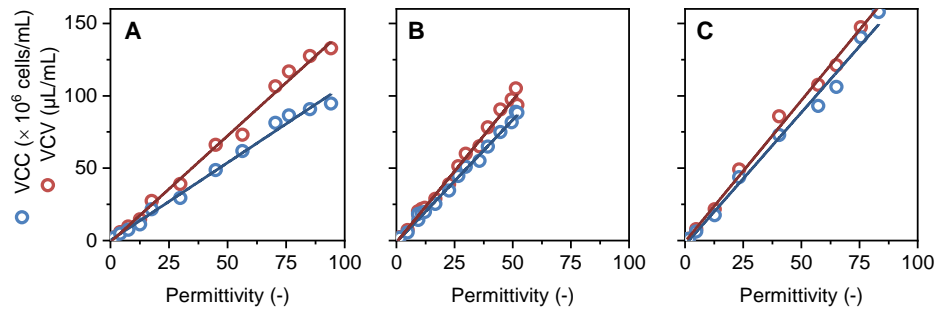


Figure 4.20 | Signal linearity of $\Delta\epsilon$ to the viable cell concentration and volume during the cell growth and infection phase of three ATF perfusion cultivations. Permittivity drop $\Delta\epsilon$ was correlated to viable cell concentration (VCC; blue circle) and viable cell volume (VCV; red circle). (A) ATF-M, (B) ATF-17pL, (C) ATF-34pL.

It was found that the first-order linear regressions (as shown in Figure 4.20) showed different slopes (also called “cell factor”) for the correlation of the permittivity signal to VCC and VCV, respectively. Therefore, the question arose, whether a median value of the slope would allow estimation of VCC and VCV in general (transferability). The median was calculated to 1.50 for VCC and 1.78 for VCV, respectively (Table 4.7).

Table 4.7 | Cell factors to determine the viable cell concentration (VCC) or viable cell volume (VCV) from the permittivity drop $\Delta\epsilon$.

Parameter	ATF-M	ATF-17pL	ATF-34pL	ATF-all
VCC	1.07	1.65	1.78	1.50
VCV	1.45	1.96	1.94	1.78

Note: Cell factors from three ATF perfusion cultivations were averaged to evaluate the transferability among each other.

In a next step, the signal linearity for each perfusion cultivation was evaluated and errors were expressed as SET (Equation 31). Averaged cell factors described perfusion cultivations ATF-17pL and ATF-34pL better than ATF-M, which showed a larger deviation. Furthermore, the VCV was equally or better described by online measured $\Delta\epsilon$ than the VCC (Table 4.8).

Table 4.8 | Statistical evaluation of a linear regression model to describe the viable cell concentration (VCC) and volume (VCV) of different perfusion cultivations with an averaged cell factor.

Parameter	ATF-M	ATF-17pL	ATF-34pL
VCC	23 %	6 %	9 %
VCV	13 %	6 %	5 %

Note: Calibration sets of all perfusion cultivations resulted in cell factors of 1.50 and 1.78 to determine VCC and VCV, respectively. The transferability was assessed by residual sum of squares analysis and expressed as percentage based on min/max measurement values (SET, Equation 31). Indicates estimated biomass parameter with highest prediction (lowest error).

To understand the poor signal linearity for ATF-M (23 %, Table 4.8) each cell factor (as listed in Table 4.7) was cross-validated for all perfusion cultivations (“validation set”, Table A7.5). The relatively high errors with ATF-M-derived cell factors, in comparison to low errors with cell factors derived from the other perfusion cultivations, clearly indicated that the linear regression differed from other cultivation measurements. This could not yet be explained. However, due to the small data set and in order to ensure an overall model evaluation, the ATF-M perfusion cultivation was retained in the testing set.

Partial least squares regression A PLS regression model was used to analyze the complex spectroscopic data set with 17 relative permittivity values ϵ generated for each measurement point. A training data set with corresponding offline values was used to create three models describing the VCC, VCV and viable cell diameter using the statistical analysis/graphing software OriginPro (described in Chapter 3.12.1). Also here, the cell decline phase was excluded due to the poor signal linearity.

First, a single data set was processed and the nSEC was determined from the PLS-derived biomass estimation to the offline measured VCC, VCV and cell diameter values (diagonals in Table 4.9). The errors of VCC and VCV were equally low with maximum 3 %, but increased to 28 % for the cell diameter. In a next step, the transferability of the calibration set to the other perfusion cultivations (“validation set”) was tested. Depending on the chosen cultivation and biomass estimate, SET strongly varied (Table 4.9). While the VCC was determined with an error of 12-41 %, the VCV was better covered with 9-31 %. The cell diameters of other perfusion cultivations were only insufficiently described with errors between 53 % and 308 %. Also here, ATF-M was identified as a perfusion cultivation with high discrepancies to the other cultivations. When ATF-17pL and ATF-34pL were solely considered, the VCV was determined with the highest precision and a maximum error of 12 %.

4.5 Potentials and limitations for the use of a capacitance probe in virus production processes

Table 4.9 | Statistical evaluation of a PLS model to describe the viable cell concentration, viable cell volume and cell diameter based on the relative permittivity spectra for three ATF perfusion cultivations.

Viable cell concentration

		Calibration set		
		#1	#2	#3
Validation set	#1	3 %	28 %	41 %
	#2	22 %	1 %	16 %
	#3	21 %	12 %	1 %

Viable cell volume

		Calibration set		
		#1	#2	#3
Validation set	#1	2 %	9 %	9 %
	#2	31 %	2 %	12 %
	#3	20 %	9 %	1 %

Cell diameter

		Calibration set		
		#1	#2	#3
Validation set	#1	15 %	129 %	308 %
	#2	53 %	5 %	243 %
	#3	103 %	108 %	28 %

Note: Standard error of calibration (nSEC; ) and standard error of transfer (SET;  indicates SET <10 %,  indicates SET <20 %,  indicates SET >20 %). #1 = ATF-M, #2 = ATF-17pL, #3 = ATF-34pL.

Next, the impact of the calibration data set on the model precision was investigated. Therefore, offline measured data was expanded by interpolated data every 6 min in accordance to spectroscopic measurement intervals. Therefore, intermediate values for VCC and VCV were derived from the linear regression model (as described above) and the cell diameter from a polynomial fit (Figure A7.11). This increased the training data set for, e.g., ATF-34pL cultivation from 10 to 1867 data points. When the extended model was validated, it resulted in an equal nSEC, but to increased SET when applied to the other perfusion cultivations (data not shown). Therefore, the approach was not further followed up.

Cole-Cole model The Cole-Cole model is a mathematical model based on physical principles of capacitance measurements. It allows the calculation of VCC, VCV and cell diameter at certain boundary conditions and assumptions (Chapter 2.3.3.1). The input data was generated from signals sampled every 6 min and encompassed $\Delta\epsilon$, f_c and σ . Then, the average membrane capacitance (C_m)

and intracellular conductivity (σ_i) were calculated for each perfusion cultivation following Equations 24 and 25. This required offline data on viable cell volume and online data on $\Delta\epsilon$, f_c and σ (details in Chapter 3.12.1). Since C_m and σ_i are assumed to be cell-specific constants in the Cole-Cole model, the mean values of both dielectric parameters were determined only for the cell growth and infection phase of each perfusion cultivation (Table 4.10).

Table 4.10 | Mean membrane capacitance (C_m) and intracellular conductivity (σ_i) for three ATF perfusion runs.

Run	C_m ($\mu\text{F}/\text{cm}^2$)	σ_i (mS/cm)
ATF-M	0.45	2.22
ATF-17pL	0.37	1.75
ATF-34pL	0.36	1.36
Mean	0.39	1.78

Mean values were calculated from measurements taken during the cell growth and infection phase.

In a next step, individual cell-specific dielectric properties and online data from the capacitance probe were used to calculate the cell diameter following Equation 23. Interestingly, calculated diameters were in the size range of the actual cell diameter, but strongly fluctuated (Figure 4.21 A). Taking a closer look on Equation 23, shows that the cell diameter is a function of C_m , σ_i , σ_0 and f_c . While C_m and σ_i were set constant and σ_0 was almost constant (not shown here), the strong fluctuation of f_c was reflecting the exact same pattern of the cell diameter variations (supportive illustration in Figure A7.11).

With the same, poorly estimated cell radius r , measured $\Delta\epsilon$ and constant C_m , the VCV was calculated following Equations 26 and 27 (Figure 4.21 B). Here, the cell volume fraction was calculated with high accuracy with nSEC low as 7 %, 3 % and 4 % for ATF-M, ATF-17pL and ATF-34pL, respectively. Considering Equation 26 and an initial small VCV ($\mu\text{L}_{\text{cells}}/\text{mL}_{\text{medium}}$), $\sigma_i \gg r_p$ and increasing $\Delta\epsilon$ while r remained in the same range, it became clear that the cell radius had only a minor effect on the VCV estimate according to the Cole-Cole model. This changed with the cell decline phase accompanied by a strong decrease in cell radius.

Then, the VCC was calculated according to Equation 28, but a strong discrepancy to offline data arose with increasing cell concentrations, in particular for ATF-M and ATF-17pL. The VCC determination was particularly sensitive to diameter changes due to its reciprocal linear correlation. This became even more evident in the decline phase (Figure 4.21 C). However, the VCC of ATF-34pL was described with a SET as low as 8 %.

Finally, the transferability of the Cole-Cole model among perfusion cultivations was assessed. Therefore, the EB66[®] cell-specific dielectric parameters C_m and σ_i were averaged (Table 4.10) and applied to estimate the biomass for each ATF perfusion cultivation. As observed previously, estimated cell diameters were poorly described and, thus, not considered for standard error calculations. The VCV was estimated with a SET of 10 %, 3 % and 12 % for ATF-M, ATF-17pL and ATF-34pL, respectively. Due to very large diameter discrepancies, errors for VCC calculation increased strongly (min. 47 % for ATF-34pL) and was not further statistically evaluated.

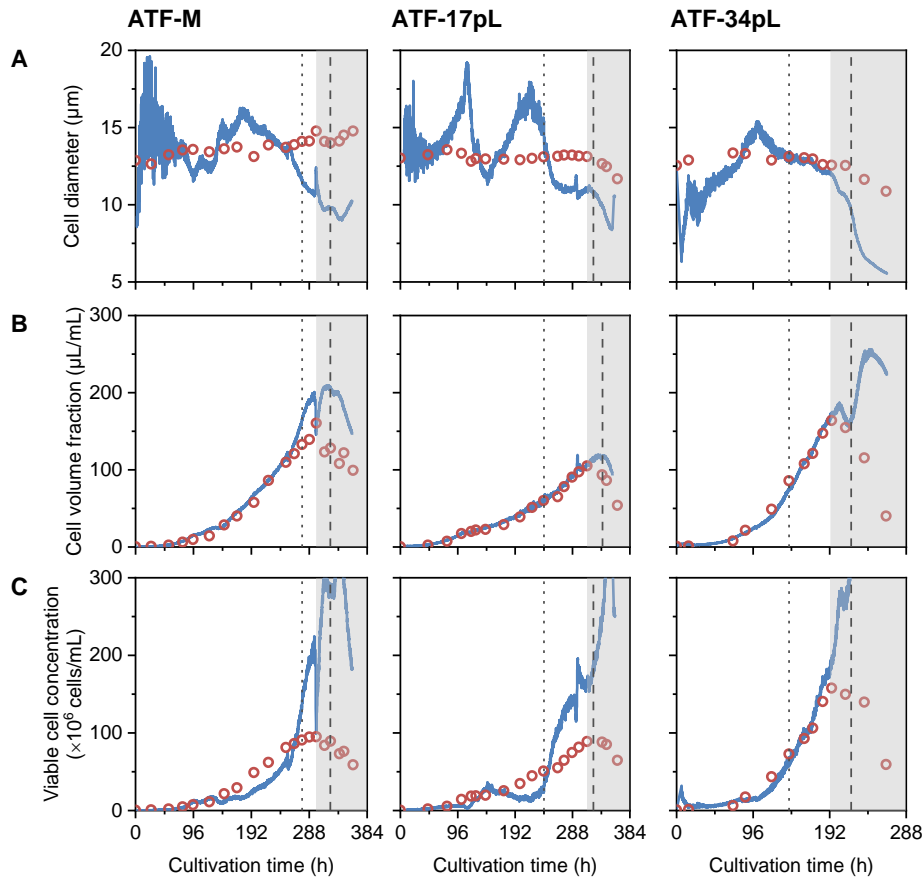


Figure 4.21 | Use of a Cole-Cole model to calculate biomass parameters based on online signals from the biomass probe. Individual ATF perfusion cultivations (described in detail in sections 4.3.2 and 4.4.2) were monitored and based on respective dielectric properties (C_m , σ_i) following parameters were calculated: (A) Viable cell diameter, (B) viable cell volume fraction and (C) viable cell concentration. Red circle = offline data; blue line = calculated value; grey area = cell decline phase (excluded from Cole-Cole model). Dotted vertical line indicates time point of infection, dashed vertical line indicates time point of maximum virus titer.

Discussion Three different models were evaluated to estimate VCC, VCV and cell diameter from capacitance probes. The measurement principle of the capacitance probe is based on the polarization of intact cells⁵ at different frequencies (but minimum two to obtain a low- and high-frequency “plateau” to measure $\Delta\epsilon$). This results in a β -dispersion, which is centered for most cells between 0.5 and 3 MHz [273, 274]. From there, the software provides data on dielectric parameters such as α , f_c , $\Delta\epsilon_{max}$, $\Delta\epsilon$, and σ (Chapter 2.3.3).

When taking a closer look on the β -dispersion between 0.3-10 MHz (as measured with the In-cyte probe), it was observed that signal plateaus were not strictly obtained in the low-frequency range (Figure 4.19). However, it remains to be investigated whether such measurement range remains meaningful for more accurate biomass estimation [151]. If required, other capacitance probes with a wider measurement range can be equally tested, i.e., the BioPAT® ViaMass with 0.1-20 MHz [275].

⁵ In the sense of a capacitance measurement, an intact cell is surrounded by a cell membrane, which allows ions moving under the influence of an electric field.

All models tested have been used before to estimate the biomass in batch or fed-batch culture [212, 213, 276], but little is known about their applicability to perfusion cultures. Therefore, the models were transferred to EB66[®] perfusion cultivations with an ATF perfusion unit using an Incyte biomass probe. Online estimations of VCC, VCV and cell diameter were subsequently assessed by statistical analysis based on nSEC and SET. Due to the small data set of three ATF runs, the transferability (SET) had to be tested among those cultivations.

(i) The linear regression model correlated the permittivity drop to offline data on the respective biomass parameter. In literature, two permittivity values are typically described: $\Delta\varepsilon_{max}$ and $\Delta\varepsilon$. Hence, both values were compared for the signal linearity to offline measured data. A better regression was obtained for $\Delta\varepsilon$ ($f_1 \approx f_c$) and confirmed a recent study [277]. Furthermore, it was reported that $\Delta\varepsilon$ was less sensitive for cell size changes due to the variable f_1 in the region of f_c [277]. This may be particularly advantageous for the estimation of VCC. Both biomass parameters (VCC, VCV) were best described in cell growth and infection phases. The viral infection had no influence on the regression quality, while the cell decline phase with sharply decreasing viabilities (data not shown) resulted in an increased regression error. Latter may have been due to a large difference between overall cell concentration measurements. The viability assay of the offline data is based on trypan blue exclusion and assigns cells into dead or alive binary system (not necessarily accurate [278]). The capacitance measurement, whereas, provides analog measurements on the impermeability of the cell membrane to charged ions with unclear threshold for determining a viable cell. Due to the poor comparability, the decline phase may remain difficult to describe. Therefore, this phase was excluded and the cell growth and infection phase was considered for further evaluation. The linear regression model described VCC and VCV of each perfusion cultivation equally well with no significant differences (Figure 4.20). However, when the cell factors were averaged and the transferability among the cultivations was tested, the VCV was described with a higher accuracy (SET) of 5-13 % (Table 4.8). Interestingly, differences in the cell factors were found for the three perfusion runs. This could not yet be explained, since obvious cellular changes were not seed and the bioreactor set-up was identical (metal and glass in measurement field may shift the signal but is not expected for changes in the slope [279]). As consequence, constant re-calibration may be required during the run. For now, well-established cultivation processes may be less affected, but it requires further investigations to increase the reproducibility between runs.

(ii) The multivariate frequency model based on PLS regression described VCV (SET 9-31 %) more accurate than VCC (Table 4.9). In contrast, the cell diameter was only poorly estimated by this model. When the calibration data set was significantly extended by data interpolation, calibration and predictive errors even increased, potentially, due to overfitting (reported elsewhere [280]). In consequence, the right choice of a robust calibration data set is essential for this tool, and precision may increase. However, PLS models require complex analysis, whereas further studies address even more complex approaches such as principal component regression (PCR) and artificial neural networks analysis (ANN) [281, 282].

(iii) For descriptive Cole-Cole modeling, dielectric parameters were derived from the β -dispersion and were used to step-wise calculate biomass parameters. First, C_m and σ_i values were calculated and the mean values were taken for further estimation of EB66[®] cell-specific values (0.4-0.7 $\mu\text{F}/\text{cm}^2$ and 1.5-5 mS/cm , respectively, being consistent with reported data [283-285]). Cell diameter estimations were strongly fluctuating, which was mainly due to the reciprocal impact of

changes in f_c . The biovolume fraction (VCV) was notably well calculated with nSEC of 3-7 % (Figure 4.21). On closer examination of Equation 26, the estimation of cell fraction $\varphi_{v,p}$ was dependent on C_m , which equational part became eliminated by its reciprocal part in r_p (Equation 23). As a result, $\varphi_{v,p}$ was predominantly defined by σ_i , which was beforehand determined by the volume fraction as described in Equation 25. The part of r_p played a subordinate role as $\sigma_i \gg r_p$. The VCC was subsequently calculated (Equation 28), but since it was particularly sensitive to the reciprocal of r_p , the estimate covered offline data only sparsely (with exception of ATF-32pL with 8 % nSEC). The high transferability among the perfusion cultivations was confirmed by averaging the C_m and σ_i values. The SET for the VCV was determined with maximum 12 %, whereas other errors increased (data not shown). The Cole-Cole model assumed constant C_m and σ_i values. This may constrain the practicability of the model as complex physiological alterations can occur during perfusion cultivations (Figure 4.24) [286-288]. An even stronger fluctuation was observed for the f_c value having a major impact on the calculated cell diameter and VCC. It requires further detailed investigations, potentially including a cross-validation to similar sensor types. Nevertheless, the Cole-Cole equation can be of great use not only in calculating the VCV with high accuracy, but also to gain further insights into the cellular state beyond usual cell analysis assays.

4.5.2 Dielectric properties of a cell population

Intact cells possess a passive electrical (dielectric) property in an electric field. With the advancing understanding of dielectric spectroscopy measurements, various models such as the Pauly-Schwan and Cole-Cole approaches were developed, which describe biological cells in an electric field by the parameters f_c , Cole-Cole α , C_m , and σ_i . Using experimental data set of perfusion cultivations, these dielectric properties were determined to gain a deeper understanding of the cell population in real-time. In the field of virus production, an online signal indicating virus dynamics would be ideally desirable.

Characteristic frequency The inflection point of the β -dispersion is described by f_c . Previous discussions on the Cole-Cole model referred already to strong f_c fluctuations impairing biomass estimation. It became obvious that f_c fluctuated particularly at the beginning of the cultivation at low cell concentrations (Figure 4.22). Values stabilized after 48 h of cultivation at concentrations of $2\text{-}4 \times 10^6$ cells/mL. In the same time, erroneous f_c measurements occurred providing repeated values of exactly 0.5 MHz (here already removed). In combination with a pulse filter and high integral time (noise smoothing function over past few measurement points by ArcView controller), fault values were entrained to subsequent measurements. In contrast to the other perfusion cultivations, ATF-34pL was inoculated from a cryo bag and f_c decreased from high values, which may have been linked to the missing equilibrium time of the probe. Due to the high signal noise primarily at low cell concentrations, the subject was not further addressed. Noticeably, certain manual interventions (in particular methionine addition) influenced the f_c signal directly (Figure 4.22 B). To the end of the cultivations, f_c values generally increased being associated with cell lysis. Overall,

EB66[®] cells had a f_c mostly in the range of 0.7 and 1.5 MHz. An association to virus infection or maximum virus titers could not be concluded.

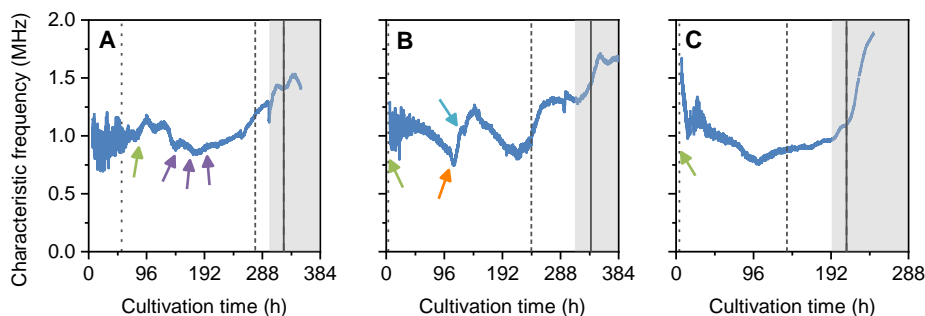


Figure 4.22 | Changes of the characteristic frequency (f_c) during perfusion cultivations. (A) Manual ATF perfusion rate control (ATF-M); (B) automated perfusion rate control (ATF-17pL); (C) inoculated from cryo bag and automated perfusion rate control (ATF-34pL). Dotted vertical line indicates start of perfusion pump; dashed vertical line indicates time point of infection; grey area indicates cell decline phase; solid vertical line indicates maximum virus titer. Arrows indicate manual interventions (green = start of perfusion operation, purple = sodium chloride addition, orange = methionine addition, turquoise = cell dilution for cryo bag preparation).

According to the Cole-Cole model, f_c is correlated reciprocally to the cell size. This relation was now further evaluated for the three ATF perfusion cultivations. Interestingly, the frequency seemed to be associated by the diameter but trends were contradictory (Figure 4.23). While f_c increased with increasing cell diameters in ATF-M, it decreased for ATF-17pL and ATF-34pL. Considering the cell diameter progression for typical cultivations, ATF-M showed a unique behavior due to rising instead of falling cell sizes (partially in Figure A7.11 and Figure 4.25).

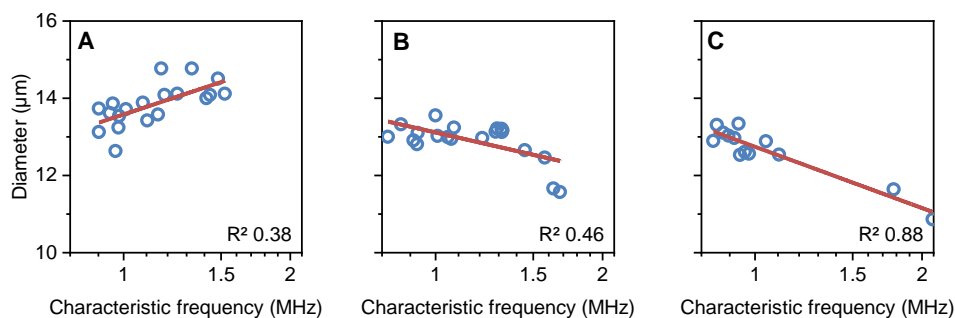


Figure 4.23 | Correlation of the characteristic frequency (f_c) to the cell diameter. Offline data on cell diameter was obtained from ViCell measurements (blue circle) and a regression was calculated (red line). (A) ATF-M; (B) ATF-17pL; (C) ATF-34pL.

Membrane capacitance and intracellular conductivity For the simplified Cole-Cole model, dielectric parameters C_m and σ_i were assumed to be biological constants. Conversely, the model allowed to calculate actual values of both parameters based on offline measured data (Figure 4.24, blue circle; following Equations 24 and 25). Previous studies reported a close correlation of both parameters to virus replication allowing the online monitoring of virus dynamics, while other data

was recorded offline. The offline data on C_m and σ_i could not be directly associated to the YFV or ZIKV replication. Hence, the resolution was increased: VCC were derived from the regression model and data on cell diameter were interpolated (Figure A7.11). The extended set of dielectric parameters met the offline data but still not enabled the tracking of virus dynamics. Overall, ATF-M and ATF-17pL cultivations showed higher σ_i fluctuations than ATF-34pL, potentially due to frequent manual interventions. With the decrease of viability, σ_i increased slightly (Figure 4.24).

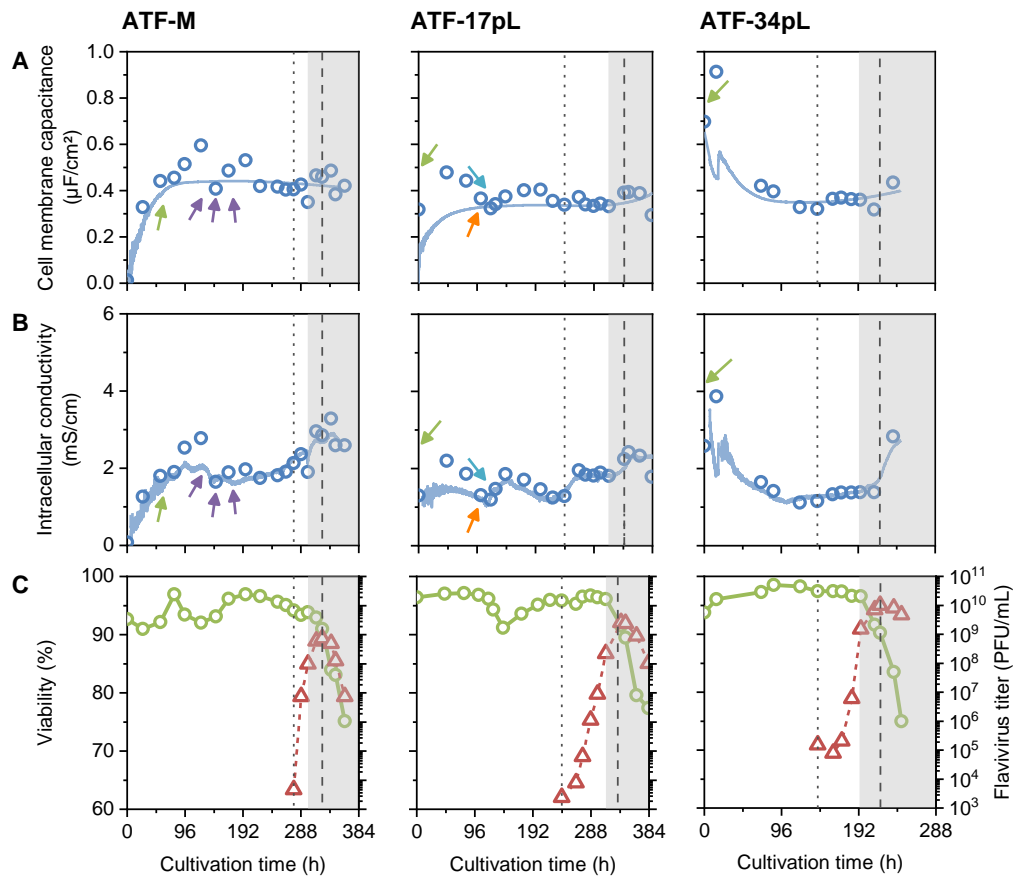


Figure 4.24 | Dielectric parameter changes in C_m and σ_i during three perfusion cultivations. Both dielectric parameters were calculated with offline (blue circle) and online data (interpolated cell diameter, permittivity-derived viable cell volume; blue line) in accordance to Equations 24 and 25. **(A)** Cell membrane capacitance; **(B)** intracellular conductivity; **(C)** cell viability (green circle) and virus titer (red triangle; ATF-M: YFV; ATF-17pL and ATF-34pL: ZIKV^{RJ}). Dotted vertical line indicates time point of infection, dashed vertical line indicates time point of maximum virus titer, grey area indicates cell decline phase. Arrows indicate manual interventions (green = start of perfusion operation, purple = sodium chloride addition, orange = methionine addition, turquoise = cell harvest for cryo bag preparation).

Cole-Cole α The Cole-Cole α ($0 \leq \alpha < 1$) coefficient reflects the distribution of polarization relaxation times, which relate to cell size heterogeneity. Thus, a linear relation of Cole-Cole α to the cell size distribution was investigated (derived from ViCell measurements and distribution expressed as full width at half maximum; Chapter 3.12.2). EB66[®] cell sizes changed during perfusion cultivations. Interestingly, while cells typically shrank in the decline phase, the ATF-M cultivation revealed the opposite trend (Figure 4.25 A). At the beginning of the cultivation, the width in

diameter changes was around 4 μm and decreased after 96 h to 3 μm for ATF-M and ATF-17pL, and to 2.5 μm for ATF-34pL. With the onset of the cell decline phase, the heterogeneity increased to 5 μm and above. The width of the distribution correlated to the Cole-Cole α derived from the Incyte probe. It revealed a linear correlation to the cell size heterogeneity, whereas coefficients of determination were low (Figure 4.25 B).

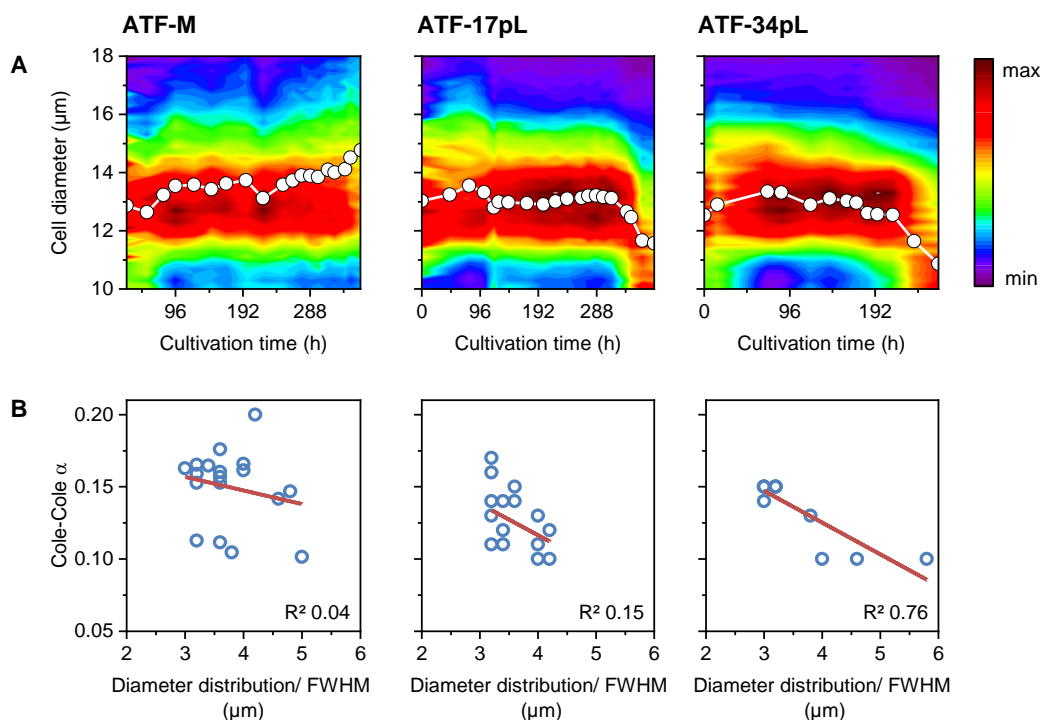


Figure 4.25 | Cell size changes during perfusion cultivations and the correlation of Cole-Cole α to the cell size heterogeneity. (A) Median cell diameter (white circle) and heat map indicating the frequency of cells in distinct cell diameter clusters (as derived from offline ViCell measurement; red = highest frequency, purple = lowest frequency). (B) Offline data on the cell size distribution (expressed as full width at half maximum, FWHM; blue circle) and linear correlation to Cole-Cole α (red line).

Discussion The data analysis of the multi-frequency capacitance measurement with the Cole-Cole equation provided additional information on cellular dielectrics. First, the characteristic frequency f_c was evaluated, usually considered to indicate diameter changes [158, 289]. A linear correlation was observed, but while two cultivations revealed an increasing f_c with decreasing cell diameters, the relation was reversed for ATF-M (Figure 4.23). In latter cultivation, cell diameters surprisingly increased to the end of the cell growth phase. This opened the question, if f_c is exclusively dependent on the cell diameter. The f_c value was strongly drifting with the supplementation of methionine, while cell diameters remained constant. When taking a closer look at Equation 8 of the Cole-Cole model, a correlation of f_c to σ_i and C_m became evident. While C_m remained relatively constant, σ_i was affected (Figure 4.24). The intracellular conductivity σ_i was previously described to change with the metabolic and physiological state of a cell [288]. This may explain observed σ_i changes, when the essential amino acid was added. Furthermore, it was reported that σ_i increased due to uptake and accumulation of free ions from the medium (can be derived from

media components but also released from lysed cells) in the cytoplasm [285, 291]. Both effects may explain the observed increase in f_c signals, while cell diameters remained constant. To the end of the cultivation, f_c values increased clearly before the onset of a cell decline phase as measured with the ViCell. Considering cell membranes becoming more permeable, free ions leached and accumulated in remaining intact cells causing increased σ_i (Figure 4.22). In consequence, σ_i and f_c may allow to monitor early cell decline phases with a higher sensitivity than trypan blue exclusion assays.

With cell inoculation and capacitance measurements, f_c signals were strongly fluctuating and subject to frequent measurement interruptions. It appeared that signals stabilized over time (exclusively with increasing cell concentration). The ArcView controller applied integrated noise filtering algorithms (integration of last measurement points). This may have resulted in a prolonged signal settling phase also explaining the time delay, as visible for σ_i and C_m (Figure 4.24). Further capacitance measurements may need to be performed at lower data smoothing settings and results to be compared.

The membrane capacitance C_m was following a similar trend to σ_i and online data showed a smoother progression than offline data due to associated cell diameter fittings (Figure 4.24, Figure A7.11). On the one hand, diameter interpolation between offline measured data points increased the resolution to online capacitance measurement intervals (every 6 min) and reduced potential assay-related cell size changes (e.g. time of cells outside of the bioreactor system until measurement), but, on the other hand, may have contributed to the loss of sensitive information at time point of sampling. During the cultivation with less manual intervention, C_m values were the same, either determined by offline or online data. In general, C_m is simplified to be a constant describing the cell membrane smoothness. More recent studies, however, revealed cell state-dependent changes, e.g., due to viability, apoptosis, exocytosis, protrusions, which were associated with decreasing C_m [292, 293]. Here, cell sizes decreased mainly in the cell decline phase, which was only weakly accompanied by increasing C_m signals by maximum 10 %. This suggested that the granularity of remaining cells slightly increased by zeiosis, being typically described for apoptotic cells [294, 295].

Finally, the Cole-Cole α parameter was investigated to describe the distribution of cell sizes. Calculated by the ArcView software, initial α values of 0.1 appeared falsely at the beginning of data recording and were excluded for further interpretation. Presumably, cell concentrations were too low and relating permittivity increments too noisy for accurate α determination. Nevertheless, with cell concentrations above $\sim 5 \times 10^5$ cells/mL, α reflected the population heterogeneity during perfusion cultivations and increased with a more homogeneous cell culture. However, regression coefficients were low and more detailed investigations may be required (ideally simple modes such as batch cultivations) to improve the correlation [296].

For viral vaccine production, online probes to monitor virus dynamics are still challenging [297, 298]. Recent studies found a correlation of dielectric parameters to the replication phases of enveloped viruses (IAV, lentivirus, baculovirus) [299]. In brief, the study reported on intracellular virus accumulation coinciding with elevating σ_i and C_m signals (1-5 % increase per hour) and virus release with a strong decreases in C_m and σ_i of some 20-30 %. These findings were transferred to the present results. First, data on viable cell diameters were interpolated (as explained above) to overcome resolution limitations by offline data measurement, similar to the approach described by

Petiot and colleagues. When cells were infected with either YFV and ZIKV in perfusion mode, C_m increased only by a rate of 0.1 % per hour or even decreased by the same rate. However, σ_i increased throughout the infection (“intracellular virus accumulation” phase) with a rate of 0.5 % per hour but still below reported values. The value increased even stronger with the cell decline phase. As discussed above, σ_i is in strong dependence of free ions in the medium and the cellular metabolite state. Such small signal changes could be equally associated to varying perfusion rate changes or impaired cell status, either due to the higher cell concentrations, but also virus infection. Finally, simpler cultivation operations, i.e. batch mode, can help to answer this open question. In the paper from Petiot, the virus release correlated with a strong decrease in both dielectric parameters. However, this could not be confirmed and flavivirus titers peaked at rather elevated levels of C_m and σ_i . Finally, flavivirus dynamics could not be monitored in perfusion cultivations. Conversely, low viral interference with dielectric parameters enabled robust biomass monitoring also during the virus infection phase. To detect small membrane-surrounded particles, such as virions, it will require a new type of biomass probe operating at a higher frequency range up to approximately 300 MHz.

4.5.3 Summary

Capacitance probes are a useful tool for online biomass estimation. Its applicability for perfusion cultivations was never described in detail. Here, three biomass models were assessed to describe VCC, VCV and cell diameter. A first-order linear regression model was used to fit $\Delta\varepsilon$ to offline measured data with the resulting regression coefficient considered as “cell factor”. The regression described accurately both VCC and VCV during the cell growth and infection phase up to very high cell concentrations. Slightly varying cell factors between cultivations were averaged and applied to other perfusion cultivations with root-mean-square standard errors of about 5-13 % for VCV. Subsequently, a partial least squares (PLS) regression model was applied to process spectroscopic frequency data. It required complex analysis and estimated VCV of other perfusion cultivations with maximum errors of 9-31 %. Finally, the Cole-Cole equation was used to calculate the parameter such as cell diameter, VCV and VCC. It required the determination of membrane capacitance C_m and intracellular conductivity σ_i , and the assumption that both are constant. This enabled the calculation of VCV with high accuracy (3-12 %). Overall, all models can be improved by outlier removal and elimination of certain calibration input data (here ATF-M). The raw data set of the ArcView controller provides further parameters such as f_c and Cole-Cole parameter α . The critical frequency f_c seems to correlate with cell diameter changes, but the tendency was not clear. The signal could be further used to detect the cell decline phase in very early stages. The Cole-Cole α was associated to the cell size distribution and increased with a more homogeneous cell population in size. In the end, C_m and σ_i of the BHK-21_{SUS} cells were investigated to identify virus-related changes. So far, flavivirus replication, i.e., YFV and ZIKV, could not be directly monitored with the capacitance probe. On the contrary, virus infection did not impair biomass signals, and biomass estimations were possible during the infection phase. Overall, the biomass probe is an essential tool to monitor cell growth and adds value at many levels of a cultivation process, e.g., options for advanced process control, continuous biomass monitoring and higher measurement accuracy compared to manual cell counting.

4.6 Hollow fiber membranes for perfusion cultivations

Membrane-based perfusion systems are widely equipped with hollow fiber modules and membranes made of PES with a nominal cut-off of 0.2 μm . When such a membrane was used for intensified flavivirus production, virions of 50 nm were strongly retained in the bioreactor system and could not be harvested with the permeate. To understand the virus retention principle and evaluate options for continuous virus harvest using membrane-based retention devices, different hollow fiber membranes were first characterized and then tested in cross-flow filtration mode for filter fouling using BHK-21_{SUS} cells infected with YFV.

4.6.1 Membrane characterization

To cover a large variety of different commercial hollow fiber membranes intended for general tangential flow filtration application, a wide range of main membrane materials used such as modified PES, PES, PS, ME and PE was used. If available, two pore sizes were tested to either retain or harvest the virus (based on nominal cut-off)⁶. This resulted in a reduced sample set of eight hollow fiber modules.

Single hollow fibers were removed from the filter housing. The fiber wall thickness was measured with a typical range between 0.10-0.15 mm. With 0.45 mm and 2.75 mm wall thickness, large-pored PS (M6) and PE (M8) membranes were significantly thicker (Table 4.11). The increased thickness was assumed to increase the effective filtration surface and to reduce direct membrane blockage (Table 4.13).

Subsequently, the pore size distribution of each membrane was measured by capillary flow porometry (Chapter 3.13.1). The membrane-specific exclusion limit (cut-off) was estimated at a cumulative pore size distribution of 90 % (D_{90}) and ranged from 0.08 μm to 1.69 μm (Figure A7.12, Table 4.11). While small-pored membranes (<0.09 μm) most likely retain a 50 nm virus particle, larger-pored membranes (>0.34 μm) can be considered to be permeable based on the pore size (Table 4.13). The width of the pore size distribution was described with the 90th percentile and expressed in relation to the estimated cut-off. Large-pored membranes tended to have a broader pore size distribution. While the PS membrane (M5, M6) had very distinct pore sizes, the PE material (M8) showed a highly heterogeneous pore size distribution (Table 4.11). This can be associated to increased pore selectivity (larger pores enable higher local permeate fluxes) resulting in a higher susceptibility to local fouling (Table 4.13).

⁶ Nominal cut-offs as specified by manufacturers are not provided here to maintain confidentiality. However, for comparability of findings, pore size distributions based on capillary flow porometry measurement are presented.

Table 4.11 | Overview on physical characteristics of hollow fiber membranes.

Membrane	Fiber wall thickness *	Estimated cut-off (D_{90}) #	Pore size distribution *
1 mPES	0.15 mm	0.09 μm	0.03 μm (30 %)
2 mPES	0.15 mm	1.08 μm	0.51 μm (47 %)
3 PES	0.10 mm	0.18 μm	0.04 μm (24 %)
4 PES	0.10 mm	0.37 μm	0.16 μm (44 %)
5 PS	0.13 mm	0.08 μm	0.01 μm (14 %)
6 PS	0.45 mm	0.34 μm	0.07 μm (22 %)
7 ME	0.15 mm	0.25 μm	0.07 μm (26 %)
8 PE	2.75 mm	1.68 μm	1.87 μm (111 %)

* Measured with digital vernier caliper with an error of ± 0.05 mm; # estimated cut-off for a cumulative distribution at 90 %; * size range width at 90th percentile and percentage to estimated cut-off in brackets.

In a next step, the electrokinetic potential of membranes and potential foulants was assessed. First, the streaming potential of each membrane material was measured at pH 7.2 and the zeta potential calculated (Chapter 3.13.2). The zeta potential was about -24 mV for most materials, whereas the mPES material showed a slightly lower surface charge with -20 mV (Table 4.12). Then, the zeta potential of the infected cell culture broth (containing colloids such as cells, particles and virions) was calculated (Chapter 3.13.3). Based on the electrophoretic mobility of all particles, a zeta potential of -16.4 ± 0.4 mV was determined at pH 7.2 and physiological salt concentration of the BGM medium. Comparing the potential of the inner membrane and potential foulants, both negative zeta potentials indicated a theoretical mutual repulsion resulting in reduced fouling. This repulsive effect was slightly lower for the mPES material (Table 4.13).

When comparing water contact angles for each material (as stated in literature), values ranged from 66° for PS to 94° for PE materials (Table 4.12). The smaller angle is typically associated to increased hydrophilicity and repulsion of organic molecules. In consequence, the hydrophobic PE membrane was theoretically most susceptible for deposition and fouling (Table 4.13).

Table 4.12 | Overview on measured zeta potential and water contact angle for tested hollow fiber membrane materials.

Membrane	Material	Zeta potential * (mV)	Water contact angle # θ_w ($^\circ$)
2	Modified polyethersulfone (mPES)	-19.7 ± 0.4	n/a
3	Polyethersulfone (PES)	-24.5 ± 0.3	68 [300]
6	Polysulfone (PS)	-23.0 ± 1.8	66 [301]
7	Mixed Ester (ME)	-24.0 ± 0.7	n/a
	- Cellulose acetate	-	44 [302]
	- Cellulose nitrate	-	67 [302]
8	Polyethylene (PE)	n/d	94 [300]

* Measured in 5 mM KCl electrolyte solution at pH 7.2 ± 0.1 ; # as stated in literature for 20 $^\circ\text{C}$. n/d = not determined due to large inner fiber diameter; n/a = not available due to unknown composition.

Table 4.13 | Structural and physicochemical membrane properties and their theoretical impact on membrane fouling.

Membrane	Fiber thickness	Pore size *	Size distribution	Repulsion with foulants	Water contact angle
1 mPES (0.09 μm)	○	–	○	+	?
2 mPES (1.08 μm)	○	+	–	+	?
3 PES (0.18 μm)	○	○	+	+	○
4 PES (0.37 μm)	○	+	–	+	○
5 PS (0.08 μm)	○	–	+	+	○
6 PS (0.34 μm)	+	+	+	+	○
7 ME (0.25 μm)	○	○	○	+	?
8 PE (1.68 μm)	+	+	–	?	–

Increased fiber thickness, narrow pore size distribution, high repulsion and low water contact angle were considered to reduce filter fouling. Properties were categorized in (–) unfavorable, (○) neutral, (+) beneficial or (?) unknown for reduced fouling. The more (+), the less susceptible to fouling and the better the membrane. * Based in the pore size, membranes were grouped for virus permeability following – < ○ < +.

Finally, all membrane materials were examined with SEM imaging to investigate structural membrane properties in detail. Differences among tested hollow fiber membranes were evaluated for the susceptibility of membrane fouling and are summarized in Table 4.14.

Judged mainly based on the frontal view of the inner membrane (Figure 4.26, Figure A7.14), the material roughness was assessed. An increased roughness is typically associated with accelerated membrane fouling due to enhanced foulant deposition. A highly jagged material surface was found for the large-pored mPES (1.08 μm) membrane. The roughness decreased from ME (0.25 μm), PES (0.18 μm), PS (0.08 μm) materials to very smooth PS (0.34 μm) and PE (1.87 μm) structures. Apart from this, the inner surface porosity was evaluated, where isolated pore entrances typically show higher local polarization (tendency for accumulation of foulants) and increased fouling. SEM imaging revealed a remarkably high surface porosity for the PS (0.34 μm) membrane, which decreased from ME and PES to PE and PS (0.08 μm) membranes. Due to the high material roughness and deep structures of the mPES membrane, its visual evaluation became difficult. However, funnel-shaped pore channels were present, as equally observed for the PE membrane, turning both membranes theoretically susceptible for rapid particle entrapment. In contrast, the PE (0.34 μm) membrane had a very open pore structure potentially leading to high permeate fluxes and reduced pore blockage.

Subsequent cross-section SEM imaging helped to further characterize surface roughness (Figure A7.13). While the surface should be ideally smooth for formation of only thin boundary layers at increased cross-flow velocity [303], the overall porosity is typically chosen high for increased permeate fluxes and low particle deposition. The mPES membrane had a very high surface roughness with distinct and deep valleys. The PES, PS (0.08 μm) and ME membranes, whereas, had a smooth structure flatter than the PS (0.34 μm) and PE membranes revealing a wavy surface. The overall porosity could be equally assessed by cross-section images (Figure A7.13). The mPES material had a high porosity, followed by decreasing porosities with PS (0.34 μm), ME, PES, PE and finally PS (0.08 μm) membranes. In particular the front view of the outer surface revealed a strong asymmetric structure for most membranes with the exception of the PE membrane (Figure A7.14).

A closer examination of the PS (0.34 μm) membrane revealed a high overall porosity in the first inner half, which then became more compact to the outer side (Figure A7.15).

Table 4.14 | Structural membrane properties (based on SEM imaging) and their theoretical impact on membrane fouling.

Membrane	Material roughness	Surface porosity	Pore structure	Surface roughness	Overall porosity
2 mPES (1.08 μm)	–	?	–	–	+
3 PES (0.18 μm)	○	○	○	+	○
5 PS (0.08 μm)	+	–	○	+	–
6 PS (0.34 μm)	+	+	+	○	+
7 ME (0.25 μm)	–	○	○	+	○
8 PE (1.68 μm)	+	–	–	○	–

Low material roughness, high surface porosity, open pore structure, low surface roughness and high overall porosity were considered to reduce fouling. Properties were categorized in (–) unfavorable, (○) neutral, (+) beneficial or (?) unknown for reduced fouling. The more (+), the less susceptible to fouling and the better the membrane. Note: Only a small selection of commercially available membranes could be analyzed and was chosen to cover the broad availability of materials used in biotechnological applications.

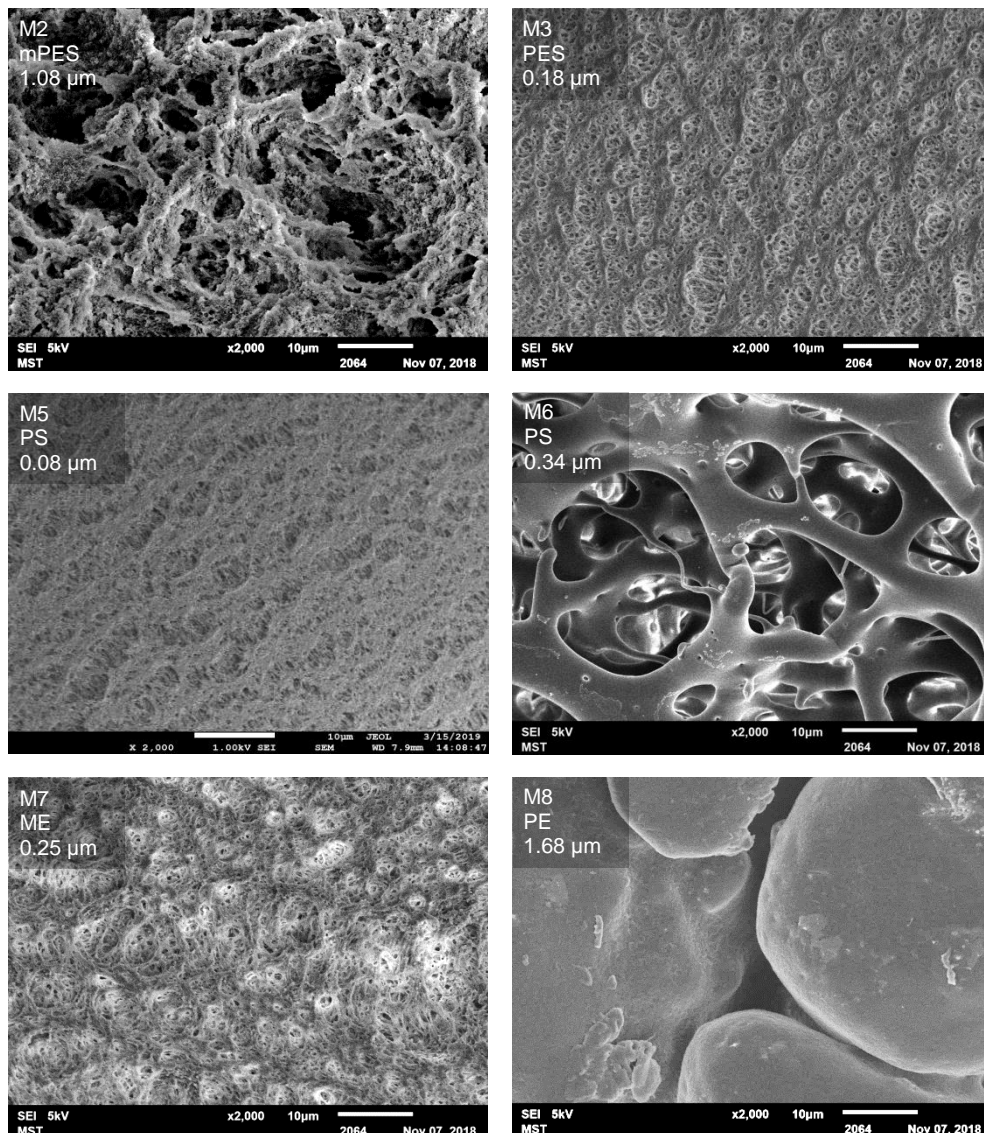


Figure 4.26 | SEM images of inner membrane surface of different hollow fiber materials. A 2000-fold magnification allowed direct comparison of roughness, surface structure and porosity of unused membranes.

Discussion From a wide range of hollow fiber modules developed or recommended for various tangential flow filtration applications (e.g. bioreactor perfusion, concentration, diafiltration and clarification), eight commercially available membranes were selected and characterized for theoretical virus retention and filter fouling (summarized in Table 4.13). If available, a small- and large-pored membrane were selected from the same material to understand the impact of the material or estimated cut-off on virus retention. While small-pored membranes can be suitable to accumulate the product in the bioreactor, large-pored membranes are potentially employed to continuously harvest virions (~50 nm). In both cases, filter fouling should be reduced to a minimum as it finally terminates the filtration process. Membrane cut-offs were estimated by first bubble point detection

and were grouped into strong-rejecting membranes (≤ 90 nm; mPES, PS), average-rejecting membranes (< 0.25 μm ; PES, ME) and low-rejecting membranes (≥ 0.34 μm ; mPES, PES, PS and PE).

The pore size distribution of membranes can be controlled to a certain extent by the manufacturing process, but is typically characteristic for the used material [174]. For the PES, PS and ME membranes, the 90th percentile of all pores were allocated in a distinct range of about 25 % in relation to the cut-off. The large-pored mPES and PE membranes, whereas, spread above 47 %. Heterogeneous pore distributions are more susceptible to fouling as larger pores allow higher local fluxes, which turns inner pore surface area to be prone for concentration polarization and deposition until pore blockage. Thus, homogeneous pore size distributions are generally considered better suited for long-term filtration operation [304].

In addition, the zeta potential was determined to assess repulsion effects. In theory, evenly charged colloids beyond the critical zeta potential (around -10 mV) with high absolute values are repulsive and therefore desirable [305, 306]. Here, the zeta potential of the inner membrane surface and the culture broth with cells revealed both negative values exceeding -17 mV. Thus, an advantageous repulsive effect between all tested membranes (measured at similar salt conditions) and the culture broth (measured at operating conditions) can be expected. However, the zeta potential is highly influenced by the pH value, salt concentration or ion valence, which may vary to a certain extent during the cultivation [305, 307].

Information regarding the water contact angle for each membrane material was obtained from literature. Thereby, PES and PS materials can be described as moderately hydrophilic, while the PE material has a hydrophobic character. Unfortunately, the blend of the ME material was unknown, but as both components (cellulose nitrate and cellulose acetate; latter at typically low content) have low water contact angles (Table 4.12), the resulting ME material can be expected to have a contact angle in between and thus can be considered hydrophilic [308]. Details about additional modifications of the mPES material are not known, but the raw material PES is typically functionalized to deliberately increase surface hydrophilicity, which clearly enhanced its roughness. Alternatively, the water contact angle can be determined experimentally, which takes influencing parameters such as surface energy, surface roughness and porosity of the specific membrane into account. Hydrophilic membranes are considered to have a repulsive effect for the deposition of organic solutes and possess a better wettability and lower initial breakthrough pressure. Therefore, hydrophilic membranes can be of great interest for reduced filter fouling [173, 188].

SEM imaging revealed significant structural differences of tested membrane materials, and properties were assessed for the theoretical fouling behavior (see Table 4.14). While a high roughness of the inner membrane surface can hinder direct pore blocking (steric exclusion of particles and non-flush deposition on highly fissured surfaces), a reduced overflow velocity in valley-like structures can equally enhance deposition [192]. Such loose deposits are particularly sensitive for cake compression, when negative pressure on the permeate side increases [193]. This could be assumed especially for mPES membranes, which additionally possesses a high specific surface area that potentially enhances particle adsorption. Deep valley-like pore channels, as observed for the PE membrane, narrowed pores and are unfavorable due to enhanced particle entrapment and membrane blockage. In contrast, the PS membrane (0.34 μm) had a very smooth and open pore structure, as well as a high overall porosity so that foulants can freely penetrate the membrane, but are finally retained in deeper, more dense layers. This can enable high initial fluxes, but as deposits enrich within the membrane and physical countermeasures (e.g. increased flow velocity, backflushing)

may not take similar effects, full blockage will be inevitable. A size-selective and flat membrane surface, as observed especially for PS (0.08 μm), but also for PES and ME membranes, enables thin boundary layers and optimum abrasive effects of the surface velocity. This reduces concentration polarization. However, if the surface porosity is low, such filters can react sensitive on pore narrowing with increasing membrane resistance. In dependence on the pore size and size of foulants, small-pored membranes (in the range of ultrafiltration application) may be even less affected by fouling due to steric exclusion for pore narrowing or pore blocking (i.e. 0.08 μm PS membrane).

As a result of the membran characterization, the large-pored PS (M6) membrane seems to combine suitable physicochemical and structural properties that can lead to a higher resistance against filter fouling, while enabling virus permeability. In contrast to the PS membrane, the widely used PES membrane has a pore size closer to the virus particle size, and an increased tendency for fouling. For virus-rejecting membrane candidates, the use of a small-pored PS membrane seems to be promising. To test this assessment, cross-flow experiments under real perfusion cultivation conditions were performed to confirm theoretical findings on filter fouling and virus retention as described in the next paragraph.

4.6.2 Performance of membranes in cross-flow operation

To evaluate fouling behavior and virus retention of the hollow fiber modules under real process conditions, a 2.5 L bioreactor system was connected to a TFF perfusion unit with a peristaltic pump. BHK-21_{SUS} cells were cultivated in batch mode and infected with YFV. Two days later, the cross-flow operation was initiated and hollow fiber membranes (M1-M8) were tested consecutively at adjusted flow velocities (to maintain a shear rate of 2000 s^{-1} ; Equation 32) and adjusted permeate fluxes (to maintain a surface-specific permeate flux of 33 $\text{L}/\text{m}^2/\text{h}$). This enabled comparable filtration conditions for all membranes, which differed in hollow fiber diameters and membrane surface areas (as stated by manufacturers). The pressure progression in the inlet, outlet and permeate tubing was recorded and the permeate stream was recycled to the bioreactor vessel (details in Chapter 3.13.5).

During the filtration experiment, the infected BHK-21_{SUS} cell culture had a concentration of 5.2×10^6 cells/mL with a viability of 80.2 % and an average cell diameter of 15.4 μm . The virus titer was determined to 9×10^4 PFU/mL and vRNA levels to 1.1×10^9 vRNA/mL. Protein and dsDNA impurity levels were as high as 255 $\mu\text{g}/\text{mL}$ and 13.7 $\mu\text{g}/\text{mL}$, respectively. The cell broth had a pH of 7.20, an osmolality of 236 mmol/kg, a turbidity of 6.90 NTU₈₈₀, and a redox potential of 97 mV.

During the filtration experiment, the transmembrane pressure (TMP) was monitored and the membrane resistance calculated in accordance to Equation 33. The membrane resistance increased fast for mPES (M1, M2), PES (M3, M4) and ME (M7) membranes with only short periods of slower resistance development (Figure 4.27). At maximum technical resistance, the permeate flow dropped and silicone tubing on the permeate side collapsed due to low pressure at permeate side. The fouling capacity of each membrane was described by the accumulated specific permeate volume (V/A_{filter}) in accordance to [309] and [177]. Thereby, a specific permeate volume of around 9-13 L/m^2 until

termination was reached for most membranes (Table 4.15). For the tested PS and PE membranes, it took longer before the resistance maximum was achieved. In particular with the two PS membranes M5 and M6, specific permeate volumes of 18 L/m² and 30 L/m² were respectively achieved. The large-pored PS membrane (M6) showed an even slower resistance development, which then accelerated slowly until it reached its maximum at 75 L/m² (Table 4.15).

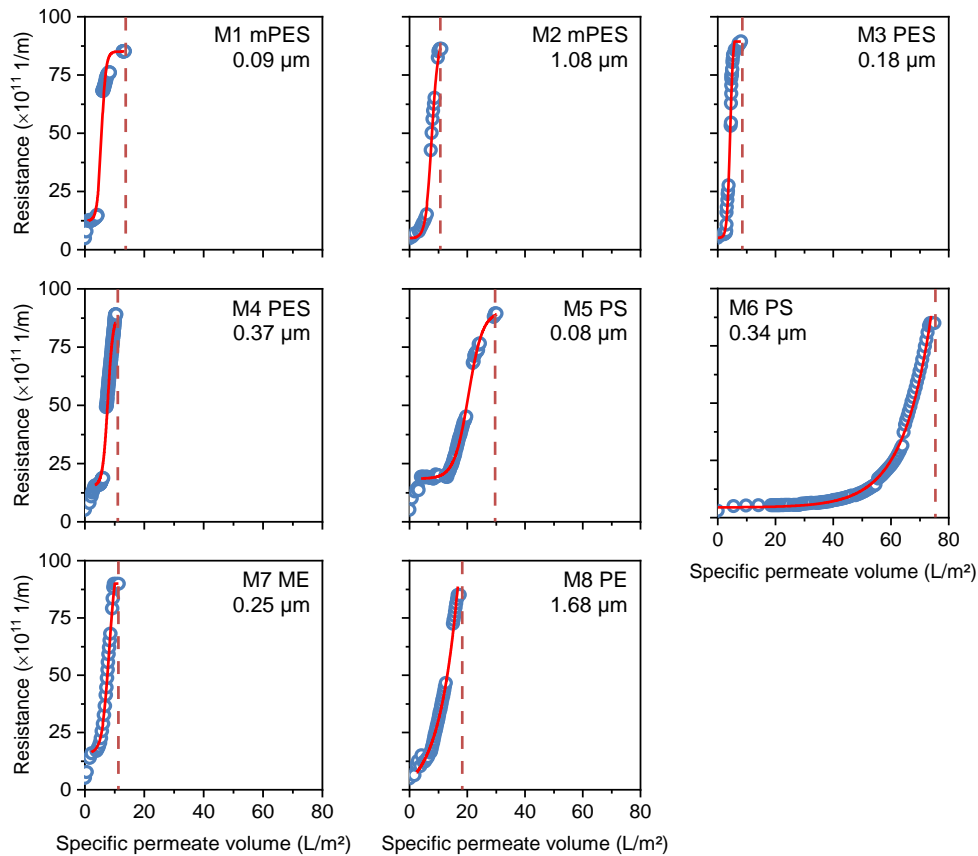


Figure 4.27 | Hollow fiber membrane resistance during perfusion operation in cross-flow filtration mode. Membranes were challenged with infected BHK-21_{SUS} cell culture broth with a fixed permeate flux of 33 L/m²/h. Filtration resistance (blue circle) increased with the specific permeate volume until reaching maximum fouling capacity. Data points were fitted using OriginPro quickfit functions (e.g. ExpGro, DoseResp) to visualize the development of membrane fouling. Red vertical line indicates maximum specific permeate volume until full membrane blockage.

Table 4.15 | Overview on maximum surface-specific permeate volumes for each hollow fiber membrane operated in cross-flow filtration mode.

Membrane	Max. specific permeate volume *
1 mPES (0.09 μm)	13 L/m ²
2 mPES (1.08 μm)	11 L/m ²
3 PES (0.18 μm)	9 L/m ²
4 PES (0.37 μm)	11 L/m ²
5 PS (0.08 μm)	30 L/m ²
6 PS (0.34 μm)	75 L/m ²
7 ME (0.25 μm)	11 L/m ²
8 PE (1.68 μm)	18 L/m ²

* Maximum specific permeate volume was reached with the cessation of permeate flow and collapse of silicon tubing (maximum membrane resistance); data derived from Figure 4.27.

While membranes were challenged with the cell culture broth at a constant surface-specific flux, samples from the inlet and permeate were routinely taken and analyzed for infectious virus titer, total vRNA level, as well as DNA and protein concentrations. In the early filtration phase, virus titers were already significantly reduced, i.e. for membranes with lower cut-offs (Figure 4.28). The membranes mPES (0.09 μm , M1) and PS (0.08 μm , M5) retained more than 99 % of the infectious virus material, whereas almost 90 % of the infectious material was retained by PES (M3, 0.18 μm) and ME (M7, 0.25 μm) membranes. The large-pored PS (0.34 μm , M6), PES (0.5 μm , M4), mPES (1.08 μm , M2) and PE (1.68 μm , M8) membranes were highly permeable for virus particles.

With progressing filter fouling (increasing membrane resistance), virus retention increased further for all membranes. The small-pored membranes retained the virus fully (below limit of detection of plaque assay), while for the PS (0.08 μm) membrane the fouling was notably delayed. For the mid-pored membranes, viral titers decreased in the permeate by more than 99 %. For the large-pored group, i.e. PES (M4, 0.5 μm) and mPES (1.08 μm , M2) membranes, virus titers in the permeate rapidly decreased to approximately 10 %. In contrast, fouling of the PS (0.34 μm , M6) membrane developed only slowly and the membrane was highly permeable for infectious virions. At the end of the filtration experiment, a high fraction of virions still passed the membrane. The PE (M8, 1.68 μm) membrane with largest pores did not retain significant virus amounts until full membrane blockage, which established surprisingly early (18 L/m²).

As an orthogonal measurement, total vRNA levels were quantified by RT-qPCR. When filter fouling progressed (increasing resistance), viral copy numbers in the permeate dropped significantly. This was in agreement with plaque assay data and suggests that there is no difference in retention of infectious and non-infectious virus material (Figure A7.16).

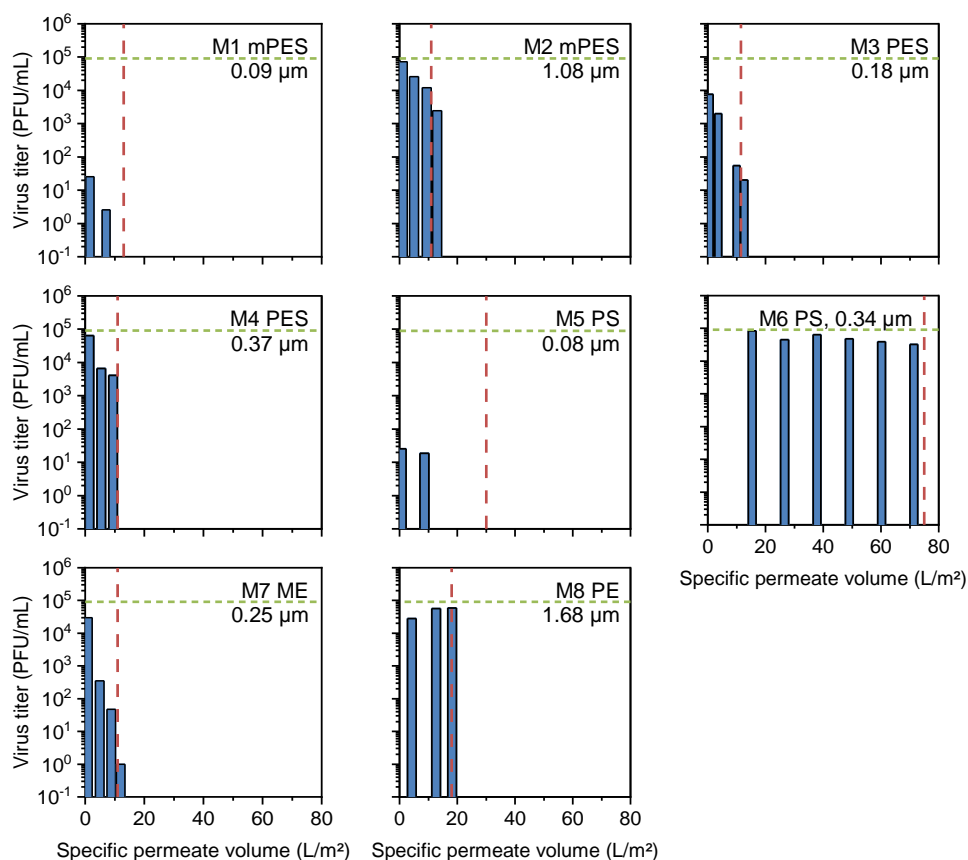


Figure 4.28 | Yellow fever virus titers in the permeate of different hollow fiber membranes to identify a suitable membrane for continuous virus harvest during perfusion operation. BHK-21_{SUS} cells were infected with YFV and hollow fiber membranes were consecutively tested in cross-flow filtration mode. Green horizontal line indicates infectious virus titer in the inlet. Red dotted vertical line indicates complete membrane blockage.

DNA and protein rejections were calculated based on depletion levels from the inlet to the permeate (following Equation 37). Similar to decreasing virus titers, the small-pored membranes mPES (0.09 μm , M1) and PS (0.08 μm , M5) revealed an initially high rejection for protein and, in particular, for DNA impurities. Notably, as the membrane resistance evolved slowly for the PS membrane, a high specific permeate volume with reduced DNA levels of 97 % ($< 0.2 \mu\text{g/mL}$) was maintained. In addition, this membrane also showed the highest protein rejection of 75 % and a reduced protein load of about 70 $\mu\text{g/mL}$ in the permeate flow. Mid-pored membranes showed a similar behavior with rejection rates increasing with evolving membrane resistance and fouling. Interestingly, the PE (1.68 μm , M8) and PS (0.34 μm , M6) membranes unveiled high rejection rates in the beginning, which then stabilized with a rejection coefficient of about 10 % (Figure 4.29).

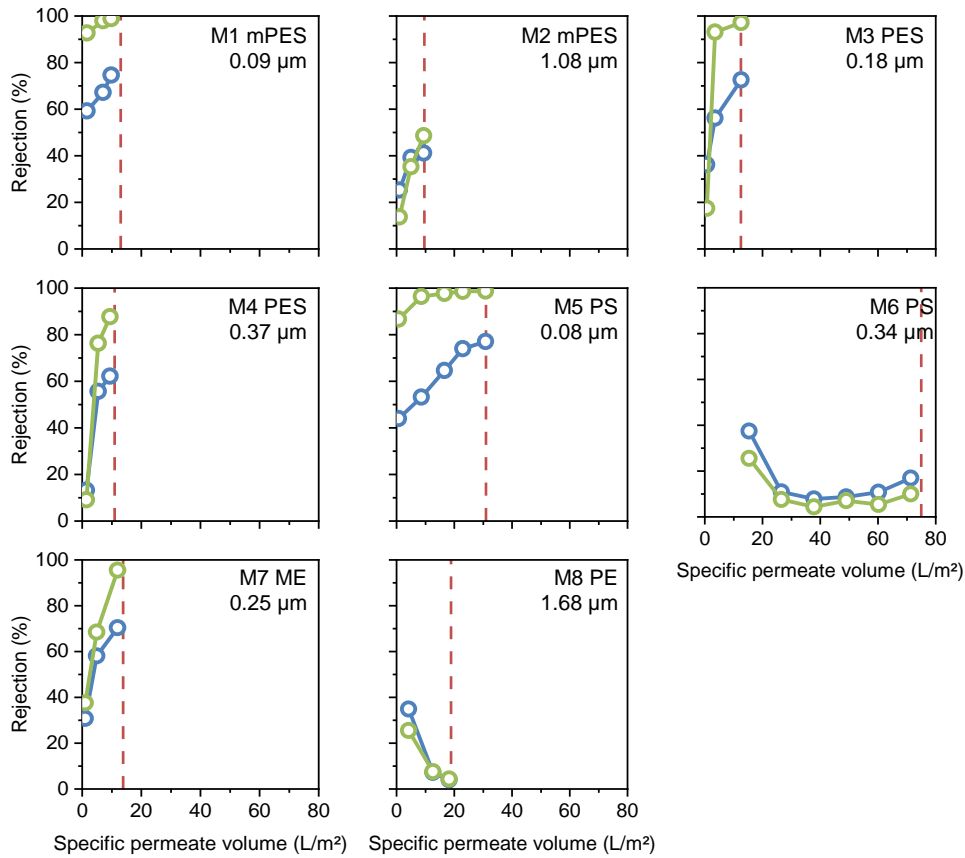


Figure 4.29 | DNA and protein rejection of different hollow fiber membranes operated in cross-flow filtration mode. Contamination levels were derived from infected BHK-21_{SUS} cells growing in BGM medium. DNA and protein samples were taken from the bioreactor vessel and permeate. Increments of DNA (green circle) and protein concentrations (blue circle) were expressed as rejection following Equation 37. Red dotted vertical line indicates complete membrane blockage.

Discussion The eight hollow fiber membranes previously characterized and evaluated regarding their theoretical susceptibility for fouling, were now successively tested in perfusion mode to assess their fouling behavior with an infected BHK-21_{SUS} cell broth. Simultaneously, YFV retention and rejection of DNA as well as protein impurities were measured.

To ensure comparability between different membrane modules, all membranes were tested in the same experimental set-up and challenged with the same culture broth. For each membrane module, the cross-flow velocity was adjusted to a shear rate of 2000 s^{-1} and the permeate flux was set to maintain a surface-specific permeate flux of $33 \text{ L/m}^2/\text{h}$. First, membrane fouling as function of the membrane resistance was monitored. The immediate increase of membrane resistance was likely due to a combination of concentration polarization (reversible to accumulation of rejected particles in the boundary layer) and a short period of deposition. The fouling progressed even faster for mPES (M1, M2) membranes, potentially due to their rough surface, which may have promoted deposition. In addition, their wide pore size distribution may have led to a primary blockage of larger pores [188], which then accelerated the subsequent fouling of smaller ones [179]. The increasing TMP (derived from decreasing pressure on the permeate side, data not shown) potentially compressed

the filter cake, leading to full membrane blockage [194]. A similar fouling tendency was observed for the small-pored PES membrane (0.18 μm , M3). Initial pore narrowing on the surface may have caused a significant reduction in the pore size, and filter cake compression decreased the permeate flux until full blockage [177]. The large-pored PES (0.37 μm , M4) and ME (0.25 μm , M7) membranes showed a short plateau in membrane resistance before increasing fast again. During this phase, most likely, an equilibrium between deposition and foulant removal (by overflow velocity) was reached. However, deposition dominated and the flux finally collapsed. The PE (1.68 μm , M8) membrane potentially blocked due to pore constriction and substantial pore closure. Interestingly, the PS membranes blocked only at very high specific permeate volumes turning them into suitable candidates for long-term filtration operation. The fouling progression indicated an initial pore narrowing for the small-pored membrane (0.08 μm , M5), and an extended equilibration phase between deposition and foulant removal. The large-pored PS membrane (0.34 μm , M6) with high porosity seemed to be hardly affected by initial foulant-membrane adsorption and pore narrowing. Their relatively high membrane thickness (approximately four times larger than other membranes) indicated to provide a larger effective separation surface area. This may have contributed to a better resistance against overall filter fouling. The round-shaped material structure enabled high fluxes across the membrane and mitigated adhesion of foulant particles. However, due to the asymmetric membrane structure and pore narrowing, an irreversible deposition was potentially formed within the membrane [264, 310]. Notably, membrane fouling progression was in close agreement with findings obtained for microfiltration processes (Figure 2.11) [177, 311]. Furthermore, experimental results from this wet-lab experiment were supported conclusively regarding the previous evaluation of structural membrane properties on theoretical filter fouling. While the widely used PES (0.18 μm) membrane blocked faster than expected under real filtration conditions, the PS membranes showed only a very slow increase in resistance against fouling with delayed fouling and highest specific permeate volumes.

SEM imaging of a selection of blocked membranes supported hypothesis that some surfaces tend to favor strong cake formation, i.e. M2, M3, and M7 (Figure A7.17). Interestingly, this became even more evident for membranes with rapid fouling behaviors, such as mPES (1.08 μm , M2), ME (0.25 μm , M7), PES (0.18 μm) and PE (1.68 μm , M8) membranes. The PS (0.34 μm , M5) membrane did not exhibit any obvious foulants on the surface, but foulants are expected to be present in high amounts in deeper membrane structures. It should be noted that specimens were dried for observation, so that actual dimensions of the cake layer could even be larger during filtration operation.

During the filter fouling experiment, samples were taken from the permeate to quantify YFV titers. The idea was to identify a membrane permeable to harvest YFV, while safely retaining cells in the bioreactor vessel. The YFV titer in the permeate decreased for each membrane simultaneously with progressing filter fouling. While rejecting membranes with small pores (<0.09 μm) fully retained the virus (~50 nm) in the bioreactor system, larger ones were only initially permeable for virions. However, as pores narrowed and the effective cut-off decreased, virions were stronger retained until the flux collapsed. The widely used PES (0.18 μm) was partially permeable, leading to an initial product loss into the permeate and subsequent accumulation in the bioreactor system. Considering this fact, it would be a preferred choice to choose a membrane that fully retains the product. For such application, the small-pored PS membrane may be a promising candidate showing virus retention above 99 % and high specific permeate fluxes. Alternatively, the large-pored PS

(0.34 μm) membrane also showed minimum fouling behavior. The larger pores enabled a high permeability for the virus and 67-99 % of infectious virus particles (>72 % following RT-qPCR data) could be constantly harvested. This turned the membrane into a suitable hollow fiber membrane for continuous virus removal.

The trend of increasing virus retention with membrane fouling was equally observed for DNA and protein impurities in the permeate. Percentage rejection increased, possibly due to increased repulsion from adsorbed foulants and steric exclusion in narrowing pore channels. Interestingly, the overall DNA rejection was significantly higher than for proteins. Notably, percentage rejection for the PS (0.34 μm , M6) and PE (1.68 μm , M8) membrane showed a contrary trend. This observation may be explained by initial adsorption of DNA and protein to the membrane material. When the adsorptive membrane capacity was reached, impurities could migrate unimpaired through the large pore channels into the permeate [188]. Especially measured protein rejections may give hints for potential product retention in other cell culture-related production process, such as recombinant protein expression in perfusion operation. As reported elsewhere, the PES membrane with a nominal cut-off of 0.2 μm partially retained expressed proteins, which was closely correlated with contamination levels (e.g. process age, cell viability) [139, 265, 312]. Filtration experiment performed in this study revealed moderate protein retentions, whereas the 0.34 μm PS membrane was permeable for proteins.

4.6.3 Summary

PES hollow fiber membranes (0.2 μm cut-off) are typically employed for membrane-based perfusion cultivations. However, when the PES membranes were used to viral vaccine production, perfusion cultivations revealed an increasing retention of labile YFV and ZIKV during the virus production phase. In a systematic study, eight hollow fiber membranes covering a wide range of materials (i.e. mPES, PES, PS, ME and PE) and pore sizes were tested to either fully retain or, ideally, completely harvest YFV. First, all membranes were characterized by their pore size distribution, and their cut-offs were estimated ranging from 0.08 μm to 1.68 μm . Zeta potential measurements provided a measure for the surface charge of the membrane and the foulants in the cultivation broth. Negative charges of about -17 mV or lower suggested a principle repulsion effect of all membranes to potential foulants. Subsequent SEM image analysis of new membranes helped to assess properties, such as surface and material roughness, as well as membrane porosity with regard to their potential fouling behavior. While the traditional PES membrane was evaluated as moderately susceptible compared to other tested membranes, the 0.34 μm PS membrane revealed promising structural properties for high permeate fluxes and low fouling (i.e. low material roughness, high surface porosity, open pore structure, low surface roughness and high overall porosity). In a next step, the analytical characterization of membrane material properties was assessed in perfusion cultivations using BHK-21_{SUS} cells infected with YFV. Membranes were successively challenged in cross-flow filtration mode to determine membrane resistance, virus retention, protein and DNA rejection. The fouling of each membrane developed from initial pore narrowing to complete pore blockage on the inlet side, resulting in solid deposition and compression of foulants. Maximum specific permeate volumes were determined, when the increasing membrane resistance exceeded the technical

maximum of the set-up. Interestingly, small- and large-pored membranes were equally sensitive to membrane blocking. In particular, rough and jagged surfaces, as observed for mPES, PES and ME membranes, were the major cause for rapid filter fouling. The PE membrane with the largest pore size (1.68 μm) finally blocked due to low membrane porosity and narrowing pore channels. The two PS (0.08 μm , 0.34 μm) membranes had the highest specific permeate volumes with 30 and 75 L/m^2 , respectively, and performed better than the tested PES membrane (9 L/m^2). Finally, virus retention was observed for all membrane materials and different pore sizes due to pore narrowing and decrease in effective cut-off. Thereby, membrane materials such as mPES and ME were strongly affected by rapid fouling. While the PES membrane was only partially permeable for YFV, the 0.08 μm PS membrane retained all virions, but also DNA and protein impurities to a high fraction. Alternatively, the 0.34 μm PS membrane was highly permeable for YFV particles and can be a vital solution for continuous virus harvesting in cross-flow filtration mode. Since it also showed low protein rejection, further applications are conceivable.

5 Conclusion

The general aim of this work was to establish a high-yield flavivirus production process with animal cells. The newly introduced virus family at the MPI required the establishment of virological quantification assays and analytics before various cell lines were screened for viral permissiveness. With the identification of suitable producer cell lines, production processes were established at 1 L bioreactor scale. To intensify virus production, the cell substrate was cultured to high concentrations by the use of membrane-based perfusion systems. For perfusion rate control, an online biomass probe was successfully integrated resulting in the highest concentrations (1.6×10^8 cells/mL) and virus titers (1×10^{10} PFU/mL) ever described for flavivirus production. To better understand characteristics and performance of different hollow fiber perfusion membranes, a thorough investigation was performed to either retain or harvest infectious virions with the permeate.

Vero cells and their limitation The attenuated YFV-17D vaccine strain was chosen as a safe model system to study flavivirus production in animal cell culture. To approach this hitherto new virus family at the MPI, virus infection was first studied in the well-established adherent Vero cell. Cell-specific titers of 10 PFU/cell are notably low and underline the general production challenge compared to high-yield viruses such as various influenza strains. For scale-up, Vero cells are cultivated on microcarriers in quasi-suspension, but decreasing cell plating efficiency in comparison to tissue culture flasks abates overall production performance. To overcome problems related to high measurement errors of microcarriers and cell numbers, the application of turbidity and capacitance probes was tested. Interestingly, the turbidity signal correlates well with microcarrier concentrations and, in turn, enables their concentration to be estimated. This can ease precise addition of conditioned microcarriers, in particular being difficult at small-scale, i.e. glass vessels, due to their adhesive nature. The capacitance probe has proven to be a vital alternative to manual cell counting. However, the relative permittivity signal is closely related to the total viable cell volume and not to cell count, eventually describing adherent cell growth better than latter. Moving from adherent to suspension cells enables various options for easier scale-up and higher cell concentrations. However, the cell growth of adapted Verosus cells was not robust and YFV titers were below those obtained from the parental adherent Vero cell. Yet, Vero cells are a good producer substrate, but their anchorage-dependency and challenging scalability of microcarrier processes makes this approach a stalemate for the project objective.

Alternative cell substrates and understanding yellow fever virus dynamics Infection studies revealed high YFV titers in suspension-adapted BHK-21_{SUS} cells. By sequential virus adaptation to other cell substrates, EB66[®] cells demonstrate excellent performance competing with cell-specific virus titers of the adherent Vero cell. During the virus adaptation process, the viral fitness was particularly improved by faster replication and higher titers in cell culture, but its consequences for the vaccine efficacy remain open. The BHK-21_{SUS} cell was used from the early project stages as a model system for understanding virus replication. First YFV MOI studies were conducted to find optimum virus production conditions and to study virus replication dynamics with imaging flow cytometry. High MOI infection conditions reveal heterogenic virus infection on a single-cell level. Based on the time-delayed expression of viral envelope proteins (as antigen for antibody-associated staining), specific host cell-responses are assumed to interfere at different stages of the viral replication cycle. The understanding of infection-triggered cellular responses is far from complete, but imaging flow cytometry can be a suitable tool to support further virological studies. From the process development perspective, it is important to confirm that all cells can be finally infected to potentially contribute to the overall virus yield. However, as virus spreading in mammalian cells was particularly slow, it requires higher MOI conditions to infect the complete cell population in batch cultivation before cells enter the typical decline phase. To overcome nutritional limitations, perfusion processes can be a vital solution to maintain viable cell states and to increase cell concentrations, finally holding great promise for process intensification. In another approach, a semi-continuous two-stage cultivation system was applied to verify that non-infectious virus material, typically the largest fraction of virus material (about 3 log higher than infectious virions), do not interfere with virus propagation. This finding was essential to validate perfusion strategies, which typically accumulate virus material for an extended time, as a promising option. Besides its investigative purpose, the two-stage cultivation facilitated increasing YFV titers and could be operated for 17 days production time. This turns the use of perfusion systems into a very attractive alternative, which could be further pursued.

Process intensification and lessons-learned for ZIKV production Small-scale pseudo-perfusion cultivations were used to scout high cell density infections for increased YFV titers. With 10-fold higher cell concentrations, the same order for cell-specific virus yields could be maintained depicting the absence of “high cell density effects”, being otherwise critical for intensified perfusion processes. In a next step, BHK-21_{SUS} and EB66[®] cells were transferred to 1 L bioreactor systems equipped with TFF or ATF perfusion units. While BHK-21_{SUS} cells grow robustly in both systems, EB66[®] cells are more shear-sensitive in chemically-defined medium and can be only cultivated in an ATF system. Latter set-up reached very high cell concentrations and were infected with an EB66[®] cell-adapted YFV seed. Titers were extremely high exceeding raw material for more than 10⁷ live-attenuated vaccine doses (4.74 log₁₀ PFU/dose based on the FDA-approved live-attenuated vaccine YF-VAX[®]). The footprint of the bioreactor vessel was as small as 700 mL and the overall process time was about two weeks. Nevertheless, manual perfusion rate control based on offline measured glutamine concentrations is still challenging.

For the successful transfer to Brazilian ZIKV production in EB66[®] cells, three important steps were made: A large-volume cryo-bag was used for direct perfusion bioreactor inoculation; a promising ZIKV^{RJ} seed was adapted by five passages to the new cell substrate; the ATF bioreactor was equipped with an online probe for biomass estimation and cell-specific perfusion rate control. As

before, this enabled extremely high EB66[®] cell concentrations together with increased cell-specific ZIKV titers, being 10-times higher than high-yield batch cultivations. This is most likely due to (i) higher cell inoculum concentration, (ii) permanent medium supply (highly vital cell state, elevated cellular activity), (iii) potential removal of inhibiting compounds, (iv) controlled process conditions (in particular pH value), (v) extended time of infection phase (few hours already beneficial), (vi) and use of fast replicating seed virus (reducing the impact of unspecific virus inactivation). For the first time, volumetric virus productivities of a perfusion cultivation exceeded batch infection cultivation by 3-fold. The interplay of minimum medium use, optimum cell growth and increased cell-specific titers turns this platform into a highly productive option for next-generation cell culture-based flavivirus manufacturing.

Online probes for in-process control The use of an online capacitance probe in perfusion bioreactors was a viable alternative to manual cell counting. While linear regression models offered reasonable fits, need for frequent recalibration diminishes its unrestricted use. Use of the PLS model resulted in a similar fitting quality, but required complex analysis of large spectroscopic data sets. The Cole-Cole model assumes constant cellular dielectric properties. Nevertheless, predicted total biovolume fractions reasonably correlated with ViCell measurements for the cell growth phase, but the model is not equally applicable for the cell decline phase. These findings are in agreement with previous studies of batch and fed-batch cultivations performed for CHO cell-based recombinant protein production. Finally, the Cole-Cole model allowed the calculation of the cell-specific membrane capacitance and the intracellular conductivity, which are reported to allow online monitoring of different virus propagation phases. Although virus-related changes in could not be confirmed, it was verified that the biomass probe can be reliably used for perfusion rate control throughout the infection phase. In addition, the biomass probe recorded parameters such as the characteristic frequency and the Cole-Cole parameter α , both being sensitive signals for, e.g., cell diameter and population heterogeneity, but eventually also for hitherto unknown cellular changes.

Choosing the right perfusion membrane A large selection of hollow fiber perfusion membranes is available, but a systematic study of membrane cut-offs and materials for virus retention or harvesting was lacking. For most perfusion bioreactors, the PES membrane with a nominal cut-off of 0.2 μm is used. However, it revealed strong flavivirus (50 nm) retention with progressing filter fouling. Hence, eight membranes made from different materials were characterized and, based on their structural and physicochemical properties, evaluated for membrane fouling. In combination with subsequent membrane filtration experiments in cross-flow operation, it allows to speculate about an “ideal” membrane for virus production: (i) flat inner surface (high surface velocity and thin boundary layer), (ii) smooth inner surface structure (reduced deposition), (iii) high porosity (high permeate flux), (iv) distinct pore size distribution (reduced pore selectivity), and (v) increased fiber thickness (larger effective surface area). This was provided by two PS membranes depicting highest specific permeate volumes. While the small-pored PS membrane fully retained virions in the bioreactor, the large-pored membrane enabled continuous product harvest in the permeate. Due to low protein rejections of latter membrane, other applications such as recombinant protein production in perfusion cultivations may be logical.

In conclusion, understanding flavivirus replication and spreading from the upstream prospective is essential to choose the appropriate process intensification approach. Infections with host cell-adapted virus strains and optimized perfusion cultivations can be considered as important milestones for a high-yield flavivirus production process. During the research project, online data of the capacitance probe were gathered and interpreted for perfusion cultivation control. While total cell volumes can be derived from linear correlations with offline data, the Cole-Cole model enables to estimate the total cell volume with reasonable accuracy at constant cell-specific dielectrics. A systematic study on membrane cut-offs and material characteristics revealed large-pored PS membranes being the most promising material for continuous virus particle harvest via the permeate. This finding is likely to be applicable to a wide range of cell culture-based perfusion processes for the production of viral vaccines.

6 Outlook

Within the framework of this project, a high-yield flavivirus production process was step-wise developed. The established perfusion process, but also findings on flavivirus replication, capacitance probe data and hollow fiber membranes along the development, offer various options for design and optimization of related applications and production processes.

Cell substrates for flavivirus production Adherent Vero cells are approved substrates for human vaccine production. Cells are typically cultured in out-scaled cultivation systems (e.g. roller bottles, CellFactory) or microcarrier bioreactors, both of which have limitations for process intensification and scale-up. Alternatively, novel fixed-bed systems such as the scale-X™, CelCradle™ or iCellis® bioreactor can be considered as suitable option for increased cell concentrations. Ultimately, the transition to suspension cells allows easy scale-up and intensified vaccine production. However, adaptation approaches of Vero cells to growth in suspension can be overrated as a newly adapted VeroSUS cell line may require costly regulatory safety studies that can cancel out potential benefits. Currently, it seems to be only a matter of time before this aspect is economically assessed, as new media and intensive laboratory work have demonstrated its biological feasibility, albeit with rather high doubling times in suspension. Alternatively, well-established suspension cells with high viral permissiveness are available. The tested BHK-21_{SUS} cell is a robust model cell line, but due to its tumorigenicity only qualified for veterinary applications. In contrast, EB66® cells have been already approved for human IAV production in Japan. In particular the high specific growth rate, high robustness and high viral permissiveness turn EB66® cells into a very promising substrate for manufacturing of viral vaccines or viral vectors for gene therapy. Whether a cell culture-based live-attenuated YFV vaccine process will be implemented in industry is currently questionable. Although presented production process is clearly outperforming the established egg-based manufacturing process, safety and efficacy studies on a cell culture-derived YFV vaccine are lacking. The effect of virus seed adaptation to animal cells, e.g. EB66® cells, on *in-vivo* behaviors (e.g. efficacy, safety) needs further investigations. Alternatively, the cell culture-based production platform can be used for other vaccine strategies such as an inactivated YFV vaccine, but also for other vaccines against emerging viral threats.

Perfusion bioreactors for vaccine production The perfusion cultivation process clearly demonstrated the advantages of shear-tolerant suspension cells for intensified YFV and ZIKV production. The principle can be easily adapted to similar cell substrates and other viruses. For this purpose, the

virus meets ideally certain requirements such as mechanical robustness, increased thermal stability and deficiency to form defective interfering particles. In this way, controlled long-term perfusion processes can reproducibly exceed the productivity of batch infections. Nowadays, different perfusion systems are available for almost each bioreactor size. With the increasing awareness of unwanted product retention in membrane-based perfusion systems, manufacturers are currently working on innovative membranes with minimum fouling. Alternative trends move towards fixed-bed solution for the cultivation of adherent cells, but also for the entrapment and expansion of suspension cells. This enables low shear stress conditions for captured (shear-sensitive) cells, while great amounts of larger particles (e.g. cells, debris, vesicles) are retained in the fixed-bed. As a fact, the load on the membrane is reduced and filter fouling is minimized. Herein findings on membrane materials and ideal structural appearances can help to design suitable membranes, in particular for virus-related cultivation processes. In addition, various membrane operations to reduce filter fouling can be investigated. Notably, the ATF system can be a suitable perfusion unit due to its continuous backflushing by inverting flow directions.

Online probes for bioreactor systems In order to achieve better process control, new online probes are desirable to monitor, i.e., cell attachment, cell growth and virus production. With the great momentum for fixed-bed bioreactors, the turbidity probe tested here can be easily used to record cell attachment kinetics after inoculation. The probe is therefore positioned over the fixed-bed in the medium. For later infection phases, it may equally detect virus-related turbidity increases in the supernatant. Considering cell growth monitoring of adherent cells, either on microcarriers or fixed-bed bioreactors, and suspension cells, the capacitance probe is a suitable online sensor. While the biomass can be monitored, the signal can be also processed to control the cultivation, i.e., by cell concentration-related perfusion rate control or concentration-triggered events such as infection, temperature shifts and product harvest. This can standardize future cultivation processes with reduced manual interventions. Current biomass probes operate in frequency ranges specific for particles in the size range of cells. Hence, smaller particles such as virions are not polarized and cannot be detected. Alternatively, a new class of capacitance probes is needed that measure at higher frequencies of about 300 MHz. However, it is expected that overlapping α - and β -dispersion effects will make data interpretation more difficult. Furthermore, particles in a similar size range, e.g. exosomes and cell debris, are always highly present and can be hardly distinguished from intact virions. Instead, further developments can be made towards greater measurement depths (currently approx. 1-2 cm) allowing a non-invasive, flexible measurement through bioreactor walls made of glass or plastic.

Overall, established flaviviruses-related assays and methods, together with mathematical modeling approaches, allow further in-depth analysis of flavivirus replication dynamics and will contribute to improving viral titers. Finally, the automated perfusion process and the highly permeable hollow fiber membranes can serve as basis for other intensified virus production processes, in particular for applications requiring high virus quantities, such as viral vectors in cancer treatment or gene therapy.

List of Figures

Figure 2.1	Transmission cycles of flaviviruses.....	4
Figure 2.2	Simplified structure of the flavivirus particle.....	5
Figure 2.3	Flaviviruses replication cycle.....	6
Figure 2.4	Global yellow fever occurrence and risk map.....	8
Figure 2.5	Global Zika fever occurrence and risk map.....	12
Figure 2.6	Flow velocity profiles of different pump systems in an external perfusion pump loop.....	18
Figure 2.7	Bioreactor set-up with perfusion units for cross-flow filtration operation.....	20
Figure 2.8	Perfusion rate control strategies for high cell concentration cultivations.....	23
Figure 2.9	Idealized β -dispersion of an animal cell culture.....	25
Figure 2.10	Dielectric parameters derived from β -dispersion.....	27
Figure 2.11	Five phases of filter blocking for an idealized microfiltration process with constant pressure and particles smaller than the pore size.....	29
Figure 2.12	Minimizing filter fouling during perfusion cultivations.....	33
Figure 4.1	Yellow fever virus production in adherent Vero cells at different scales.....	61
Figure 4.2	Evaluation of bead-to-bead transfer for the scale-up of Vero cells on Cytodex-1 microcarriers.....	62
Figure 4.3	Time course of turbidity measurement after Cytodex-1 microcarrier addition in stirred tank bioreactors.....	64
Figure 4.4	Time course of capacitance measurement during Vero cell growth on Cytodex-1 microcarriers.....	65
Figure 4.5	Adherent Vero cell adaptation to suspension growth in SMIF8 medium.....	67
Figure 4.6	Yellow fever virus production using VeroSUS cells in spinner and shake flasks.....	68
Figure 4.7	Infectious virus titers during sequential passaging of yellow fever virus in different suspension cell lines.....	71
Figure 4.8	Impact of multiplicity of infection on yellow fever virus titers in BHK-21SUS cells.....	73
Figure 4.9	Infection dynamics of yellow fever virus in BHK-21SUS cells at different multiplicities of infection.....	73
Figure 4.10	Yellow fever virus production in a semi-continuous two-stage shake flask cultivation.....	75
Figure 4.11	Pseudo-perfusion cultivations of BHK-21SUS cells in shake flasks with different perfusion rate strategies.....	78
Figure 4.12	Yellow fever virus production with BHK-21SUS cells in pseudo-perfusion cultivation and shake flasks.....	79
Figure 4.13	Yellow fever virus production with BHK-21SUS cells in a 1 L bioreactor and tangential flow filtration (TFF) perfusion system.....	82
Figure 4.14	Yellow fever virus production with EB66® cells in a 1 L bioreactor with tangential flow filtration perfusion system.....	83
Figure 4.15	Yellow fever virus production with EB66® cells in a 1 L bioreactor with alternating tangential flow filtration (ATF) perfusion system.....	84
Figure 4.16	ZIKV ^{PE} production with BHK-21SUS cells in a 3 L bioreactor and alternating tangential flow filtration (ATF) perfusion system.....	90
Figure 4.17	Sequential passaging of Zika virus in EB66® cells.....	92
Figure 4.18	Zika virus production with EB66® cells in a 1 L bioreactor with alternating tangential flow filtration (ATF) perfusion system and automated perfusion rate control.....	94

List of Figures

Figure 4.19	Measurement data of the capacitance probe and input variables for biomass modeling.	99
Figure 4.20	Signal linearity of $\Delta\epsilon$ to the viable cell concentration and volume during the cell growth and infection phase of three ATF perfusion cultivations.....	101
Figure 4.21	Use of a Cole-Cole model to calculate biomass parameters based on online signals from the biomass probe.....	105
Figure 4.22	Changes of the characteristic frequency (f_c) during perfusion cultivations.....	108
Figure 4.23	Correlation of the characteristic frequency (f_c) to the cell diameter.	108
Figure 4.24	Dielectric parameter changes in C_m and σ_i during three perfusion cultivations.	109
Figure 4.25	Cell size changes during perfusion cultivations and the correlation of Cole-Cole α to the cell size heterogeneity.	110
Figure 4.26	SEM images of inner membrane surface of different hollow fiber materials.	117
Figure 4.27	Hollow fiber membrane resistance during perfusion operation in cross-flow filtration mode.	120
Figure 4.28	Yellow fever virus titers in the permeate of different hollow fiber membranes to identify a suitable membrane for continuous virus harvest during perfusion operation.	122
Figure 4.29	DNA and protein rejection of different hollow fiber membranes operated in cross-flow filtration mode.	123
Figure A7.1	Turbidity measurement for adherent Vero cell inoculation.	162
Figure A7.2	Impact of ultra-sonication on cell concentration and infectious virus titers.	162
Figure A7.3	Cell budding of VeroSUS cells in SMIF8 medium.	163
Figure A7.4	Impact of BHK-21 _{SUS} passage number on yellow fever virus production.	163
Figure A7.5	Yellow fever virus passaging in EB66 [®] cells.	164
Figure A7.6	Yellow fever virus and Zika virus inactivation in CDM4Avian medium.	164
Figure A7.7	Characterization of suspension cell growth in shake flask batch cultures.	165
Figure A7.8	Decrease in the percentage of yellow fever virus titers (permeate vs. bioreactor) during membrane-based TFF and ATF perfusion cultivations.	166
Figure A7.9	Ratio of infectious virus titer to viral copy number (PFU/vRNA) of Zika virus infected EB66 [®] cells.....	166
Figure A7.10	Changes in pH values during EB66 [®] perfusion cultivation and virus infection.	167
Figure A7.11	Interpolated cell diameters of EB66 [®] cells during perfusion cultivations.	168
Figure A7.12	Pore size distributions of tested hollow fiber membranes according to bubble point measurements.	168
Figure A7.13	Oblique SEM images of the cross-section of unused and blocked hollow fiber membranes.....	169
Figure A7.14	Frontal SEM imaging of the inner and outer surface of unused hollow fiber membranes.....	170
Figure A7.15	Cross-sectional SEM images of an unused PS 0.34 μm membrane.....	171
Figure A7.16	Viral RNA copy numbers in permeate decrease with filter fouling in different hollow fiber membranes during perfusion operation.	172
Figure A7.17	SEM imaging of inner membrane surfaces after complete membrane blockage for filter fouling experiments.	173

List of Tables

Table 3.1	Overview of adherent (upper part) and suspension cell lines (lower part).....	35
Table 3.2	Overview of basal cell growth media.....	35
Table 3.3	Standard conditions to cultivate suspension cell lines.	36
Table 3.4	Assignment of vessel equipment to top-plate ports.....	41
Table 3.5	BHK-21 _{SUS} perfusion media supplementation	42
Table 3.6	EB66 [®] perfusion media supplementation	43
Table 3.7	Overview of flaviviruses used in this study.	46
Table 3.8	ViCell settings for different cell lines.	48
Table 3.9	Primers and probes used for real-time RT-qPCR.....	51
Table 3.10	RT-qPCR kits with different principles were tested for the quantification of flavivirus RNA copy numbers.	52
Table 3.11	Tested hollow fiber filter modules for filter fouling and virus retention in cross-flow operation.....	56
Table 4.1	Process results from yellow fever virus production in adherent Vero cells at different scales.	62
Table 4.2	Overview on screened cell substrates for yellow fever virus production.....	70
Table 4.3	Process data for yellow fever virus production with BHK-21 _{SUS} and EB66 [®] cells. Cultivations were performed in batch mode and shake flasks (upper part), and in pseudo-perfusion operation in shake flasks and perfusion operation in stirred-tank bioreactor systems with membrane- based perfusion units (lower part).	85
Table 4.4	Maximum virus titers and cell-specific yields of different Zika virus isolates achieved in adherent Vero and BHK-21 cells.	89
Table 4.5	Process data for Zika virus production in adherent Vero cells and suspension-adapted BHK-21 _{SUS} and EB66 [®] cells. Cultivations were performed in batch operation (upper part) and in perfusion operation with stirred-tank bioreactor systems (lower part).	95
Table 4.6	Signal linearity of $\Delta\epsilon_{max}$ and $\Delta\epsilon$ to offline data.....	100
Table 4.7	Cell factors to determine the viable cell concentration (VCC) or viable cell volume (VCV) from the permittivity drop $\Delta\epsilon$	101
Table 4.8	Statistical evaluation of a linear regression model to describe the viable cell concentration (VCC) and volume (VCV) of different perfusion cultivations with an averaged cell factor.....	102
Table 4.9	Statistical evaluation of a PLS model to describe the viable cell concentration, viable cell volume and cell diameter based on the relative permittivity spectra for three ATF perfusion cultivations.	103
Table 4.10	Mean membrane capacitance (C_m) and intracellular conductivity (σ_i) for three ATF perfusion runs.	104
Table 4.11	Overview on physical characteristics of hollow fiber membranes.....	114
Table 4.12	Overview on measured zeta potential and water contact angle for tested hollow fiber membrane materials.	114
Table 4.13	Structural and physicochemical membrane properties and their theoretical impact on membrane fouling.	115
Table 4.14	Structural membrane properties (based on SEM imaging) and their theoretical impact on membrane fouling.	116

Table 4.15 Overview on maximum surface-specific permeate volumes for each hollow fiber membrane operated in cross-flow filtration mode.	121
Table A7.1 List of consumables and materials.	158
Table A7.2 List of equipment.	159
Table A7.3 Validated measurement ranges of different assays for metabolite quantification.	160
Table A7.4 Decreasing time intervals for different medium exchange strategies with BGM as basal growth medium for the pseudo-perfusion cultivation of BHK-21 _{SUS} cells.	165
Table A7.5 Transferability of cultivation-specific cell factors to other cultivations to determine the viable cell concentration and viable cell volume.	167

List of Publications

Parts of the following publications and supervised theses were included in this work:

Peer-reviewed journal articles

Nikolay A, Léon A, Schamborn K, Genzel Y, Reichl U. Process intensification of EB66[®] cell cultivations leads to high-yield yellow fever and Zika virus production. *Applied Microbiology and Biotechnology* 2018, 102(20):8725-8737

Nikolay A, Castilho L, Reichl U, Genzel Y. Propagation of Brazilian Zika virus strains in static and suspension cultures using Vero and BHK cells. *Vaccine* 2018, 36:3140-3145

Gallo-Ramírez LE*, **Nikolay A***, Genzel Y, Reichl U. Bioreactor concepts for cell culture-based viral vaccine production. *Expert Review of Vaccines* 2015, 14(9):1181-1195

* authors contributed equally

Book chapter

Nikolay A*, Bissinger T*, Gränicher G, Wu Y, Genzel Y, Reichl U. Perfusion control for high cell density cultivation and viral vaccine production. In *Animal Cell Biotechnology: Methods and Protocols*, Fourth Edition. Editor Ralf Pörtner

* authors contributed equally

Supervised thesis

Pelz L (2019). Optimierung der Produktion von Gelbfiebertviren mit BHK-21 Zellen. Master Thesis, Department of Life Sciences, Technische Universität München.

Seemann W (2018). Zellkulturbasierte Produktion von Gelbfiebertviren in Pseudo-Perfusion und der Transfer in Bioreaktoren. Master Thesis, Faculty for Life Sciences, Otto von Guericke University, Magdeburg.

Bartels E (2016). Etablierung und Validierung verschiedener Assays zur Quantifizierung von Flaviviren: RT-qPCR, Plaque Assay und Durchflusszytometrie. Bachelor Thesis, Faculty for Process and Systems Engineering, Otto von Guericke University, Magdeburg.

Hermann K (2015). Identifizierung geeigneter Zellsubstrate und Optimierung von Bioreaktorprozessen zur Zellkultur basierten Produktion von Gelbfieber Viren. Master Thesis, Department of Life Sciences, Technische Universität Braunschweig

Talks

Nikolay A, Seemann W, Kozakiewicz F, Hundt B, Léon A, Schwamborn K, Genzel Y, Reichl U. Cell culture-based perfusion processes for flavivirus production. Young Scientist Cell Culture Biotechnology Retreat, Germany, 2018

Nikolay A, Genzel Y, Reichl U. Stable animal cell growth in perfusion processes: Using on-line permittivity sensors to control cell-specific perfusion rates. 5th BioProScale, Germany, 2018

Nikolay A, Castilho L, Genzel Y, Reichl U. Process intensification: Yellow fever virus and Zika virus production in suspension cells. 13th PEACe conference, Spain, 2017

Nikolay A, Genzel Y, Reichl U. Process intensification for cell culture-based flavivirus production. IVT Kolloquium OvGU Magdeburg, Germany, 2017

Posters

Nikolay A, Grooth J, Genzel Y, Wood J, Reichl U. Virus harvesting in perfusion culture: Choosing the right membrane. ESACT, Denmark, 2019

Nikolay A, Léon A, Schwamborn K, Genzel Y, Reichl U. Flavivirus production in perfusion processes using the EB66[®] cell line. Vaccine Technology VII, Canada, 2018

Nikolay A, Léon A, Schwamborn K, Genzel Y, Reichl U. The EB66[®] cell line for yellow fever vaccine production at high cell concentrations. Cell Culture Engineering XVI, USA, 2018

Nikolay A, Castilho L, Genzel Y, Reichl U. Process intensification of yellow fever virus and zika virus production in perfusion bioreactors. 25th ESACT, Switzerland, 2017

Nikolay A, Castilho L, Tanuri A, Reichl U, Genzel Y. Production of yellow fever virus and Zika virus in perfusion bioreactors. Himmelfahrtstagung, Germany, 2017

Nikolay A, Castilho L, Tanuri A, Reichl U, Genzel Y. Propagation of Brazilian Zika virus strains in static, microcarrier-based and suspension cultures using BHK and Vero cells. 1st ESACT Frontiers Retreat, France, 2016

Nikolay A, Hermann K, Genzel Y, Reichl U. Evaluation of producer cell lines for yellow fever virus production in up to 1 L bioreactor scale. Vaccine Technology VI, Portugal, 2016

Vazquez-Ramirez D, **Nikolay A**, Genzel Y, Reichl U. On-line monitoring tools in batch and (semi-) perfusion cultivations for vaccine production. Germany, BioProScale IV, 2016

Nikolay A, Scharfenberg K, Patel P, Niedrig M, Genzel Y, Reichl U. Towards yellow fever 17D virus production in Vero suspension cells. 24th ESACT, Spain, 2015

Bibliography

1. WHO (2016). *Yellow fever global vaccine stockpile in emergencies*. <https://www.who.int/en/news-room/feature-stories/detail/yellow-fever-global-vaccine-stockpile-in-emergencies> (06.02.2019).
2. Theiler M, Smith HH (1937). *The use of yellow fever virus modified by in vitro cultivation for human immunization*. *J Exp Med* 65, 787–800.
3. Monath TP, Woodall JP, Gubler DJ, Yuill TM, Mackenzie JS, *et al.* (2016). *Yellow fever vaccine supply: a possible solution*. *Lancet* 387, 1599–1600.
4. Wilder-Smith A, Leong WY (2017). *Importation of yellow fever into China: assessing travel patterns*. *J Travel Med* 24, 1–4.
5. Cao-Lormeau VM, Blake A, Mons S, Lastere S, Roche C, *et al.* (2016). *Guillain-Barre Syndrome outbreak associated with Zika virus infection in French Polynesia: a case-control study*. *Lancet* 387, 1531–1539.
6. Mlakar J, Korva M, Tul N, Popovic M, Poljsak-Prijatelj M, *et al.* (2016). *Zika Virus Associated with Microcephaly*. *N Engl J Med* 374, 951–958.
7. Gallo-Ramirez LE, Nikolay A, Genzel Y, Reichl U (2015). *Bioreactor concepts for cell culture-based viral vaccine production*. *Expert Rev Vaccines* 14, 1181–1195.
8. Monath TP, Lee CK, Julander JG, Brown A, Beasley DW, *et al.* (2010). *Inactivated yellow fever 17D vaccine: Development and nonclinical safety, immunogenicity and protective activity*. *Vaccine* 28, 3827–3840.
9. Pereira RC, Silva ANMR, Souza MCO, Silva MV, Neves PPCC, *et al.* (2015). *An inactivated yellow fever 17DD vaccine cultivated in Vero cell cultures*. *Vaccine* 33, 4261–4268.
10. Jayme DW, Smith SR (2000). *Media formulation options and manufacturing process controls to safeguard against introduction of animal origin contaminants in animal cell culture*. *Cytotechnol* 33, 27–36.
11. Warnock JN, Al-Rubeai M (2006). *Bioreactor systems for the production of biopharmaceuticals from animal cells*. *Biotechnol Appl Bioc* 45, 1–12.
12. Clincke M-F, Mölleryd C, Zhang Y, Lindskog E, Walsh K, *et al.* (2013). *Very high density of CHO cells in perfusion by ATF or TFF in WAVE bioreactor™. Part I. Effect of the cell density on the process*. *Biotechnol Prog* 29, 754–767.
13. Genzel Y, Vogel T, Buck J, Behrendt I, Ramirez DV, *et al.* (2014). *High cell density cultivations by alternating tangential flow (ATF) perfusion for influenza A virus production using suspension cells*. *Vaccine* 32, 2770–2781.
14. Gubler DJ (2002). *The Global Emergence/Resurgence of Arboviral Diseases As Public Health Problems*. *Arch Med Res* 33, 330–342.
15. Monath TPC, Lindsey HS, Nuckolls JG, Chappell WA, Henderson BE (1970). *Comparison of Methods for Removal of Nonspecific Inhibitors of Arbovirus Hemagglutination*. *Appl Microbiol* 20, 748–753.

16. Aitken TH, Tesh RB, Beaty BJ, Rosen L (1979). *Transovarial transmission of yellow fever virus by mosquitoes (Aedes aegypti)*. *Am J Trop Med Hyg* 28, 119–121.
17. Monath TP, Vasconcelos PFC (2015). *Yellow fever*. *J Clin Virol* 64, 160–173.
18. Murphy FA, Fauquet CM, Bishop DHL, Ghabrial SA, Jarvis A, *et al.* (1995). *Virus Taxonomy: Classification and Nomenclature of Viruses*, Volume 1: Springer Vienna.
19. Brinton MA (1986). *Replication of Flaviviruses*. In *The Togaviridae and Flaviviridae*, S Schlesinger and MJ Schlesinger, eds. Boston, MA: Springer New York, 327–374.
20. Monath TP, Gershman M, Erin Staples J, Barrett ADT (2013). *Yellow fever vaccine*. In *Vaccines (Sixth Edition)*, SA Plotkin, WA Orenstein and PA Offit, eds. London: W.B. Saunders, 870-968.
21. Sampath A, Padmanabhan R (2009). *Molecular targets for flavivirus drug discovery*. *Antiviral Res* 81, 6–15.
22. Smit JM, Moesker B, Rodenhuis-Zybert I, Wilschut J (2011). *Flavivirus cell entry and membrane fusion*. *Viruses* 3, 160-171.
23. Monath TP, Vasconcelos PF (2015). *Yellow fever*. *J Clin Virol* 64, 160–173.
24. Randolph VB, Stollar V (1990). *Low pH-induced cell fusion in flavivirus-infected Aedes albopictus cell cultures*. *J Gen Virol* 71, 1845–1850.
25. Staples JE, Monath TP (2011). *Yellow Fever*. In *Tropical Infectious Diseases: Principles, Pathogens and Practice*, Volume 3, RL Guerrant, DH Walker and PF Weller, eds. Edinburgh: W.B. Saunders, 492–503.
26. Neufeldt CJ, Cortese M, Acosta EG, Bartenschlager R (2018). *Rewiring cellular networks by members of the Flaviviridae family*. *Nat Rev Microbiol* 16, 125–142.
27. Lindenbach BD, Rice CM (1997). *trans-Complementation of yellow fever virus NS1 reveals a role in early RNA replication*. *J Virol* 71, 9608–9617.
28. Kuhn RJ, Zhang W, Rossmann MG, Pletnev SV, Corver J, *et al.* (2002). *Structure of dengue virus: implications for flavivirus organization, maturation, and fusion*. *Cell* 108, 717–725.
29. Mukhopadhyay S, Kuhn RJ, Rossmann MG (2005). *A structural perspective of the flavivirus life cycle*. *Nat Rev Microbiol* 3, 13–22.
30. Lorenz IC, Allison SL, Heinz FX, Helenius A (2002). *Folding and dimerization of tick-borne encephalitis virus envelope proteins prM and E in the endoplasmic reticulum*. *J Virol* 76, 5480–5491.
31. Vercoutter-Edouart AS, Slomianny MC, Dekeyser-Beseme O, Haeuw JF, Michalski JC (2008). *Glycoproteomics and glycomics investigation of membrane N-glycosylproteins from human colon carcinoma cells*. *Proteomics* 8, 3236–3256.
32. Bryant JE, Holmes EC, Barrett ADT (2007). *Out of Africa: A Molecular Perspective on the Introduction of Yellow Fever Virus into the Americas*. *PLOS Pathog* 3, 75–83.
33. Strode GK (1951). *Yellow Fever*, Volume 15: New York, N.Y. & London, McGraw-Hill Book Co., Inc.
34. Brunette G, Kozarsky P, Magill A, Shlim D (2009). *CDC Health Information for International Travel 2010*, Volume 1: Elsevier Health Sciences.

35. Leta S, Beyene TJ, De Clercq EM, Amenu K, Kraemer MUG, *et al.* (2018). *Global risk mapping for major diseases transmitted by Aedes aegypti and Aedes albopictus*. *Int J Infect Dis* 67, 25–35.
36. Jentes ES, Pomeroy G, Gershman MD, Hill DR, Lemarchand J, *et al.* (2011). *The revised global yellow fever risk map and recommendations for vaccination, 2010: consensus of the Informal WHO Working Group on Geographic Risk for Yellow Fever*. *Lancet Infect Dis* 11, 622–632.
37. Theiler M, Sellards AW (1926). *The relationship of L icterohemorrhagicae and L icteroides*. *Amer J Trop Med* 6, 383–402.
38. Theiler M, Sellards AW (1928). *The immunological relationship of yellow fever as it occurs in West Africa and in South America*. *Ann Trop Med Parasitol* 22, 449–460.
39. Sellards AW, Hindle E (1928). *The preservation of yellow fever virus*. *Br Med J* 1, 713–714.
40. Stokes A, Bauer JH, Hudson NP (1928). *The transmission of yellow fever to Macacus rhesus, Preliminary note*. *J Amer Med Assoc*, 253–255.
41. Frierson JG (2010). *The Yellow Fever Vaccine: A History*. *Yale J Biol Med* 83, 77–85.
42. Rey M (1966). *Epidemiological and clinical aspects of encephalitis following yellow fever vaccination*. *Bull Soc Méd Afr Noire* 11, 560–574.
43. Smith HH (1938). *Yellow fever vaccination with cultured virus (17D) without immune serum*. *Amer J Trop Med* 18, 437–468.
44. Beasley DWC, McAuley AJ, Bente DA (2015). *Yellow fever virus: Genetic and phenotypic diversity and implications for detection, prevention and therapy*. *Antiviral Res* 115, 48–70.
45. Beck A, Tesh RB, Wood TG, Widen SG, Ryman KD, *et al.* (2014). *Comparison of the live attenuated yellow fever vaccine 17D-204 strain to its virulent parental strain Asibi by deep sequencing*. *J Infect Dis* 209, 334–344.
46. Fox JP, Lennette EH, Manso C, Aguiar JRS (1942). *Encephalitis in man following vaccination with 17 d yellow fever virus*. *Am J Epidemiol* 36, 117–142.
47. Sawyer WA, Meyer KF, Eaton MD, Bauer JH, Putnam P, *et al.* (1944). *Jaundice in army personnel in the western region of the United States and its relation to vaccination against yellow fever (parts II, III, and IV)*. *Am J Epidemiol* 40, 35–107.
48. WHO (1995). *Requirements for yellow fever vaccine No. 3 - Annex 2*. In *Technical Report Series, Volume 872*, WHO, ed. Geneva
49. Friede M (2013). *Influenza Vaccine Production: Impact of technology, scale and other vaccines on financial viability*. In *WHO-HHS Meeting on Business Models*, WHO, ed.
50. Staples JE, Monath TP, Gershman MD, Barrett ADT (2018). *Yellow Fever Vaccines*. In *Plotkin's Vaccines, Volume 7*, SA Plotkin, WA Orenstein, PA Offit and KM Edwards, eds.: Elsevier, 1181–1265.
51. Ferguson M, Shin J, Knezevic I, Minor P, Barrett A (2010). *WHO Working Group on Technical Specifications for Manufacture and Evaluation of Yellow Fever Vaccines, Geneva, Switzerland, 13-14 May 2009*. *Vaccine* 28, 8236–8245.

52. Menezes M, Fernandes L, Homma A (2015). *Serious adverse events associated with yellow fever vaccine*. Hum Vaccin Immunother 11, 2183–2187.
53. WHO/WHE/IHM (2017). *International Coordinating Group on Vaccine Provision for Yellow Fever - Annual meeting 13/14 September 2016*. Geneva: World Health Organization: WHO.
54. WHO (2016). *Global strategy to eliminate yellow fever epidemics (EYE)*. In SAGE. WHO.
55. UNICEF (2016). *Yellow Fever Vaccine: Current Supply Outlook - UNICEF Supply Division*. Denmark: UNICEF
56. WHO (2017). *Eliminate Yellow fever Epidemics (EYE): a global strategy, 2017-2026*. Wkly Epidemiol Rec 92, 193–204.
57. Wikan N, Smith DR (2016). *Zika virus: history of a newly emerging arbovirus*. Lancet Infect Dis 16, 119–126.
58. Brasil P, Pereira JP, Moreira ME, Ribeiro Nogueira RM, Damasceno L, et al. (2016). *Zika Virus Infection in Pregnant Women in Rio de Janeiro*. N Engl J Med 375, 2321–2334.
59. Sun J, Wu D, Zhong H, et al. (2016). *Presence of zika virus in conjunctival fluid*. JAMA Ophthalmology 134, 1330–1332.
60. Osuna CE, Lim S-Y, Deleage C, Griffin BD, Stein D, et al. (2016). *Zika viral dynamics and shedding in rhesus and cynomolgus macaques*. Nat Medicine 22, 1448.
61. Baud D, Gubler DJ, Schaub B, Lanteri MC, Musso D (2017). *An update on Zika virus infection*. Lancet 390, 2099–2109.
62. Johansson MA, Mier-y-Teran-Romero L, Reefhuis J, Gilboa SM, Hills SL (2016). *Zika and the Risk of Microcephaly*. N Engl J Med 375, 1–4.
63. Garcez PP, Loiola EC, Madeiro da Costa R, Higa LM, Trindade P, et al. (2016). *Zika virus impairs growth in human neurospheres and brain organoids*. Science 352, 816–818.
64. Tang H, Hammack C, Ogden SC, Wen Z, Qian X, et al. (2016). *Zika Virus Infects Human Cortical Neural Progenitors and Attenuates Their Growth*. Cell Stem Cell 18, 587–590.
65. Rasmussen SA, Jamieson DJ, Honein MA, Petersen LR (2016). *Zika Virus and Birth Defects — Reviewing the Evidence for Causality*. N Engl J Med 374, 1981–1987.
66. Cao-Lormeau V-M, Blake A, Mons S, Lastère S, Roche C, et al. (2016). *Guillain-Barré Syndrome outbreak associated with Zika virus infection in French Polynesia: a case-control study*. Lancet 387, 1531–1539.
67. Siu R, Bukhari W, Todd A, Gunn W, Huang QS, et al. (2016). *Acute Zika infection with concurrent onset of Guillain-Barré Syndrome*. Neurol 87, 1623–1624.
68. do Rosario MS, de Jesus PA, Vasilakis N, Farias DS, Novaes MA, et al. (2016). *Guillain-Barre Syndrome After Zika Virus Infection in Brazil*. Am J Trop Med Hyg 95, 1157–1160.
69. Chang AY, Lynch R, Martins K, Encinales L, Cadena Bonfanti AÁ, et al. (2018). *Long-term clinical outcomes of Zika-associated Guillain-Barré syndrome*. Emerg Microbes Infect 7, 132–148.

70. Kraemer MU, Sinka ME, Duda KA, Mylne AQ, Shearer FM, *et al.* (2015). *The global distribution of the arbovirus vectors Aedes aegypti and Ae. albopictus.* eLife 4, 8347.
71. Chouin-Carneiro T, Vega-Rua A, Vazeille M, Yebakima A, Girod R, *et al.* (2016). *Differential Susceptibilities of Aedes aegypti and Aedes albopictus from the Americas to Zika Virus.* PLOS Negl Trop Dis 10, 4543–4567.
72. Göertz GP, Vogels CBF, Geertsema C, Koenraadt CJM, Pijlman GP (2017). *Mosquito co-infection with Zika and chikungunya virus allows simultaneous transmission without affecting vector competence of Aedes aegypti.* PLOS Negl Trop Dis 11, 5654.
73. Mansuy JM, Dutertre M, Mengelle C, Fourcade C, Marchou B, *et al.* (2016). *Zika virus: high infectious viral load in semen, a new sexually transmitted pathogen?* Lancet Infect Dis 16, 405.
74. Foy BD, Kobylinski KC, Foy JLC, Blitvich BJ, Travassos da Rosa A, *et al.* (2011). *Probable Non-Vector-borne Transmission of Zika Virus, Colorado, USA.* Emerg Infect Dis 17, 880–882.
75. Murray KO, Gorchakov R, Carlson AR, Berry R, Lai L, *et al.* (2017). *Prolonged Detection of Zika Virus in Vaginal Secretions and Whole Blood.* Emerg Infect Dis 23, 99–101.
76. Mead PS, Duggal NK, Hook SA, Delorey M, Fischer M, *et al.* (2018). *Zika Virus Shedding in Semen of Symptomatic Infected Men.* N Engl J Med 378, 1377–1385.
77. Cavalcanti MG, Cabral-Castro MJ, Gonçalves JLS, Santana LS, Pimenta ES, *et al.* (2017). *Zika virus shedding in human milk during lactation: an unlikely source of infection?* Int J Infect Dis 57, 70–72.
78. WHO (2016). *WHO Zika Virus (ZIKV) Vaccine Target Product Profile (TPP): Vaccine to Protect Against Congenital Zika Virus Syndrome for Use During an Emergency.* Geneva: WHO/UNICEF.
79. Wilder-Smith A, Vannice K, Durbin A, Hombach J, Thomas SJ, *et al.* (2018). *Zika vaccines and therapeutics: landscape analysis and challenges ahead.* BMC medicine 16, 84.
80. WHO *WHO Vaccine Pipeline Tracker.* https://www.who.int/immunization/research/vaccine_pipeline_tracker_spreadsheets/en/ (01/10/2019).
81. Dowd KA, DeMaso CR, Pelc RS, Speer SD, Smith ARY, *et al.* (2016). *Broadly Neutralizing Activity of Zika Virus-Immune Sera Identifies a Single Viral Serotype.* Cell Rep 16, 1485–1491.
82. Aliota MT, Dudley DM, Newman CM, Mohr EL, Gellerup DD, *et al.* (2016). *Heterologous Protection against Asian Zika Virus Challenge in Rhesus Macaques.* PLOS Negl Trop Dis 10, 5168.
83. Plotkin SA, Graham BS (2018). *Zika Virus.* In Plotkin's Vaccines, Volume 7, SA Plotkin, WA Orenstein, PA Offit and KM Edwards, eds.: Elsevier, 1266–1267.
84. Poland GA, Kennedy RB, Ovsyannikova IG, Palacios R, Ho PL, *et al.* (2018). *Development of vaccines against Zika virus.* Lancet Infect Dis.
85. Shapiro-Mendoza CK, Rice ME, Galang RR, Fulton AC, VanMaldeghem K, *et al.* (2017). *Pregnancy Outcomes After Maternal Zika Virus Infection During*

- Pregnancy - U.S. Territories, January 1, 2016-April 25, 2017*. MMWR 66, 615–621.
86. Aliota MT, Bassit L, Bradrick SS, Cox B, Garcia-Blanco MA, *et al.* (2017). *Zika in the Americas, year 2: What have we learned? What gaps remain? A report from the Global Virus Network*. Antiviral Res 144, 223–246.
 87. McShane H, Williams A (2011). *Tuberculosis vaccine promises sterilizing immunity*. Nat Medicine 17, 1185.
 88. Messer RJ, Dittmer U, Peterson KE, Hasenkrug KJ (2004). *Essential role for virus-neutralizing antibodies in sterilizing immunity against Friend retrovirus infection*. PNAS 101, 12260–12265.
 89. Harper DM, Franco EL, Wheeler CM, Moscicki A-B, Romanowski B, *et al.* (2006). *Sustained efficacy up to 4.5 years of a bivalent L1 virus-like particle vaccine against human papillomavirus types 16 and 18: follow-up from a randomised control trial*. Lancet 367, 1247–1255.
 90. Stettler K, Beltramello M, Espinosa DA, Graham V, Cassotta A, *et al.* (2016). *Specificity, cross-reactivity, and function of antibodies elicited by Zika virus infection*. Science 353, 823–826.
 91. Dejnirattisai W, Supasa P, Wongwiwat W, Rouvinski A, Barba-Spaeth G, *et al.* (2016). *Dengue virus sero-cross-reactivity drives antibody-dependent enhancement of infection with zika virus*. Nat Immuno 17, 1102–1108.
 92. Pantoja P, Perez-Guzman EX, Rodriguez IV, White LJ, Gonzalez O, *et al.* (2017). *Zika virus pathogenesis in rhesus macaques is unaffected by pre-existing immunity to dengue virus*. Nat Commun 8, 15674.
 93. Halai U-A, Nielsen-Saines K, Moreira ML, de Sequeira PC, Junior JPP, *et al.* (2017). *Maternal Zika Virus Disease Severity, Virus Load, Prior Dengue Antibodies, and Their Relationship to Birth Outcomes*. Clin Infect Dis 65, 877–883.
 94. Faden RR, Krubiner CB, Lyerly AD, Little MO, August A, *et al.* (2017). *Ethics, pregnancy, and ZIKV vaccine research & development*. Vaccine 35, 6819–6822.
 95. Yasumura Y, Kawakita Y (1963). *A line of cells derived from African green monkey kidney*. Nippon Rinsho 21, 1209–1210.
 96. Sheets R (2000). *History and Characterization of the Vero Cell Line*. In USPHS CBER/OVRR/DVRPA/VVB for the Vaccines and Related Biological Products. Advisory Committee Meeting held on May 12, 2000.
 97. Osada N, Kohara A, Yamaji T, Hirayama N, Kasai F, *et al.* (2014). *The genome landscape of the african green monkey kidney-derived vero cell line*. DNA Res 21, 673–683.
 98. Petriccioni JC, Levenbook IS, Wierenga DE, Qi YH (1987). *Early passage primate cell immortality is independent of tumorigenicity*. In Vitro Cell Dev Biol 23, 523–526.
 99. Manohar M, Orrison B, Peden K, Lewis AM, Jr. (2008). *Assessing the tumorigenic phenotype of VERO cells in adult and newborn nude mice*. Biolog 36, 65–72.
 100. Andreani NA, Renzi S, Piovani G, Ajmone Marsan P, Bomba L, *et al.* (2017). *Potential neoplastic evolution of Vero cells: in vivo and in vitro characterization*. Cytotechnol 69, 741–750.

101. Aubrit F, Perugi F, Léon A, Guéhenneux F, Champion-Arnaud P, *et al.* (2015). *Cell substrates for the production of viral vaccines*. *Vaccine* 33, 5905–5912.
102. Montagnon BJ, Vincent-Falquet JC (1998). *Experience with the Vero cell line*. *Dev Biol Stand* 93, 119–123.
103. Litwin J (1992). *The growth of Vero cells in suspension as cell-aggregates in serum-free media*. *Cytotechnology* 10, 169-174.
104. Shen CF, Elahi M, Ansorge S, Krishnan L, Gilbert R, *et al.* (2018). *Development of suspensions adapted Vero cell culture process for production of viruses*. In *Vaccine Technology VII*. Montreal, Canada: ECI Symposium Series.
105. Rourou S, Zakkour MB, Kallel H (2018). *Adaptation of Vero cells to suspension culture and rabies virus production on different SERUM free media*. In *Vaccine Technology VII*. Montreal, Canada: ECI Symposium Series.
106. Macpherson I, Stoker M (1962). *Polyoma transformation of hamster cell clones--an investigation of genetic factors affecting cell competence*. *Virology* 16, 147–151.
107. Pay TW, Boge A, Menard FJ, Radlett PJ (1985). *Production of rabies vaccine by an industrial scale BHK 21 suspension cell culture process*. *Dev Biol Stand* 60, 171–174.
108. Kompala DS, Ozturk SS (2005). *Optimization of High Cell Density Perfusion Bioreactors*. In *Cell Culture Technology for Pharmaceutical and Cell-Based Therapies*, Volume 1, SS Ozturk and WS Hu, eds. Boca Raton: CRC Press, 387–411.
109. Radlett PJ (1987). *The use of BHK suspension cells for the production of foot and mouth disease vaccines*. Berlin, Heidelberg: Springer Berlin Heidelberg, pp. 129–146.
110. WHO (2013). *Annex 3 - Recommendations for the evaluation of animal cell cultures as substrates for the manufacture of biological medicinal products and for the characterization of cell banks*. In *Replacement of Annex 1 of WHO Technical Report Series*, No 878. Geneva: WHO.
111. Reid LM, Jones CL, Holland J (1979). *Virus Carrier State Suppresses Tumorigenicity of Tumor Cells in Athymic (Nude) Mice*. *J Gen Virol* 42, 609–614.
112. Lalosevic D, Lalosevic V, Lazarevic-Ivanc L, Knezevic I (2008). *BHK-21 cell culture rabies vaccine: immunogenicity of a candidate vaccine for humans*. *Dev Biol Stand* 131, 421–429.
113. Lalosevic D, Stankov S, Lazarevic-Ivanc L, Lalosevic V, Knezevic I (1998). *Immunogenicity of BHK-rabies vaccine in human volunteers*. *Med Pregl* 51 Suppl 1, 17–19.
114. Halstead SB, Hills SL, Dubischar K (2018). *33 - Japanese Encephalitis Vaccines*. In *Plotkin's Vaccines*, Volume 7, SA Plotkin, WA Orenstein, PA Offit and KM Edwards, eds.: Elsevier, 511–548.
115. Brooks SA (2004). *Appropriate glycosylation of recombinant proteins for human use*. *Molec Biotechn* 28, 241–255.
116. Ghaderi D, Zhang M, Hurtado-Ziola N, Varki A (2012). *Production platforms for biotherapeutic glycoproteins. Occurrence, impact, and challenges of non-human sialylation*. *Biotechnol Genet Eng Rev* 28, 147–175.

117. Guehenneux F, Moreau K, Esnault M, Mehtali M (2007). *Method of making a virus using duck embryonic derived stem cell lines* V SE, ed.
118. Brown SW, Mehtali M (2010). *The Avian EB66(R) Cell Line, Application to Vaccines, and Therapeutic Protein Production*. PDA J Pharm Sci Technol 64, 419–425.
119. Madeline B, Ribaud S, Xenopoulus A, Simler J, Schamborn K, *et al.* (2010). *Culturing a Duck ES-Derived Cell Line in Single-Use Bioreactors*.
120. Manwaring J, Larsen J, Sharh M, Wight M, Aubrit F, *et al.* *Development of chemically-defined medium for virus vaccine production in a duck suspension cell line*. In ESACT 2017. Lausanne, Switzerland.
121. White KM, Ayllon J, Mena I, Potenski A, Krammer F, *et al.* (2018). *Influenza B virus reverse genetic backbones with improved growth properties in the EB66® cell line as basis for vaccine seed virus generation*. Vaccine 36, 1146–1153.
122. Léon A, David A-L, Madeline B, Guianvarc'h L, Dureau E, *et al.* (2016). *The EB66® cell line as a valuable cell substrate for MVA-based vaccines production*. Vaccine 34, 5878–5885.
123. Olivier S, Jacoby M, Brillon C, Bouletreau S, Mollet T, *et al.* (2010). *EB66 cell line, a duck embryonic stem cell-derived substrate for the industrial production of therapeutic monoclonal antibodies with enhanced ADCC activity*. MAbs 2, 405–415.
124. Lagassé HAD, Alexaki A, Simhadri VL, Katagiri NH, Jankowski W, *et al.* (2017). *Recent advances in (therapeutic protein) drug development*. F1000Res 6, 113–113.
125. Tapia F, Vázquez-Ramírez D, Genzel Y, Reichl U (2016). *Bioreactors for high cell density and continuous multi-stage cultivations: options for process intensification in cell culture-based viral vaccine production*. Appl Microbiol Biotechnol 100, 2121–2132.
126. Sun L, Xiong Z, Zhou W, Liu R, Yan X, *et al.* (2015). *Novel konjac glucomannan microcarriers for anchorage-dependent animal cell culture*. Biochem Eng J 96, 46–54.
127. Reiter M, Mundt W (2003). *Method for large scale production of virus antigen* Volume CA2469644, BH SA, ed.
128. Losa J (2018). *Packed-bed reactors for the production of yellow fever virus vaccines* Max Planck Institute Magdeburg.
129. Preissmann A, Wiesmann R, Buchholz R, Werner RG, Noé W (1997). *Investigations on oxygen limitations of adherent cells growing on macroporous microcarriers*. Cytotechnol 24, 121–134.
130. Drugmand J-C, Esteban G, Alaoui N, Jafâr N, Havelange N, *et al.* (2009). *On-line monitoring: animal cell cultivation in iCELLis™ fixed-bed reactor using dielectric measurements*. In Proceedings of the 21st Annual Meeting of the European Society for Animal Cell Technology (ESACT). Dublin: Springer, pp. 395–399.
131. Tapia F, Vogel T, Genzel Y, Behrendt I, Hirschel M, *et al.* (2014). *Production of high-titer human influenza A virus with adherent and suspension MDCK cells cultured in a single-use hollow fiber bioreactor*. Vaccine 32, 1003–1011.
132. Silva A, Roldão A, Teixeira A, Fernandes P, Sousa MQ, *et al.* (2015). *Cell Immobilization for the Production of Viral Vaccines*. In Animal Cell Culture, Volume 9, M Al-Rubeai, ed.: Springer International Publishing, 541–563.

133. Broise D, Noiseux M, Lemieux R, Massie B (1991). *Long-term perfusion culture of hybridoma: a "grow or die" cell cycle system*. *Biotechnol Bioeng* 38, 781–787.
134. Kamaraju H, Wetzel K, Kelly WJ (2010). *Modeling shear-induced CHO cell damage in a rotary positive displacement pump*. *Biotechnol Prog* 26, 1606–1615.
135. Löffelholz C, Blaschczok K, Dittler I, Lehmann N, Kaiser S, *et al.* (2016). *Investigations into mechanical stress caused to CHO suspension cells by single-use magnetically levitated, bearingless centrifugal pump*. Levitronix GmbH.
136. Tolbert WR (1983). *Cell culture pumping system*. Volume 4,417,861, US Patent, ed.: Monsanto Company.
137. Shevitz J (2003). *Fluid filtration system*. Volume 6,544,424. US: Refined Technology Company.
138. Mercier SM, Diepenbroek B, Martens D, Wijffels RH, Streefland M (2015). *Characterization of apoptosis in PER.C6(R) batch and perfusion cultures*. *Biotechnol Bioeng* 112, 569–578.
139. Kelly W, Scully J, Zhang D, Feng G, Lavengood M, *et al.* (2014). *Understanding and modeling alternating tangential flow filtration for perfusion cell culture*. *Biotechnol Prog* 30, 1291–1300.
140. Wright B, Bruninghaus M, Vrabel M, Walther J, Shah N, *et al.* (2015). *A novel seed-train process: Using high-density cell banking, a disposable bioreactor, and perfusion technologies*. In *BioProc Int*, Volume 13.
141. Seth G, Hamilton RW, Stapp TR, Zheng L, Meier A, *et al.* (2013). *Development of a new bioprocess scheme using frozen seed train intermediates to initiate CHO cell culture manufacturing campaigns*. *Biotechnol Bioeng* 110, 1376–1385.
142. Konstantinov K, Goudar C, Ng M, Meneses R, Thrift J, *et al.* (2006). *The "push-to-low" approach for optimization of high-density perfusion cultures of animal cells*. *Adv Biochem Eng Biot* 101, 75–98.
143. Karst DJ, Steinhoff RF, Kopp MRG, Serra E, Soos M, *et al.* (2017). *Intracellular CHO Cell Metabolite Profiling Reveals Steady-State Dependent Metabolic Fingerprints in Perfusion Culture*. *Biotechnol Prog* 33, 879–890.
144. Ozturk SS (1996). *Engineering challenges in high density cell culture systems*. *Cytotechnol* 22, 3–16.
145. Dowd JE, Jubb A, Kwok KE, Piret JM (2003). *Optimization and control of perfusion cultures using a viable cell probe and cell specific perfusion rates*. *Cytotechnol* 42, 35–45.
146. Hiller GW, Ovalle AM, Gagnon MP, Curran ML, Wang W (2017). *Cell-controlled hybrid perfusion fed-batch CHO cell process provides significant productivity improvement over conventional fed-batch cultures*. *Biotechnol Bioeng* 114, 1438–1447.
147. Nikolay A, Bissinger T, Gränicher G, Wu Y, Genzel Y, *et al.* (in press). *Perfusion control for high cell density cultivation and viral vaccine production*. In *Animal Cell Biotechnology: Methods and Protocols*, R Pörtner, ed. Totowa, NJ: Humana Press.
148. Degouys V, Cerckel I, Garcia A, Harfield J, Dubois D, *et al.* (1993). *Dielectric spectroscopy of mammalian cells*. *Cytotechnol* 13, 195–202.
149. Davey C, Guan Y, Kemp R, Kell D (1997). *The Viable Cell Monitor: A Dielectric spectroscope for Growth and Metabolic Studies of Animal Cells on Macroporous*

- Beads*. In *New Developments and New Applications in Animal Cell Technology*, Volume 8, O-WMe al., ed.: Academic Publishers, 321–328.
150. Ducommun P, Kadouri A, von Stockar U, Marison IW (2002). *On-line determination of animal cell concentration in two industrial high-density culture processes by dielectric spectroscopy*. *Biotechnol Bioeng* 77, 316–323.
 151. Carvell JP, Dowd JE (2006). *On-line Measurements and Control of Viable Cell Density in Cell Culture Manufacturing Processes using Radio-frequency Impedance*. 50, 35–48.
 152. Junker BH, Wang HY (2006). *Bioprocess monitoring and computer control: Key roots of the current PAT initiative*. *Biotechnol Bioeng* 95, 226–261.
 153. Fricke R, Schnabel R, Beck K, Fricke R, Mitarbeitern (1936). *Oberfläche und Wärmehalt beim kristallisierten Magnesiumhydroxyd*. *Z Elektrochem angew Phy Chem* 42, 881–889.
 154. Höber R (1912). *Ein zweites Verfahren, die Leitfähigkeit im Innern von Zellen zu messen*. *Pflügers Arch* 148, 189–221.
 155. Gabriel S, Lau RW, Gabriel C (1996). *The dielectric properties of biological tissues: III. Parametric models for the dielectric spectrum of tissues*. *Phys Med Biol* 41, 2271–2293.
 156. Fricke H (1925). *The electric capacity of suspensions with special reference to blood*. *J Gen Physiol* 9, 137–152.
 157. Schwan H (1950). *Die Bestimmungen der dielektrischen und magnetischen Eigenschaften inhomogener Dielektriken, insbesondere biologischer Körper, im Dezimeterwellenbereich. III Auswerteverfahren zur Bestimmung der elektrischen und magnetischen Stoffkonstanten im Dezimeterwellengebiet*. *Ann Phys* 440, 287–310.
 158. Davey CL, Kell DB (1995). *The low-frequency dielectric properties of biological cells*. In *Bioelectrochem CT*, D Walz, H Berg and G Milazzo, eds. Basel: Birkhäuser Basel, 159–207.
 159. Cole KS (1968). *Membranes, Ions and Impulses*. In *Classical Biophysics*, JW Moore, ed. Berkeley: University of California Press, 268–268.
 160. Schwan HP (1957). *Electrical Properties of Tissue and Cell Suspensions*. In *Advances in Biological and Medical Physics*, Volume 5, JH Lawrence and CA Tobias, eds.: Elsevier, 119–289.
 161. Pliquet U (2010). *Bioimpedance: A Review for Food Processing*. *J Food Eng* 2, 74–94.
 162. Cole KS, Cole RH (1941). *Dispersion and Absorption in Dielectrics I. Alternating Current Characteristics*. *The Journal of Chemical Physics* 9, 341–351.
 163. Pauly H, Schwan HP (1959). *Über die Impedanz einer Suspension von kugelförmigen Teilchen mit einer Schale*. In *Z Naturforsch B*, Volume 14. p. 125.
 164. Hanai T (1960). *Theory of the dielectric dispersion due to the interfacial polarization and its application to emulsions*. *Kolloid-Z* 171, 23–31.
 165. Harris CM, Todd RW, Bungard SJ, Lovitt RW, Morris JG, et al. (1987). *Dielectric permittivity of microbial suspensions at radio frequencies: a novel method for the real-time estimation of microbial biomass*. *Enzyme Microb Tech* 9, 181–186.
 166. Markx GH, Davey CL, Kell DB, Morris P (1991). *The dielectric permittivity at radio frequencies and the bruggeman probe: novel techniques for the on-line*

- determination of biomass concentrations in plant cell cultures. *J Biotechnol* 20, 279–290.
167. Cole KS, Cole RH (1941). *Dispersion and Absorption in Dielectrics I. Alternating Current Characteristics*. *J Chem Phys* 9, 341–351.
168. Davey CL, Davey HM, Kell DB, Todd RW (1993). *Introduction to the dielectric estimation of cellular biomass in real time, with special emphasis on measurements at high volume fractions*. *Anal Chim Acta* 279, 155–161.
169. Castilho LR, Medronho RA (2002). *Cell Retention Devices for Suspended-Cell Perfusion Cultures*. In *Tools and Applications of Biochemical Engineering Science*, K Schügerl, AP Zeng, JG Aunins, A Bader, W Bell, H Biebl, M Biselli, MJT Carrondo, LR Castilho, HN Chang, et al., eds. Berlin, Heidelberg: Springer Berlin Heidelberg, 129–169.
170. Wang S, Godfrey S, Ravikrishnan J, Lin H, Vogel J, et al. (2017). *Shear contributions to cell culture performance and product recovery in ATF and TFF perfusion systems*. *J Biotechnol* 246, 52–60.
171. Walther J, McLarty J, Johnson T (2018). *The effects of alternating tangential flow (ATF) residence time, hydrodynamic stress and filtration flux on high-density perfusion cell culture*. *Biotechnol Bioeng* 116, 320–332.
172. Bolton GR, Apostolidis AJ (2017). *Mechanistic modeling of the loss of protein sieving due to internal and external fouling of microfilters*. *Biotechnol Prog* 33, 1323–1333.
173. Mulder J (1996). *Basic Principles of Membrane Technology*, Volume 2: Springer.
174. Zeman LJ, Zydney AL (2017). *Microfiltration and ultrafiltration: principles and applications*: CRC Press.
175. Fane AG, Tang CY, Wang R (2011). *Membrane Technology for Water: Microfiltration, Ultrafiltration, Nanofiltration, and Reverse Osmosis*. In *Treatise on Water Science*, P Wilderer, ed. Oxford: Elsevier, 301–335.
176. Melin T, Rautenbach R (2007). *Membranverfahren: Grundlagen der Modul- und Anlagenauslegung*: Springer Berlin Heidelberg.
177. Trzaskus KW, de Vos WM, Kemperman A, Nijmeijer K (2015). *Towards controlled fouling and rejection in dead-end microfiltration of nanoparticles – Role of electrostatic interactions*. *J Membr Sci* 496, 174–184.
178. Hanemaaijer JH, Robbertsen T, van den Boomgaard T, Gunnink JW (1989). *Fouling of ultrafiltration membranes. The role of protein adsorption and salt precipitation*. *J Membr Sci* 40, 199–217.
179. Cho J, Amy G, Pellegrino J (2000). *Membrane filtration of natural organic matter: factors and mechanisms affecting rejection and flux decline with charged ultrafiltration (UF) membrane*. *J Membr Sci* 164, 89–110.
180. Hwang K-J, Liao C-Y, Tung K-L (2008). *Effect of membrane pore size on the particle fouling in membrane filtration*. *Desalination* 234, 16-23.
181. Chudacek MW, Fane AG (1984). *The dynamics of polarisation in unstirred and stirred ultrafiltration*. *J Membr Sci* 21, 145–160.
182. Schafer A (1999). *Natural organics removal using membranes / Andrea Iris Schafer*, Sydney: UNESCO Centre for Membrane Science and Technology, Chemical Engineering and Industrial Chemistry, University of New South Wales.

183. Bauser H, Chmiel H, Stroh N, Walitza E (1982). *Interfacial effects with microfiltration membranes*. J Membr Sci 11, 321–332.
184. Wang H, Yu T, Zhao C, Du Q (2009). *Improvement of hydrophilicity and blood compatibility on polyethersulfone membrane by adding polyvinylpyrrolidone*. Fiber Polym 10, 1–5.
185. Pinnau I, Freeman BD (1999). *Formation and Modification of Polymeric Membranes: Overview*. In Membrane Formation and Modification, Volume 744. American Chemical Society, 1–22.
186. Cowan S, Ritchie S (2007). *Modified Polyethersulfone (PES) Ultrafiltration Membranes for Enhanced Filtration of Whey Proteins*. Sep Sci Technol 42, 2405–2418.
187. Meireles M, Aimar P, Sanchez V (1991). *Effects of protein fouling on the apparent pore size distribution of sieving membranes*. J Membr Sci 56, 13–28.
188. Cornelissen ER (1997). *Membrane fouling in waste water filtration: causes, consequences and prevention*. Netherlands: University of Twente.
189. Dietz P, Hansma PK, Inacker O, Lehmann H-D, Herrmann K-H (1992). *Surface pore structures of micro- and ultrafiltration membranes imaged with the atomic force microscope*. J Membr Sci 65, 101–111.
190. Hirose M, Ito H, Kamiyama Y (1996). *Effect of skin layer surface structures on the flux behaviour of RO membranes*. J Membr Sci 121, 209–215.
191. Wenzel RN (1949). *Surface Roughness and Contact Angle*. J Phys Colloid Chem 53, 1466–1467.
192. Marshall AD, Munro PA, Trägårdh G (1993). *The effect of protein fouling in microfiltration and ultrafiltration on permeate flux, protein retention and selectivity: A literature review*. Desalination 91, 65–108.
193. Vrijenhoek EM, Hong S, Elimelech M (2001). *Influence of membrane surface properties on initial rate of colloidal fouling of reverse osmosis and nanofiltration membranes*. J Membr Sci 188, 115–128.
194. Rana D, Matsuura T (2010). *Surface Modifications for Antifouling Membranes*. Chem Rev 110, 2448–2471.
195. Ulbricht M, Richau K, Kamusewitz H (1998). *Chemically and morphologically defined ultrafiltration membrane surfaces prepared by heterogeneous photo-initiated graft polymerization*. Colloids Surf 138, 353–366.
196. Futselaar H (1993). *The transverse flow membrane module. Construction, performance and applications.*, Volume Ph.D. Thesis. Netherlands University of Twente.
197. Hiller GW, Clark DS, Blanch HW (1993). *Cell retention–chemostat studies of hybridoma cells—analysis of hybridoma growth and metabolism in continuous suspension culture in serum-free medium*. Biotechnol Bioeng 42, 185–195.
198. Radoniqi F, Zhang H, Bardliving CL, Shamlou P, Coffman J (2018). *Computational fluid dynamic modeling of alternating tangential flow filtration for perfusion cell culture*. Biotechnol Bioeng 115, 2751–2759.
199. Jordan I, Vos A, Beilfuß S, Neubert A, Breul S, et al. (2009). *An avian cell line designed for production of highly attenuated viruses*. Vaccine 27, 748–756.
200. Nikolay A (2014). *Investigation of hollow fiber based high cell density cultivations of BHK-21 cells for continuous bovine respiratory syncytial virus vaccine*

- manufacturing*. Volume Master. Institute for Biotechnology: Technical University of Braunschweig.
201. Lohr V, Genzel Y, Behrendt I, Scharfenberg K, Reichl U (2010). *A new MDCK suspension line cultivated in a fully defined medium in stirred-tank and wave bioreactor*. *Vaccine* 28, 6256–6264.
 202. Scharfenberg K, Wagner R (1995). *A Reliable Strategy for The Achievement of Cell Lines Growing in Protein-Free Medium*. In *Animal Cell Technology: Developments Towards the 21st Century*, EC Beuvery, JB Griffiths and WP Zeijlemaker, eds. Dordrecht: Springer Netherlands, 619–623.
 203. Tapia F, Jordan I, Genzel Y, Reichl U (2017). *Efficient and stable production of Modified Vaccinia Ankara virus in two-stage semi-continuous and in continuous stirred tank cultivation systems*. *PLOS One* 12, 182553.
 204. Pelz L (2019). *Optimization of yellow fever virus production with BHK- 21 cells*. Max Planck Institute Magdeburg.
 205. Bock A, Sann H, Schulze-Horsel J, Genzel Y, Reichl U, *et al.* (2009). *Growth behavior of number distributed adherent MDCK cells for optimization in microcarrier cultures*. *Biotechnol Prog* 25, 1717–1731.
 206. Hierholzer JC, Killington RA (1996). *2 - Virus isolation and quantitation*. In *Virology Methods Manual*, BWJ Mahy and HO Kangro, eds. London: Academic Press, 25–46.
 207. Domingo C, Patel P, Yillah J, Weidmann M, Mendez JA, *et al.* (2012). *Advanced yellow fever virus genome detection in point-of-care facilities and reference laboratories*. *J Clin Microbiol* 50, 4054–4060.
 208. Lanciotti RS, Kosoy OL, Laven JJ, Velez JO, Lambert AJ, *et al.* (2008). *Genetic and serologic properties of Zika virus associated with an epidemic, Yap State, Micronesia, 2007*. *Emerg Infect Dis* 14, 1232–1239.
 209. Bartels E (2016). *Etablierung und Validierung verschiedener Assays zur Quantifizierung von Flaviviren: RT-qPCR, Plaque Assay und Durchflusszytometrie* In Institute of Process Engineering, Volume Bachelor. Otto von Guericke University Magdeburg.
 210. Frensing T, Pflugmacher A, Bachmann M, Peschel B, Reichl U (2014). *Impact of defective interfering particles on virus replication and antiviral host response in cell culture-based influenza vaccine production*. *Appl Microbiol Biotechnol* 98, 8999–9008.
 211. Wold S (1978). *Cross-Validatory Estimation of the Number of Components in Factor and Principal Components Models* AU - Wold, Svante. *Technometrics* 20, 397–405.
 212. Opel CF, Li J, Amanullah A (2010). *Quantitative modeling of viable cell density, cell size, intracellular conductivity, and membrane capacitance in batch and fed-batch CHO processes using dielectric spectroscopy*. *Biotechnol Prog* 26, 1187–1199.
 213. Konakovsky V, Yagtu AC, Clemens C, Müller MM, Berger M, *et al.* (2015). *Universal Capacitance Model for Real-Time Biomass in Cell Culture*. *Sensors* 15, 22128–22150.
 214. Fairbrother F, Mastin H (1924). *Studies in electro-endosmosis. Part I*. *J Chem Soc* 125, 2319–2330.

215. Bock A (2012). *Überwachung und Regelung von Hochzelldichtekultivierungen in der Influenza-Impfstoffproduktion*. In Fakultät für Verfahrens- und Systemtechnik, Volume Ph.D. Magdeburg: OvGU Magdeburg.
216. Ghosh Roy S, Sadigh B, Datan E, Lockshin RA, Zakeri Z (2014). *Regulation of cell survival and death during Flavivirus infections*. World J Biol Chem 5, 93–105.
217. Laurent-Rolle M, Morrison J, Rajsbaum R, Macleod Jessica ML, Pisanelli G, *et al.* (2014). *The Interferon Signaling Antagonist Function of Yellow Fever Virus NS5 Protein Is Activated by Type I Interferon*. Cell Host Microbe 16, 314–327.
218. Crespi M, Chiu MN, Struthers JK, Schoub BD, Lyons SF (1988). *Effect of interferon on Vero cells persistently infected with Sendai virus compared to Vero cells persistently infected with SSPE virus*. Arch Virol 98, 235–251.
219. Brand OM, Allen WP (1970). *Preparation of noninfectious arbovirus antigens*. Appl Microbiol 20, 298–302.
220. Muller JA, Harms M, Schubert A, Jansen S, Michel D, *et al.* (2016). *Inactivation and Environmental Stability of Zika Virus*. Emerg Infect Dis 22, 1685–1687.
221. Souza MCO, Freire MS, Schulze EA, Gaspar LP, Castilho LR (2009). *Production of yellow fever virus in microcarrier-based Vero cell cultures*. Vaccine 27, 6420–6423.
222. Chen A, Poh SL, Dietzsch C, Roethl E, Yan ML, *et al.* (2011). *Serum-free microcarrier based production of replication deficient influenza vaccine candidate virus lacking NS1 using Vero cells*. BMC Biotechnol 11, 73–81.
223. Rehberg M, Ritter JB, Genzel Y, Flockerzi D, Reichl U (2013). *The relation between growth phases, cell volume changes and metabolism of adherent cells during cultivation*. J Biotechnol 164, 489–499.
224. Wang Y, Ouyang F (1999). *Bead-to-bead transfer of Vero cells in microcarrier culture*. Cytotechnology 31, 221–224.
225. Jiang Y, van der Welle JE, Rubingh O, van Eikenhorst G, Bakker WAM, *et al.* (2019). *Kinetic model for adherent Vero cell growth and poliovirus production in batch bioreactors*. Process Biochemi.
226. El Wajgali A, Esteban G, Fournier F, Pinton H, Marc A (2012). *Impact of microcarrier coverage on using permittivity for on-line monitoring high adherent Vero cell densities in perfusion bioreactors*. Biochem Eng J 70, 173–179.
227. Bissinger T, Fritsch J, Mihut A, Wu Y, Liu X, *et al.* (in press). *Semi-perfusion cultures of suspension MDCK cells enable high cell concentrations and efficient influenza A virus production*. Vaccine.
228. Rodrigues AF, Soares HR, Guerreiro MR, Alves PM, Coroadinha AS (2015). *Viral vaccines and their manufacturing cell substrates: New trends and designs in modern vaccinology*. Biotechnol J 10, 1329–1344.
229. Nikolay A (2014). *Investigation of hollow fiber based high cell density cultivations of BHK-21 cells for continuous bovine respiratory syncytial virus vaccine manufacturing*. In Faculty of Life Sciences, Volume Master Thesis. Braunschweig: Technische Universität Braunschweig, p. 109.
230. Lauring AS, Frydman J, Andino R (2013). *The role of mutational robustness in RNA virus evolution*. Nat Rev Microbiol 11, 327.

231. Ciota AT, Lovelace AO, Jones SA, Payne A, Kramer LD (2007). *Adaptation of two flaviviruses results in differences in genetic heterogeneity and virus adaptability*. J Gen Virol 88, 2398–2406.
232. Stock NK, Boschetti N, Herzog C, Appelhans MS, Niedrig M (2012). *The phylogeny of yellow fever virus 17D vaccines*. Vaccine 30, 989–994.
233. Stock NK, Laraway H, Faye O, Diallo M, Niedrig M, et al. (2013). *Biological and phylogenetic characteristics of yellow fever virus lineages from West Africa*. J Virol 87, 2895–2907.
234. Lee C-J, Liao C-L, Lin Y-L (2005). *Flavivirus activates phosphatidylinositol 3-kinase signaling to block caspase-dependent apoptotic cell death at the early stage of virus infection*. J Virol 79, 8388–8399.
235. Byk LA, Iglesias NG, De Maio FA, Gebhard LG, Rossi M, et al. (2016). *Dengue Virus Genome Uncoating Requires Ubiquitination*. mBio 7, 804–816.
236. Post PR, Carvalho R, Galler R (1991). *Glycosylation and secretion of yellow fever virus nonstructural protein NS1*. Virus Res 18, 291–302.
237. Butt AM, Nasrullah I, Qamar R, Tong Y (2016). *Evolution of codon usage in Zika virus genomes is host and vector specific*. Emerg Microbes Infect 5, 96–107.
238. Bae H-G, Nitsche A, Teichmann A, Biel SS, Niedrig M (2003). *Detection of yellow fever virus: a comparison of quantitative real-time PCR and plaque assay*. J Virol Methods 110, 185–191.
239. Mukherjee S, Lin T-Y, Dowd KA, Manhart CJ, Pierson TC (2011). *The infectivity of prM-containing partially mature West Nile virus does not require the activity of cellular furin-like proteases*. J Virol 85, 12067–12072.
240. Kouretova J, Hammamy MZ, Epp A, Harges K, Kallis S, et al. (2017). *Effects of NS2B-NS3 protease and furin inhibition on West Nile and Dengue virus replication*. J Enzyme Inhib Med Chem 32, 712–721.
241. Sinigaglia L, Gracias S, Décembre E, Fritz M, Bruni D, et al. (2018). *Immature particles and capsid-free viral RNA produced by Yellow fever virus-infected cells stimulate plasmacytoid dendritic cells to secrete interferons*. Sci Rep 8, 10889.
242. Zanini F, Pu S-Y, Bekerman E, Einav S, Quake SR (2018). *Single-cell transcriptional dynamics of flavivirus infection*. eLife 7, 32942.
243. Koishi AC, Suzukawa AA, Zanluca C, Camacho DE, Comach G, et al. (2018). *Development and evaluation of a novel high-throughput image-based fluorescent neutralization test for detection of Zika virus infection*. PLOS Negl Trop Dis 12, 6342.
244. Gardner CL, Ryman KD (2010). *Yellow fever: a reemerging threat*. Clin Lab Med 30, 237–260.
245. Fernandez-Garcia MD, Meertens L, Chazal M, Hafirassou ML, Dejarnac O, et al. (2016). *Vaccine and Wild-Type Strains of Yellow Fever Virus Engage Distinct Entry Mechanisms and Differentially Stimulate Antiviral Immune Responses*. MBio 7, 1915–1956.
246. Laske T, Heldt FS, Hoffmann H, Frensing T, Reichl U (2016). *Modeling the intracellular replication of influenza A virus in the presence of defective interfering RNAs*. Virus Res 213, 90–99.

247. Frensing T, Heldt FS, Pflugmacher A, Behrendt I, Jordan I, *et al.* (2013). *Continuous Influenza Virus Production in Cell Culture Shows a Periodic Accumulation of Defective Interfering Particles*. PLOS One 8, 72288.
248. Otsuki K, Maeda J, Yamamoto H, Tsubokura M (1979). *Studies on avian infectious bronchitis virus (IBV). III. Interferon induction by and sensitivity to interferon of IBV*. Arch Virol 60, 249–255.
249. Wood HA, Johnston LB, Burand JP (1982). *Inhibition of Autographa californica nuclear polyhedrosis virus replication in high-density Trichoplusia ni cell cultures*. Virology 119, 245–254.
250. Thomassen YE, Rubingh O, Wijffels RH, van der Pol LA, Bakker WAM (2014). *Improved poliovirus D-antigen yields by application of different Vero cell cultivation methods*. Vaccine 32, 2782–2788.
251. Rourou S, van der Ark A, van der Velden T, Kallel H (2007). *A microcarrier cell culture process for propagating rabies virus in Vero cells grown in a stirred bioreactor under fully animal component free conditions*. Vaccine 25, 3879–3889.
252. Kamen A, Henry O (2004). *Development and optimization of an adenovirus production process*. J Gene Med 6 Suppl 1, 184–292.
253. Bock A, Schulze-Horsel J, Schwarzer J, Rapp E, Genzel Y, *et al.* (2011). *High-density microcarrier cell cultures for influenza virus production*. Biotechnol Prog 27, 241–250.
254. Vazquez-Ramirez D, Genzel Y, Jordan I, Sandig V, Reichl U (2018). *High-cell-density cultivations to increase MVA virus production*. Vaccine 36, 3124–3133.
255. Zhang Y (2017). *High cell density perfusion process development for antibody producing Chinese Hamster Ovary cells*. In TRITA-BIO-Report, Volume 2017:14. Stockholm: KTH Royal Institute of Technology, p. 79.
256. Nikolay A, Léon A, Schwamborn K, Genzel Y, Reichl U (2018). *Process intensification of EB66® cell cultivations leads to high-yield yellow fever and Zika virus production*. Appl Microbiol Biotechnol 102, 8725–8737.
257. Merten O-W, Kierulff JV, Castignolles N, Perrin P (1994). *Evaluation of the new serum-free medium (MDSS2) for the production of different biologicals: Use of various cell lines*. Cytotechnol 14, 47–59.
258. Perrin P, Madhusudana S, Gontier-Jallet C, Petres S, Tordo N, *et al.* (1995). *An experimental rabies vaccine produced with a new BHK-21 suspension cell culture process: use of serum-free medium and perfusion-reactor system*. Vaccine 13, 1244–1250.
259. Vickroy B, Lorenz K, Kelly W (2007). *Modeling shear damage to suspended CHO cells during cross-flow filtration*. Biotechnol Prog 23, 194–199.
260. Vishwanathan N, Chantelauze C, Richard S, Voisard D, Monchois V, *et al.* (2019). *Case study: Unexpected impact of shear stress on intensified process* In ESACT (Poster). Copenhagen.
261. Vázquez-Ramírez D, Jordan I, Sandig V, Genzel Y, Reichl U (2019). *High titer MVA and influenza A virus production using a hybrid fed-batch/perfusion strategy with an ATF system*. Appl Microbiol Biotechnol 103, 3025–3035.
262. Yuk IHY, Olsen MM, Geyer S, Forestell SP (2004). *Perfusion cultures of human tumor cells: a scalable production platform for oncolytic adenoviral vectors*. Biotechnol Bioeng 86, 637–642.

263. Reis R, Gadam S, Frautschy LN, Orlando S, Goodrich EM, *et al.* (1997). *High performance tangential flow filtration*. *Biotechnol Bioeng* 56, 71–82.
264. Henry C, Brant JA (2012). *Mechanistic analysis of microfiltration membrane fouling by buckminsterfullerene (C60) nanoparticles*. *J Membr Sci* 415-416, 546–557.
265. Wang SB, Godfrey S, Radoniqi F, Lin H, Coffman J (2019). *Larger Pore Size Hollow Fiber Membranes as a Solution to the Product Retention Issue in Filtration-Based Perfusion Bioreactors*. *Biotechnol J* 14, 1800137.
266. Petiot E, Jacob D, Lanthier S, Lohr V, Ansorge S, *et al.* (2011). *Metabolic and Kinetic analyses of influenza production in perfusion HEK293 cell culture*. *BMC Biotechnol* 11, 84.
267. Searles JA, Todd P, Kompala DS (1994). *Viable Cell Recycle with an Inclined Settler in the Perfusion Culture of Suspended Recombinant Chinese Hamster Ovary Cells*. *Biotechnol Prog* 10, 198–206.
268. Nikolay A, Castilho LR, Reichl U, Genzel Y (2017). *Propagation of Brazilian Zika virus strains in static and suspension cultures using Vero and BHK cells*. *Vaccine* 36, 3140–3145.
269. Calvet G, Aguiar RS, Melo ASO, Sampaio SA, de Filippis I, *et al.* (2016). *Detection and sequencing of Zika virus from amniotic fluid of fetuses with microcephaly in Brazil: a case study*. *Lancet Infect Dis* 16, 653–660.
270. Barreto-Vieira DF, Jacome FC, da Silva MAN, Caldas GC, de Filippis AMB, *et al.* (2017). *Structural investigation of C6/36 and Vero cell cultures infected with a Brazilian Zika virus*. *PLOS One* 12, 121–143.
271. Jordan I, Horn D, John K, Sandig V (2013). *A Genotype of Modified Vaccinia Ankara (MVA) that Facilitates Replication in Suspension Cultures in Chemically Defined Medium*. *Viruses* 5, 321–339.
272. Rüdiger D, Kupke SY, Laske T, Zmora P, Reichl U (2019). *Multiscale modeling of influenza A virus replication in cell cultures predicts infection dynamics for highly different infection conditions*. *PLOS Comput Biol* 15, 1006819.
273. Pethig R, Willis MR (1979). *Dielectric and electronic properties of biological materials*. *Biochem Educ* 8, 376–384.
274. Yardley JE, Kell DB, Barrett J, Davey CL (2000). *On-Line, Real-Time Measurements of Cellular Biomass using Dielectric Spectroscopy*. *Biotechnol Genet Eng Rev* 17, 3–36.
275. Sartorius (2014). *Product sheet: BioPAT® ViaMass Standardized Online Biomass Measurement in Single-Use Fermentation*.
276. Dabros M, Dennewald D, Currie DJ, Lee MH, Todd RW, *et al.* (2009). *Cole-Cole, linear and multivariate modeling of capacitance data for on-line monitoring of biomass*. *Bioproc Biosyst Eng* 32, 161–173.
277. Ansorge S, Esteban G, Schmid G (2010). *On-line monitoring of responses to nutrient feed additions by multi-frequency permittivity measurements in fed-batch cultivations of CHO cells*. *Cytotechnol* 62, 121–132.
278. Altman SA, Randers L, Rao G (1993). *Comparison of Trypan Blue Dye Exclusion and Fluorometric Assays for Mammalian Cell Viability Determinations*. *Biotechnol Prog* 9, 671–674.

279. Fernandes J, Currie J, Ramer K, Zhang A (2019). *Development of Capacitance Tools: At-Line Method for Assessing Biomass of Mammalian Cell Culture and Fixed Cell Calibration Standard*. *Biotechnol J* 14, 1800283.
280. Faber NM, Rajkó R (2007). *How to avoid over-fitting in multivariate calibration—The conventional validation approach and an alternative*. *Anal Chim Acta* 595, 98–106.
281. Cannizzaro C, Gugerli R, Marison I, von Stockar U (2003). *On-line biomass monitoring of CHO perfusion culture with scanning dielectric spectroscopy*. *Biotechnol Bioeng* 84, 597-610.
282. Nicholson DJ, Kell DB, Davey CL (1996). *Deconvolution of the dielectric spectra of microbial cell suspensions using multivariate calibration and artificial neural networks*. *Bioelectrochem Bioenerg* 39, 185-193.
283. Stinstra JG, Hopenfeld B, MacLeod RS (2005). *On the Passive Cardiac Conductivity*. *Ann Biomed Sci* 33, 1743–1751.
284. Roth BJ (2000). *The Electrical Conductivity of Tissues*. In *The Biomedical Engineering Handbook*, Volume 1, 2 Edition, JD Bronzino, ed.: CRC Press LLC.
285. Labeed FH, Coley HM, Hughes MP (2006). *Differences in the biophysical properties of membrane and cytoplasm of apoptotic cells revealed using dielectrophoresis*. *Biochim Biophys Acta* 1760, 922–929.
286. Fehrenbach R, Comberbach M, Pêtre JO (1992). *On-line biomass monitoring by capacitance measurement*. *J Biotechnol* 23, 303–314.
287. Noll T, Biselli M (1998). *Dielectric spectroscopy in the cultivation of suspended and immobilized hybridoma cells*. *J Biotechnol* 63, 187–198.
288. Ansorge S, Esteban G, Schmid G (2010). *Multifrequency permittivity measurements enable on-line monitoring of changes in intracellular conductivity due to nutrient limitations during batch cultivations of CHO cells*. *Biotechnol Prog* 26, 272–283.
289. Ansorge S, Henry O, Aucoin M, Voyer R, Carvell JP, et al. (2010). *Monitoring the Cell Size Distribution of Mammalian Cell Cultures Using On-Line Capacitance Measurements*. Dordrecht: Springer Netherlands, pp. 853–859.
291. Winkelmeier P, Glauner B, Lindl T (1993). *Quantification of cytotoxicity by cell-volume and cell-proliferation*. *ATLA-Altern Lab Anim* 21, 269–280.
292. Zimmermann D, Zhou A, Kiesel M, Feldbauer K, Terpitz U, et al. (2008). *Effects on capacitance by overexpression of membrane proteins*. *Biochem Biophys Res Commun* 369, 1022-1026.
293. Wang X, Becker FF, Gascoyne PRC (2002). *Membrane dielectric changes indicate induced apoptosis in HL-60 cells more sensitively than surface phosphatidylserine expression or DNA fragmentation*. *Biochim Biophys Acta* 1564, 412–420.
294. Cohen JJ (1993). *Apoptosis*. *Immunol Today* 14, 126–130.
295. Smith A, Parkes M, Atkin-Smith G, Tixeira R, Kh Poon I (2017). *Cell disassembly during apoptosis*. *WikiJ Med* 4.
296. Markx GH, Davey CL, Kell DB (1991). *To what extent is the magnitude of the Cole—Cole α of the β -dielectric dispersion of cell suspensions explicable in terms of the cell size distribution?* *J Electroanal Chem* 320, 195–211.

-
297. Grein TA, Loewe D, Dieken H, Salzig D, Weidner T, *et al.* (2018). *High titer oncolytic measles virus production process by integration of dielectric spectroscopy as online monitoring system*. *Biotechnol Bioeng* 115, 1186–1194.
298. Pais DAM, Portela RMC, Carrondo MJT, Isidro IA, Alves PM (2019). *Enabling PAT in insect cell bioprocesses: In situ monitoring of recombinant adeno-associated virus production by fluorescence spectroscopy*. *Biotechnol Bioeng in print*.
299. Petiot E, Ansorge S, Rosa-Calatrava M, Kamen A (2017). *Critical phases of viral production processes monitored by capacitance*. *J Biotechnol* 242, 19–29.
300. Ahmad NA, Leo CP, Ahmad AL, Ramli WKW (2015). *Membranes with Great Hydrophobicity: A Review on Preparation and Characterization*. *Sep Purif Rev* 44, 109–134.
301. Vargha-Butler EI, Zubovits TK, Hamza HA, Neumann AW (1985). *Surface tension effects in the sedimentation of polymer particles in various liquid mixtures*. *J Disper Sci Technol* 6, 357–379.
302. Wypych G (2016). *Handbook of Polymers*: Elsevier Science.
303. Choi H, Zhang K, Dionysiou DD, Oerther DB, Sorial GA (2005). *Influence of cross-flow velocity on membrane performance during filtration of biological suspension*. *Journal of Membrane Science* 248, 189-199.
304. Jonsson G (1985). *Molecular weight cut-off curves for ultrafiltration membranes of varying pore sizes*. *Desalination* 53, 3–10.
305. Breite D, Went M, Prager A, Schulze A (2016). *The critical zeta potential of polymer membranes: how electrolytes impact membrane fouling*. *RSC Advances* 6, 98180–98189.
306. Cai H, Fan H, Zhao L, Hong H, Shen L, *et al.* (2016). *Effects of surface charge on interfacial interactions related to membrane fouling in a submerged membrane bioreactor based on thermodynamic analysis*. *J Colloid Interface Sci* 465, 33–41.
307. Schäfer AI, Pihlajamäki A, Fane AG, Waite TD, Nyström M (2004). *Natural organic matter removal by nanofiltration: effects of solution chemistry on retention of low molar mass acids versus bulk organic matter*. *J Membr Sci* 242, 73–85.
308. Dizge N, Soydemir G, Karagunduz A, Keskinler B (2011). *Influence of type and pore size of membranes on cross flow microfiltration of biological suspension*. *Journal of Membrane Science* 366, 278-285.
309. Ruiz-García A, Melián-Martel N, Nuez I (2017). *Short Review on Predicting Fouling in RO Desalination*. *Membr* 7, 62.
310. Wang F, Tarabara VV (2008). *Pore blocking mechanisms during early stages of membrane fouling by colloids*. *J Colloid Interface Sci* 328, 464–469.
311. Xiao K, Shen Y, Huang X (2013). *An analytical model for membrane fouling evolution associated with gel layer growth during constant pressure stirred dead-end filtration*. *J Membr Sci* 427, 139-149.
312. Karst DJ, Serra E, Villiger TK, Soos M, Morbidelli M (2016). *Characterization and comparison of ATF and TFF in stirred bioreactors for continuous mammalian cell culture processes*. *Biochem Eng J* 110, 17–26.

7 Appendix

This chapter lists additional information on Materials and Methods, and provides some additional results as addressed in Results and Discussion.

A7.1 Materials and devices

Table A7.1 | List of consumables and materials.

Product name	Supplier
Amino acid derivatization pack and standards	Waters
CellTrics filter	Sysmex
Cryo.S	Greiner
CryoMACS freezer bag 50	Miltenyi Biotec
Cytodex 1 microcarrier	GE Healthcare Life Sciences
DAG-T-502 carbon paint	Ted Pella
Fluorinert FC-43	3M
HiScreen MabSelect SuRe LX	GE Healthcare Life Sciences
InnuPrep Plasmid mini kit	Analytik Jena
MEM non-essential amino acids solution	Gibco
NucleoSpin RNA Clean-up	Macherey & Nagel
NucleoSpin RNA Virus kit	Macherey & Nagel
Pen-Strep	Gibco
PES membrane (0.2 µm, 470 cm ²)	Spectrum Labs
PES membrane (0.2 µm, 1300 cm ²)	Refine
QIAquick gel extraction kit	Qiagen
QuantiNova Probe RT-PCR kit	Qiagen
Quant-iT PicoGreen dsDNA Assay Kit	Thermo Scientific
Qubit Protein Assay Kit	Thermo Scientific
Quick Start Bradford Protein Assay	Bio Rad
RevertAidH Minus RT kit	Invitrogen
RotorDisc 100	Qiagen
Shake flask, no baffles (125 mL, 250 mL) #431143	Corning
Shake flask, three baffles (125 mL, 250 mL) #431405	Corning
CellStar T-flask, treated (25 cm ² , 75 cm ² , 175 cm ²)	Greiner bio one
TranscriptAid T7 High Yield Transcription kit	Thermo Scientific
TrypLE Selected	Gibco
Ultra-clear centrifugation tube	Beckman Coulter

Table A7.2 | List of equipment.

Product name	Supplier
120U/DV	Watson-Marlow
AccQ-TAG Ultra HPLC	Waters
Åkta Explorer 100	GE Healthcare Bio-Sciences AB
ArcView 265 with a 4–20 mA output box	Hamilton
ATF2 with C24U-v2.0 controller	Repligen
BioProfile 100 Plus	Nova Biomedical
BioStat B Plus with 1 L Univessel	Sartorius
Cedex Bio Analyzer	Roche CustomBiotech
DasGip DCU with 0.7 L and 2.5 L vessel	Eppendorf
Dencytee	Hamilton
DIN rail bus connector (2201732)	PhoenixContact
DO probe InPro 6800	Mettler Toledo
DO probe Z010023525	Applikon
ez-control unit	Applikon
Fast Gene Mini Centrifuge	NIPPON Genetics
Fuchs-Rosenthal hemocytometer	Glaswarenfabrik Hecht
Heat block	Grant Instruments
Heracell T6060 incubator	Heraeus
Image StreamX Mark II	Amnis
Incyte	Hamilton
inoLab pH meter	WTW
KR2i pump	Spectrum Labs
KrosFlo Digital Pressure Monitor	Spectrum Labs
Mithras LB 940	Berthold Technologies
Mobius 3 L stirred tank vessel	Merck Millipore
Mr. Frosty	Nalgene
Multi-Spin PCV-3000	Grant-bio
Multitron Pro shaking incubator, 50 mm throw	Infors HT
Optima TM LE-80K ultracentrifuge with SW28	Beckman Coulter
pH probe 405 DPas sc k8s	Mettler Toledo
pH probe Z001023551	Applikon
PharMed BPT NSF-51, ID 0.76 mm, wall 0.86 mm	Saint-Gobain Biopharma
Porolux 500	Porometer
Pressure transducer ACPM-799-01N	Spectrum Labs
Quorum Q150T ES	Quorum
RE40D Refractometer	Mettler Toledo
Resistance thermometer pT10	UMO MK
Rotor-Gene Q	Qiagen
SEM JSM-6010LA	JOEL
SurPASS electrokinetic analyzer	Anton Paar
Thermomixer Block	Eppendorf
Tecan Nano Quant infinite M200	Tecan
Vapro pressure osmometer	Wescor
VialTweeter UP200St sonicator	Hielscher Ultrasonics
ViCell XR cell counter	Beckman Coulter
Zetasizer Nano ZS	Malvern Instruments

Table A7.3 | Validated measurement ranges of different assays for metabolite quantification.

Device	Metabolite	Measurement range	Rel. standard dev.
BioProfile 100 Plus	Glucose	2.8 – 41.1 mM	11.0 %
	Glutamate	0.2 – 2.6 mM	4.7 %
	Glutamine	0.2 – 2.6 mM	3.4 %
	Lactate	2.2 – 333.0 mM	1.6 %
	Ammonium	0.2 – 5.2 mM	2.2 %
Cedex Bio Analyzer	Pyruvate	0.2 – 8.0 mM	5 %
AccQ-TAG Ultra HPLC	Anionic amino acids	1.25 – 15.00 μ M	< 7 %

A7.2 Standard operating procedures

Available on request from Bioprocess Engineering Department.

A7.2.1 SOP – Flavivirus plaque assay

Document: V_11 v02
Date: 26.10.2017
Author: Nikolay, Best

A7.2.2 SOP – One-step TaqMan RT-qPCR

Document: V_13 v01
Date: 01.11.2017
Authors: Nikolay, Bartels

A7.2.3 SOP – Synthesis of *in-vitro* RNA copy number standards

Document: V_13 v01
Date: 13.10.2018
Authors: Wasik, Nikolay

A7.2.4 SOP – Immunostaining for flow cytometric flavivirus detection

Document: V_13 v01
Date: 04.04.2018
Authors: Coronel, Bartels, Fritsche, Kupke, Nikolay

A7.4 Supplementary

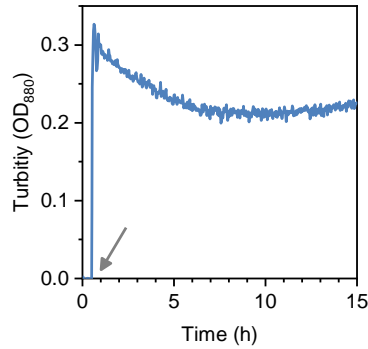


Figure A7.1 | Turbidity measurement for adherent Vero cell inoculation. The signal was zeroed in Z-Medium with a microcarrier concentration of 3.1 g/L. Subsequent cell inoculation (29 cells/MC, indicated by arrow) resulted in turbidity increase and the slow decrease correlated with cell adhesion to the carriers.

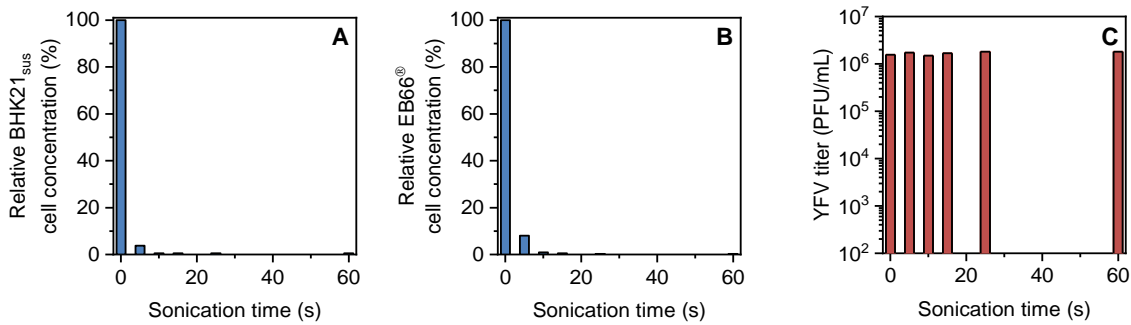


Figure A7.2 | Impact of ultra-sonication on cell concentration and infectious virus titers. Relative cell concentrations of (A) BHK-21_{SUS} and (B) EB66[®] cells quickly decreased, while (C) the infectious YFV titer was not impaired by sonication. Sonication was performed with 1 mL working volume at 4 °C and an energy input of 150 W/s (90 % amplitude, 80 % pulse time).

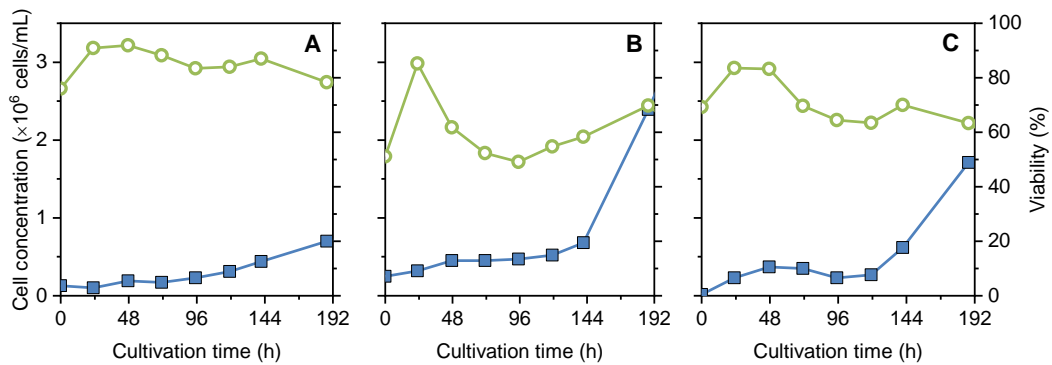


Figure A7.3 | Cell budding of Verosus cells in SMIF8 medium. Adherent Vero cells were maintained in (A) CD-U3, (B) BGM and (C) SMIF8 medium at super-confluency state for 356 days. Cells in supernatant (blue square) were regularly harvested. To increase viability (green circle), viable cells were concentrated by centrifugation and resuspended in conditioned medium for further experiments.

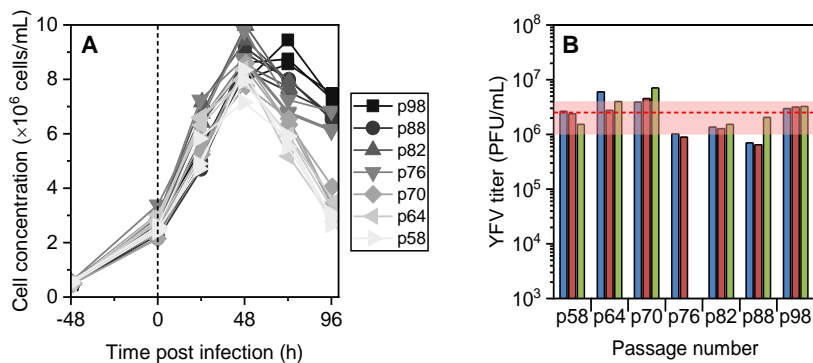


Figure A7.4 | Impact of BHK-21_{SUS} passage number on yellow fever virus production. (A) BHK-21_{SUS} were cultivated and infected at every 6th or 10th passage following the exact same procedure (biological triplicates indicated by one symbol). Dashed vertical line indicates time point of infection. (B) YFV titers of each passage was measured (blue, red and green bars indicate one biological experiment). Red area indicates standard deviation and dashed horizontal line indicates arithmetic mean of all passages.

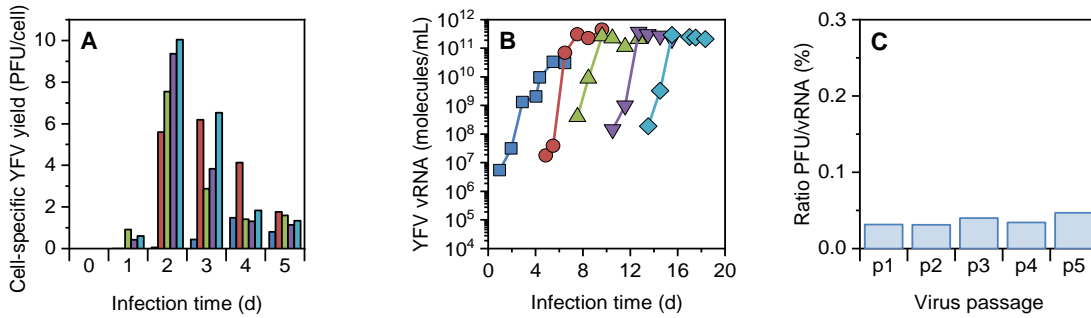


Figure A7.5 | Yellow fever virus passaging in EB66[®] cells. Cells were cultivated in shake flasks with CDM4Avian medium and were infected at 4.3×10^6 ($\pm 0.8 \times 10^6$) cells/mL reaching final concentrations of 1.4×10^7 ($\pm 0.1 \times 10^7$) cells/mL 48 hpi. **(A)** Cell-specific virus yields at fixed time intervals for each virus passage. **(B)** Viral RNA (vRNA) copy numbers over continuing virus passaging. **(C)** Ratio of infectious YFV particles (PFU) to vRNA levels at time point of maximum infectious virus titer for each virus passage (expressed in percentage). Each virus passage is indicated by a different color (blue = p1, red = p2, green = p3, purple = p4, turquoise = p5).

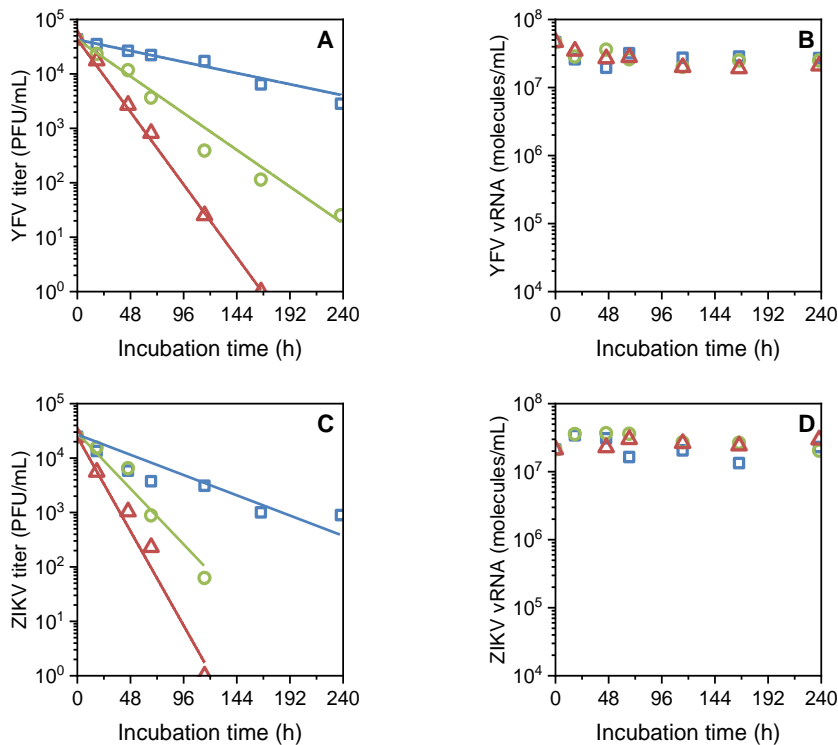


Figure A7.6 | Yellow fever virus and Zika virus inactivation in CDM4Avian medium. Temperature-dependent virus inactivation in basal growth medium (without cells) at 4 °C (blue), 33 °C (green) and 37 °C (red). **(A, C)** Logarithmic decrease of infectious virus titers. Slope of linear regression describes half-life time $t_{1/2}$ (first-order kinetic) of infectious virus particles (with increasing temperature for YFV: 63 h, 20 h, 11 h; and for ZIKV: 41 h, 14 h, 8 h). **(B, D)** Viral RNA copy numbers.

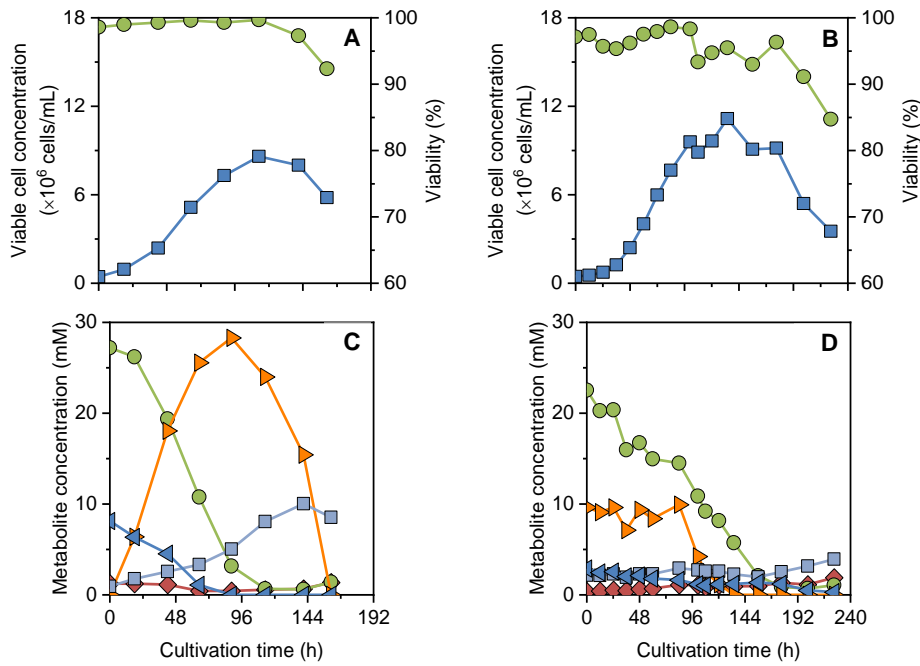


Figure A7.7 | Characterization of suspension cell growth in shake flask batch cultures. (A, C) BHK-21_{SUS} and (B, D) EB66[®] cells with respective metabolite profiles. Cell concentrations (blue square) and viability (green circle); glucose (●), glutamine (◄), glutamate (◆), lactate (▶), ammonia (■); median of n=3.

Table A7.4 | Decreasing time intervals for different medium exchange strategies with BGM as basal growth medium for the pseudo-perfusion cultivation of BHK-21_{SUS} cells.

Sample	RV/d-based exchange intervals (h)	Glucose-based exchange intervals (h)	Glutamine-based exchange intervals (h)
1	23	80	20
2	26	18	19
3	23	30	10
4	22	15	8.0
5	25	14	6.0
6	-	12	5.0
7	-	10	4.0
8	-	7.0	3.5
9	-	7.5	3.5 *
10	-	5.5	-
11	-	6.0	-

* Handling issues for intervals below 3.5 h required switch from the glutamine-based exchange strategy to a glucose-based strategy (indicated by arrow).

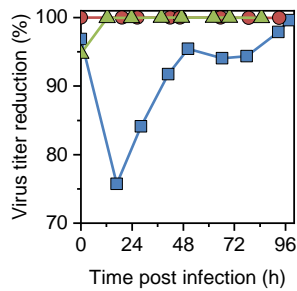


Figure A7.8 | Decrease in the percentage of yellow fever virus titers (permeate vs. bioreactor) during membrane-based TFF and ATF perfusion cultivations. BHK-21_{SUS} perfusion run in TFF configuration (blue square); EB66[®] perfusion run in either TFF configuration and GRO-I medium (red circle) or ATF configuration and CDM4Avian medium (green triangle).

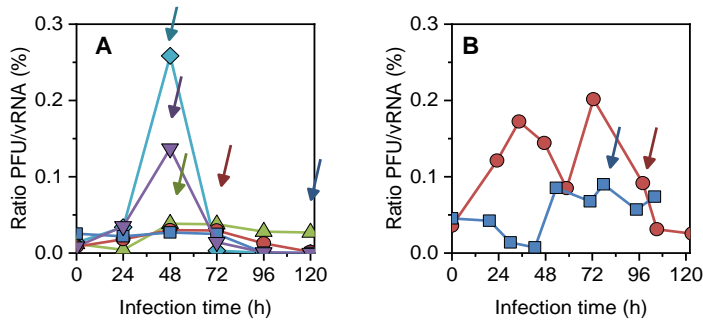


Figure A7.9 | Ratio of infectious virus titer to viral copy number (PFU/vRNA) of Zika virus infected EB66[®] cells. (A) Batch cultivation in shake flasks during ZIKV passaging in EB66[®] cells. Each virus passage is indicated by a different color (blue = p1, red = p2, green = p3, purple = p4, turquoise = p5). (B) Perfusion cultivation in bioreactors during ZIKV infection (blue = ATF-17pL, red = ATF-34pL). Arrow indicates time point of maximum, infectious ZIKV titer.

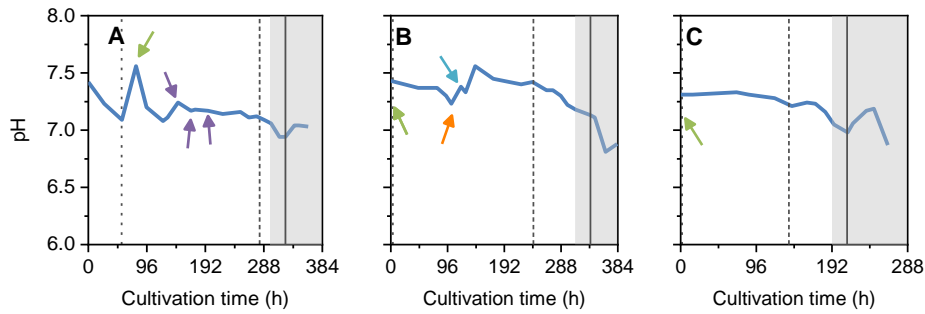


Figure A7.10 | Changes in pH values during EB66[®] perfusion cultivation and virus infection. (A) Manual ATF perfusion rate control (ATF-M); (B) perfusion rate control (ATF-17pL); (C) inoculated from a cryo bag and automated perfusion rate control (ATF-34pL). Arrows indicate manual interventions (green = start of perfusion operation, purple = sodium chloride addition, orange = methionine addition, turquoise = cell harvest for cryo bag preparation). Dotted vertical line indicates start of perfusion pump; dashed vertical line indicates time point of infection; grey area indicates cell decline phase; solid vertical line indicates maximum virus concentration.

Table A7.5 | Transferability of cultivation-specific cell factors to other cultivations to determine the viable cell concentration and viable cell volume.

Viable cell concentration

		Calibration set		
		#1	#2	#3
Validation set	#1	3.1 %	19 %	22 %
	#2	31 %	2.3 %	5 %
	#3	37 %	3 %	3.6 %

Viable cell volume

		Calibration set		
		#1	#2	#3
Validation set	#1	2.8 %	14 %	14 %
	#2	29 %	2.4 %	3 %
	#3	20 %	7 %	2.2 %

Cell factors, as listed in Table 4.7, were used to estimate the viable cell concentration and viable cell volume of other perfusion cultivations. Signal linearity to offline measured data was expressed as normalized standard error of calibration (nSEC, Equation 30) or root-mean-square standard error of transfer (SET, Equation 31).

■ Indicates nSEC, validation set = calibration set;
 ■ indicates SET <10 %; ■ indicates SET <20 %; ■ indicates SET >20 %.

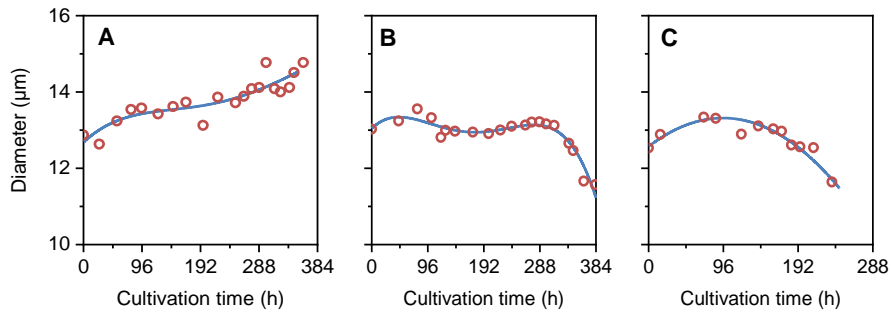


Figure A7.11 | Interpolated cell diameters of EB66® cells during perfusion cultivations. Offline data (red circle) were fitted by a polynomial function (blue line) for data interpolation. (A) ATF-M; (B) ATF-17pL; (C) ATF-34pL.

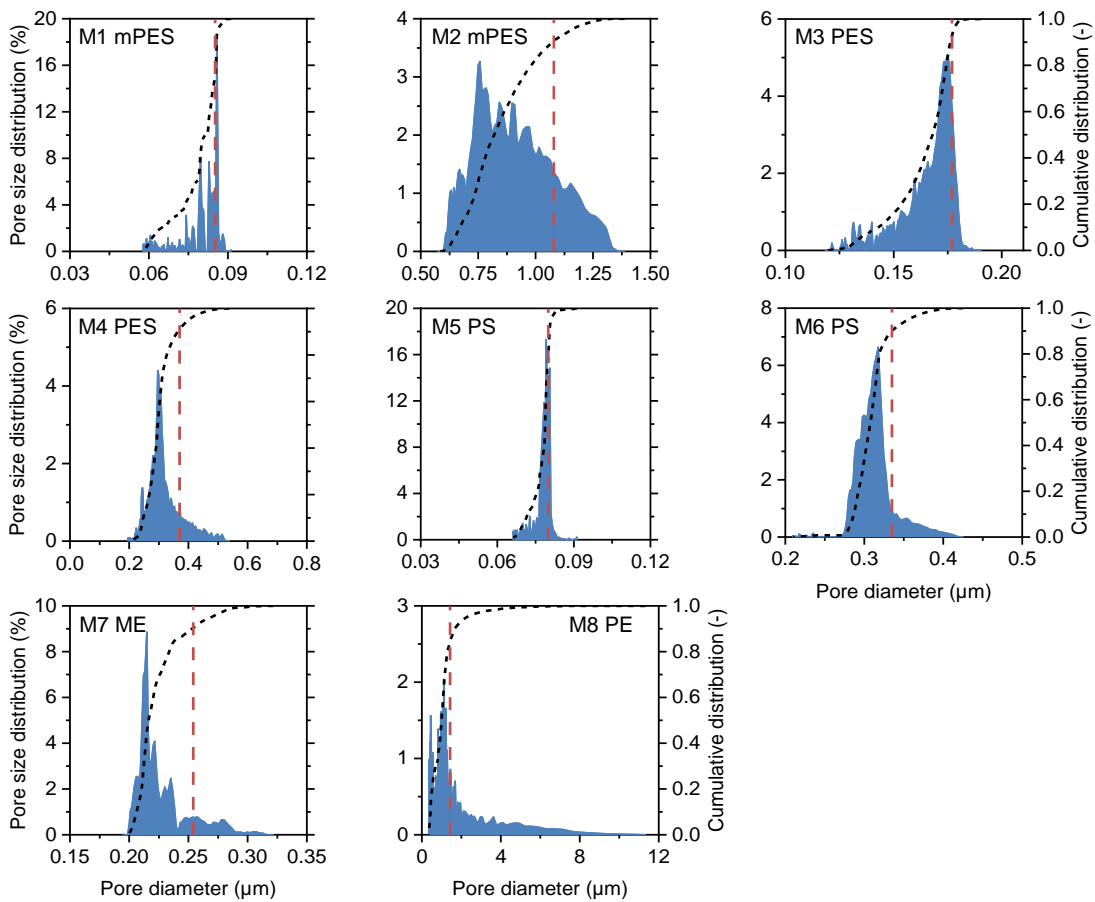


Figure A7.12 | Pore size distributions of tested hollow fiber membranes according to bubble point measurements. Membranes were wetted in the pore-filling liquid Fluorinert FC-43 and pore sizes were measured with capillary flow porometry. Blue area: Normalized cumulative distribution summed up to a cumulative distribution of 1 (black dashed line). Red dashed vertical line indicates estimated cut-off (D_{90}) of membranes.

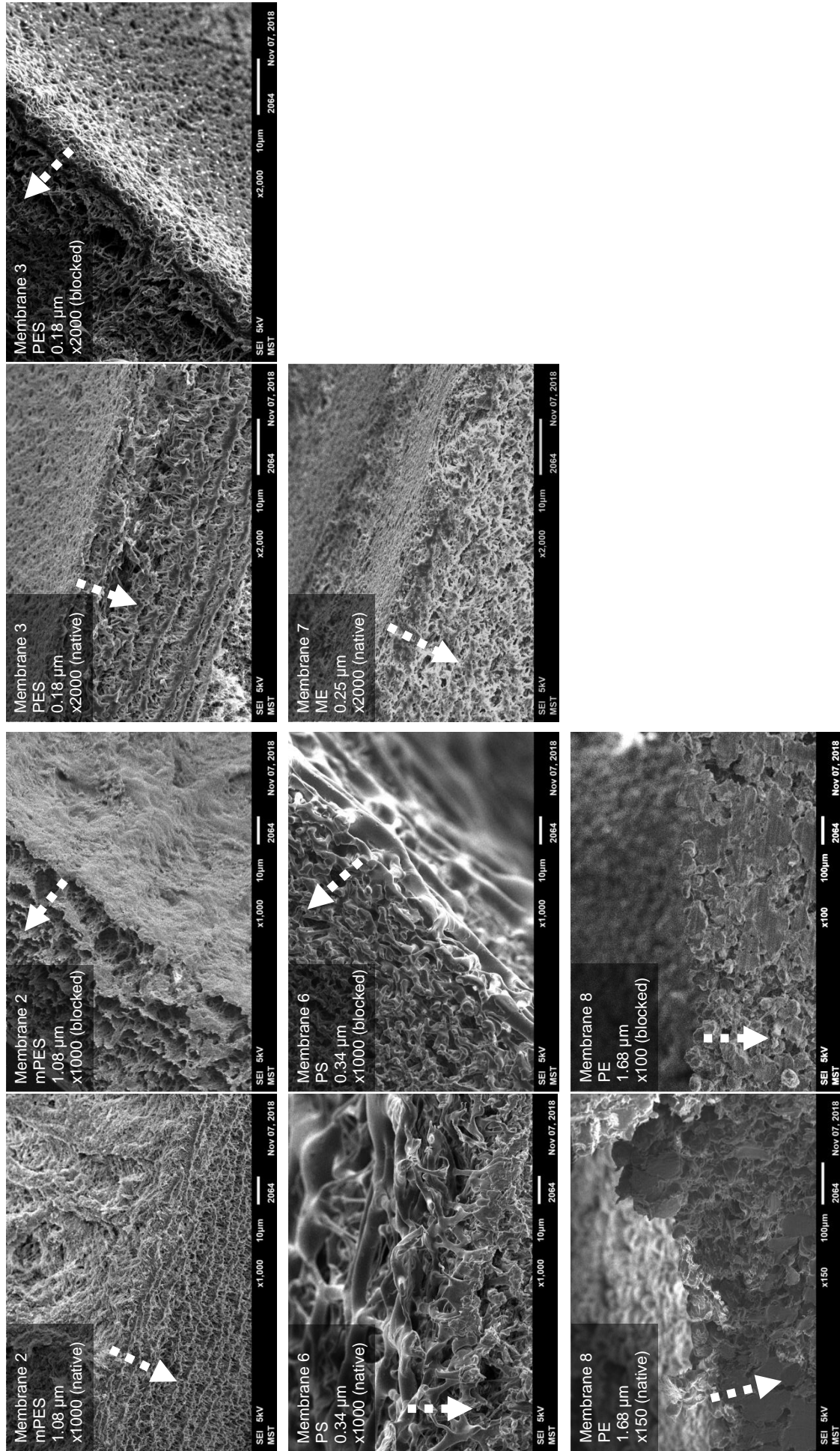


Figure A7.13 | Oblique SEM images of the cross-section of unused and blocked hollow fiber membranes. Surface-related membrane fouling was in particular observed for highly jagged membranes (#2), whereas smooth surface structures with open pore structures (such as for #6 and #8) did not reveal a filter cake formation. Cross-section images enabled a better understanding on the inner membrane structure. Arrow indicates permeate flow direction across the membrane.

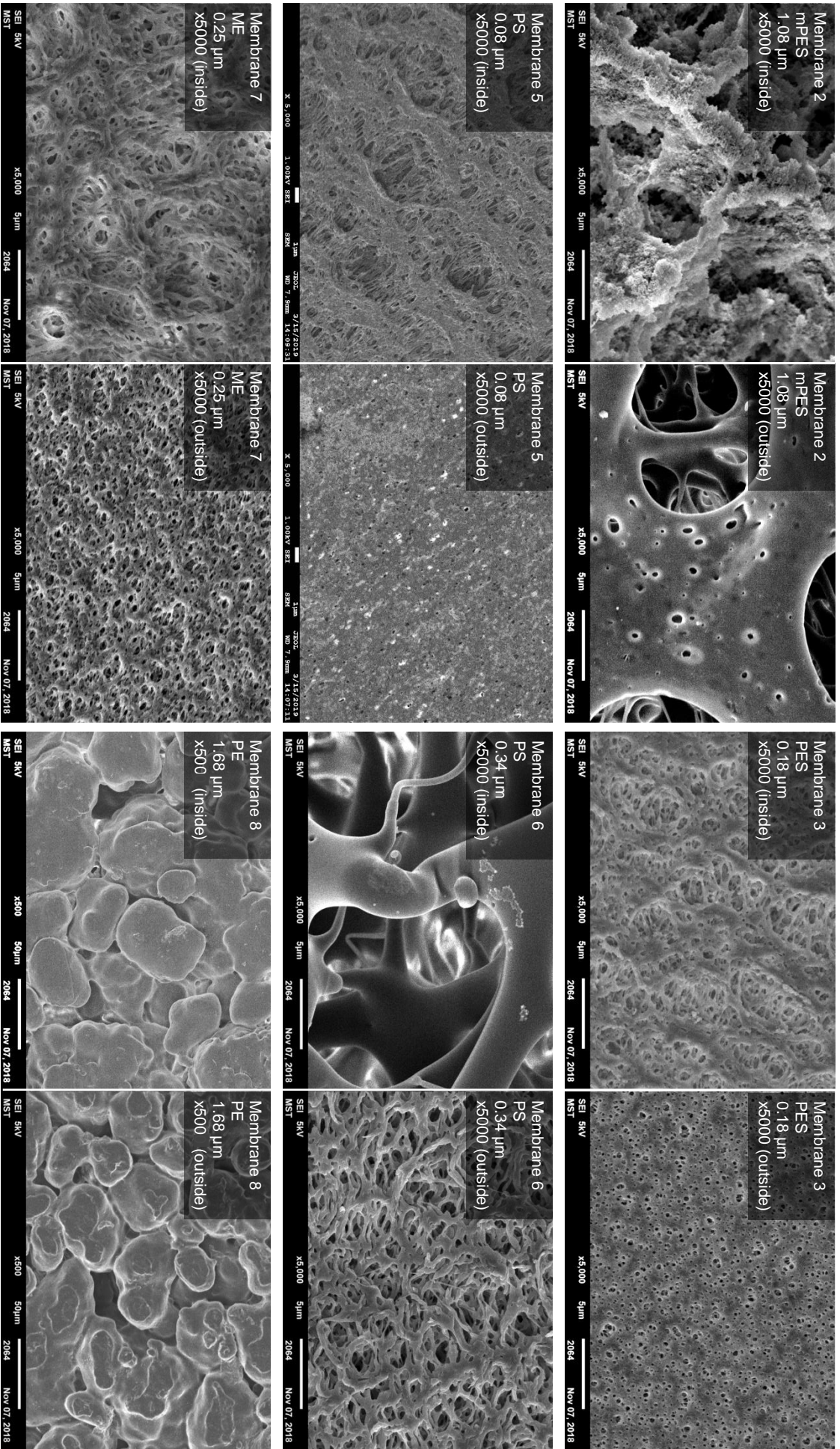


Figure A7.14 | Frontal SEM imaging of the inner and outer surface of unused hollow fiber membranes. Most membranes revealed an asymmetric structure with the exception of #8.

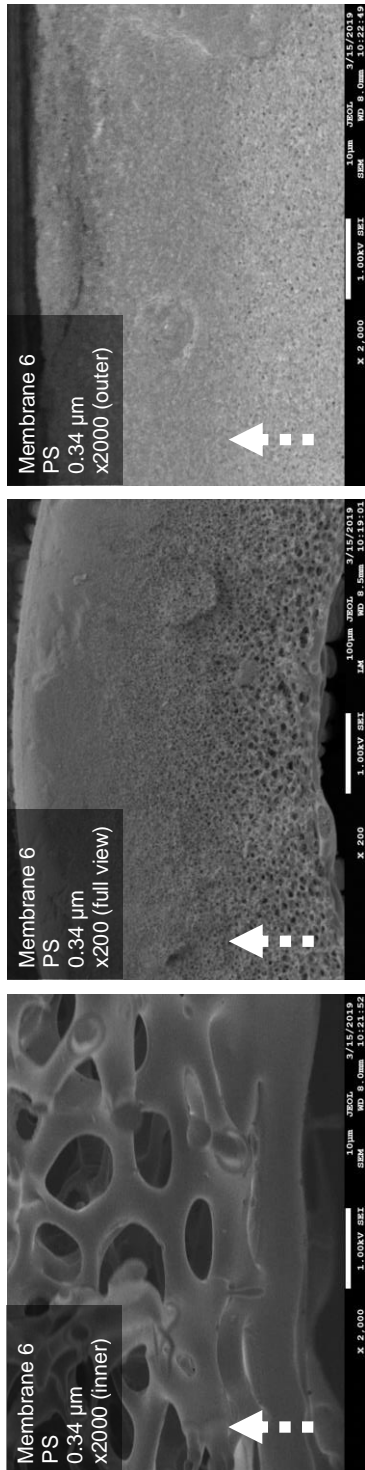


Figure A7.15 | Cross-sectional SEM images of an unused PS 0.34 μm membrane. (Left) Inner membrane side; (middle) full view across membrane thickness; (right) outer membrane side. Arrow indicates permeate flow direction.

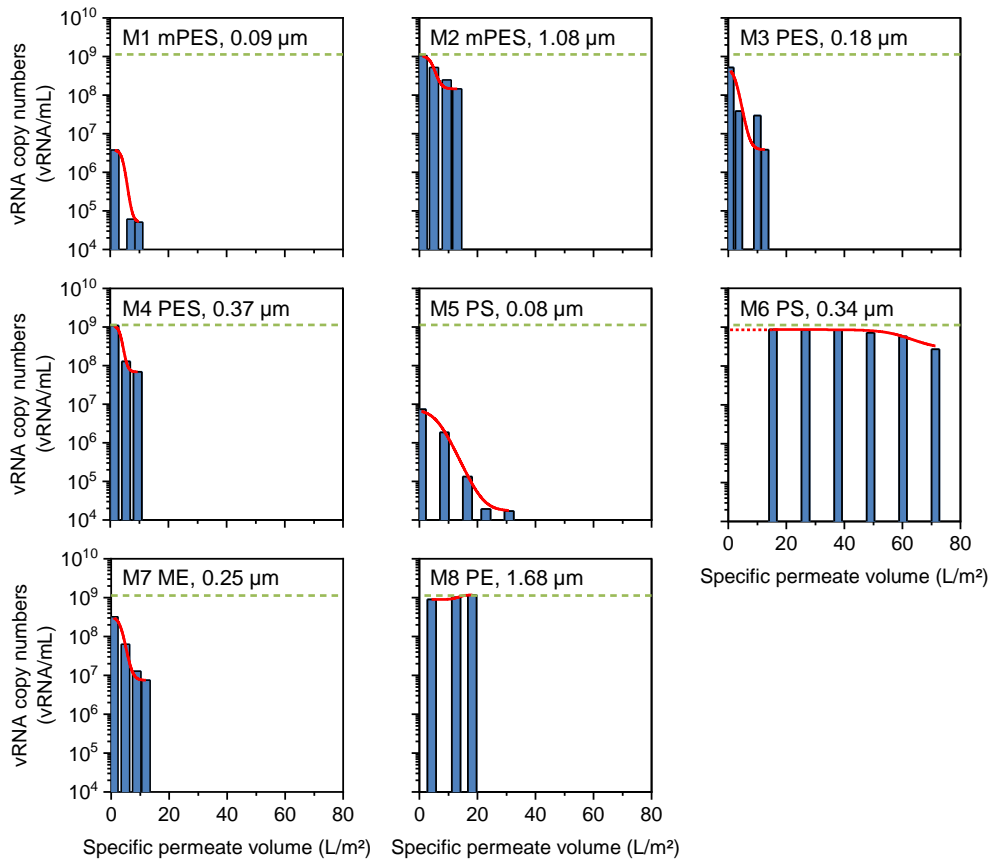


Figure A7.16 | Viral RNA copy numbers in permeate decrease with filter fouling in different hollow fiber membranes during perfusion operation. Green dashed horizontal line indicates vRNA copy number in the inlet. Data fitting (red solid line) visualizes virus retention progression.

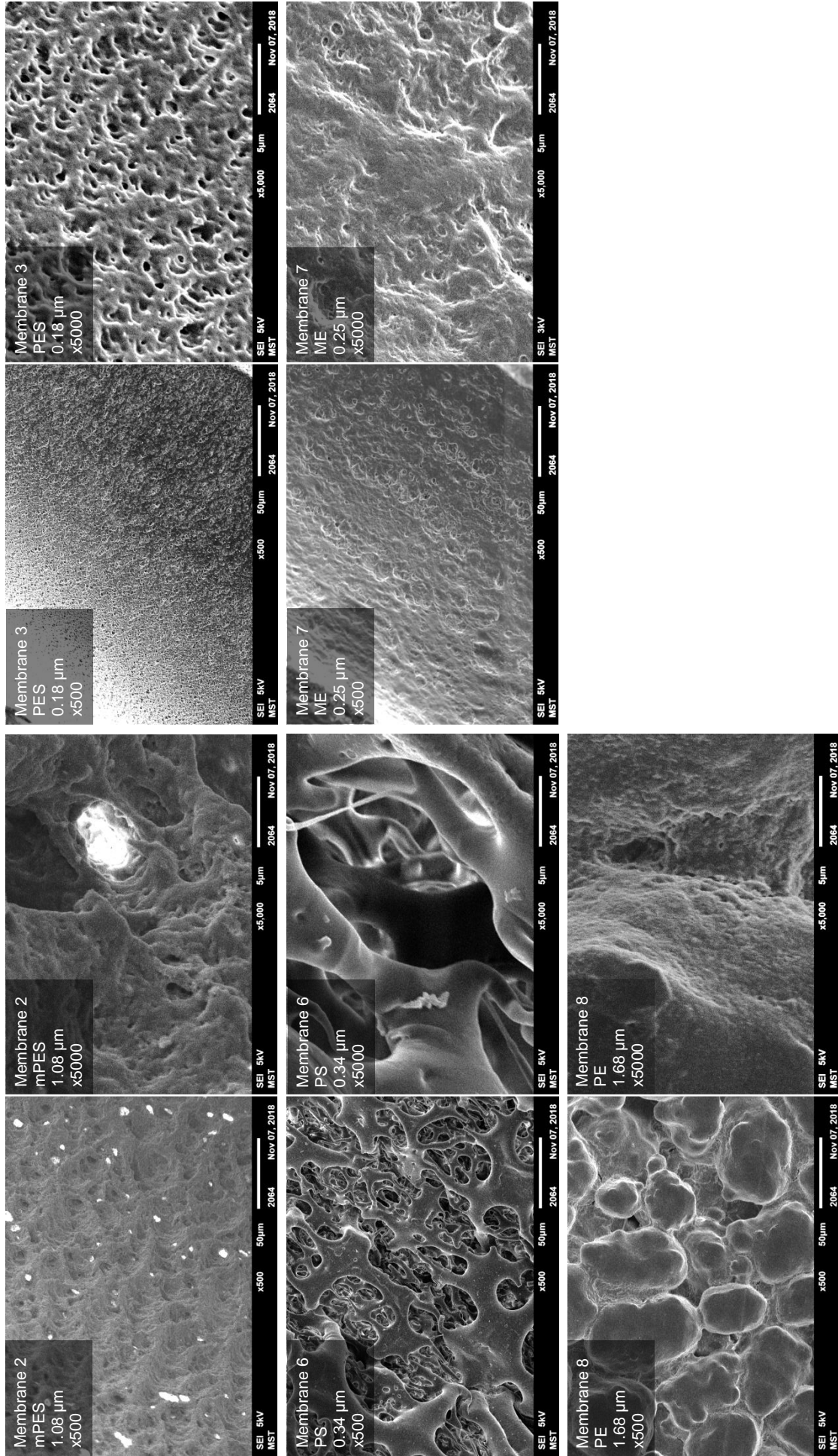


Figure A7.17 | SEM imaging of inner membrane surfaces after complete membrane blockage for filter fouling experiments. Membranes were operated in cross-flow filtration mode to harvest yellow fever virus from infected BHK-21 sus cells. Membranes were dried for SEM imaging potentially modifying the filter cake appearance. White artefacts on mPES membranes are related to insufficient chromium sputtering.

